


Probing the physicochemical properties of the Leo Ring and the Leo I group

Sameer,¹  Jane C. Charlton,¹ Glenn G. Kacprzak,^{2,3} Anand Narayanan,⁴ Sriram Sankar,⁵ Philipp Richter,⁶ Bart P. Wakker,⁷ Nikole M. Nielsen,^{2,3} and Christopher W. Churchill⁸

¹Department of Astronomy & Astrophysics, 525 Davey Lab, The Pennsylvania State University, University Park, PA 16802, USA

²Centre for Astrophysics and Supercomputing, Swinburne University of Technology, Hawthorn, Victoria 3122, Australia

³ARC Centre of Excellence for All Sky Astrophysics in 3 Dimensions (ASTRO 3D)

⁴Department of Earth and Space Sciences, Indian Institute of Space Science & Technology, Thiruvananthapuram 695547, Kerala, INDIA

⁵South African Astronomical Observatory, Cape Town (SAAO)

⁶Institut für Physik und Astronomie, Universität Potsdam, Haus 28, Karl-Liebknecht-Str. 24/25, D-14476, Potsdam, Germany

⁷Department of Astronomy, University of Wisconsin-Madison, 475 N. Charter Street, Madison, WI 53706, USA

⁸Department of Astronomy, New Mexico State University, Las Cruces, NM 88003, USA

Accepted 2022 January 5. Received 2022 January 5; in original form 2021 October 13

ABSTRACT

We present an absorption line study of the physical and chemical properties of the Leo H I Ring and the Leo I Group as traced by 11 quasar sightlines spread over a $\approx 600 \times 800$ kpc² region. Using *HST*/COS G130/G160 archival observations as constraints, we couple cloud-by-cloud, multiphase, Bayesian ionization modeling with galaxy property information to determine the plausible origin of the absorbing gas along these sightlines. We search for absorption in the range $600 \text{ km s}^{-1} < cz < 1400 \text{ km s}^{-1}$ consistent with the kinematics of the Leo Ring/Group. We find absorption plausibly associated with the Leo Ring towards five sightlines. Along three other sightlines, we find absorption likely to be associated with individual galaxies, intragroup gas, and/or large scale filamentary structure. The absorption along these five sightlines is stronger in metal lines than expected from individual galaxies, indicative of multiple contributions, and of the complex kinematics of the region. We also identify three sightlines within a $7^\circ \times 6^\circ$ field around the Leo Ring, along which we do not find any absorption. We find that the metallicities associated with the Leo Ring are generally high, with values between solar and several times solar. The inferred high metallicities are consistent with an origin of the ring as tidal debris from a major galaxy merger.

Key words: galaxies: groups: general – galaxies: interactions – quasars: absorption lines

1 INTRODUCTION

The circumgalactic medium (CGM) is an important and dynamic interface between a galaxy and its surroundings. This medium is host to a significant fraction of the baryons in galaxies (Wakker & Savage 2009; Werk et al. 2014), and therefore harbours most of the cosmic-fuel that forms stars in the galaxies. It is also the site where the energy output from stellar feedback and AGN activity is deposited. The CGM, therefore, is intertwined with the evolution of galaxies (Tumlinson et al. 2017).

The CGM is influenced by a wealth of processes such as in-

flows, outflows, recycled accretion, tidal interactions, and by the effects of cosmic rays and magnetic fields. These processes determine the properties of the CGM such as density, temperature, and metallicity, which are complex and non-uniform even in a single galaxy, and which globally depend on galaxy properties such as mass, star formation rate, and environment. Spectra of background quasars are sensitive probes of the gas along their sightlines, allowing us to resolve the different structures and processes shaping the CGM of intervening galaxies.

The low surface density of bright quasars often results in only one quasar sight-line passing through a given galaxy. Though statistically useful to describe an ensemble, a single data-point per galaxy can limit our understanding of the physical processes within

* E-mail: sxx15@psu.edu

the CGM. [Keeney et al. \(2013\)](#) presented a study of three QSOs probing the galaxy ESO 157-49, an edge-on spiral, at impact parameters $\rho < 200 h_{70}^{-1}$ kpc, with absorption along the two major axis sightlines being consistent with a “galactic fountain” of recycled gas; while the absorption along the other minor axis sightline was found to trace outflows. [Bowen et al. \(2016\)](#) identified four sightlines passing through the halo of the spiral galaxy, NGC 1097, within 0.2-0.6 virial radii disk of gas rotating roughly planar to, but more slowly than, the inner disk observed from 21 cm data, and which also includes gas infalling from the IGM, recreates the data well. [Chen et al. \(2014\)](#), using a quadruply-lensed quasar, demonstrated that multiple-QSO probes offer crucial insights into physical properties of the CGM around galaxies. [Péroux et al. \(2018\)](#) studied a region of ≈ 30 kpc² associated with the CGM of a $z \approx 1$ galaxy using an intervening foreground absorber, aided by the identification of bright, extended background galaxies. Their study suggests efficient metal mixing on kpc-scales in the galaxy’s CGM.

[Lehner et al. \(2015\)](#), using a sample of 18 sightlines probing the M31 halo within a projected distance of $\approx 2R_{vir}$ ($R_{vir} = 300$ kpc for M31), associate the absorption probed by these sightlines with the CGM of M31 since the absorption centroids are within 40–90 km s⁻¹ of the systemic velocity of M31. For 7/18 sightlines which are within R_{vir} , they detect absorption in low ions (C II, Si II) through intermediate (Si III, Si IV) and high ions (C IV, O VI), suggesting that the CGM of M31 is extended out to at least its virial radius. In a followup study, [Lehner et al. \(2020\)](#) identified several additional sightlines yielding a total of 43 QSOs probing the CGM of M31 from 25 to 569 kpc. They do not find an azimuthal dependence of CGM properties, however there is a dependence on the projected distance.

FIRE simulations of $z=0$ Milky Way analogs ([Anglés-Alcázar et al. 2017](#)) suggest that galaxy-galaxy interactions and intergalactic transfer of mass from other galaxies via galactic winds dominates the gas accretion for a considerable period of a galaxy’s evolution. It is therefore expected that gas transfer could be detected in CGM observations of galaxy groups. H I 21-cm maps have revealed telltale signatures of such interactions, which are seen, for example, in the form of hydrogen gas extending from the disk of the M31 galaxy to M33 ([Wolfe et al. 2013](#)). [de Blok et al. \(2018\)](#) presented a study of an extended H I distribution centered on the M81 triplet - M81, M82, and NGC 3077. They detect small H I clouds and complexes which are spatially proximal to the main H I tidal features of the triplet, suggesting they are all debris of the interaction that formed the triplet. This debris is similar to the tidal features arising in simulations, indicative of gas transfer from the satellites onto the more massive galaxy. Moreover, it is plausible that these interactions have resulted in the strong star-formation driven molecular outflows observed in M82 ([Leroy et al. 2015](#)).

Association of absorption components with particular galaxies in galaxy groups is challenging. There is often an ambiguity about which galaxy might be responsible for the absorption, and in some cases the gas may not be bound to a particular galaxy. Studies hint that the CGM of groups is more extended, and their kinematics broadened as compared to those of isolated galaxies due to a superposition of individual galaxy halos in the group ([Bordoloi et al. 2011](#)), or by intergalactic gas transfer between the group members ([Nielsen et al. 2018a](#)).

[Kacprzak et al. \(2010\)](#) in their work on the CGM of galaxy groups found two galaxies associated with a DLA at $z=0.313$, with three more galaxies in close vicinity. The authors posit that metal-enriched winds are an unlikely origin for the DLA because of its

low metallicity, $\log Z/Z_{\odot} \approx -1.0$. They favor an origin of the absorption from tidal debris and/or a diffuse intragroup medium based on perturbed morphologies for three galaxies and extended optical tidal tails. In their study of the same DLA system at $z=0.313$, [Guber et al. \(2018\)](#) demonstrate by help of optical spectroscopy with UVES that the strongly varying dust depletion in the different absorber components (as traced by the Mn II, Ca II, and Ti II ratios) represents the best parameter to discriminate between dust-rich disk components and (dust-poor) tidal features in group environments. To gather a better understanding of the origin of this DLA, [Chen et al. \(2019\)](#) mapped the CGM using nebular emission-lines with VLT/MUSE. However, due to the redshift and surface brightness limits, only a partial view of the CGM could be obtained. Nevertheless, by combining the quasar absorption line data, MUSE gas kinematics, ionization conditions, and group galaxy motions, they concluded that the DLA originates in streams of gas stripped from sub-L* group members. Their study demonstrates that interactions in low-mass galaxy groups can pollute the intragroup medium with metal-enriched gas from star-forming regions. [Richter et al. \(2018\)](#) studied the chemical and physical conditions in one of the tidal gas streams (Spur 2) around the Whale galaxy, NGC 4631. They combined *HST*/COS observations of a background quasar with the 21-cm data from the HALOGAS project, and conclude that the observed properties of region probed by the sightline favor a tidal disruption scenario in which a now closely separated (≈ 6 kpc) satellite galaxy, NGC 4627, stripped metal- and dust-poor gas out of the outer-disk of NGC 4631.

Despite these recent efforts to better understand the nature of the CGM in galaxy groups, there remains many questions. Recent results disagree as to whether the CGM metallicity is elevated in group environments ([Lehner 2017](#); [Pointon et al. 2020](#)). Compounding the disagreement, all of these studies were done on a limited number of galaxy groups lacking measured velocity dispersions or quantified group properties. Therefore, a general characterization of the gas distribution in galaxy groups remains an open question.

The Leo Ring is a vast region of H I gas detected in 21-cm emission, nearly 200 kpc in diameter. It is in the environment of the Leo-I group, and because of its proximity to the Milky Way, the combined region is an ideal place to study the distribution of gas in a galaxy group. The Leo-I group is so nearby ($D \leq 15$ Mpc) that even faint dwarf galaxies can be detected. [Müller et al. \(2018\)](#) identified 36 new potential dwarf galaxy candidates in their $500^{\circ} \times 500^{\circ}$ survey of *gr* SDSS images within the extended region of the Leo-I group. Very Large Array (VLA) 21-cm maps show the presence of gas clumps in the Leo Ring ([Schneider 1985](#)). The origin of the Leo Ring has been disputed - either inflowing material or tidal debris from an interaction. [Rosenberg et al. \(2014\)](#), using three QSO sightlines behind the Leo Ring, measured a metallicity $\approx 0.1 Z_{\odot}$ which is higher than expected for pristine gas but lower than expected from a major galaxy interaction. Using numerical simulations, [Michel-Dansac et al. \(2010\)](#) showed that the ring can plausibly be produced by a head on collision between M96 and NGC 3384.

Evidence is now mounting in favor of a tidal origin of the Leo Ring. [Corbelli et al. \(2021\)](#) have performed Multi Unit Spectroscopic Explorer (*MUSE*) optical integral field spectroscopy of three H I clumps in the Leo Ring, detected ionized hydrogen in the ring, and identified four nebular regions fueled by massive stars. Using the metal emission lines of [O III], [N II], and [S II] they inferred metallicities \gtrsim solar, inconsistent with an origin from primordial inflowing gas. The origin of the Leo Ring via such a galaxy-galaxy

encounter is in agreement with hydrodynamical simulations (Bekki et al. 2005; Michel-Dansac et al. 2010).

In this work, we identify three lines of sight passing directly through the Leo H I Ring and associated regions of interaction and five lines of sight passing through the same Leo Group at larger distances from the H I ring detected in 21cm. We also identify three sightlines in the same field which do not show any absorption within the heliocentric velocity range of 600-1400 km s⁻¹ related to the group. For each sightline with detected absorption, we conduct cloud-by-cloud, multiphase, Bayesian ionization modeling analysis (Sameer et al. 2021)[S21] and consider whether absorption is due to tidal debris, and/or an individual dwarf galaxy, and/or the CGM of one or more galaxies, and/or the intragroup medium at large. The paper is organized as follows: in Section 2 we describe the spectral observations that are analysed in this work; in Section 3 we describe the methodology used to determine the physical conditions of an absorber; in Section 4 we present our results; in Section 5 we summarize and discuss conclusions about the physical conditions in the Leo Group region based on the absorption seen along the sightlines. We conclude in Section 6. Throughout this work, we assume a cosmology with $H_0 = 70 \text{ km s}^{-1} \text{ Mpc}^{-1}$, $\Omega_M = 0.3$, and $\Omega_\Lambda = 0.7$. Abundances of heavy elements are given in the notation $[X/Y] = \log(X/Y) - \log(X/Y)_\odot$ with solar relative abundances taken from Grevesse et al. (2010). All the distances given are in physical units. All the logarithmic values are presented in base-10.

2 OBSERVATIONS AND DATA

The background quasars in this study have UV spectra from the Cosmic Origins Spectrograph (COS) on the Hubble Space Telescope (*HST*). Table 1 presents the details of the observations of the 12 sightlines with COS observations in the field around Leo Ring and the Leo I group. The 7° × 6° field, containing the Leo Ring along with the 12 sightlines, is shown in Figure 1. We do not study sightline SA because of the poor S/N ratio of 0.1.

The UV *HST*/COS spectra in this study are taken from the Barbara A. Mikulski Archive for Space Telescopes (MAST). The observations use the G130M and G160M gratings spanning observed wavelength ranges of 1135-1457 Å and 1399-1794 Å, respectively. The spectra have an average resolving power of $R \approx 20,000$ and cover a range of ions including the H I Lyman series, C II, C III, C IV, N V, Si II, Si III and Si IV. The spectra were reduced following the procedures in Wakker et al. (2015). In essence, spectra are processed with CALCOS v3.2.1 and are aligned using a crosscorrelation, and then shifted to ensure that (1) the velocities of the interstellar lines match the 21cm H I profile, and (2) the velocities of the lines in a single absorption system are aligned properly. The exposures are then collectively combined by summing total counts per pixel prior to converting to flux.

Along all the sightlines, on the low end of the velocity range of interest, the H I Ly α absorption could be affected by the right wing of the geocoronal airglow emission line. The strength of the airglow emission varies from observation to observation, and depends on solar activity. The shape of the emission profile, however, does not vary much. The location and amplitude change, and must be determined from a fit to the data for each sightline. We use the publicly available community generated airglow templates¹ (Bourrier et al.

2018) to fit the emission profile, and inspect whether it is affecting the H I Ly α absorption of interest. We fit the H I Ly α geocoronal emission template for each sightline and show that it does not significantly affect the H I Ly α absorption of interest. The emission line, and the corresponding template fit for sightlines SB-SL are shown in Figures B1 – L1. In most of these figures a plateau can be seen on the blueward side of the Galactic Ly α trough that is elevated about the Galactic absorption by a wing of the geocoronal airglow emission line. Such a wing is surely also elevating the flux on the redward side of Galactic Ly α as well. In these cases, it appears that a simple scaling of the airglow emission template to fit the observed geocoronal emission is failing. The response of the COS detector becomes non-linear when the count rate is high enough. As a result, if the model is scaled to match the counts at the peak of the Ly α emission, the wings may be underscaled. Furthermore, because of the COS optics, the geocoronal Ly α emission fills the COS aperture, which is difficult to model. The excess counts from the wings of the bright geocoronal Ly α emission could cause an incorrect flux zero point in the H I Ly α absorption profiles of our Leo I group absorbers, affecting them at velocities of 600 km s⁻¹ up to $\sim 1000 \text{ km s}^{-1}$. To address this problem which is noticeably affecting sightlines SC, SG, and SH, we obtain 100 MC realizations, varying the flux zero level (by an amount drawn from a uniform distribution between 0 and average of affected contiguous pixels) to explore the range of parameter space that is consistent with the data in the presence of such a systematic zero-point uncertainty.

In addition to the effect of H I Ly α airglow emission, the O I $\lambda 1302$ transition is also affected by the O I geocoronal emission. We minimize its effect by using observations taken during orbital night, i.e when the Sun is below the horizon. We use the TIMEFILTER module from the COSTOOLS package to filter unwanted data (SUN_ALT > 0) and rerun the CALCOS pipeline on the filtered data to generate the airglow emission corrected spectrum. However, this step considerably reduces the signal-to-noise of the corrected region of the spectrum covering O I $\lambda 1302$.

We performed continuum normalization by fitting a cubic spline to the spectrum. We estimated the statistical uncertainties in the continuum fits using “flux randomization” Monte Carlo simulations (e.g. Peterson et al. 1998), varying the flux in each pixel of the spectrum by a random Gaussian deviate based on the spectral uncertainty. The pixel-error weighted average and standard deviation of 1000 iterations was adopted as the flux and uncertainty of the continuum fit, respectively.

For galaxies with redshift measurements, we have determined their heliocentric velocities and plotted them in Figure 1 colored by their cz . We adapted contours from Schneider et al. (1989) revealing the ringlike distribution of intergalactic H I. Contours are shown at 0.1, 0.2, 0.4, 0.8, 1.6, and 3.2 Jy km s⁻¹ per beam. 1 Jy km s⁻¹ per beam corresponds to a column density of $\approx 2 \times 10^{19} \text{ cm}^{-2}$ for the Arecibo beam size. We also show the velocity field of the H I gas mapped by Westerbork Synthesis Radio Telescope (adapted from Michel-Dansac et al. 2010). We used the plot digitization software WebPlotDigitizer (Rohatgi 2021) to extract the information from adapted figures. Five sightlines C, D, F, G, and H are potentially tracing the gas associated with the Leo Ring.

We have investigated possible biases that could arise from the use of archival data, in our case, aimed at probing the general surroundings of the Leo Ring region. The sightline towards SB is from a program to investigate quasar outflows, the background quasars in this study have $z > 0.4$ selected to study intrinsic absorption. The sightlines towards SC and SI are from a program to probe the

¹ <https://www.stsci.edu/hst/instrumentation/cos/calibration/airglow>

Table 1. List of the twelve sightlines with COS observations in the $7^\circ \times 6^\circ$ field containing the Leo Ring

Sightline ID	QSO. ^a	RA (J2000)	Dec (J2000)	z_{qso}^b	z_{abs}^c	cz_{abs}^d (km s ⁻¹)	PID ^e	Observed Wavelength (Å)	S/N^f	Observation Date
SA	SDSS J104029.17+105318.1	160.12	10.89	0.1363	-	-	12533	1135-1435	0.1	2011-11-11
SB	SDSS J104244.24+164656.1	160.68	16.78	0.9780	0.0024	720	14777	1132-1795	6.0	2017-11-13
SC	SDSS J104335.87+115129.0	160.90	11.86	0.7940	0.0024	720	14071	1132-1434	11.7	2015-11-23
SD	SDSS J104709.83+130454.6	161.79	13.08	0.4006	0.0028	840	12198 & 14071	1132-1443	6.7	2011-05-30 & 2015-12-01
SE	SDSS J104741.74+151332.2	161.92	15.23	0.3858	0.0023	690	13342 & 13833	1132-1777	23.2	2014-12-21 & 2015-02-05
SF	SDSS J104816.24+120734.8	162.07	12.13	0.2911	0.0030	900	12198	1142-1443	3.7	2011-06-03
SG	SDSS J104843.49+130605.8	162.18	13.10	0.2185	0.0027	810	12198	1142-1766	4.2	2011-07-02
SH	SDSS J105125.73+124746.2	162.86	12.80	1.2828	0.0027	810	12603 & 14777	1147-1795	7.3	2013-05-17 & 2018-01-04
SI	SDSS J105220.63+101751.7	163.09	10.30	0.2462	-	-	14071	1142-1444	4.9	2002-12-19
SJ	SDSS J105945.23+144142.9	164.94	14.70	0.6317	0.0024	720	12248	1135-1795	9.1	2011-06-01
SK	SDSS J105956.14+121151.1	164.98	12.20	0.9927	-	-	12603	1142-1468	7.5	2012-11-11
SL	4C10.30	165.20	10.77	0.4230	-	-	12603	1133-1465	4.8	2012-11-15

Notes—^a QSO SDSS name; ^b QSO redshift from NED; ^c Absorber redshift determined from the centroid of the strongest metal-line absorption or the H I Ly α absorption when no metal-lines are observed. The redshift corresponding to H I Ly α centroid is presented when the metal-line absorption is absent; ^d Heliocentric velocity corresponding to the absorber redshift; ^e proposal ID. ^f Median signal to noise ratio of the spectrum. We do not analyse sightline SA because of the poor S/N ratio of ≈ 0.1 .

Table 2. Candidate galaxies responsible for the absorption along the sightlines

Galaxy	RA (J2000)	DEC (J2000)	z^a	Morphological ^b Type	M_r^c (mag)	Reference ^d
M95	10 43 57.69	+11 42 13.63	0.00256	SB(r)b	-19.34	H α rotation map from Walter et al. (2008)
M96	10 46 45.74	+11 49 11.78	0.00301	SAB(rs)ab	-20.47	H α rotation map from Sil'chenko et al. (2003)
M105	10 47 49.60	+12 34 53.87	0.00292	E1	-20.91	Stellar line-of-sight velocity map from Sil'chenko et al. (2003)
NGC3384	10 48 16.90	+12 37 45.48	0.00244	SB0	-19.46	Stellar line-of-sight velocity map from Sil'chenko et al. (2003)
NGC3412	10 50 53.31	+13 24 43.71	0.00288	SB0	-19.53	Major axis values from Aguerri et al. (2003)
NGC3489	11 00 18.57	+13 54 04.40	0.00232	SAB0	-19.12	Systemic velocity adopted from NED database
NGC 3377	10 47 42.33	+13 59 09.30	0.00232	E5-6	-18.30	Systemic velocity adopted from NED database

Notes—^a Redshift of the galaxy; ^b Morphological classification of Galaxy from NED database; ^c Absolute Magnitude determined from r -band SDSS AB magnitude; ^d Reference paper from which the galaxy velocities in the direction of sightline are determined.

interface between the disk and the CGM of gas-rich galaxies using a sample of 35 QSOs; the QSOs have z between 0.003–0.05. The QSO towards SC has a $z \approx 0.79$. The sightline towards SD, SF and SG are QSOs behind the Leo Ring. The sightline towards SE is from two separate programs, investigating outskirts of galaxy clusters at z between 0.1–0.55. The sightlines towards SK, SL, and SH are from a program, to investigate baryonic cycling in galaxies with z between 0.02–0.5. Since the Leo Ring absorption is expected to be below $z \approx 0.0035$, we are certain that our sample selection is not biased in any way.

3 METHODOLOGY

We model the observed absorption systems using the photoionization code CLOUDY ver17.02 ([Ferland et al. 2017](#)), and synthesize the expected absorption profiles and compare them to the observed profiles in order to infer the column densities, Doppler parameters, and physical conditions of the absorbing gas. We adopt a slightly

modified approach to the CMBM method described in S21. The main difference is that, in S21, we optimized on the measured column density of an ion that was considered to trace a gas phase in the absorption system. The free parameters were metallicity and hydrogen number density. In this work, we incorporated three additional free parameters - neutral hydrogen column density, redshift of the absorber, and Doppler broadening parameter. This approach was adopted because of the comparatively lower $S/N \lesssim 10$ in the data, so as to account for the uncertainty in the precise determination of absorption centroids, Doppler parameters, and column densities. By utilizing the shapes of the absorption profiles and centering of individual components, the CMBM method allows for more rigorous constraints on model parameters than methods which average together components and utilize CLOUDY modeling of total column densities derived from the data. Recent works (e.g. [Zahedy et al. 2019](#), S21, [Haislmaier et al. 2021](#)) that perform component-wise and phase-wise modelling, find that an absorption system often has

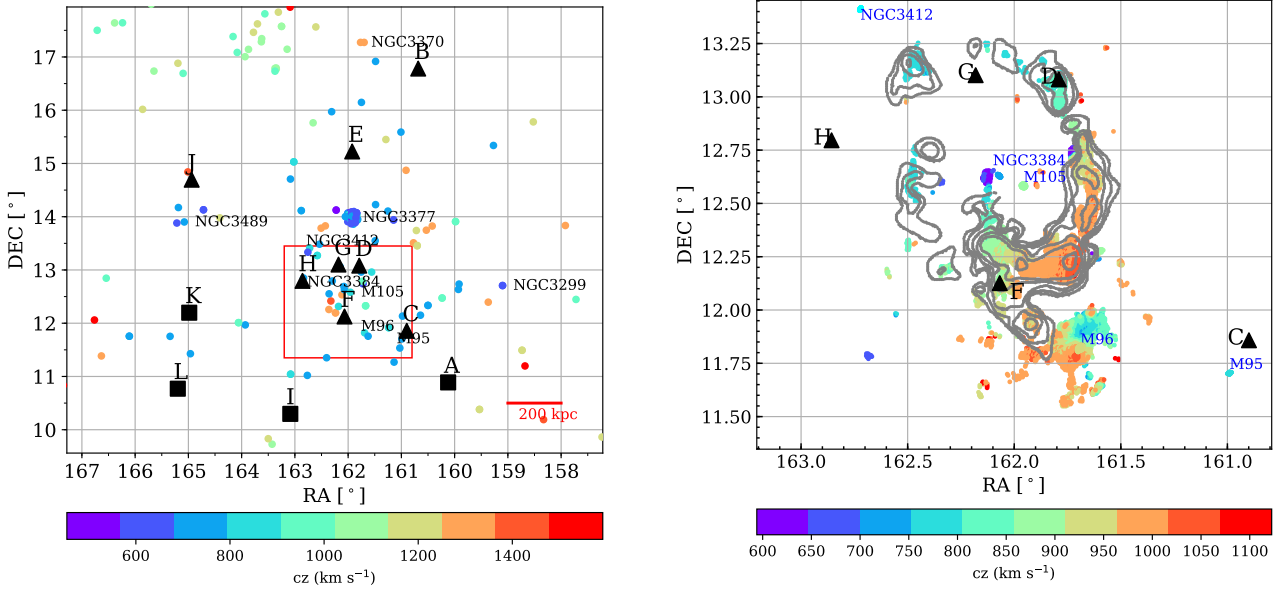


Figure 1. Left - A map showing the locations of 12 sightlines (A-L) with COS observations in the $\approx 7^\circ \times 6^\circ$ field containing the Leo Ring. We do not search for absorption towards SA because of the poor S/N (≈ 0.1). Triangles denote the sightlines with detected absorption between $600 \text{ km s}^{-1} < cz < 1400 \text{ km s}^{-1}$, while squares denote the sightlines which do not show absorption within this velocity range. One unit length in the grid corresponds to $\approx 200 \text{ kpc}$ at the redshift of $z=0.0025$. We indicate the heliocentric velocities of the galaxies in the field using a colormap shown below. Right - A zoom-in of the Leo Ring region shown using contours from Schneider et al. (1989) revealing the ringlike distribution of intergalactic H I. Contours are shown at 0.1, 0.2, 0.4, 0.8, 1.6, and 3.2 Jy km s^{-1} per beam. 1 Jy km s^{-1} per beam corresponds to a column density of $\approx 2 \times 10^{19} \text{ cm}^{-2}$ for the Arecibo beam size. We also show the velocity field of the H I gas mapped by Westerbork Synthesis Radio Telescope (adapted from Michel-Dansac et al. 2010). Five sightlines C, D, F, G, and H are potentially tracing the gas associated with the Leo Ring.

a metallicity that varies by more than an order of magnitude between components and phases.

CLOUDY has many tunable parameters. The three most important tunable parameters are metallicity relative to solar abundance (Z), hydrogen number density (n_{H}), and neutral hydrogen column density, $N(\text{H I})$. We generate photoionization thermal equilibrium (PIE) models adopting the Khaire et al. (2019)[KS19, Q18] model for the extragalactic background radiation (EBR) to determine the volume density of ionizing photons, n_γ . The KS19 EBR incorporates recent estimates of H I distribution in the IGM (Inoue et al. 2014), QSO emissivities, cosmic star formation rate density, and far UV dust extinction (Khaire & Srianand 2015). The shape and intensity of the radiation field are sources of systematic uncertainty in ionization modeling. An exploration of the systematic effects due to this choice is described in Acharya & Khaire (2021). Depending on whether the gas is high or low density, they find a variation of 4-6.3 and 1.6-3.2 times in the inferred density and metallicity, respectively. The equilibrium temperature, T , is self-consistently determined by CLOUDY by a balance between heating and cooling processes. We do not consider the systematic effects arising from the choice of EBR. We adopt a solar abundance pattern (Grevesse et al. 2010) when generating the CLOUDY models. Though deviations from such a pattern are common (Zahedy et al. 2021), the wavelength coverage of constraining transitions and the low S/N of the data make it unfeasible to constrain an additional model parameter for these data. For similar reasons, we also do not consider depletion due to dust in our modeling. This is a reasonable assumption as the sightlines are primarily probing the CGM of galaxies. The effects of dust depletion are expected to be more prominent for ISM gas.

PIE models are generated on a 3-D grid at the fiducial redshift of $z=0.0025$. The grid is $\log Z/Z_\odot \in [-3.0, 1.5]$, $\log n_{\text{H}} \in [-6.0, 1.0]$, and $\log N(\text{H I}) \in [11.0, 20.0]$, and obtained with a 0.1 dex step-size. It is a time-consuming endeavor to construct CLOUDY models over such a large grid, thus to increase efficiencies we employ distributed parallel processing on the Stampede2² and the CyberLAMP³ clusters to obtain models in a short amount of time.

In certain intervening absorbers, N v, because of its comparatively high ionization potential ($\approx 77.5 \text{ eV}$), could arise in gas with $T > 10^5 \text{ K}$ where the ionization is regulated by collisions between energetic free electrons and metal ions. In cases, where we have strong N v absorption detected, we model the absorption arising in such a phase using photo-collisional (PC) models. PC models are obtained on a 4-D grid with $\log T \in [2.0, 6.5]$, being the fourth dimension of the grid, in addition to $[\log Z/Z_\odot, \log n_{\text{H}}, \text{ and } \log N(\text{H I})]$. The temperature in such a model is no longer set by a balance between heating and cooling processes.

We begin by choosing a transition with unsaturated lines, with a high enough S/N to resolve the component structure. We use this species to obtain an initial guess for the component structure, and refer to this as the “constraining ion”. The constraining ion sets the location in redshift space for an absorber. The component structure is determined by fitting a Voigt profile (VP) model corresponding to the highest log-evidence and the least model complexity, evaluated using Bayes factor. We model the VPs using an analytic approximation (Tepper-García 2006) for the Voigt-Hjerting function as

² <https://www.tacc.utexas.edu/systems/stampede2>

³ <https://wikispaces.psu.edu/display/CyberLAMP/>

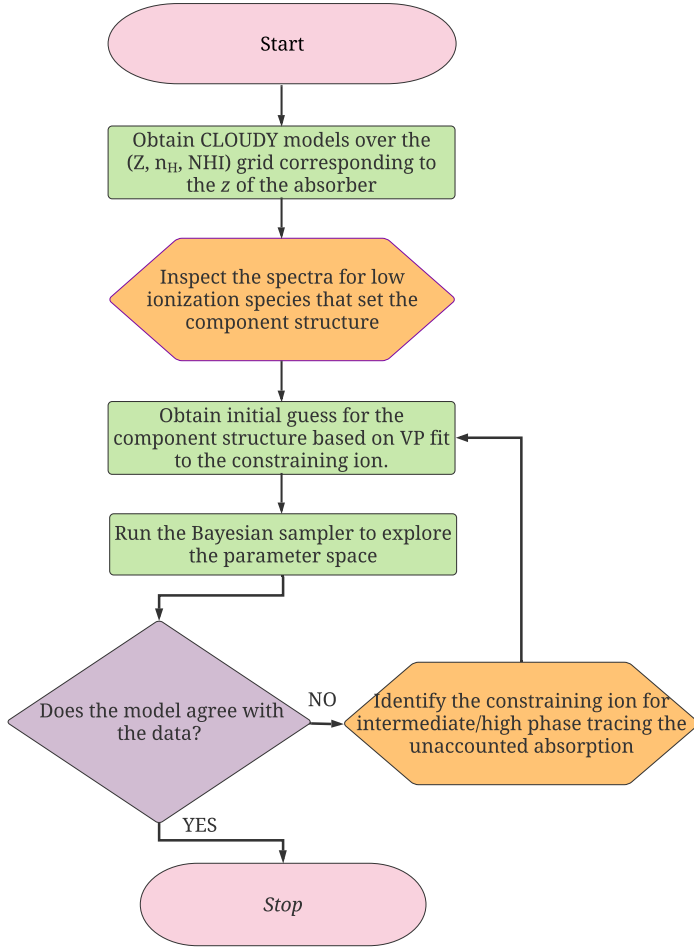


Figure 2. A flowchart showing the workflow involved in obtaining the models that best describe the conditions present in an absorption system.

implemented in the VoigtFit package (Krogager 2018). The properties of various atomic line transitions are adopted from linetools⁴ package. If a model that fits the low-ionization transitions (e.g., Si II, C II) cannot produce the observed amount of high-ionization absorption (e.g., C IV), or adequately match the profile of the Ly α , we will use more than one constraining ion. The other constraining ions represent the different phases of gas, with distinct regions having different densities along the line-of-sight. For example, we would typically constrain on Si II, C II, or Si III for the low-ionization gas, and on C IV for high-ionization gas. For some components, which have only H I Ly α detected, we use the H I Ly α as the constraining ion.

Every cloud in a model is identified uniquely by five parameters: $\log Z$, $\log n_{\text{H}}$, $\log N(\text{H I})$, z , b_{nt} . We adopt uniform priors on $\log Z$, $\log n_{\text{H}}$, and $\log N(\text{H I})$ in the ranges specified above. We use a uniform prior on b_{nt} (the non-thermal contribution to the Doppler parameter of a cloud) ranging between [0, 100] and defined in km s^{-1} . We determine the Doppler broadening parameter b for all the transitions arising in a phase using the equation $b^2 = b_{\text{nt}}^2 + b_{\text{t}}^2$, where $b_{\text{t}} = \sqrt{2kT/m}$ is the line broadening due to temperature and

b_{nt} the line broadening due to turbulence and other non-thermal effects. The non-thermal broadening component is assumed to be the same for all transitions in the same phase. For z , we use a Gaussian prior with a mean value and a standard deviation based on the error estimate, both of which are obtained from the VP fit to that ion.

We then determine the parameters that best describe the conditions ($\log Z$, $\log n_{\text{H}}$, $\log N(\text{H I})$, z , and b_{nt}) present in all the clouds by synthesizing VPs (using the compiled line profiles for the appropriate instrument/grating) and comparing to the data using PyMultinest (Buchner et al. 2014). The exploration of the parameter space is challenging when multiple, well separated modes with similar probabilities exist. PyMultinest is a nested sampling algorithm which is adept at addressing this challenge (Buchner 2021). During the log-likelihood evaluation the values at the sampled points are determined by interpolation on the preconstructed 3D-grid. The interpolant is generated by triangulating the grid data with Qhull (Barber et al. 1996), and on each triangle performing linear barycentric interpolation. We ensure that the pixels which are contaminated by blending effects or are too noisy are masked during the log-likelihood evaluation. A summary of our methodology is given in the form of a flowchart in Figure 2.

In all of the absorbers of interest, the H I Ly α absorption falls on the wings of the Galactic H I Ly α absorption. To determine the Galactic $N(\text{H I})$, we first fit a VP to the Galactic Si II absorption to determine the absorption centroid(s), depending on the number of components seen in Galactic Si II. These centroids are then used to fix the number of components and their locations in Galactic $N(\text{H I})$. A VPfit is then obtained by fitting the Galactic Ly α with this information. We divide the continuum normalized spectrum with this VP fit to determine the $N(\text{H I})$ of the absorber of interest. We compare our best fit values of Galactic $\log N(\text{H I})$ with the EBHIS (Winkel et al. 2016) database and find agreement within 0.05 dex in all but one case - SB. Wakker et al. (2011) found the ratio between $\log N(\text{H I}; \text{Ly}\alpha)$ and $\log N(\text{H I}; 21 \text{ cm})$ to be statistically consistent with 1 in their study of 59 AGN spectra. In appendix A1, we show the comparison between the $\log N(\text{H I}; \text{Ly}\alpha)$ and $\log N(\text{H I}; 21 \text{ cm})$ for the 11 sightlines in this study. The Galactic Ly α is blended with the absorption from the AGN itself, preventing a reliable measurement of Galactic $\log N(\text{H I})$ towards SB. However, the absorption of interest is not affected by this measurement towards SB. The comparison is shown in Figure. The VP fits corresponding to the maximum likelihood model for the eleven sightlines are shown in Figures B2–L2.

4 RESULTS

We discuss the findings from the application of our methodology to 11 quasar sightlines in the Leo Ring region for which we can probe absorption between heliocentric velocities of 600–1400 km s^{-1} . Positions of these sightlines, SB – SL, were shown in Figure 1 along with the galaxies in the region. A magnified view of the Leo Ring region that could contribute to absorption in each sightline is also shown in Figure 1. Sightline SA is not discussed further because of the poor S/N of its spectrum (≈ 0.1). The absorber redshift is defined based on the centroid of the strongest metal line absorption or the H I Ly α absorption when no metal-lines are observed. We present the posterior results for physical properties of the best model in Table 3 and show these properties using a violin plot for each sightline. We present the posterior distributions of inferred column densities and the Doppler broadening parameters for the

⁴ <https://linetools.readthedocs.io/en/latest/linelist.html>

observed transitions in all the components, and in all the model phases in Table M1.

For each sightline, we also discuss the possibility of a gas cloud tracing absorption associated with particular galaxies. Since there is an ambiguity in associating a particular galaxy with an absorption line, we quantify this using a modified prescription of likelihood parameter (LP) described in French & Wakker (2017). The LP is defined as follows:

$$LP = e^{-\left(\frac{\rho}{R_{vir}}\right)^2} \times e^{-\left(\frac{\Delta V}{V_{esc}}\right)^2} \quad (1)$$

where, ρ denotes the impact parameter between the galaxy and the line of sight, V_{esc} is the galaxy's escape velocity, R_{vir} is the galaxy's virial radius, and ΔV denotes the difference between the absorber's velocity (V_{abs}) and possible velocities within the galaxy's halo, $V_{abs} - (V_{gal} \pm V_{esc})$. We assume that all the gas associated with a galaxy is within the escape velocity of the halo; all absorption-line systems appear to be within the escape velocity of the halo (Kacprzak 2017). In the case of galaxies with measured rotation curves or stellar line-of-sight velocity fields, V_{gal} is determined by extrapolating the galaxy's rotation curve or velocity map in the direction of the sightline, whereas in the case of dwarfs and galaxies where this information is absent, V_{gal} is set equal to the systemic velocity of the galaxy. The $\pm V_{esc}$ term in equation 1 accounts for the fact that almost all absorption (even from outflows) in many transitions is bound to galaxies at or below the escape velocity (Stocke et al. 2013; Mathes et al. 2014; Tumlinson et al. 2011; Bordoloi et al. 2014; Kacprzak et al. 2019). In Table 2, we present the literature references for the rotation curves. The virial radius, R_{vir} , and virial mass, M_{vir} , of each galaxy are determined according to the combined ‘‘halo matching’’ and constant mass-to-light ratio technique described in Stocke et al. (2013; see their Figure 1). We adopt the B -band magnitude from the SIMBAD database (Wenger et al. 2000) in the determination of R_{vir} and M_{vir} . When the B -band magnitude is unavailable, we use the color transformation $B = (g + 0.21) + 0.39(g - r)$ (Jester et al. 2005) on SDSS model magnitudes to estimate the B -band magnitude. Given the low- z of our sample, we do not carry out K -corrections to galaxy luminosities.

4.1 SB: The $z = 0.00240$ absorber towards the quasar J1043+1151

A system plot of the $z = 0.0024$ absorber, with H I Ly α as the constraining transition, is shown in Figure 4. This system shows absorption in H I Ly α only. We do not see low, intermediate, or high ionization, metal line absorption.

We model the absorption in H I Ly α using a single component. With access to only the H I Ly α profile among Lyman series lines, and with no detections of metal lines, the properties of this system are poorly constrained. The $\log N(\text{H I})$ is determined to be $15.3^{+1.0}_{-0.8}$. Ionization modeling yields a 2σ upper limit on the metallicity of $\log Z/Z_{\odot} \lesssim -0.35$, a hydrogen number density, $\log n_{\text{H}} > -2.6$, and a small line of sight thickness of <1 pc. The temperature is determined to be relatively well constrained at $\log T \approx 4$. These limits are primarily due to the relatively narrow H I Ly α profile that does not allow for a lower density/higher temperature.

The physical properties of this absorption system are summarized in Table 3. The CLOUDY model corresponding to the maximum likelihood estimate (MLE) is shown overlaid on the spectral data in Figure 4. We show the properties of this H I cloud graphically using violin plots to the right of the system plot. The violin plots show the

probability density for different values of metallicity, hydrogen density, and temperature. In Figures B3 and B4, the probability density functions (PDFs) of the properties, in the form of corner plots, for the H I-only cloud are presented.

4.1.1 Galaxy Properties and Physical Interpretation

The closest galaxy which could contribute to the absorption at the redshift of the absorber is a dwarf galaxy, dw1045+16, consistent with a velocity of $c z \approx 700 \text{ km s}^{-1}$. However, the absorber is at a large projected separation of $\approx 3.7 R_{vir}$ from that galaxy. The large separation results in a very low LP of $\sim 10^{-7}$. Figure 3 shows the two nearest galaxies along with their virial radii relative to the position of SB. Table 4 lists the properties of these galaxies. Given these large separations, the weak H I Ly α absorption ($\log N(\text{H I}) \approx 15.3$) is as likely to be associated with a large scale filamentary structure as with any individual galaxy (Penton et al. 2002; Wakker et al. 2015; Bouma et al. 2021). The velocity of an extension of the Leo Ring H I gas is large ($\approx 850 \text{ km s}^{-1}$) compared with the velocity of this absorption at 700 km s^{-1} , and also SB is at an impact parameter of ≈ 750 kpc from the detected H I. It is therefore not likely to be directly related to gas released by the interaction.

4.2 SC: The $z = 0.00238$ absorber towards the quasar J1043+1151

A system plot of the $z = 0.00238$ absorber, with the constraining transitions, is shown in Figure 5. This system shows absorption in the low-ionization transitions of N I, C II, S II, Si II, and Fe II, and the intermediate-ionization transitions of Si III and Si IV. The system would classify as a strong Mg II absorber based on the observed strengths of Si II and C II (Narayanan et al. 2005).

We find that a two component model is able to best explain the absorption centered at $\approx 710 \text{ km s}^{-1}$, with two nearly coincident phases of gas, a broad higher ionization component producing N V absorption, and a narrow lower ionization component which even produces detected weak N I absorption. Both of these clouds contribute to the absorption detected in C II, Si III, and Si IV. We also observe absorption in C II and Si II at $\approx 878 \text{ km s}^{-1}$, which we model using a single narrow component. There is also absorption seen in H I at $\approx 1032 \text{ km s}^{-1}$, with no associated metals detected.

The absorption centered at $\approx 710 \text{ km s}^{-1}$ needs a high ionization gas phase traced by N V (shown as a blue curve) to explain the broad absorption associated with it. This phase of gas also explains some of the absorption seen in the wings of C II and Si III. A lower ionization gas phase traced by narrow Si IV (shown as red curve) explains most of the absorption seen in these same transitions. The metallicity of the gas phase traced by N V is $\log Z/Z_{\odot} \approx 0.8$, with a low hydrogen density $\log n_{\text{H}} \approx -4.2$, and a high temperature of $\log T \approx 4.5$. This cloud also predicts significant C IV absorption along with modest absorption in O VI. The lower ionization gas phase traced by Si IV produces the dominant absorption seen in transitions of Si II, C II, and Si III, with a neutral hydrogen column density of $\log N(\text{H I}) \approx 18.0$, a density of $\log n_{\text{H}} \approx -2.7$, and a metallicity of $\log Z/Z_{\odot} \approx -0.1$. We also observe some C IV absorption arising from this cloud. The two clouds constituting this absorption have line of sight thicknesses of ≈ 8 kpc and 5 kpc, respectively.

We also explore the possibility of N V arising in a collisionally ionized phase by using PC models to explain the N V absorption. The metallicities are quite similar to the values obtained in the photoionized case. The temperature for the N V phase is, however,

Table 3. Gas phases in the absorbers

Sightline	Constraining ion cloud	cz (km s ⁻¹)	b_{nt} (km s ⁻¹)	b_t (km s ⁻¹)	$b_{t,H\text{I}}$ (km s ⁻¹)	b (km s ⁻¹)	$\log \frac{Z}{Z_\odot}$	$\log \frac{n(\text{H})}{\text{cm}^{-3}}$	$\log \frac{T}{\text{K}}$	$\log \frac{N(\text{H I})}{\text{cm}^{-2}}$	$\log \frac{L}{\text{kpc}}$
(1)	(2)	(3)	(4)	(5)	(6)	(7)	(8)	(9)	(10)	(11)	(12)
SB	H I ₀	722.1 ^{+1.9} _{-1.6}	3.8 ^{+12.1} _{-3.3}	12.7 ^{+4.1} _{-4.0}	12.7 ^{+4.1} _{-4.0}	14.4 ^{+4.9} _{-2.8}	< -0.35	> -2.63	3.99 ^{+0.24} _{-0.33}	15.28 ^{+1.02} _{-0.77}	< -2.26
SC ^a	N v ₀	710.0 ^{+2.9} _{-3.5}	50.5 ^{+4.5} _{-4.4}	6.4 ^{+0.4} _{-0.4}	24.0 ^{+1.4} _{-1.6}	51.0 ^{+4.4} _{-4.4}	0.81 ^{+0.15} _{-0.13}	-4.18 ^{+0.03} _{-0.03}	4.54 ^{+0.05} _{-0.06}	14.62 ^{+0.10} _{-0.15}	0.93 ^{+0.16} _{-0.22}
	Si iv ₁	716.4 ^{+0.2} _{-0.3}	14.7 ^{+0.8} _{-0.6}	2.9 ^{+0.1} _{-0.1}	15.4 ^{+0.5} _{-0.5}	14.9 ^{+0.8} _{-0.6}	-0.13 ^{+0.08} _{-0.11}	-2.73 ^{+0.03} _{-0.04}	4.16 ^{+0.03} _{-0.03}	17.97 ^{+0.13} _{-0.09}	0.74 ^{+0.12} _{-0.10}
	C II ₁	878.6 ^{+0.8} _{-1.0}	3.7 ^{+1.9} _{-1.3}	3.9 ^{+0.2} _{-0.1}	13.6 ^{+0.5} _{-0.4}	5.4 ^{+1.5} _{-0.8}	-1.18 ^{+0.25} _{-0.31}	-1.92 ^{+0.21} _{-0.21}	4.05 ^{+0.03} _{-0.03}	18.36 ^{+0.04} _{-0.04}	-0.67 ^{+0.36} _{-0.32}
	H I ₀	1035.8 ^{+1.8} _{-1.8}	29.0 ^{+3.0} _{-5.4}	12.7 ^{+3.7} _{-6.4}	12.7 ^{+3.7} _{-6.4}	31.7 ^{+2.5} _{-4.3}	< -0.37	> -2.56	3.99 ^{+0.22} _{-0.62}	14.12 ^{+0.11} _{-0.06}	< -3.09
SC ^b	N v ₀	706.8 ^{+12.3} _{-9.1}	41.9 ^{+16.3} _{-16.9}	19.8 ^{+5.2} _{-2.5}	73.9 ^{+11.9} _{-9.1}	46.3 ^{+15.1} _{-14.3}	0.37 ^{+0.64} _{-0.65}	-1.74 ^{+2.49} _{-1.98}	5.52 ^{+0.13} _{-0.11}	13.10 ^{+0.50} _{-0.59}	-0.59 ^{+2.16} _{-2.52}
	Si iv ₁	716.2 ^{+0.3} _{-0.5}	16.4 ^{+0.1} _{-0.1}	3.3 ^{+0.1} _{-0.1}	17.3 ^{+0.3} _{-0.4}	16.7 ^{+0.1} _{-0.1}	-0.44 ^{+0.07} _{-0.05}	-2.92 ^{+0.03} _{-0.03}	4.26 ^{+0.02} _{-0.02}	18.23 ^{+0.06} _{-0.07}	1.30 ^{+0.08} _{-0.10}
	C II ₁	878.6 ^{+0.8} _{-1.0}	3.4 ^{+1.5} _{-1.2}	4.0 ^{+0.1} _{-0.1}	14.0 ^{+0.5} _{-0.5}	5.3 ^{+1.1} _{-0.70}	-1.21 ^{+0.23} _{-0.27}	-2.07 ^{+0.18} _{-0.16}	4.07 ^{+0.03} _{-0.03}	18.31 ^{+0.04} _{-0.05}	-0.44 ^{+0.30} _{-0.32}
	H I ₀	1035.8 ^{+1.6} _{-1.8}	28.0 ^{+3.2} _{-4.0}	13.9 ^{+4.7} _{-3.7}	13.9 ^{+4.7} _{-3.7}	31.4 ^{+2.8} _{-3.4}	< 0.12	> -2.94	4.07 ^{+0.25} _{-0.27}	14.14 ^{+0.10} _{-0.06}	< -2.25
SD	Si iv ₀	844.4 ^{+1.6} _{-1.7}	18.9 ^{+3.3} _{-2.8}	3.2 ^{+0.3} _{-0.5}	17.1 ^{+1.3} _{-2.4}	19.1 ^{+3.2} _{-2.7}	-0.06 ^{+0.48} _{-0.41}	-2.98 ^{+0.10} _{-0.12}	4.25 ^{+0.06} _{-0.13}	16.92 ^{+0.55} _{-0.64}	0.59 ^{+0.51} _{-0.59}
	H I ₀	978.4 ^{+3.7} _{-8.0}	3.0 ^{+3.1} _{-2.8}	12.5 ^{+5.7} _{-8.0}	12.5 ^{+5.7} _{-8.0}	13.1 ^{+5.3} _{-8.0}	< -0.65	> -2.85	3.98 ^{+0.32} _{-0.89}	16.79 ^{+0.86} _{-1.52}	< -1.24
SE ^a	H I ₀	700.7 ^{+1.6} _{-0.9}	14.5 ^{+4.5} _{-3.8}	23.3 ^{+2.6} _{-5.5}	23.3 ^{+2.6} _{-5.5}	27.5 ^{+1.9} _{-2.6}	-0.38 ^{+0.43} _{-0.40}	-3.33 ^{+0.22} _{-0.10}	4.52 ^{+0.09} _{-0.23}	14.09 ^{+0.09} _{-0.06}	-1.08 ^{+0.36} _{-0.80}
	C iv ₀	704.6 ^{+2.8} _{-3.3}	27.0 ^{+2.6} _{-2.5}	7.0 ^{+0.5} _{-0.5}	24.3 ^{+1.9} _{-1.8}	27.8 ^{+2.5} _{-2.4}	1.19 ^{+0.21} _{-0.18}	-4.48 ^{+0.08} _{-0.07}	4.55 ^{+0.06} _{-0.07}	13.30 ^{+0.18} _{-0.23}	0.16 ^{+0.21} _{-0.22}
SE ^b	H I ₀	701.7 ^{+0.6} _{-0.6}	7.9 ^{+3.6} _{-3.7}	15.0 ^{+1.6} _{-0.9}	15.0 ^{+1.6} _{-0.9}	17.1 ^{+2.3} _{-1.7}	-0.04 ^{+0.22} _{-0.22}	-2.71 ^{+0.21} _{-0.21}	4.14 ^{+0.09} _{-0.05}	15.09 ^{+0.41} _{-0.36}	-1.93 ^{+0.28} _{-0.17}
	C iv ₀	706.6 ^{+2.2} _{-2.8}	25.4 ^{+3.7} _{-2.6}	14.3 ^{+0.1} _{-0.2}	49.5 ^{+0.3} _{-0.5}	29.2 ^{+3.3} _{-2.3}	0.59 ^{+0.15} _{-0.14}	-2.19 ^{+0.60} _{-1.01}	5.17 ^{+0.00} _{-0.01}	12.55 ^{+0.23} _{-0.27}	-1.27 ^{+0.94} _{-0.63}
SF	Si II ₁	909.9 ^{+1.3} _{-1.3}	11.9 ^{+0.8} _{-0.9}	1.3 ^{+0.3} _{-0.1}	7.1 ^{+1.4} _{-0.4}	12.0 ^{+0.8} _{-0.9}	1.01 ^{+0.08} _{-0.19}	-2.75 ^{+0.08} _{-0.13}	3.48 ^{+0.16} _{-0.05}	17.59 ^{+0.16} _{-0.13}	0.30 ^{+0.25} _{-0.21}
SG	C iv ₀	817.2 ^{+1.4} _{-2.5}	17.8 ^{+5.0} _{-4.8}	4.7 ^{+0.5} _{-0.5}	16.1 ^{+1.7} _{-1.5}	18.4 ^{+4.9} _{-4.6}	1.44 ^{+0.05} _{-0.12}	-4.04 ^{+0.11} _{-0.11}	4.20 ^{+0.09} _{-0.09}	13.61 ^{+0.14} _{-0.14}	-0.67 ^{+0.25} _{-0.23}
	Si iv ₀	861.3 ^{+5.5} _{-3.8}	10.1 ^{+0.9} _{-2.2}	2.6 ^{+0.7} _{-0.4}	13.5 ^{+3.6} _{-2.1}	10.4 ^{+0.9} _{-2.1}	1.14 ^{+0.31} _{-0.47}	-3.58 ^{+0.22} _{-0.17}	4.04 ^{+0.21} _{-0.15}	14.14 ^{+0.57} _{-0.41}	-1.19 ^{+0.47} _{-0.32}
	H I ₁	942.8 ^{+5.6} _{-4.5}	9.2 ^{+10.9} _{-8.2}	13.2 ^{+4.5} _{-3.0}	13.2 ^{+4.5} _{-3.0}	16.5 ^{+7.8} _{-3.8}	< -0.05	> -2.82	4.02 ^{+0.25} _{-0.22}	15.38 ^{+1.05} _{-1.05}	< -1.49
	H I ₂	1056.7 ^{+4.2} _{-4.3}	11.1 ^{+11.3} _{-9.9}	12.6 ^{+4.5} _{-7.0}	12.6 ^{+4.5} _{-7.0}	16.9 ^{+9.1} _{-4.4}	< -0.01	> -2.79	3.99 ^{+0.26} _{-0.70}	14.21 ^{+0.59} _{-0.40}	< -2.68
	H I ₃	1297.2 ^{+27.1} _{-26.3}	5.3 ^{+5.2} _{-4.8}	13.1 ^{+26.7} _{-7.9}	13.1 ^{+26.7} _{-7.9}	14.8 ^{+25.5} _{-7.8}	< 0.54	> -3.95	4.01 ^{+0.97} _{-0.81}	13.64 ^{+2.98} _{-2.39}	< 1.04
SH	Si III ₀	766.8 ^{+0.3} _{-0.8}	16.3 ^{+0.2} _{-0.7}	6.7 ^{+0.1} _{-0.1}	35.3 ^{+0.5} _{-0.5}	17.6 ^{+0.2} _{-0.6}	-1.68 ^{+0.10} _{-0.11}	-3.35 ^{+0.02} _{-0.02}	4.88 ^{+0.01} _{-0.01}	15.43 ^{+0.11} _{-0.09}	1.68 ^{+0.14} _{-0.11}
	Si III ₁	818.0 ^{+1.3} _{-0.9}	1.2 ^{+1.0} _{-1.0}	3.4 ^{+0.3} _{-0.3}	17.8 ^{+1.7} _{-1.8}	3.6 ^{+0.5} _{-0.5}	1.46 ^{+0.03} _{-0.09}	-4.21 ^{+0.15} _{-0.14}	4.29 ^{+0.08} _{-0.09}	15.45 ^{+0.23} _{-0.21}	1.57 ^{+0.34} _{-0.36}
	H I ₂	899.5 ^{+2.7} _{-2.9}	4.6 ^{+6.6} _{-4.1}	12.4 ^{+2.1} _{-1.8}	12.4 ^{+2.1} _{-1.8}	13.5 ^{+3.4} _{-1.6}	< -0.23	> -2.25	3.97 ^{+0.14} _{-0.14}	14.52 ^{+0.39} _{-0.40}	< -3.56
	H I ₃	976.8 ^{+5.1} _{-7.5}	40.1 ^{+14.3} _{-11.4}	36.3 ^{+7.2} _{-23.6}	36.3 ^{+7.2} _{-23.6}	53.9 ^{+9.7} _{-7.5}	< -0.04	> -3.83	4.90 ^{+0.16} _{-0.91}	14.08 ^{+0.05} _{-0.05}	< 1.12
SJ	H I ₀	650.6 ^{+2.8} _{-2.4}	4.0 ^{+6.4} _{-3.6}	9.5 ^{+3.7} _{-4.7}	9.5 ^{+3.7} _{-4.7}	10.9 ^{+3.4} _{-2.9}	< 0.51	> -2.25	3.74 ^{+0.29} _{-0.60}	14.17 ^{+0.54} _{-0.30}	< -3.9
	C iv ₀	720.1 ^{+1.5} _{-1.5}	16.4 ^{+3.3} _{-3.0}	7.2 ^{+0.5} _{-0.5}	24.7 ^{+1.7} _{-1.6}	17.9 ^{+3.0} _{-2.7}	0.55 ^{+0.12} _{-0.13}	-4.04 ^{+0.04} _{-0.04}	4.57 ^{+0.06} _{-0.06}	14.42 ^{+0.09} _{-0.08}	0.51 ^{+0.16} _{-0.17}

Properties of the different gas phases contributing to the absorption towards different sightlines. Notes: (1) Sightline ID (2) Constraining ion tracing a phase. In the case of SC and SE, we explore both PIE and photo-collisional models because of the detection of N v absorption, earmarked with ^a and ^b, respectively; (3) Heliocentric velocity of the component; (4) Non-thermal Doppler broadening parameter of constraining ion; (5) Thermal Doppler broadening parameter of the constraining ion; (6) Thermal Doppler broadening parameter measured for H I; (7) Total Doppler broadening parameter of the constraining ion, obtained from the distributions in (4) and (5); (8) log metallicity; (9) log hydrogen number density; (10) log neutral hydrogen column density; (11) log temperature in Kelvin (10) log thickness in kpc. The marginalized posterior values of model parameters are given as the median along with the upper and lower bounds associated with a 95% credible interval. The marginalized posterior distributions for the cloud properties for columns (3-11) are presented in Figures B3 - J6 respectively. We present the inferred column densities and total Doppler broadening parameter (b), for every ion and in each model component, in all of the sightlines in Table M1.

high with $\log T \approx 5.5$. We present the results for both the PIE and the PC model in Table 3, and the models superimposed on the data are presented in Figures 5 and C3, respectively. The most plausible origin of the high ionization N v phase could be better determined if the C iv and O vi were covered. We cannot discriminate between the two models due to the lack of coverage of the other higher ionization transitions. The constraints on the Si iv cloud at $\approx 716 \text{ km s}^{-1}$ are affected by which model for the origin of the N v absorption applies, however, the difference is only a 0.3 dex reduction in $\log Z/Z_\odot$ and a 0.2 dex reduction in $\log n_{\text{H}}$ when the N v is collisionally ionized.

Interestingly, the lower ionization gas phase at $\approx 716 \text{ km s}^{-1}$ shows appreciable detections in N I and O I. For the assumed solar abundance pattern, the inferred metallicity of this phase is consistent with solar metallicity within the uncertainties.

The absorption centered at $\approx 878 \text{ km s}^{-1}$ produces damping wings in H I Ly α with a column density of $\log N(\text{H I}) \approx 18.4$. This gas phase explains the narrow absorption profiles seen in C II and Si II. The metallicity is constrained to be $\log Z/Z_\odot \approx -1.0$. Only low ionization and intermediate ionization absorption is observed to arise in this gas phase with a density of $\log n_{\text{H}} \approx -1.9$. The line of sight thickness is constrained to be $\approx 0.2 \text{ kpc}$.

Table 4. Galaxies likely to be contributing to the absorption towards different sightlines

Sightline	Constraining	V_{abs}	Galaxy	RA	Dec	V_{gal}	V_{esc}	$g-r$	$\log \frac{M_{vir}}{M_{\odot}}$	R_{vir}	ρ	ρ/R_{vir}	LP	
ID	ion cloud	(km s^{-1})	Name	(deg)	(deg)	(km s^{-1})	(km s^{-1})	(mag)		(kpc)	(kpc^3)	(kpc^{-3})		
(1)	(2)	(3)	(4)	(5)	(6)	(7)	(8)	(9)	(10)	(11)	(12)	(13)	(14)	
SB	H _I _0	722.1	NGC 3377	161.93	13.99	696.1	66.8	0.7	11.2	141.0	543.6	3.9	$3e-7^{+5e-8}_{-2e-7}$	
		722.1	dw1045+16	161.48	16.92	695.8	16.5	0.9	9.4	37.4	138.9	3.7	$8e-8^{+6e-7}_{-8e-8}$	
SC	N _v _0	710.0	M 95	160.99	11.7	700.0	91.7	0.8	11.5	181.2	35.1	0.2	$0.95^{+0.01}_{-0.67}$	
		710.0	LeG09*	160.64	12.15	695.8	19.8	0.6	9.6	44.6	68.9	1.5	$0.05^{+0.04}_{-0.05}$	
	Si _{IV} _1	716.4	M 95	160.99	11.7	700.0	91.7	0.8	11.5	181.2	35.1	0.2	$0.93^{+0.03}_{-0.69}$	
		716.4	M 96	161.69	11.82	900.0	111.5	0.9	11.8	240.6	179.6	0.7	$0.04^{+0.34}_{-0.04}$	
	C _{II} _1	878.6	M 96	161.69	11.82	900.0	111.5	0.9	11.8	240.6	179.6	0.7	$0.55^{+0.02}_{-0.41}$	
		878.6	NGC 3384	162.07	12.63	840.0	113.8	0.7	11.7	173.9	259.3	1.5	$0.1^{+0.01}_{-0.08}$	
	H _I _0	878.6	M 105	161.96	12.58	950.0	96.0	0.9	11.6	207.8	283.5	1.4	$0.09^{+0.07}_{-0.08}$	
		1035.8	M 96	161.69	11.82	900.0	111.5	0.9	11.8	240.6	179.6	0.7	$0.13^{+0.42}_{-0.13}$	
			1035.8	M 105	161.96	12.58	950.0	96.0	0.9	11.6	207.8	283.5	1.4	$0.07^{+0.09}_{-0.07}$
	SD	Si _{IV} _0	844.4	M 105	161.96	12.58	915.0	96.0	0.9	11.6	207.8	118.1	0.6	$0.42^{+0.30}_{-0.38}$
844.4			NGC 3384	162.07	12.63	740.0	113.8	0.7	11.7	173.9	99.2	0.6	$0.31^{+0.41}_{-0.29}$	
844.4			M 96	161.69	11.82	780.0	111.5	0.9	11.8	240.6	293.1	1.2	$0.16^{+0.07}_{-0.14}$	
844.4			NGC 3412	162.72	13.41	864.9	71.6	0.7	11.3	156.3	214.0	1.4	$0.14^{+0.01}_{-0.11}$	
H _I _0		978.4	M 105	161.96	12.58	915.0	96.0	0.9	11.6	207.8	118.1	0.6	$0.47^{+0.25}_{-0.42}$	
		978.4	NGC 3412	162.72	13.41	864.9	71.6	0.7	11.3	156.3	214.0	1.4	$0.01^{+0.1}_{-0.01}$	
SE	H _I _0	700.7	NGC 3377	161.93	13.99	696.1	66.8	0.7	11.2	141.0	221.6	1.6	$0.08^{+0.00}_{-0.06}$	
		700.7	NGC 3384	162.07	12.63	732.1	113.8	0.7	11.7	173.9	488.6	2.8	$3e-4^{+3e-5}_{-3e-4}$	
	C _{IV} _0	704.6	NGC 3377	161.93	13.99	696.1	66.8	0.7	11.2	141.0	221.6	1.6	$0.08^{+0.00}_{-0.06}$	
		704.6	NGC 3384	162.07	12.63	732.1	113.8	0.7	11.7	173.9	488.6	2.8	$3e-4^{+2e-5}_{-3e-4}$	
SF	Si _{II} _1	909.9	M 105	161.96	12.58	910.0	96.0	0.9	11.6	207.8	105.2	0.5	$0.77^{+0.0}_{-0.49}$	
		909.9	M 96	161.69	11.82	800.0	111.5	0.9	11.8	240.6	111.1	0.5	$0.31^{+0.5}_{-0.29}$	
		909.9	NGC 3384	162.07	12.63	800.0	113.8	0.7	11.7	173.9	94.5	0.5	$0.29^{+0.45}_{-0.27}$	
SG	C _{IV} _0	817.2	NGC 3384	162.07	12.63	720.0	113.8	0.7	11.7	173.9	91.0	0.5	$0.37^{+0.39}_{-0.35}$	
		817.2	M 105	161.96	12.58	895.0	96.0	0.9	11.6	207.8	126.8	0.6	$0.36^{+0.33}_{-0.33}$	
		817.2	NGC 3412	162.72	13.41	864.9	71.6	0.7	11.3	156.3	135.6	0.9	$0.3^{+0.17}_{-0.27}$	
		817.2	UGC05944*	162.58	13.27	810.0	27.5	0.6	10.0	61.6	88.0	1.4	$0.12^{+0.01}_{-0.09}$	
	Si _{IV} _0	861.3	M 105	161.96	12.58	895.0	96.0	0.9	11.6	207.8	126.8	0.6	$0.61^{+0.08}_{-0.5}$	
		861.3	NGC 3412	162.72	13.41	864.9	71.6	0.7	11.3	156.3	135.6	0.9	$0.47^{+0.0}_{-0.31}$	
		861.3	NGC 3384	162.07	12.63	720.0	113.8	0.7	11.7	173.9	91.0	0.5	$0.16^{+0.56}_{-0.16}$	
	H _I _1	942.8	M 105	161.96	12.58	895.0	96.0	0.9	11.6	207.8	126.8	0.6	$0.54^{+0.15}_{-0.47}$	
		942.8	NGC 3412	162.72	13.41	864.9	71.6	0.7	11.3	156.3	135.6	0.9	$0.14^{+0.33}_{-0.13}$	
	H _I _2	1056.7	M 105	161.96	12.58	895.0	96.0	0.9	11.6	207.8	126.8	0.6	$0.04^{+0.39}_{-0.04}$	
		1056.7	NGC 3412	162.72	13.41	864.9	71.6	0.7	11.3	156.3	135.6	0.9	$4e-4^{+0.03}_{-4e-4}$	
	H _I _3	1297.2	NGC 3389	162.12	12.53	1298.1	88.4	0.3	11.4	130.1	190.1	1.5	$0.12^{+0.0}_{-0.08}$	
		1297.2	NGC 3338	160.53	13.75	1301.8	77.5	0.8	11.4	168.8	576.5	3.4	$9e-6^{+3e-8}_{-6e-6}$	
SH	Si _{III} _0	766.8	NGC 3384	162.07	12.63	680.0	113.8	0.7	11.7	173.9	147.5	0.8	$0.27^{+0.22}_{-0.25}$	
		766.8	M 96	161.69	11.82	800.0	111.5	0.9	11.8	240.6	347.5	1.4	$0.11^{+0.01}_{-0.09}$	
	Si _{III} _1	818.0	NGC 3412	162.72	13.41	864.9	71.6	0.7	11.3	156.3	139.7	0.9	$0.29^{+0.16}_{-0.26}$	
		818.0	M 105	161.96	12.58	900.0	96.0	0.9	11.6	207.8	203.2	1.0	$0.19^{+0.19}_{-0.18}$	
	H _I _2	818.0	M 96	161.69	11.82	800.0	111.5	0.9	11.8	240.6	347.5	1.4	$0.12^{+0.0}_{-0.09}$	
		818.0	NGC 3384	162.07	12.63	680.0	113.8	0.7	11.7	173.9	147.5	0.8	$0.11^{+0.36}_{-0.11}$	
	H _I _3	899.5	M 105	161.96	12.58	900.0	96.0	0.9	11.6	207.8	203.2	1.0	$0.38^{+0.0}_{-0.24}$	
		899.5	NGC 3412	162.72	13.41	864.9	71.6	0.7	11.3	156.3	139.7	0.9	$0.36^{+0.09}_{-0.31}$	
			976.8	M 105	161.96	12.58	900.0	96.0	0.9	11.6	207.8	203.2	1.0	$0.2^{+0.18}_{-0.18}$
			976.8	NGC 3412	162.72	13.41	864.9	71.6	0.7	11.3	156.3	139.7	0.9	$0.04^{+0.29}_{-0.04}$

Sightline ID	Constraining ion cloud	V_{abs} (km s ⁻¹)	Galaxy Name	RA (deg)	Dec (deg)	V_{gal} (km s ⁻¹)	V_{esc} (km s ⁻¹)	$g-r$ (mag)	$\log \frac{M_{vir}}{M_{\odot}}$	R_{vir} (kpc)	ρ (kpc)	ρ/R_{vir}	LP
(1)	(2)	(3)	(4)	(5)	(6)	(7)	(8)	(9)	(10)	(11)	(12)	(13)	(14)
SI	No absorption		M 96	161.69	11.82	903.0	111.5	0.9	11.8	240.6	474.2	2.0	-
			M 95	160.99	11.70	767.5	91.7	0.8	11.5	181.2	490.7	2.7	-
			NGC 3384	162.07	12.63	732.1	113.8	0.7	11.7	173.9	476.3	2.7	-
			M 105	161.96	12.58	876.0	96.0	0.9	11.6	207.8	570.3	2.7	-
SJ	H I_0	650.6	NGC 3489	165.08	13.9	697.0	68.6	3.8	11.2	149.8	144.1	1.0	$0.25^{+0.15}_{-0.23}$
		650.6	LSBCD640-08*	165.22	13.88	656.5	21.6	0.5	9.7	48.7	144.5	3.0	$1e - 4^{+1e-5}_{-1e-4}$
	C IV_0	720.1	NGC 3489	165.08	13.9	697.0	68.6	3.8	11.2	149.8	144.1	1.0	$0.35^{+0.05}_{-0.28}$
		720.1	LeG33	165.19	14.17	695.8	15.7	0.7	9.3	35.6	102.9	2.9	$2e - 5^{+1e-3}_{-2e-5}$
SK	No absorption		NGC 3489	165.08	13.90	697.0	68.6	3.8	11.2	149.8	305.2	2.0	-
			dw1101+11*	165.34	11.75	695.8	15.3	0.0	9.3	34.4	101.2	2.9	-
			NGC 3384	162.07	12.63	732.1	113.8	0.7	11.7	173.9	540.8	3.1	-
			M 96	161.69	11.82	903.0	111.5	0.9	11.8	240.6	751.1	3.1	-
SL	No absorption		dw1059+11*	164.96	11.43	695.8	15.9	0.4	9.3	36.1	124.4	3.4	-
			M 96	161.69	11.82	903.0	111.5	0.9	11.8	240.6	833.0	3.5	-
			NGC 3489	165.08	13.90	697.0	68.6	3.8	11.2	149.8	560.6	3.7	-
			NGC 3384	162.07	12.63	732.1	113.8	0.7	11.7	173.9	673.3	3.9	-

Notes: (1) Sightline ID (2) Constraining ion (3) Absorption centroid (4) Galaxy name (5) Right ascension in degrees; (6) Declination in degrees; (7) Galaxy's systemic velocity. For galaxies earmarked with \star , we derive systemic velocity based on the adopted distance modulus of 30.06 (Müller et al. 2018); (8) Escape velocity of the Galaxy halo; (9) $g-r$ -band SDSS AB magnitude; (10) and (11) The virial mass and the virial radius determined according to the combined “halo matching” and constant mass-to-light ratio technique; (12) Impact parameter in kpc (13) Ratio of impact parameter to the virial radius; (14) Likelihood parameter determined using equation 1. We present an estimate obtained by setting V_{gal} equal to the velocity in the direction of rotation map extension, and the bounds represent the minimum and maximum values of the LP function within the range $V_{abs} - (V_{gal} + V_{esc}) \leq \Delta V \leq V_{abs} - (V_{gal} - V_{esc})$. We list at least two galaxies or all galaxies with LP estimate >0.1 . Columns 4-7 are obtained from SIMBAD database (Wenger et al. 2000).

The absorption centered at $\approx 1032 \text{ km s}^{-1}$ does not show a clear detection of absorption in metals. There is a possible detection of Si II $\lambda 1260$ at 2σ level at this velocity. The absence of absorption in Si II $\lambda 1190$, 1193, and in C II, however, argues against this identification. The background quasar has a relatively high redshift, so its spectrum has a higher density of lines and this candidate Si II is ruled as a blend, and the spectral region is masked out when modelling. We obtain an upper limit on the metallicity of $\lesssim -0.4$. The relatively narrow H I absorption constrains the temperature to be $\log T \approx 4$.

In Table 3 we present the posterior results for the four clouds identified in this absorption system. Figure 5 shows CLOUDY models, using the MLE values superimposed on the data. The probability density distributions of metallicity, hydrogen number density, and temperature corresponding to each one of the constraining ions are summarized in the form of violin plots. The PDFs of the properties of the different clouds are presented using corner plots in Figures C5 – C12.

We explore the consequences of zero-point uncertainty of the H I Ly α flux for the components between $710\text{--}720 \text{ km s}^{-1}$. This uncertainty could arise through a contribution to the observed flux from wings to the geocoronal airglow emission as we described in § 2. The violin plots showing the distribution of parameters for 100 MC realizations (with different zero point values) are presented in Figure C4. We find that the posteriors for various phases are still in agreement within uncertainties of the values presented in Table 3 for SC^b.

4.2.1 Galaxy Properties and Physical Interpretation

The nearest galaxy which could be responsible for the dominant absorption at $\approx 710 \text{ km s}^{-1}$ is M95, which is at an impact parameter of $35 \text{ kpc}/0.2R_{vir}$. An extension of its rotation curve in the direction of SC would be consistent with the absorption at $\approx 710 \text{ km s}^{-1}$. The LP for M95 to explain these components is determined to be ~ 0.9 . There is also a dwarf galaxy candidate LeG09, and it has a LP of ≈ 0.04 , so it could also contribute. However, given the predicted strength of C IV absorption from this phase, it is unlikely to have a significant contribution from a dwarf galaxy at a separation of $1.5R_{vir}$ (Bordoloi et al. 2014). Moreover, the Lyman Limit system, with $\log N(\text{H I}) \approx 18$ and solar metallicity, in the low ionization phase at this velocity is consistent with gas arising in H II regions of low- z star forming-galaxies (Pilyugin et al. 2014), and not with dwarf galaxies (see Figure 10 in Zahedy et al. 2021). M96 could also contribute, and shows an LP of ≈ 0.04 , however the absorption is much beyond the escape velocity of halo of M96. Hence these high metallicity components, $\log Z/Z_{\odot} \approx 0.8$ and ≈ -0.1 are highly likely to be associated with M95.

The absorption at $\approx 879 \text{ km s}^{-1}$ has a LP of ≈ 0.5 for association with M96. M96 is at an impact parameter of $0.7R_{vir}$ from SC and an extension of its rotation curve would be consistent with producing absorption at $\approx 900 \text{ km s}^{-1}$. The next likely galaxy candidate is NGC 3384 which is at an impact parameter of $1.5R_{vir}$ and has a LP of ~ 0.1 . M105 is at an impact parameter $1.4R_{vir}$ and it also has a LP of $\lesssim 0.1$. These galaxies along with their virial radii are shown in Figure 3. Based on the predicted $\text{EW}_{\text{MgII}, \lambda 2796} \approx 0.12 \text{ \AA}$, we do not expect contribution to absorption from NGC 3384 or M

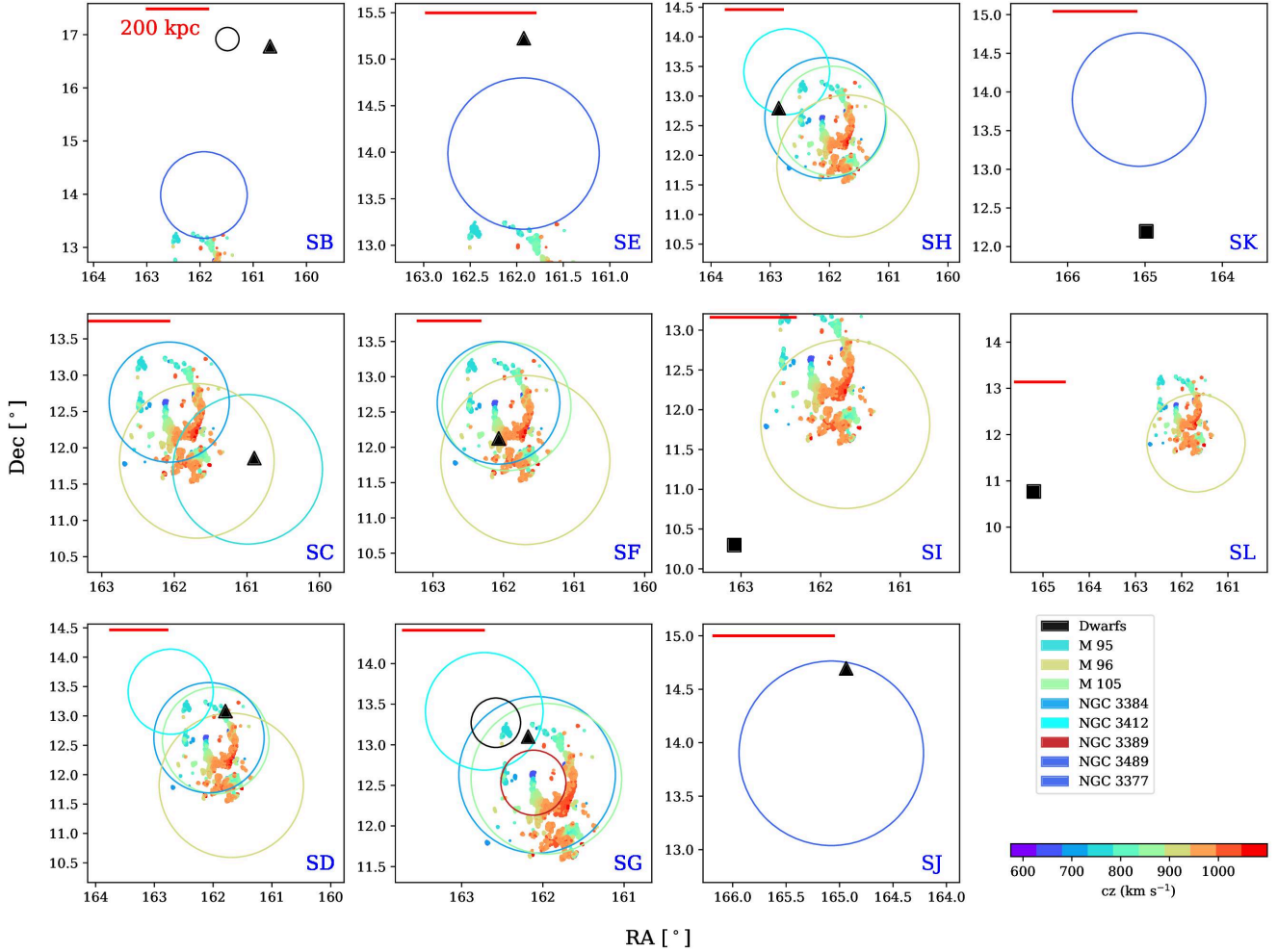


Figure 3. Plots showing the galaxies that are potentially contributing to the absorption along the respective sightline indicated at the bottom-right of each panel. We show only those galaxies which have a $LP \geq 0.1$. The filled triangle denotes the location of the quasar sightline. The circle is centered at the location of the galaxy, and its radius corresponds to the virial radius of the galaxy. We indicate major galaxies in different colors corresponding to their cz , while the dwarfs are shown in black. We also overlay the Leo Ring as seen in Figure 1. The red horizontal line at the top-left in each panel corresponds to 200 kpc at the redshift of the absorber.

105, both of which are at $> 1.4R_{vir}$ (Nielsen et al. 2013). We suggest that this sub-solar metallicity component, $\log Z/Z_{\odot} \approx -1.0$, is associated with M96.

The Leo Ring itself is thought to have formed from a head on collision between M96 and NGC 3384 (now at the center of the ring) (Michel-Dansac et al. 2010). The gas at the lower right of the ring (Fig. 1), closest to M96, is at a higher velocity than the two galaxies, $\approx 1050 \text{ km s}^{-1}$, and so cannot arise directly from the galaxies themselves. The absorption that we see only in $\text{H I Ly}\alpha$ at 1035 km s^{-1} could share the kinematics with the lower right of the ring, though the sightline is at an impact parameter of $\approx 100 \text{ kpc}$ from that location. It is also possible that the absorption is unrelated to the interaction that created the ring.

4.3 SD: The $z = 0.00279$ absorber towards the quasar J1047+1304

A system plot of the $z = 0.00279$ absorber with the constraining transitions is shown in Figure 6. This system shows absorption in the low ionization transitions of C II and Si II, and the intermediate

ionization transitions of Si III and Si IV. Absorption is not detected in the lower ionization (neutral) transitions. The higher ionization transitions, C IV and O VI are not covered by the observations, but N V is not detected. We model the absorption as two components, one component tracing the absorption seen in low and intermediate ionization transitions, at $\approx 845 \text{ km s}^{-1}$, and one component in H I , without any metals, at $\approx 978 \text{ km s}^{-1}$. Table 3 summarizes the posterior results for these two clouds. We observe a peculiarity in the $\text{H I Ly}\alpha$ profile at $\approx 845 \text{ km s}^{-1}$; the flux shows a sharp discontinuity from the saturation level at this velocity which is unexpected based on the observed metal absorption. The profile at this velocity is therefore assumed to be saturated.

The blueward cloud at $\approx 845 \text{ km s}^{-1}$ is consistent with solar metallicity, has a density of $\log n_{\text{H}} \approx -3.0$, and a temperature of $\log T \approx 4.25$. The line of sight thickness is $L \approx 4 \text{ kpc}$. The H I cloud at 978 km s^{-1} is unconstrained. We determine an upper limit on the metallicity of $\log Z/Z_{\odot} \lesssim -0.65$. The density is determined to be $\gtrsim -2.85$, and the line of sight thickness is an upper limit, $L \lesssim 60 \text{ pc}$. The properties of the two clouds are sketched in Figure 6. The PDFs

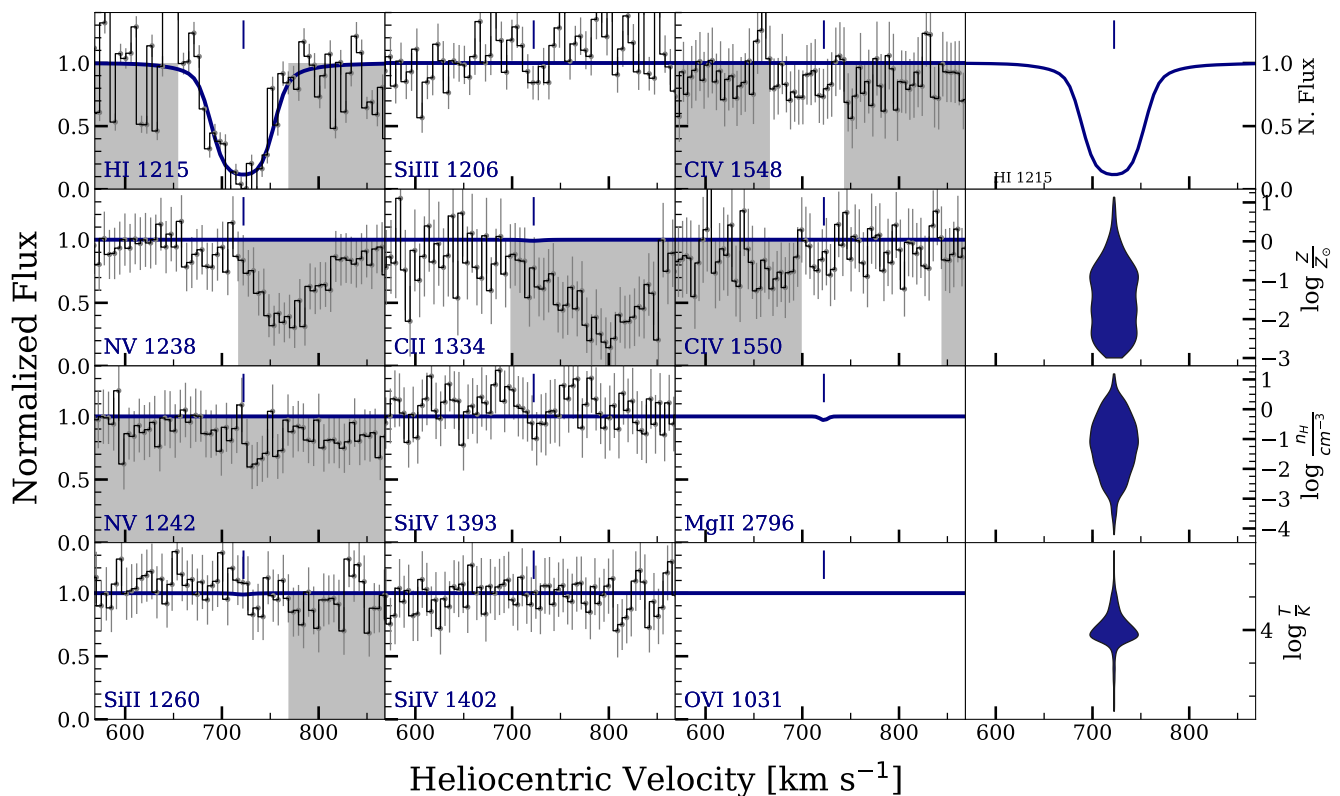


Figure 4. CLOUDY models for the $z = 0.0024$ absorber towards SB, obtained using the MLE values of the best fit model. The models are superimposed on the observed spectra obtained with *HST/COS* in the wavelength regions corresponding to important constraining transitions. 1σ error bars are superimposed on the data. The centroid of the H I Ly α absorption component as determined from the VP fit is indicated by the vertical tick mark on top of each panel. The photoionized gas phase is traced only by the H I cloud (shown as a blue curve). A summary of the properties of this cloud are shown in the form of violin plots using filled blue color. The width of the filled blue shapes to represent the relative probability densities of the values given on the vertical axes. The regions shaded in grey show the pixels that were not used in the evaluation of the log-likelihood. We show only the transitions that might be detected for an absorber with this relatively weak H I Ly α line.

of the properties of the two clouds are presented using corner plots in Figures D3 – D5.

Previously, the absorption at $z = 0.00279$ towards this quasar was studied by Rosenberg et al. (2014). They determine $\log N(\text{H I})=19.1$ from the Westerbork 21 cm emission map, and obtain $\log N(\text{H I})= 18.8 \pm 0.3$ from a nominal fit to the H I Ly α . We obtain a $\log N(\text{H I})\approx 17.2$ when we add the absorption in the two components. Rosenberg et al. (2014) obtain a lower metallicity of $\log Z/Z_{\odot}\approx -1$ because of the larger adopted column density and also because all the H I is associated with only one component which is all assumed to be related to the metals.

4.3.1 Galaxy Properties and Physical Interpretation

The absorption component at $\approx 845 \text{ km s}^{-1}$ has solar metallicity and is kinematically consistent with arising in the Leo Ring at the location of sightline SD. The galaxies NGC3384 and M105 are also within an impact parameter of $0.6R_{\text{vir}}$ of the sightline. M96 and NGC 3412 are within an impact parameter of $1.4R_{\text{vir}}$. These four galaxies have LP between 0.1–0.4, but we do not anticipate significant contribution to Mg II absorption (with predicted $\text{EW}_{\text{MgII},\lambda 2796}\approx 0.4$) from M96 or NGC 3412 at their large impact parameters. Table 4 lists galaxies with LP > 0.1. The Leo Ring and/or the

galaxies, M 105 and NGC 3384, could potentially explain the solar metallicity component along this sightline.

The H I-only absorption at 978 km s^{-1} is most likely to be related to M105, because it is relatively close to an extension of the kinematics based on its velocity map, and it is at an impact parameter of just $0.6R_{\text{vir}}$. The LP for M105 is determined to be 0.5. The next likely candidate, NGC 3412, has a lower LP of 0.01 and the absorption is much beyond the escape velocity of halo of NGC 3412. This absorption is unlikely to be associated with the Leo Ring as we do not see gas consistent with the observed velocity at this location. Alternatively, rather than being associated with a specific galaxy, this absorption could be related to loose material at large in this interacting group environment.

4.4 SE: The $z = 0.0023$ absorber towards the quasar J1047+1513

A system plot of the $z = 0.0023$ absorber is shown in Figure 7. This system shows strong C IV and N V absorption, and modest absorption in Si III. We find that a single phase model does not satisfactorily explain the H I profile shape, and also does not produce the observed amount of N V absorption in a phase that would agree both with Si III and C IV. We, therefore, model the absorption using two phases, a low ionization phase centered at $\approx 701 \text{ km s}^{-1}$ that produces the

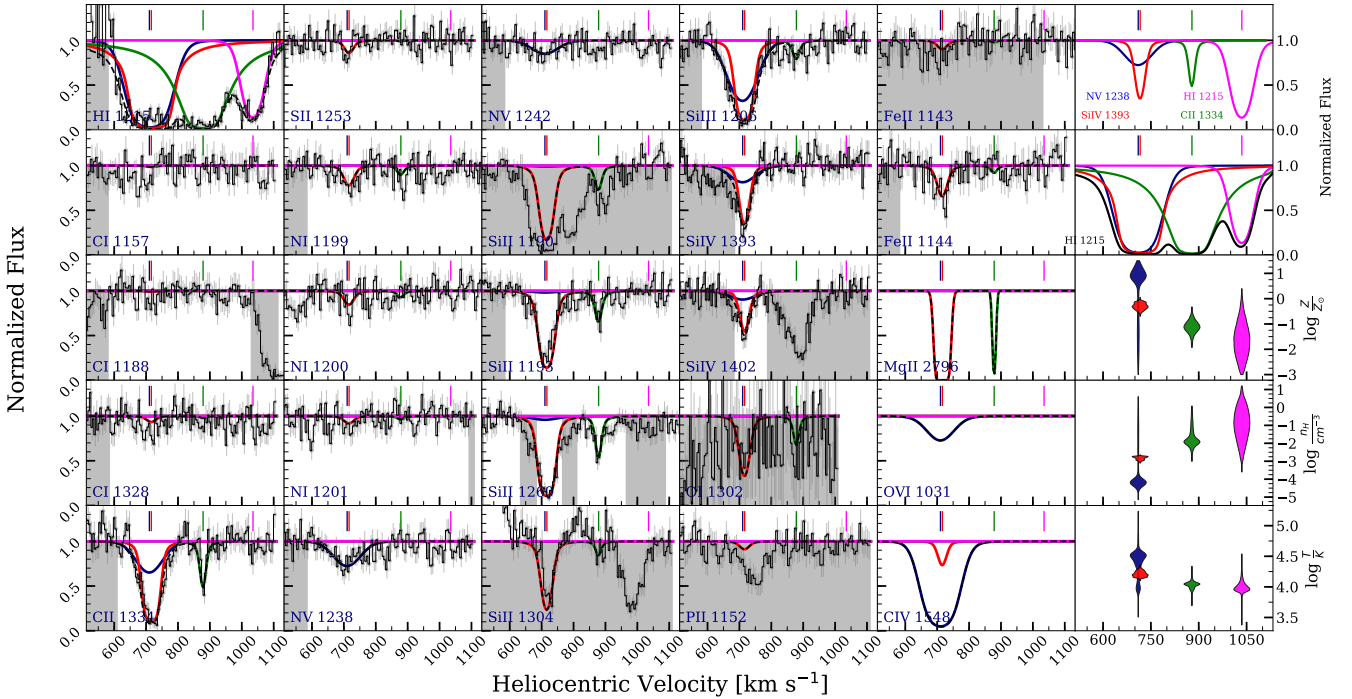


Figure 5. CLOUDY models for the $z = 0.00238$ absorber towards SC obtained using the MLE values, superimposed on the *HST*/COS spectra, displayed with one sigma errors. The centroids of absorption components as determined from the VP fits to constraining ions are indicated by the vertical tick marks on top of each panel. The photoionized gas phases are traced by four clouds - two coincident phases, one of which is a higher ionization phase tracing the broad N v absorption (blue curve) and the other tracing the bulk of the lower ionization absorption (shown as a red curve), the offset redward cloud traced by C II (shown as a green curve), and the H I-only cloud (shown as a magenta curve). The superposition of these four models is shown by the black dashed curve. A summary of the properties of these four clouds is shown in the form of violin plots using filled colors. The regions shaded in grey show the pixels that were not used in the evaluation of the log-likelihood.

modest absorption seen in Si III, and the bulk of the absorption in H I, and a high ionization phase centered at $\approx 705 \text{ km s}^{-1}$ that produces absorption seen in C IV and N V.

The properties of the low ionization cloud are determined to be $\log Z/Z_{\odot} \approx -0.4$, $\log n_{\text{H}} \approx -3.3$, and $\log T \approx 4.5$. The high ionization phase is determined to have a $\log Z/Z_{\odot} \approx 1$, a low density of $\log n_{\text{H}} \approx -4.5$, and a temperature of $\log T \approx 4.5$. The PDFs of the properties of the two clouds are presented using corner plots in Figures E4 – E7.

We also obtain a model in which the high ionization phase is collisionally ionized. We obtain similar properties for the metallicities of the two clouds compared with the PIE case. The temperature, however, for the high phase is higher $\log T \approx 5.2$ compared to $\log T \approx 4.5$ for the photoionized case. We also see from Figure E2 that possible zero-point uncertainties are negligible for $v > 600 \text{ km s}^{-1}$. A system plot showing the PC model is shown in Figure E3. Other physical properties of these clouds are summarized in Table 3.

4.4.1 Galaxy Properties and Physical Interpretation

Only the galaxy NGC 3377 is within $2R_{\text{vir}}$ of sightline SE, and it is at the fairly large separation of $1.6R_{\text{vir}}$. The LP is found to be ≤ 0.1 for the absorption to be associated with this galaxy. The absorption is consistent with being within the escape velocity of the halo of NGC 3377. The Leo Ring gas would also potentially match kinematically, within 50–100 km s^{-1} of this absorber, if it extended to lower H I column densities on the topside (see Fig. 1). The relatively strong C IV absorption in the high ionization phase,

$\text{EW}_{\text{C IV}, \lambda 1548} \approx 0.23 \text{ \AA}$, at this rather large distance ($\rho \approx 220 \text{ kpc}$) is unexpected from an elliptical galaxy like NGC 3377 (Liang & Chen 2014). We attribute this high metallicity absorption to be associated with the Leo Ring gas, and the bulk of H I absorption that also produces the modest absorption in Si III could either be from the Leo Ring gas or from NGC 3377.

4.5 SF: The $z = 0.0030$ absorber towards the quasar J1047+1513

A system plot of the $z = 0.0030$ absorber, with the constraining transitions, is shown in Figure 8. This system shows absorption in many low ionization transitions, including, C I, N I, Si II, and C II. We also observe absorption in the intermediate ionization transitions, Si III and Si IV. The data are noisy for this quasar and that leads to some uncertainty in the shape of the H I Ly α profile. Nonetheless, we are able to derive a one component model, that is consistent with the data. In addition to this metal-line absorption, the H I Ly α profile extends up to $\approx 1400 \text{ km s}^{-1}$. Only the component with metal lines detected can be constrained by models.

The physical parameters describing this absorption system are summarized using violin plots in Figure 8, and also presented in Table 3. The metallicity of the cloud centered at $\approx 910 \text{ km s}^{-1}$ is $\log Z/Z_{\odot} \approx 1.0$, while its density is $\log n_{\text{H}} \approx -2.7$. The size of the cloud along the line of sight is $\approx 2 \text{ kpc}$. The PDFs of the properties of this cloud are presented using corner plots in Figures F5–F6.

We performed two experiments to account for any systematic uncertainty in correctly modeling the Galactic Ly α absorption and

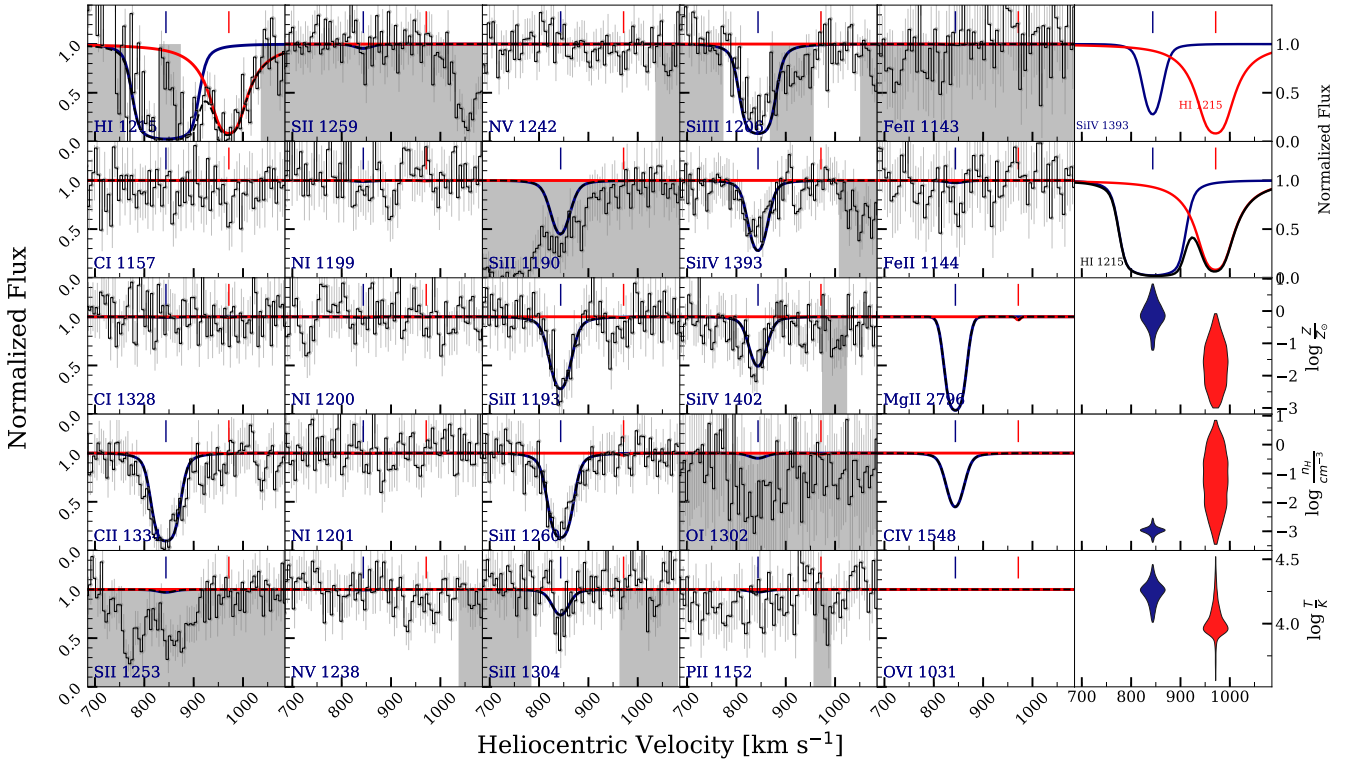


Figure 6. CLOUDY models for the $z = 0.00279$ absorber towards SD obtained using the MLE values, superimposed on the *HST/COS* spectra, displayed with their 1σ errors. The centroids of absorption components as determined from the VP fits to constraining ions are indicated by the vertical tick marks on top of each panel. The photoionized gas phases are traced by two clouds - the blueward cloud (shown as blue curve), and the offset redward cloud (shown as a red curve). The superposition of these two models is shown by the black dashed curve. A summary of the properties of these two clouds is shown in the form of violin plots using filled colors. The region shaded in grey shows the pixels that were not used in the evaluation of the log-likelihood.

the geocoronal emission due to the noisy nature of the H I profile. The main goal is to assess whether the metallicity of the metal line absorber is indeed super-solar. In the first experiment, our prior included only the information from metals, the observed H I profile was masked when determining the constraints. Even considering just the metal lines, we inferred a metallicity of $\log Z/Z_{\odot} = 0.60 \pm 0.15$ for the cloud at $\approx 910 \text{ km s}^{-1}$. The synthetic profiles based on this model are shown in Figure F3. It may seem counterintuitive that it is possible to infer a metallicity without using the hydrogen lines. However, the strong detected Si IV absorption must arise in an ionized zone of absorption, which has only $\log N(\text{H}) \sim 19$ regardless of the size of any shielded neutral layers, and thus must have high metallicity to produce the strong Si IV. In the second experiment, we forced the prior on $\log N(\text{H I})$ to only take values greater than 19.5. The system plot showing the model profiles for this experiment is shown in Figure F4. It would appear that the solution is not an acceptable fit to the Ly α , but it is hard to tell for certain. Regardless of this, even for this much larger $N(\text{H I})$ the metallicity that we obtained was $\log Z/Z_{\odot} = 0.21 \pm 0.08$. Both these extreme experiments reveal that the “true” metallicity of this system has to be super-solar.

This absorber was previously studied by Rosenberg et al. (2014). They used a column density, $\log N(\text{H I})$, of 19.5 as measured from the 21cm emission map. By associating all of the H I absorption to the observed metal line absorption, they determined a metallicity consistent with $\log Z/Z_{\odot} \approx -1$. However, from our modeling we find that a one component gas-phase with $\log N(\text{H I})$

of ≈ 17.6 , centered on the metal absorption, explains all the observed metal absorption.

4.5.1 Galaxy Properties and Physical Interpretation

Three luminous galaxies lie within a virial radius of sightline SF, as shown in Figure 3. M105 is at an impact parameter of $0.5R_{\text{vir}}$, and the extension of its velocity map in the direction of SF could explain the absorption at $\approx 900 \text{ km s}^{-1}$. The LP is determined to be ≈ 0.8 . The other galaxies, M96 and NGC 3384, are also within $0.5R_{\text{vir}}$ of this sightline, and the absorption centroid is consistent within the escape velocity of halo of these galaxies. The LP for these two galaxies is ≈ 0.3 .

The Leo Ring gas, however, would also be at a velocity consistent with the metal line absorption in this region. The gas could be more directly related to the ring itself if the interaction that produced the ring has distributed the gas that was connected to the individual galaxies.

Note also the extension of H I Ly α absorption (without associated metals) out to velocities as high as 1400 km s^{-1} , indicating a kinematically complex structure along this sightline.

4.6 SG: The $z = 0.0027$ absorber towards the quasar J1048+1306

A system plot of the $z = 0.0027$ absorber, with the constraining transitions, is shown in Figure 9. This system shows strong metal line

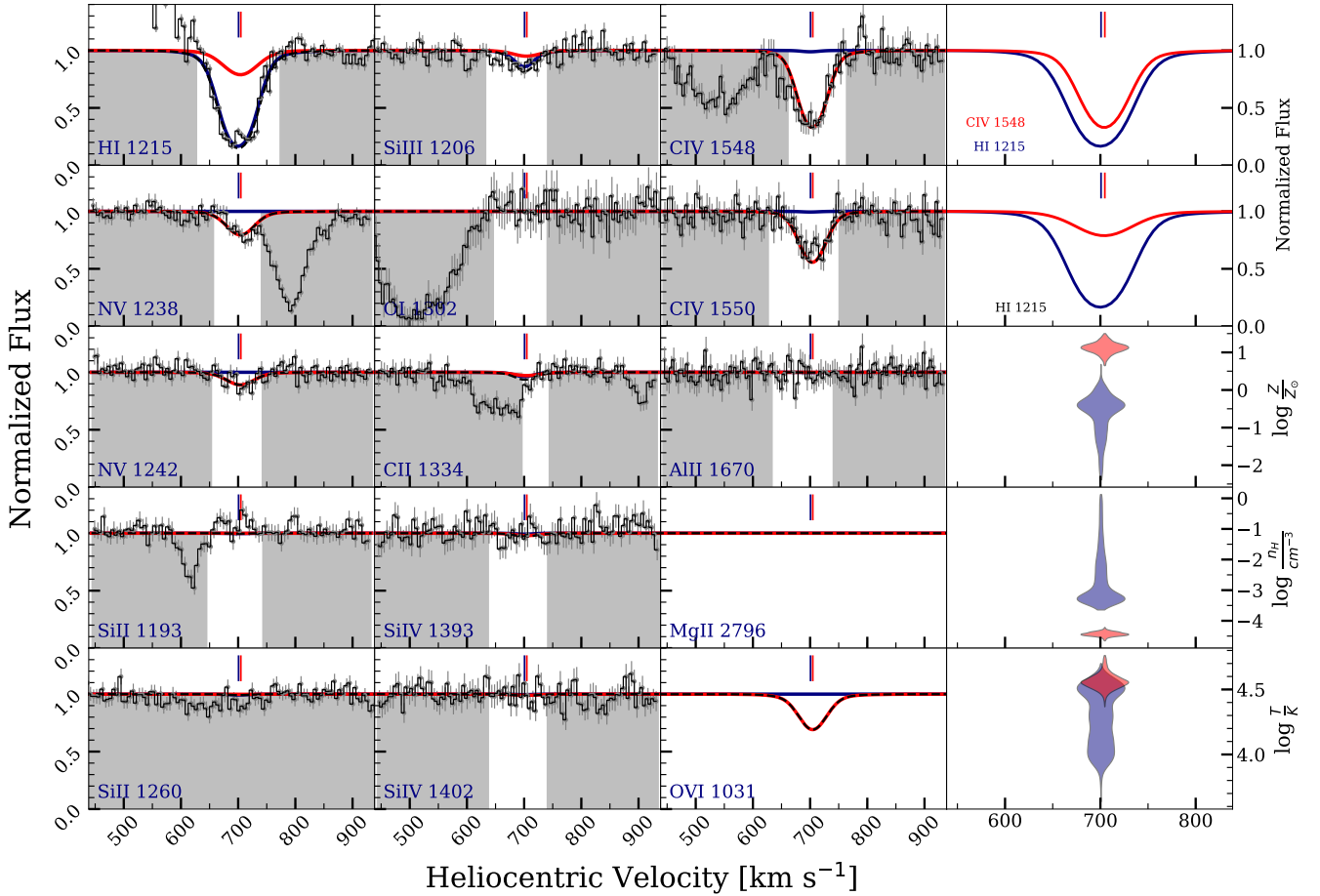


Figure 7. CLOUDY models for the $z = 0.0023$ absorber towards SE obtained using the MLE values. The spectral data are shown in gray with 1σ errors. The centroids of absorption components as determined from the VP fits to constraining ions are indicated by the vertical tick marks on top of each panel. The blue-colored curve traces the dominant absorption seen in H I. The red-colored curve traces the absorption seen in the higher ionization C IV and N V transitions.

The violin plots show the full posterior distribution of the physical properties of the cloud. The region shaded in grey shows the pixels that were not used in the evaluation of the log-likelihood.

absorption only at two velocities, $\approx 817 \text{ km s}^{-1}$ and $\approx 861 \text{ km s}^{-1}$, detected in Si III, Si IV, and C IV. Five distinct components are apparent in H I Ly α , centered at velocities of 817, 861, 943, 1057, and 1297 km s^{-1} .

We find that the Si III, Si IV, and C IV arise in the same gas phase for the gas clouds at ≈ 817 and $\approx 861 \text{ km s}^{-1}$. These two clouds have similar properties, high metallicities of $\log Z/Z_{\odot} \approx 1.4$, temperatures of $\log T \approx 4.2$, and low densities of $\log n_{\text{H}} \approx -4.0$ and -3.6 , respectively. The line of sight cloud thicknesses are $L \approx 200$ pc and 600 pc, respectively. The physical parameters describing this absorption system are summarized using violin plots in Figure 9 and in Table 3. The three components detected in H I Ly α , but not in metal lines, are poorly constrained. The PDFs of the properties of these clouds are presented using corner plots in Figures G4 – G13.

This absorber has been previously studied by Rosenberg et al. (2014). Based on the absence of radio emission at the location of the QSO, they place an upper limit on the $\log N(\text{H I})$ of 18.73, and do not derive a metallicity because of the noisy data.

We explore the consequences of zero-point uncertainty of the H I Ly α flux for the components between 815–865 km s^{-1} . The violin plots showing the distribution of parameters for 100 MC realizations are presented in Figure G3. We find that the posteriors

for various phases are still in agreement within uncertainties of the values presented in Table 3 for SG. The metallicity of the C IV phase at 815 km s^{-1} is still well constrained by the rapid decline on the blueward side of the Ly α profile, and not heavily dependent on the zero-point. The Si IV phase at $\approx 861 \text{ km s}^{-1}$, however, is more significantly affected by the presence of a zero-point uncertainty, since its Ly α profile is blended with others on both sides.

4.6.1 Galaxy Properties and Physical Interpretation

The metal-line components at 817 and 861 km s^{-1} are consistent with the Leo Ring kinematics at the position of SG. The galaxy M105, with an impact parameter of $0.6 R_{\text{vir}}$ and a velocity of 880–900 km s^{-1} in this direction, could also contribute to the absorption. It has an LP of ≈ 0.35 . NGC 3412 with an impact parameter $0.9 R_{\text{vir}}$ and velocity $\approx 860 \text{ km s}^{-1}$ could also contribute (a LP of ≈ 0.3). As with SF, it is not straightforward to distinguish between absorption arising in individual galaxies as compared to the ring because the gas in the ring likely originated in the surrounding galaxies.

The H I-only component at 943 km s^{-1} is likely to be associated with M105, and it has a LP of ≈ 0.6 . The next likely candidate is NGC 3412 with a LP of ≈ 0.2 . The H I-only component at 1057 km s^{-1}

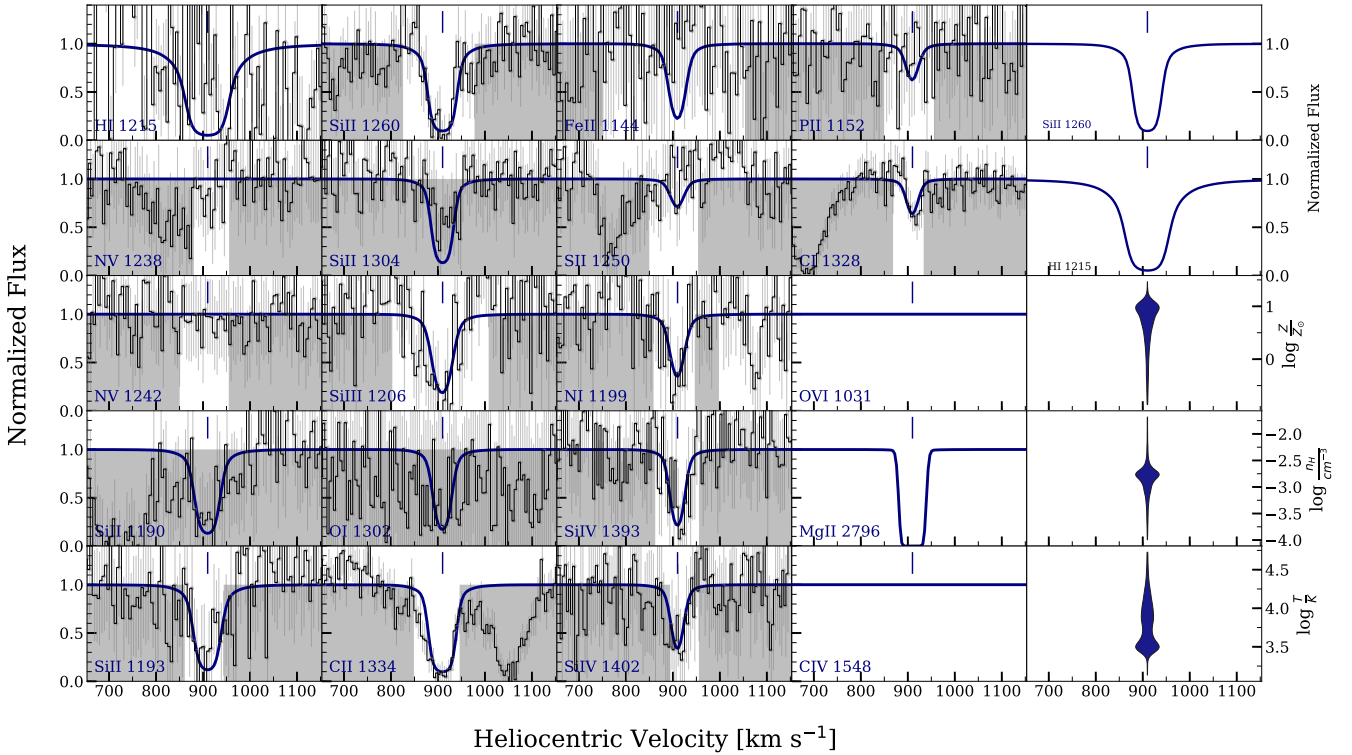


Figure 8. CLOUDY models for the $z = 0.0030$ absorber towards SF obtained using the MLE values. The spectral data are shown in gray with 1σ errors. The centroids of absorption components as determined from the VP fits to constraining ions are indicated by the vertical tick marks on top of each panel. One phase of photoionized gas if found to explain the absorption seen in the data. A summary of the properties of this cloud is shown using the violin plots. The region shaded in grey shows the pixels that were not used in the evaluation of the log-likelihood.

could also be associated with M105, but it has a very low LP of ≈ 0.04 . The H I-only component at 1314 km s^{-1} shows a possible association with NGC 3389 with a LP of 0.1, however, it is at an impact parameter of $1.5R_{\text{vir}}$ from the galaxy. These H I-only components are unlikely to be associated with the Leo Ring at the location of SG because of the mismatch in kinematics, but they could be from other gas "at large" in the group.

4.7 SH: The $z = 0.0028$ absorber towards the quasar J1051+1247

A system plot of the $z = 0.0028$ absorber, with the constraining transitions, is shown in Figure 10. This system shows metal line absorption at $\approx 767 \text{ km s}^{-1}$ and $\approx 818 \text{ km s}^{-1}$ in C II and Si III, and in the Si IV and C IV doublets. The G160M observation of the C IV is quite noisy to place a meaningful constraint on the presence/absence of C IV for the $\approx 818 \text{ km s}^{-1}$ component. Two additional, distinct H I components, without detected metals, are also seen, centered at ≈ 900 and $\approx 977 \text{ km s}^{-1}$.

Table 3 lists constraints on the physical parameters describing this absorption system, which are summarized using violin plots in Figure 10. The component at 767 km s^{-1} has a low metallicity of $\log Z/Z_{\odot} \approx -1.7$, a low density of $\log n_{\text{H}} \approx -3.4$, a high temperature of $\log T \approx 4.9$, and a line of sight thickness of $\approx 50 \text{ kpc}$. The stronger metal line component at 818 km s^{-1} has a supersolar metallicity of $\log Z/Z_{\odot} \approx 1.4$, hydrogen density $\log n_{\text{H}} \approx -4.2$, temperature of $\log T \approx 4.3$, and line of sight thickness of $\approx 40 \text{ kpc}$. The H I clouds at $\approx 900 \text{ km s}^{-1}$ and $\approx 977 \text{ km s}^{-1}$ are less certain in their properties. The metallicity is determined to be $\log Z/Z_{\odot}$

< -0.2 and < 0 , and $\log n_{\text{H}} > -2.25$ and > -3.8 . The PDFs of the properties of these clouds are presented using corner plots in Figures H4 – H11.

We explore the consequences of zero-point uncertainty of the H I Ly α flux for the components between $765\text{--}820 \text{ km s}^{-1}$. The violin plots showing the distribution of parameters for 100 MC realizations with different zero-point values are presented in Figure H3. We find that the posteriors for various phases are still in agreement within uncertainties of the values presented in Table 3 for SH. Our conclusions about the nature of the absorption system are not affected by the presence of a zero-point uncertainty.

4.7.1 Galaxy Properties and Physical Interpretation

The galaxies NGC 3384 and M96 which are at $0.8R_{\text{vir}}$ and $1.4R_{\text{vir}}$ could contribute to the low metallicity absorption at 767 km s^{-1} . They have LPs of 0.3 and 0.1, respectively. With only $\log Z/Z_{\odot} \approx -1.7$, the gas would have to be inflowing toward one/both of these galaxies. Several galaxies could contribute to the contrasting, supersolar metallicity absorption at 818 km s^{-1} , however their impact parameters are large to produce such strong absorption, with NGC 3412 being the closest at $0.9R_{\text{vir}}$. The other galaxies that could contribute are listed in Table 4. The velocity of an extension of the Leo Ring would also be kinematically consistent with the super-solar metallicity component at 818 km s^{-1} , so we favor an interpretation with a contribution from the ring, with possible contributions from the other galaxies and intragroup environment.

Among the sightlines studied here, SH is unusual in the con-

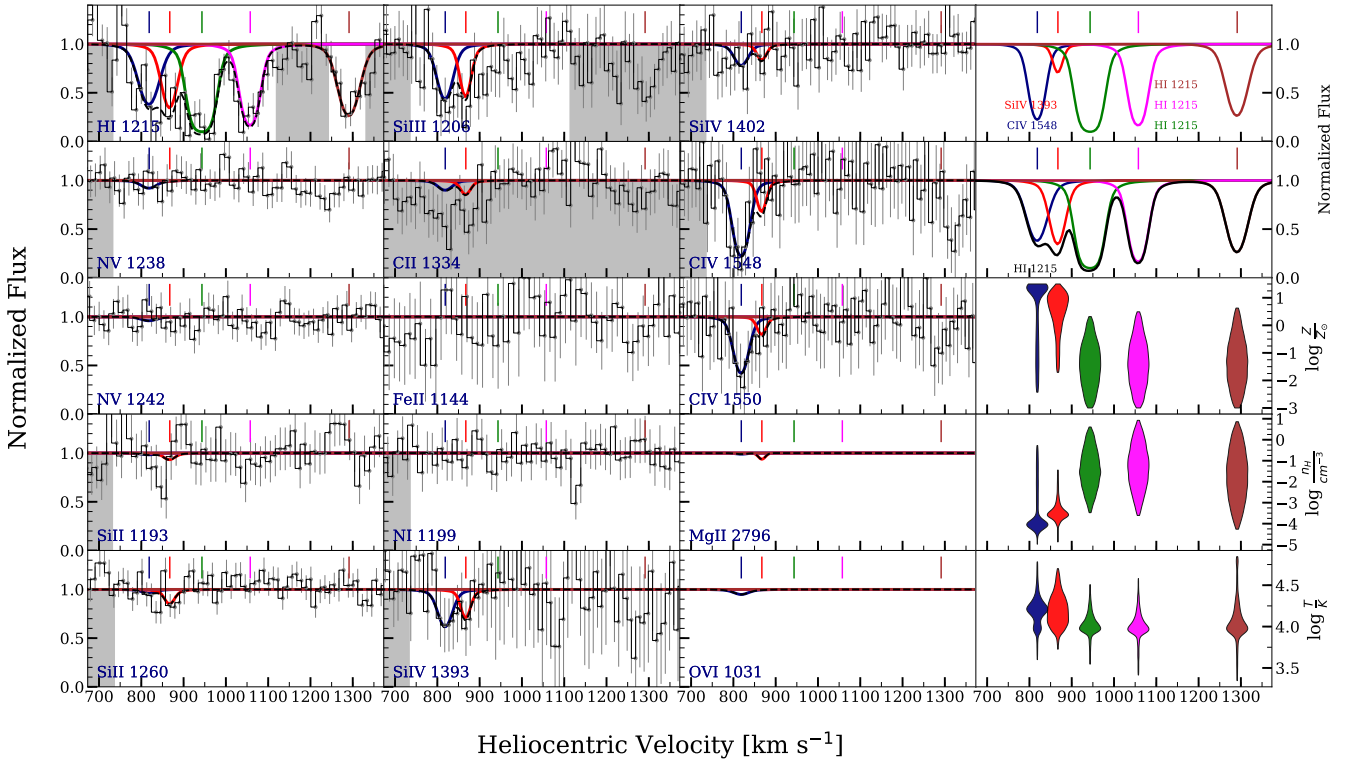


Figure 9. CLOUDY models for the $z = 0.0027$ absorber towards SG obtained using the MLE values. The spectral data are shown in gray with 1σ errors. The centroids of absorption components as determined from the VP fits to constraining ions are indicated by the vertical tick marks on top of each panel. The data has been binned by 2 pixels for display purposes. The photoionized gas phases are traced by five clouds - the blueward cloud constrained on Si III (shown as a blue curve), and the blended redward cloud constrained on Si III (shown as red curve), the three offset H I-only clouds shown as green, magenta, and brown curves. The superposition of these three models is shown by the black dashed curve. A summary of the properties of these five clouds is shown using violin plots. The region shaded in grey shows the pixels that were not used in the evaluation of the log-likelihood.

trasting metallicities of components at similar velocities. However, such examples are seen in the literature (Zahedy et al. 2019; Norris et al. 2021) where they can be interpreted as a combination of pristine inflow and metal-enriched outflows or recycled accretion.

4.8 SI: Lack of absorption towards the quasar J1052+1017

We do not see any absorption in H I Ly α , the low ionization transition of Si II, and the intermediate ionization transition of Si III towards this quasar within the heliocentric velocity range of 600–1400 km s $^{-1}$. Figure 11 shows the non-detections in these transitions.

4.8.1 Galaxy Properties and Physical Interpretation

The nearest galaxy to this sightline is M96 at a projected separation of $\approx 2.0 R_{vir}$. The galaxies within a projected separation of $3R_{vir}$ are listed in Table 4.

4.9 SJ: The $z = 0.0024$ absorber towards the quasar J1059+1441

A system plot of the $z = 0.0027$ absorber, with the constraining transitions is shown in Figure 12. This system shows absorption in two components, a H I-only component without any metals at ≈ 651 km s $^{-1}$ (shown as a blue curve), and another component at ≈ 720 km s $^{-1}$ (shown as a red curve) which shows absorption in the

low ionization transition of C II, but only a 3σ detection in Si II, we also observe absorption in the intermediate ionization transitions of Si III and Si IV, and in the higher ionization transition of C IV. We do not observe absorption in any of the neutral transitions.

The blueward component is not well constrained. We set an upper limit on its metallicity of $\log Z/Z_{\odot} < 0.5$ and the hydrogen density is a lower limit with $\log n_{\text{H}} > -2.25$. The redward component is well constrained to have $\log n_{\text{H}} \approx -4.0$, while its metallicity would be $\log Z/Z_{\odot} \approx 0.5$ in order to explain all of the H I Ly α absorption centered at 720 km s $^{-1}$ and produce the strong absorption seen in C IV. The constraints are illustrated in the violin plots included in Figure 12. The PDFs of the properties of this cloud are presented using corner plots in Figures J3 – J6.

4.9.1 Galaxy Properties and Physical Interpretation

Sightline J is relatively isolated from galaxies as compared to most of the others, with only one galaxy, NGC 3489, at $1R_{vir}$ that could be responsible for the absorption, with an LP of ~ 0.25 . There are also a couple of dwarf galaxies, however, they are at large separations $\geq 2.9R_{vir}$, and unlikely to contribute to the absorption with an LP of $\sim 10^{-4}$. The component at ≈ 650 km s $^{-1}$ is likely to be associated with NGC 3489. An extension of the Leo Ring in this direction would have a relatively low velocity, consistent with the absorption at 720 km s $^{-1}$, although it is at a relatively large distance of 550 kpc from the part of the ring detected in 21-cm. The observed C IV absorption is quite strong compared to expectations for such

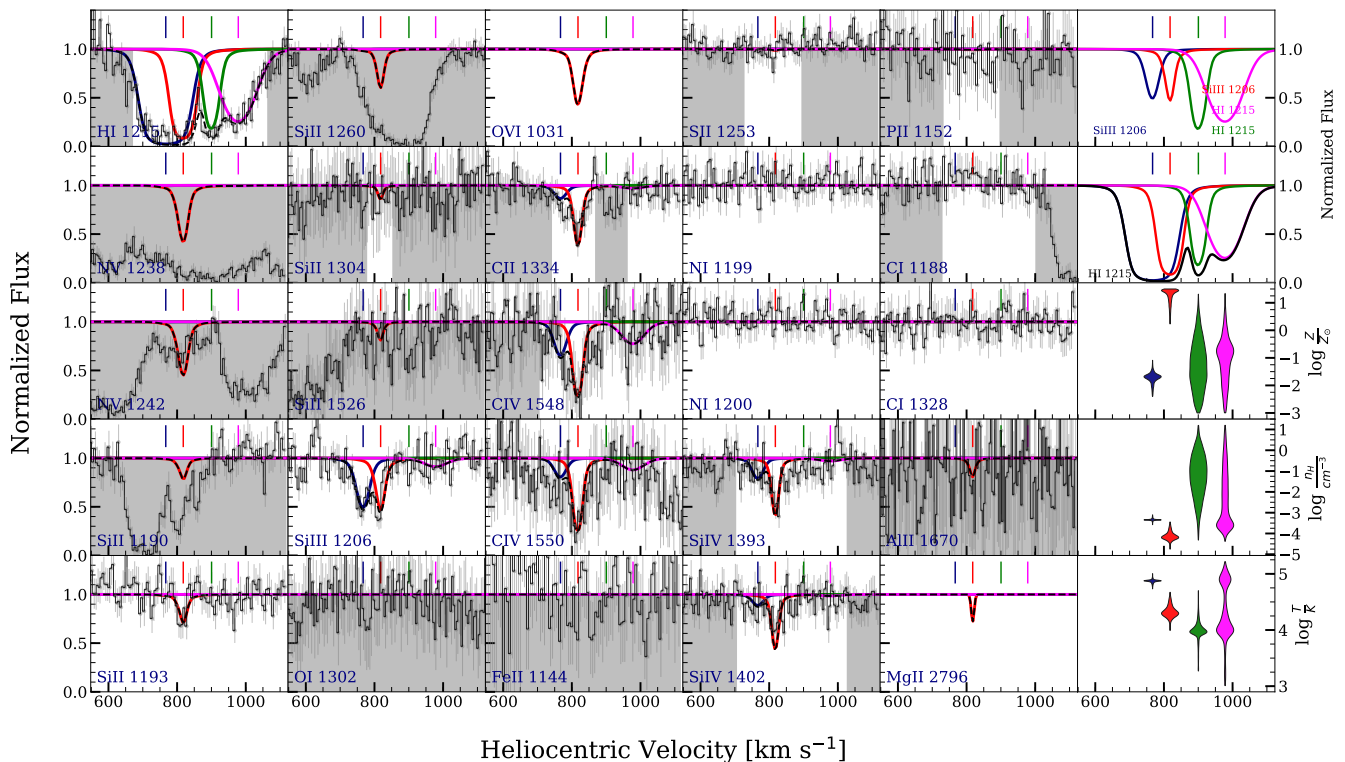


Figure 10. CLOUDY models for the $z = 0.0028$ absorber towards SH obtained using the MLE values. The spectral data are shown in gray with 1σ errors. The centroids of absorption components as determined from the VP fits to constraining ions are indicated by the vertical tick marks on top of each panel. The photoionized gas phases are traced by four clouds - the blueward cloud optimized on Si iv (shown as a blue curve), and the blended redward clouds optimized on Si iv (shown as red and green curves), and the offset redward cloud optimized on C ii (shown as a magenta curve). The superposition of these three models is shown by the black dashed curve. A summary of the properties of these four clouds is shown in violin plots. The region shaded in grey shows the pixels that were not used in the evaluation of the log-likelihood.

galaxies (Burchett et al. 2016). Given the strong C iv absorption, we favor an origin of the metal-rich material in gas related to the interaction that produced the Leo Ring.

4.10 SK: Lack of absorption towards the quasar J1059+1211

We do not see any absorption in H i Ly α , the low ionization transition of Si ii, and the intermediate ionization transition of Si iii towards this quasar within the heliocentric velocity range of 600-1400 km s $^{-1}$. Figure 13 shows the non-detections in these transitions.

4.10.1 Galaxy Properties and Physical Interpretation

The nearest galaxies to this sightline is NGC 3489 at a projected separation of $\approx 2.0 R_{vir}$. It is reasonable that no absorption is detected in SK given such a large galaxy separation. Galaxies within $\approx 3.0 R_{vir}$ to this sightline are shown in Table 4.

4.11 SL: Lack of absorption towards the quasar J1100+1046

We do not see any absorption in H i Ly α , the low ionization transition of Si ii, and the intermediate ionization transition of Si iii towards this quasar within the heliocentric velocity range of 600-1400 km s $^{-1}$. Figure 14 shows the non-detections in these transitions.

4.11.1 Galaxy Properties and Physical Interpretation

The nearest galaxy to this sightline is a dwarf galaxy, dw1059+11, at a separation of $3.4 R_{vir}$. The large separation is consistent with the lack of absorption along SL.

5 SUMMARY AND DISCUSSION

A general picture of the gaseous content of the Universe is emerging from studies of quasar sightlines through regions at various impact parameters from galaxies of different types (masses, morphologies, star formation rates, etc.). From these we learn in a statistical sense the covering factors and radial distributions of gas around galaxies in H i, low, intermediate, and high ionization gas. The dependencies of these properties on the environment (isolated, group, or cluster) of the galaxies also provide a measure of the contributing processes and also on the larger-scale gas distribution. In addition to the statistical studies, there have been several cases of multiple lines of sight through individual galaxies (e.g. Rao et al. 2013; Lehner et al. 2015, 2020) that yield information about the variations of properties within a single galaxy.

With this study of the Leo Ring/group we aimed to make connections between these different methods by studying 11 lines of sight through a $7^\circ \times 6^\circ$ region. In each case where absorption is detected, there is potential contribution to the absorption from one or more luminous galaxies (within one or two virial radii), from dwarf

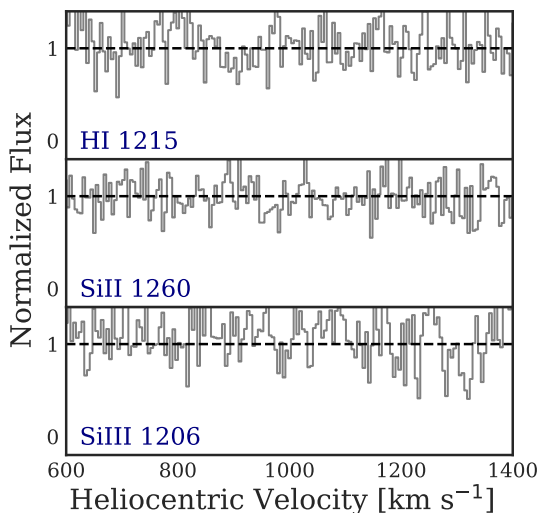


Figure 11. The spectral data for SI showing lack of absorption in H I Ly α , Si II, and Si III within the heliocentric velocity range of 600–1400 km s $^{-1}$.

galaxies, from an intragroup medium, from the specific interaction debris known as the Leo Ring, and from the general larger scale filamentary structure. We benefit from the close proximity of the group because it is possible to detect even faint galaxies in the region, and thus know a great deal about the galaxy and H I distribution. It is so nearby, however, at 600–1400 km s $^{-1}$, that we had to overcome the challenge of fitting Galactic Ly α and correcting for geocoronal emission in order to analyze the Ly α absorption from our Leo Ring/Group sightlines. With our component-by-component, Bayesian methods, and careful treatment for Galactic Ly α , we are able to consider which objects/processes are shaping the multiphase absorption along each sightline. This allows us to consider whether there is a coherency in properties across the region. We can also infer whether similar complexities, which may be unseen, are potentially influencing the general absorption properties along sightlines in surveys of galaxies at higher redshifts.

Figure 15 shows a map of the Leo Ring region, with the equivalent widths (EWs) of absorption (between 600 and 1400 km s $^{-1}$) indicated by the size of the colored circles for H I Ly α , Si II, and C IV. We can see that the absorption is stronger close to the 200 \times 200 kpc 2 region of the H I ring. The EW of H I Ly α , in these cases, is tied to the kinematic spread of the H I more so than to the column density of H I. Besides in the sightlines close to the ring (SC, SD, SF, SG, and SH within 250 kpc), metals are also detected in SE and SJ. Sightline SB has only a H I Ly α detection, while SI, SK, and SL do not have any detected absorption in the relevant velocity range.

Figure 16 shows the absorption profiles of H I Ly α for all of the sightlines, with the model profiles superimposed. The expected velocities for extensions of large nearby galaxies (M95, M96, M105, NGC3384, and NGC3412) in the direction of the quasar sightlines are shown as shaded regions superimposed on the profiles. The expected velocities of the Leo Ring absorption at the position of the sightline are also shaded in pink for sightlines SC, SD, SE, SF, SG, SH, and SJ for which some of the H I Ly α absorption is seen coincident with that velocity. The width of the shaded regions account for expected velocities within the escape velocity of a galaxy’s halo. For sightline SB, the absorption does not appear to be related

to specific galaxies. For each sightline, the panel also shows the EW of H I Ly α , the column density of H I given by the sum of the model components, the distance to the center of the Leo Ring (ρ_o), and the ρ/R_{vir} value to the nearest galaxy. Note that the $N(\text{H I})$ value need not be large for a system with large EW, if it is composed of several components. In that case the EW is large due to the kinematic spread of these components. We see that sightlines with the strongest H I Ly α profiles are both close to the Leo Ring, and close to their nearest galaxy. This is not surprising given that the ring formed in a galaxy group environment, but it does lead to some ambiguity in distinguishing between the two origins. As we have discussed, multiple origins for the absorption components at different velocities along such single sightlines is likely.

Constraints on metallicity, density, temperature, and line of sight thickness of the gas have been derived for each absorption component using CLOUDY modeling as described in section 4. Figure 17 summarizes these results. Most violin plots have large uncertainties because there are no detections in the component for any of the metal line transitions. We note that most components, and particularly all the ones that are plausibly kinematically associated with the Leo Ring, have metallicities of greater than the solar value (up to several times Z_{\odot}). Densities are typically low, between 10^{-4} and 10^{-3} cm $^{-3}$. Most absorption components are produced by gas with a line of sight thickness between 1 and 10kpc. Those components with a velocity consistent with an extension of the Leo Ring (as detected in 21cm) in the direction of the sightline are circled in black. We find that all sightlines with detections except SB have one or more components likely to be associated with the Leo Ring or extended gas that resulted from the same interaction. The properties of this subset of well-constrained components are uniform, with supersolar metallicities and low densities.

5.1 LEO RING ABSORPTION

The similarity in properties of the subset of components identified in Figure 17 suggests that there is a coherent structure of tidal debris in this region, consistent with the origin of the Leo Ring proposed in other previous investigations (Michel-Dansac et al. 2010). Corbelli et al. (2021) also found metallicities close to the solar value for three H I clumps near SF using nebular emission lines, and concluded that the metals arose in the nearby large galaxy, M105, and were removed by tidal forces. The metallicities and kinematic spreads of the absorbers that we confirm throughout the entire Leo Ring region are consistent with this, given that the origin of the debris is from giant galaxies that themselves have solar or supersolar metallicity, based on the expectations from the mass-metallicity relationship (Tremonti et al. 2004). The mass of the ring, from 21-cm studies, is about two billion solar masses (Schneider 1985). Here, we estimate the mass of the ring: $\pi \frac{d^2}{4} L n_H \mu m_H$

$$M \approx \left[\frac{d/2}{kpc} \right]^2 \left[\frac{L}{kpc} \right] \left[\frac{n_H}{cm^{-3}} \right] \times 1.1 \times 10^8 M_{\odot} \quad (2)$$

Assuming the gas is spread over a circular region with diameter 200 kpc, and that the thickness of the region is 10 kpc, the average gas density is $10^{-3.5}$ cm $^{-3}$, and $\mu=1.4$ accounts for the presence of helium and heavy elements in the gas, we determine the mass to be 3.5 billion solar masses.

It is reassuring that the basic properties that we have inferred for our quasar sightlines yield a mass roughly consistent with 21-cm observations for the Leo Ring. However, it is also clear that

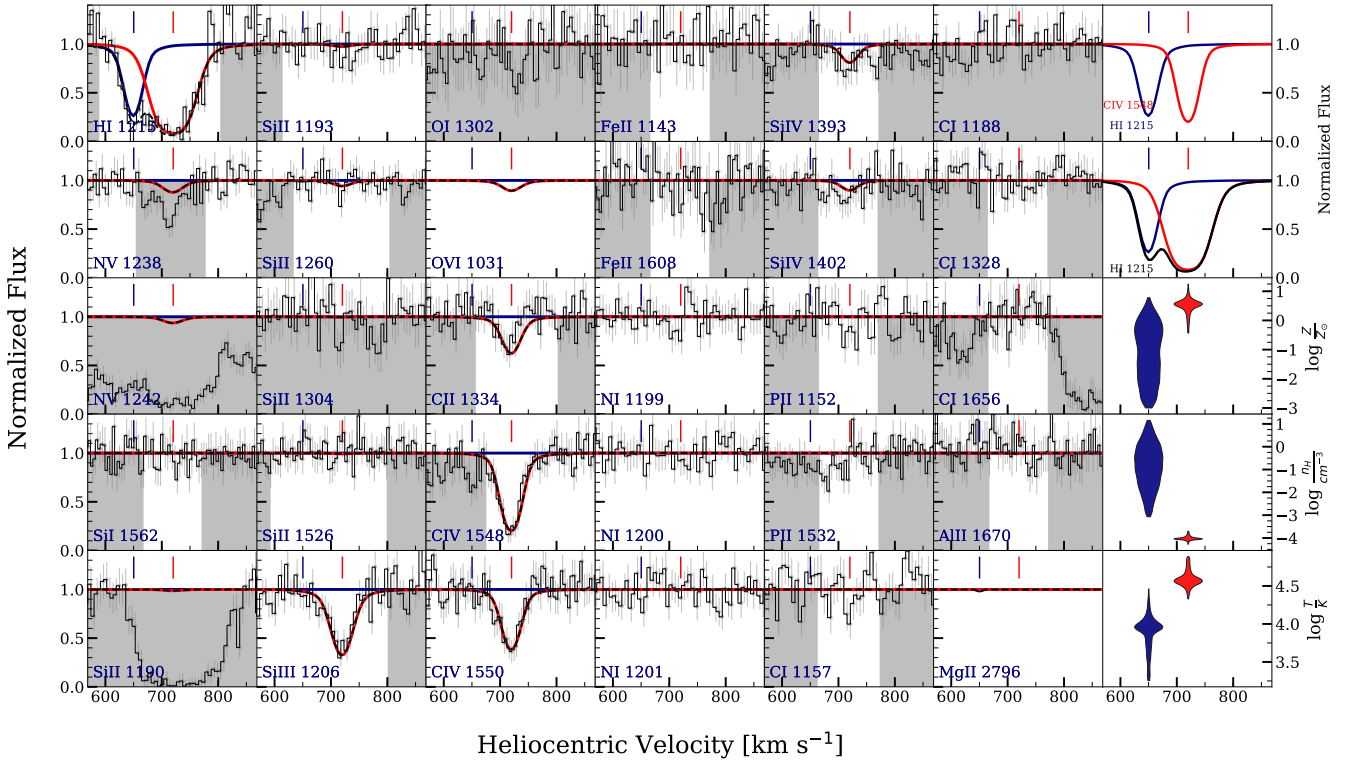


Figure 12. CLOUDY models for the $z = 0.0028$ absorber towards SJ obtained using the MLE values. The spectral data are shown in gray with 1σ errors. The centroids of absorption components as determined from the VP fits to constraining ions are indicated by the vertical tick marks on top of each panel. The photoionized gas phases are traced by two clouds - the blueward cloud constrained on H I (shown as a blue curve), and the redward cloud constrained on C IV (shown as red curve). The superposition of these two models is shown by the black dashed curve. A summary of the properties of these two clouds is shown using the violin plots. The region shaded in grey shows the pixels that were not used in the evaluation of the log-likelihood. The $N \nu \lambda 1238$ line is contaminated by O IV $\lambda 787$ absorption from a $z = 0.5765$ absorber, hence it is masked out.

the region is not as homogeneous in density as we have assumed. Evidence for a clumpy medium is provided by the fact that the H I column densities from 21-cm emission observations (over a large beam size of about $\approx 1.75' \times 0.65'$) are an order of magnitude or more larger than those from our models along the pencil beams we are studying. For example, [Rosenberg et al. \(2014\)](#) found from Westerbork observations that $\log N(\text{H I}) = 19.1$ for SD compared to our model sum of components of only 17.2. For SF, [Rosenberg et al. \(2014\)](#) find $\log N(\text{H I}) = 19.5$ and obtain a metallicity of $\log Z/Z_{\odot} \approx -1$ by associating all the metal absorption to a phase with $\log N(\text{H I}) = 19.5$, compared to $\log N(\text{H I}) = 17.6$ and a metallicity of ≈ 1 for our models. For SG, our model values only sum to $\log N(\text{H I}) = 15.4$ and the sightline is just outside of the contours for detected 21-cm emission which implies an $\log N(\text{H I})$ value greater than 18 is unlikely. In a clumpy medium we expect that small regions inside the beam might have $N(\text{H I})$ values one or more orders of magnitude bigger than others. These small regions may occupy a very small fraction of the beam but would average out to a much larger value than typical for a pencil beam measurements. We thus believe that there is no inconsistency, and that the tidal debris has structure on small scales.

5.2 COMPARISON OF SIGHTLINES TO ABSORPTION SIGNATURES OF GALAXIES AND GALAXY GROUPS

It is clear that lines of sight through the Leo Ring environment produce relatively strong absorption from gas with high metallicity, and with complex kinematics. However, sightlines close to the ring are also close to the galaxy group that is related to the ring. In order to better understand the major contributing factors to the observed absorption signatures, we consider the EWs of several key transitions as a function of impact parameter from the nearest galaxy and perform as simple benchmarking with CGM absorbers in the literature. Through this, we explore the impact on observed signatures due to proximity to a gas rich region, i.e. the Leo Ring. To consider how to interpret absorption as related to individual galaxies, to the group gas, and/or to the Leo ring itself, we compare to studies that probe the CGM of a wide range of galaxies. We have plotted the observed equivalent widths as a function of impact parameter for star forming and for quenched galaxies ([Tumlinson et al. 2013](#); [Kacprzak et al. 2021](#)), for dwarfs up to massive ellipticals ([Bordoloi et al. 2014](#); [Johnson et al. 2017](#); [Zahedy et al. 2019](#)), from surveys probing galaxy disk-CGM interface ([Borthakur et al. 2015](#)) to galaxy halos ([Werk et al. 2013](#)), and from surveys indifferent to galaxy properties ([Nielsen et al. 2013](#); [Liang & Chen 2014](#)). Our goal is to consider whether the equivalent widths are typical at that impact parameter from the individual galaxies, or whether the complex group environment is leading to larger values.

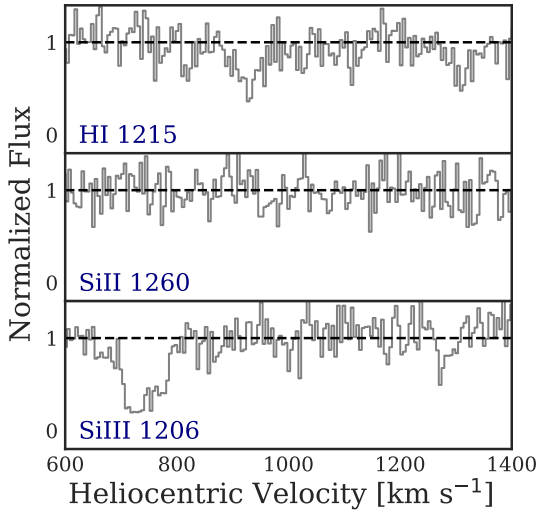


Figure 13. The spectral data for SK showing lack of absorption in H I Ly α , Si II, and Si III within the heliocentric velocity range of 600-1400 km s⁻¹.

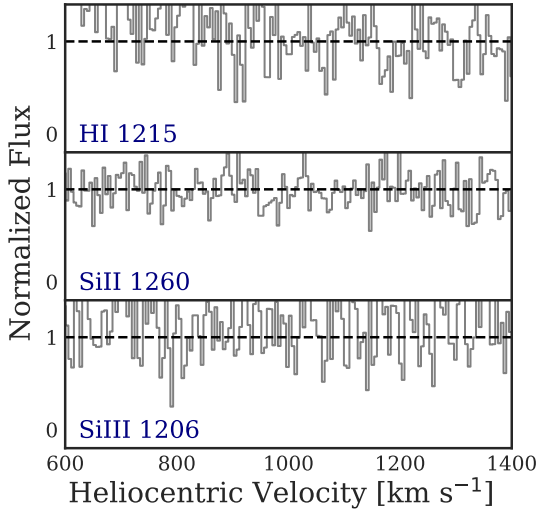


Figure 14. The spectral data for SL showing lack of absorption in H I Ly α , Si II, and Si III within the heliocentric velocity range of 600-1400 km s⁻¹.

Figure 18 shows this comparison for several key transitions. The EWs plotted are the values for the entire system, integrating over the full velocity range, and they are plotted against the ρ/R_{vir} value for the nearest galaxy. For Mg II, C IV and O VI these are model predictions, since these transitions are not covered. The actual values could be larger if hidden phases (e.g. collisionally ionized gas) are contributing (Narayanan et al. 2021). In general, the five sightlines closest to the ring center (SC, SD, SF, SG, and SH) have H I Ly α , low ionization (Si II and Mg II), intermediate ionization (Si III and Si IV), and C IV EWs that are among the largest of absorbers at the same ρ/R_{vir} from their nearest galaxies. These strong absorption lines in our sample, compared to respective ones in relatively isolated environments, could be potentially due to contributions from

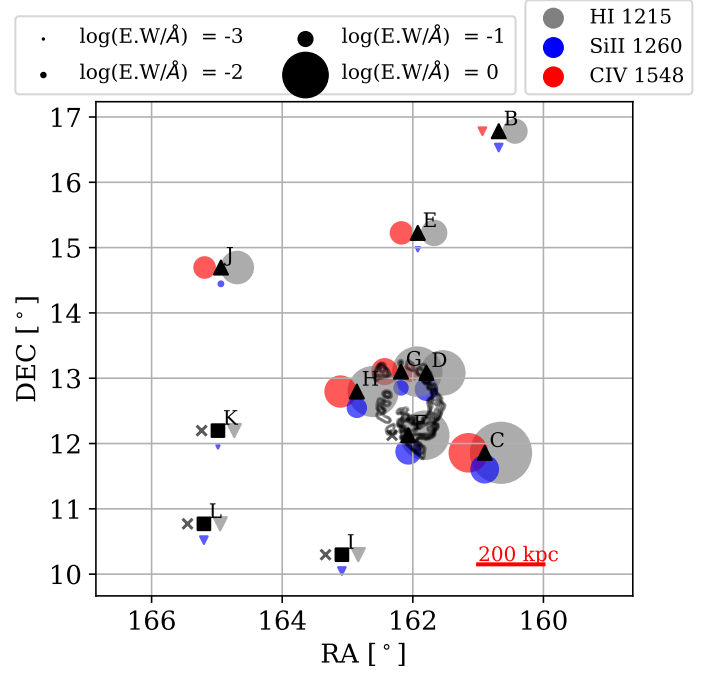


Figure 15. A map of the Leo Ring field showing the 11 sightlines and the rest-frame EW measurement for absorption seen in H I Ly α , Si II, and C IV. Sightlines with H I absorption detected in the range between 600 and 1400 km s⁻¹ are shown as triangles. Sightlines with H I non-detections between 600 and 1400 km s⁻¹ are shown as squares. The EWs of absorption in several transitions are indicated by the size of the colored circles (gray for H I Ly α , blue for Si II, and red for C IV). We overlay the contours from Schneider et al. (1989) to indicate the distribution of intergalactic H I which is potentially traced by some of the sightlines.

multiple galaxies and/or from the gaseous Leo Ring. At larger distances from the Leo Ring, we note that SE (≈ 400 kpc) and SJ (≈ 550 kpc) have unusually large EWs of Si III and C IV. The even more distant sightline SB (at ≈ 825 kpc), on the other hand, does not have metal absorption detected, and has only typical absorption in Ly α . In summary, however, it is clear that there is a lot of gas spread out throughout this entire Leo Ring/Group region. Although, this analysis invokes various assumptions and simplifications, it serves as an illustrative tool to highlight the impact of complex environments on the observables in our pencil beam probes.

The Leo Ring region presents an ideal location where we can consider the differences in the absorption properties for sightlines near isolated galaxies and those through galaxy groups. Nielsen et al. (2018b) found that sightlines through galaxy groups have stronger Mg II absorption than isolated galaxies, with a median EW of 0.65 Å in groups compared to 0.41 Å for isolated galaxies, within an impact parameter of 200 kpc from the nearest galaxy. A similar finding was reported by Dutta et al. (2021) who found ≈ 2 -3 times stronger Mg II absorption in higher overdensity group environments. Group sightlines also have more absorption components at larger velocities, though they do not have a large enough kinematic spread to be consistent with a superposition of two or more galaxies contributing to the sightline. This leads Nielsen et al. (2018b) to conclude that the gas from the individual galaxies is spread out in an intragroup medium through outflows and tidal stripping. In this nearby Leo Ring environment we see a distribution of intragroup gas consistent with such a scenario. The collision between NGC3384 and M96 is

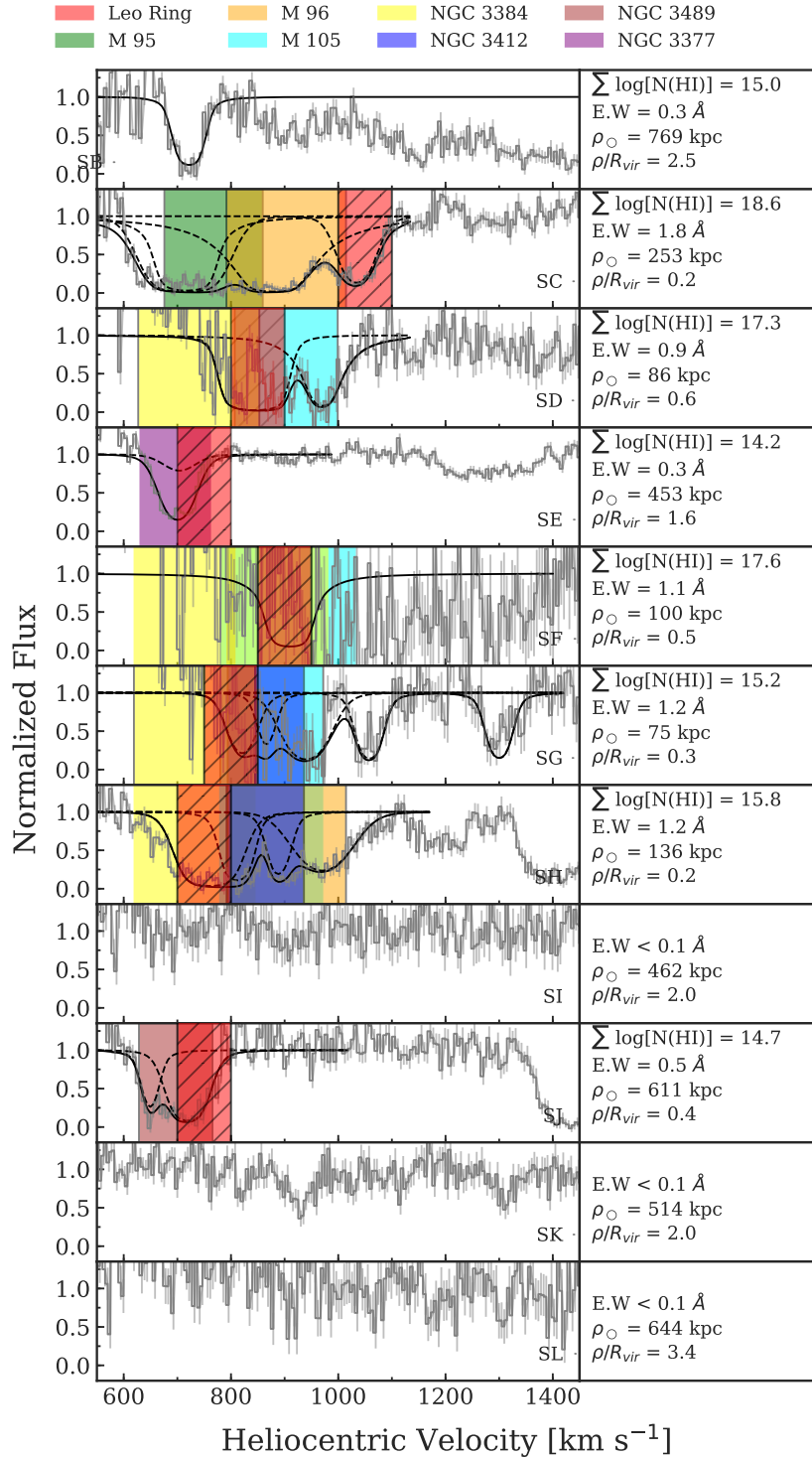


Figure 16. A plot showing the H I Ly α profiles for the 11 sightlines in this study, with the model profiles superimposed. The expected velocities for extensions of Leo Ring and other large nearby galaxies are shown as shaded regions, in colors according to the key. The Leo Ring association is shaded in red and hatched. The width of the shaded region accounts for expected velocities within the escape velocity of a galaxy’s halo.

To the right of the spectra, we list the sum of the N(H I) values from our model, the total EW measured from the solid black model profile (except for SF, where we give the EW measured for the entire absorption trough), the impact parameter to the center of the Leo Ring, and the ratio of that impact parameter to the virial radius of the nearest galaxy.

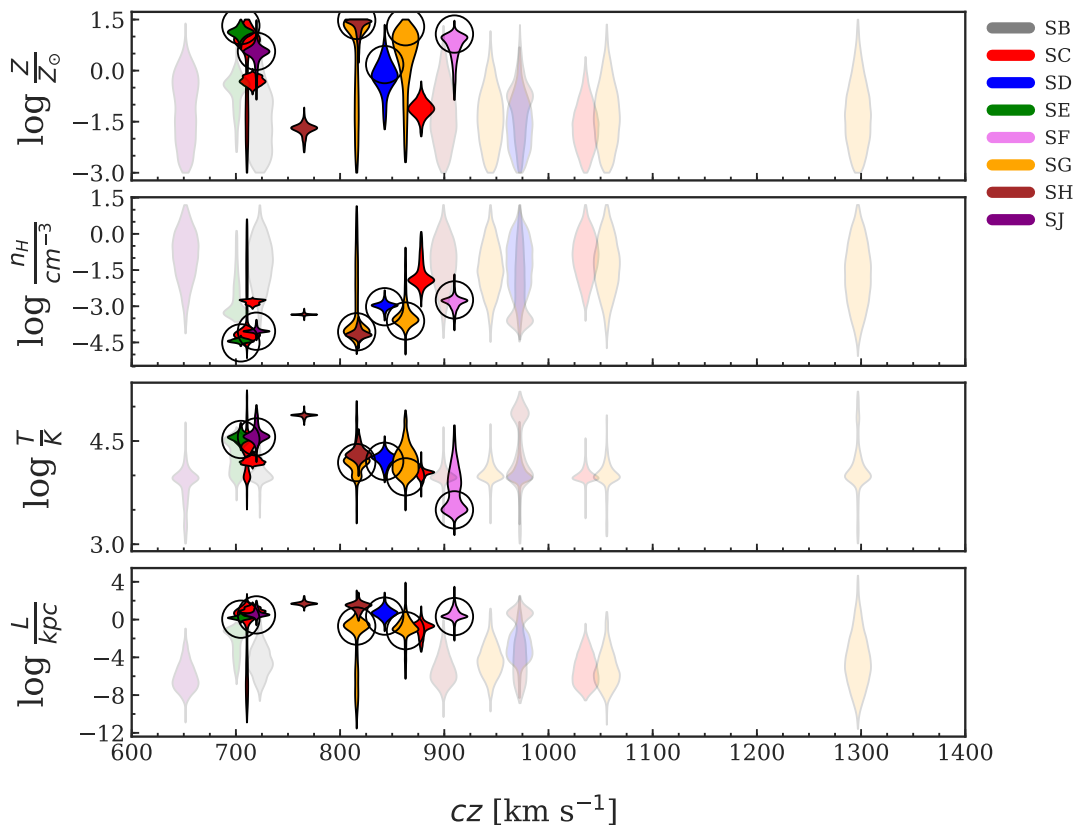


Figure 17. Constraints on metallicity, density, temperature, and line of sight thickness of the gas have been derived for each absorption component using `CLOUDY` modeling. The different sightlines are denoted by different colors as indicated in the key. Symbols circled in black are components with velocities consistent with those expected for the Leo H I ring in that direction. Very light shading is used to designate violin plots corresponding to components with H I-only absorption. These light shaded violin plots are presented as limits in Table 3.

thought to have occurred 1.2Gyr ago, based on simulations (Michel-Dansac et al. 2010), and we would expect that in another couple of billion years the gas will to some extent disperse. The cross section for metal-enriched, absorbing gas could remain substantial for a significant amount of time.

Absorption in C IV is commonly found to occur in a variety of environments, from isolated galaxies to galaxy groups, mainly detected within the virial radii of the galaxies (Burchett et al. 2016; Pradeep et al. 2019; Manuwal et al. 2021). In the Leo Ring region there is detected C IV in 4/5 of the sightlines for which there is C IV coverage. The one sightline, SB, which does not have detected C IV has its closest galaxy at $3.7R_{vir}$. The equivalent widths in Fig. 18 of C IV along our sightlines are at the high end of the distributions from other samples at the same ρ/R_{vir} . The high C IV equivalent widths are suggestive that more than just a single undisturbed galaxy is contributing along these sightlines.

The O VI EWs in the Leo Ring region, predicted by our models, are low compared to the other systems. This is consistent with the results of Pointon et al. (2017) that absorbers through galaxy groups have weaker O VI absorption than isolated galaxies. We note, however, that in our Leo Ring sightlines we would not be aware of collisionally ionized O VI gas, because the O VI is not covered by the observations and we are only predicting it based on the phases of gas that we can observe.

Outside of the region that is likely to show absorption due to the Leo Ring itself, we also see Ly α absorption towards SB. The H I

Ly α EW is 0.2 Å, and the N(H I) value from our model/fit is 14.7. Sightline SB has no known galaxies within $3.5R_{vir}$, however, absorption of this strength is not unusual due to larger scale structures like filaments (Wakker et al. 2015; Bouma et al. 2021; Wilde et al. 2021). It is also not unusual to have sightlines $1-3R_{vir}$ from the nearest galaxy without detected H I Ly α absorption, like sightlines SI, SK, and SL. In fact, using $dN/dz = 30$ for $\log N(\text{H I}) > 14$ (Kim et al. 2021), we estimate there is only an 8% chance of detecting such absorption along a random sightline between 600 and 1400 km s $^{-1}$. The small probability of seeing H I Ly α absorption along a random sightline highlights the fact that SI, SK, and SL are not unusual.

5.3 GALAXY CENTERED CONSIDERATIONS

In this discussion the focus has so far been on understanding the contributions from the Leo Ring, galaxies, and large scale structure to the absorption along the various sightlines. We have concluded that the Leo Ring gas itself is responsible for significant absorption along sightlines within $\approx 500\text{kpc}$ of its center, and that this high metallicity gas is the result of interactions between high metallicity galaxies which spreads it out over the region. Now, rather than considering the origin of the absorbing gas and its relationship to the galaxies, we also want to reverse this and consider what absorption the large galaxies in the field are contributing at the positions of the sightlines, and whether this is reasonable based on their properties.

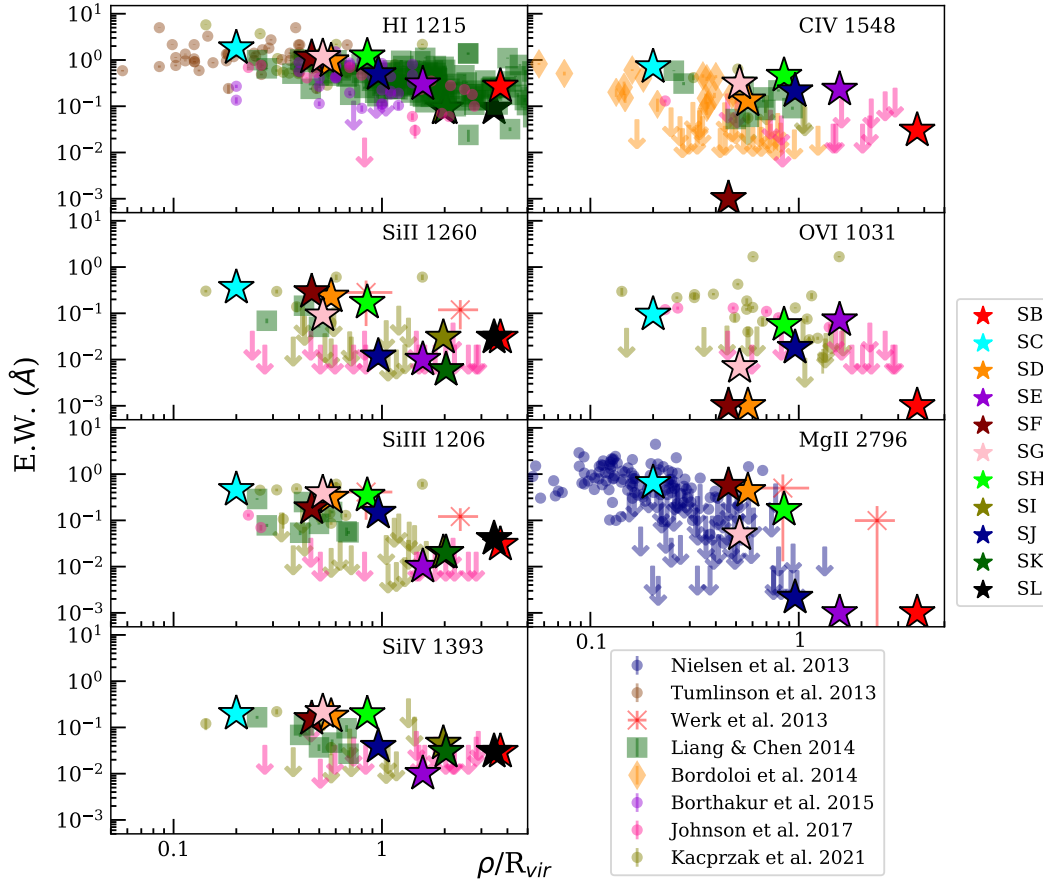


Figure 18. Rest frame EWs for key transitions are plotted against the impact parameter to the nearest galaxy, in units of its virial radius. The EWs are determined based on our best model fits to the observed data. For Mg II, O VI, and in some cases C IV (for SC, SD and SF), the measurements are based on predicted absorption profiles from our CLOUDY models, since the spectra did not cover these transitions. In these cases, an additional hidden phase could produce absorption in these transitions, which would not be shown here. These values are compared between our sightlines through the Leo Group, shown as different colored stars, and observations of various other low redshift samples of absorption line systems, noted by the colors/types of the smaller symbols.

Note that in cases like SC, SG, and SH, with several absorbing components along the same sightline, it is likely that both galaxies and the Leo Ring itself are contributing absorption at different velocities.

The SB(r)b spiral M95 is only $0.2R_{vir}$ away from SC. It would be very unusual not to see metal-line absorption at that impact parameter, and thus we associate the two components at $\approx 710 \text{ km s}^{-1}$ directly with this galaxy. They are each $\sim 10 \text{ kpc}$ in dimension and separated by few km s^{-1} in velocity, consistent with arising in the same halo. The next closest sightline to M95 is SF, at an impact parameter of $1.2R_{vir}$ for which we do not necessarily expect metal line absorption, but would probably detect H I Ly α . SF is, however, is clearly in a region disturbed by the interaction so there may not be an identifiable contribution from M95 along the SF sightline.

The SAB(rs)ab galaxy, M96, is likely to be responsible for the 879 km s^{-1} component in SC, given its impact parameter of $0.7R_{vir}$. The EWs of the metal lines for just this component are H I = 0.97 \AA , Si II = 0.06 \AA , Si III = 0.03 \AA , Si IV < 0.01 \AA , with C IV and O VI not detected, and this would be consistent with expectations at that impact parameter. The metallicity of $\log Z/Z_{\odot} \approx -1$, however, is low, and possibly suggestive of a contribution from infalling material. There is an even closer sightline to M96, sightline SF at $0.5R_{vir}$. It would not be unusual that we don't see detected metal

line absorption at the expected velocity of $\approx 800 \text{ km s}^{-1}$, however, we see from Fig. 18 that H I Ly α is almost always detected at this small impact parameter. The absence of Ly α absorption from M96 along the SF sightline could simply be a reflection of the noisy spectrum, or it is possible that since M96 was involved in the interaction that produced the ring, that its H I distribution is disturbed.

M105 is an early type E1 galaxy at $\approx 0.5R_{vir}$ from both SD and SF. For both sightlines we would expect absorption between 900 and 950 km s^{-1} based on extensions of the H I emission map of the galaxy (Sil'chenko et al. 2003). From Johnson et al. (2017), we would expect to detect H I Ly α with an EW between 0.3 and 2 \AA , but we may or may not see metal lines detected. Along sightline SD we find H I Ly α absorption at this velocity and the EW in the aligned component is at the lower end of that range typical for early type galaxies. It is likely that the metals along sightline SD, at lower velocity, are related to the Leo Ring. For SF, because of its location so close to the ring, it is difficult to separate contributions from individual galaxies and those from the debris.

The SB type galaxy, NGC3412 is probed by sightlines SG and SH within a virial radius (at $0.9R_{vir}$) for both. It could contribute to the absorption seen in metals and the H I component at $\approx 943 \text{ km s}^{-1}$, however, NGC3384 and M105 can also contribute to absorption at

these velocities, as could the Leo Ring. Similarly, in SH, NGC3412 could contribute at 818 km s^{-1} and 900 km s^{-1} , but other galaxies and the Leo Ring are equally or more likely to contribute.

NGC 3384, an SB(s) galaxy, is close to sightlines SD ($0.6R_{vir}$), SF ($0.5R_{vir}$), SG ($0.5R_{vir}$), and SH ($0.8R_{vir}$), for which absorption would be expected at $\approx 700\text{--}800 \text{ km s}^{-1}$. For all four of these sightlines we would expect H I Ly α absorption with EW between 0.1 and 2 Å based on Figure 18. We may or may not typically see metal lines at these impact parameters. In Figure 16 we see that we do not detect H I Ly α absorption at the predicted velocity towards any of the four sightlines. This implies that NGC 3384 is unusual, and we propose that this is because it specifically was the victim of a head on collision with M96, which left it with little gas of its own (Michel-Dansac et al. 2010).

There are many dwarf galaxies in the Leo Ring region, cataloged by Müller et al. (2018), however only a few are at small impact parameters from our sightlines. It is possible to detect fainter dwarfs than usual for absorption lines studies because of the proximity of this Leo Group region. Nonetheless, we do not see a contribution from dwarfs to the absorption profiles along the sightlines we have studied.

6 CONCLUSION: LESSONS FOR HIGHER REDSHIFT

We have determined that the relatively large, Leo Ring region including the sightlines SC-SH and SJ, has a covering factor of nearly 1 of supersolar metallicity, low density gas. Though it fills the region, the distribution of the gas is clumpy and the kinematics are complex. Some of the absorption components are associated with specific galaxies in the Leo Group, while others are generally associated with gas in the region which has been liberated from individual galaxies. The absorption strengths in both H I Ly α and metal lines are large, suggesting the need for contributions from the gas from more than one galaxy. Much of the absorption that we see within the region is thus likely to be due to tidal debris and the intragroup medium.

The specifics of the distribution of debris in the region is surely related to the nature of the galaxy encounter, which is believed to be a head on collision between NGC 3384 and M96 (Michel-Dansac et al. 2010). The geometry of the encounter is important for creating a ring without other obvious signs of interaction such as tidal tails and shells. Though there is some star formation seen in the ring, the high metallicities, inferred through both our absorption studies and by Corbelli et al. (2021) in emission, must be due to pre-enriched gas with its origin in the galaxies in the region. The Leo Ring is a structure that is visible in H I emission because it is in the local Universe, but there is presumably hidden debris in other more distant galaxy groups, which would be detected through absorption studies using background quasars. Indeed Nielsen et al. (2018b) concluded that differences between Mg II absorption in isolated galaxies and in groups could be explained by intragroup gas. The importance of such enriched gas with tidal origins in groups will depend on its covering factor and its longevity. Certain types of interactions will distribute larger amounts of gas, and tidal features may last 1-2 billion years, but afterwards the dispersed gas will continue to have absorption signatures.

Most of the absorption that we are observing from the Leo Group intragroup medium arises in a single phase (with similar density and temperature over a large region) though it does have clumpiness and substructures that we may not be probing with our

random sightlines. It is important to note that gas with the same density will yield different absorption signatures at different redshifts. The gas we are probing in the Leo Ring region now produces C IV absorption due to photoionization because of its density as compared to the density of ionizing photons in the extragalactic background. At a higher redshift, it is likely that significant photoionized O VI absorption would be observed from gas with these same conditions. We also cannot address whether an additional warm/hot phase is present without coverage of higher ionization transitions (e.g. O VII and Ne VIII).

Observations of lines of sight through other known interacting galaxies in the local universe, and through a variety of galaxy groups will be important diagnostics of the conditions of such regions. For example, the M81 triplet (Chynoweth et al. 2008; de Blok et al. 2018), has a very extended distribution of H I debris detected through 21-cm emission. Looking at conditions component by component is very important in such analysis. For example, in this work, if all of the H I was incorrectly associated with the single components that show metals in most sightlines, the inferred metallicity would be much lower, and one might mistake the material to be of primordial origin. As we look back to earlier epochs in the Universe, where there is no hope of detecting tidal debris through any other method but quasar absorption lines, the ability to recognize the absorption signatures of tidal material will be very important.

ACKNOWLEDGEMENTS

We thank the anonymous reviewer for their constructive feedback which helped improve the quality of manuscript. Computations for this research were performed on the Pennsylvania State University's Institute for Computational and Data Sciences' Roar super-computer. The authors also acknowledge the Texas Advanced Computing Center (TACC) at The University of Texas at Austin for providing HPC resources that have contributed to the research results reported within this paper. G.G.K. and N.M.N. acknowledge the support of the Australian Research Council through *Discovery Project* grant DP170103470. Parts of this research were supported by the Australian Research Council Centre of Excellence for All Sky Astrophysics in 3 Dimensions (ASTRO 3D), through project number CE170100013. A.N acknowledges the support for this work through grant number EMR/2017/002531 from the Department of Science and Technology, Government of India. This research made use of Astropy, a community-developed core Python package for Astronomy (Astropy Collaboration et al. 2013), NumPy (Harris et al. 2020), MATPLOTLIB (Hunter 2007), and SciPy (Virtanen et al. 2020). This research has made use of the HSLA database, developed and maintained at STScI, Baltimore, USA. This research has made use of the NASA/IPAC Extragalactic Database (NED), which is operated by the Jet Propulsion Laboratory, California Institute of Technology, under contract with NASA. We acknowledge the work of people involved in the design, construction and deployment of the COS on-board the Hubble Space Telescope, and thank all those who obtained data for the sight-lines studied in this paper. We thank KITP for hosting the Fundamentals of Gaseous Halos workshop (supported by the NSF under Grant No. NSF PHY-1748958) during which some of the ideas presented in this work were formulated.

DATA AVAILABILITY

The data underlying this article will be shared on reasonable request to the corresponding author.

References

- Acharya A., Khaire V., 2021, *MNRAS*,
- Aguerri J. A. L., Debattista V. P., Corsini E. M., 2003, *MNRAS*, **338**, 465
- Anglés-Alcázar D., Faucher-Giguère C.-A., Kereš D., Hopkins P. F., Quataert E., Murray N., 2017, *MNRAS*, **470**, 4698
- Astropy Collaboration et al., 2013, *A&A*, **558**, A33
- Barber C. B., Dobkin D. P., Huhdanpaa H., 1996, *ACM Trans. Math. Softw.*, **22**, 469–483
- Bekki K., Koribalski B. S., Ryder S. D., Couch W. J., 2005, *MNRAS*, **357**, L21
- Bordoloi R., et al., 2011, *ApJ*, **743**, 10
- Bordoloi R., et al., 2014, *ApJ*, **796**, 136
- Borthakur S., et al., 2015, *ApJ*, **813**, 46
- Bouma S. J. D., Richter P., Wendt M., 2021, *A&A*, **647**, A166
- Bourrier V., et al., 2018, VizieR Online Data Catalog, [pp J/A+A/615/A117](https://vizier.cesr.cnrs.fr/vizieR/J/A+A/615/A117)
- Bowen D. V., Chelouche D., Jenkins E. B., Tripp T. M., Pettini M., York D. G., Frye B. L., 2016, *ApJ*, **826**, 50
- Buchner J., 2021, arXiv e-prints, [p. arXiv:2101.09675](https://arxiv.org/abs/2101.09675)
- Buchner J., et al., 2014, *A&A*, **564**, A125
- Burchett J. N., et al., 2016, *ApJ*, **832**, 124
- Chen H.-W., Gauthier J.-R., Sharon K., Johnson S. D., Nair P., Liang C. J., 2014, *MNRAS*, **438**, 1435
- Chen H.-W., Boettcher E., Johnson S. D., Zahedy F. S., Rudie G. C., Cooksey K. L., Rauch M., Mulchaey J. S., 2019, *ApJ*, **878**, L33
- Chynoweth K. M., Langston G. I., Yun M. S., Lockman F. J., Rubin K. H. R., Scoles S. A., 2008, *AJ*, **135**, 1983
- Corbelli E., Mannucci F., Thilker D., Cresci G., Venturi G., 2021, arXiv e-prints, [p. arXiv:2104.07133](https://arxiv.org/abs/2104.07133)
- Dutta R., et al., 2021, *MNRAS*, **508**, 4573
- Ferland G. J., et al., 2017, *Rev. Mex. Astron. Astrofis.*, **53**, 385
- French D. M., Wakker B. P., 2017, *ApJ*, **837**, 138
- Grevesse N., Asplund M., Sauval A. J., Scott P., 2010, *Ap&SS*, **328**, 179
- Guber C. R., Richter P., Wendt M., 2018, *A&A*, **609**, A85
- Haislmaier K. J., Tripp T. M., Katz N., Prochaska J. X., Burchett J. N., O’Meara J. M., Werk J. K., 2021, *MNRAS*, **502**, 4993
- Harris C. R., et al., 2020, *Nature*, **585**, 357
- Hunter J. D., 2007, *Computing in Science & Engineering*, **9**, 90
- Inoue A. K., Shimizu I., Iwata I., Tanaka M., 2014, *MNRAS*, **442**, 1805
- Jester S., et al., 2005, *AJ*, **130**, 873
- Johnson S. D., Chen H.-W., Mulchaey J. S., Schaye J., Straka L. A., 2017, *ApJ*, **850**, L10
- Kacprzak G. G., 2017, in Fox A., Davé R., eds, *Astrophysics and Space Science Library* Vol. 430, *Gas Accretion onto Galaxies*. p. 145 ([arXiv:1612.00451](https://arxiv.org/abs/1612.00451)), [doi:10.1007/978-3-319-52512-9_7](https://doi.org/10.1007/978-3-319-52512-9_7)
- Kacprzak G. G., Murphy M. T., Churchill C. W., 2010, *MNRAS*, **406**, 445
- Kacprzak G. G., Pointon S. K., Nielsen N. M., Churchill C. W., Muzahid S., Charlton J. C., 2019, *ApJ*, **886**, 91
- Kacprzak G. G., Nielsen N. M., Nateghi H., Churchill C. W., Pointon S. K., Nanayakkara T., Muzahid S., Charlton J. C., 2021, *MNRAS*, **500**, 2289
- Keeney B. A., Stocke J. T., Rosenberg J. L., Danforth C. W., Ryan-Weber E. V., Shull J. M., Savage B. D., Green J. C., 2013, *ApJ*, **765**, 27
- Khaire V., Srianand R., 2015, *MNRAS*, **451**, L30
- Khaire V., et al., 2019, *MNRAS*, **486**, 769
- Kim T. S., et al., 2021, *MNRAS*, **501**, 5811
- Krogager J.-K., 2018, arXiv e-prints, [p. arXiv:1803.01187](https://arxiv.org/abs/1803.01187)
- Lehner N., 2017, *Gas Accretion via Lyman Limit Systems*. p. 117, [doi:10.1007/978-3-319-52512-9_6](https://doi.org/10.1007/978-3-319-52512-9_6)
- Lehner N., Howk J. C., Wakker B. P., 2015, *ApJ*, **804**, 79
- Lehner N., et al., 2020, *ApJ*, **900**, 9
- Leroy A. K., et al., 2015, *ApJ*, **814**, 83
- Liang C. J., Chen H.-W., 2014, *MNRAS*, **445**, 2061
- Manuwal A., Narayanan A., Udhvani P., Srianand R., Savage B. D., Charlton J. C., Misawa T., 2021, *MNRAS*, **505**, 3635
- Mathes N. L., Churchill C. W., Kacprzak G. G., Nielsen N. M., Trujillo-Gomez S., Charlton J., Muzahid S., 2014, *ApJ*, **792**, 128
- Michel-Dansac L., et al., 2010, *ApJ*, **717**, L143
- Müller O., Jerjen H., Binggeli B., 2018, *A&A*, **615**, A105
- Narayanan A., Charlton J. C., Masiero J. R., Lynch R., 2005, *ApJ*, **632**, 92
- Narayanan A., et al., 2021, *MNRAS*, **505**, 738
- Nielsen N. M., Churchill C. W., Kacprzak G. G., Murphy M. T., 2013, *ApJ*, **776**, 114
- Nielsen N. M., Kacprzak G. G., Pointon S. K., Churchill C. W., Murphy M. T., 2018a, *ApJ*, **869**, 153
- Nielsen N. M., Kacprzak G. G., Pointon S. K., Churchill C. W., Murphy M. T., 2018b, *ApJ*, **869**, 153
- Norris J. M., Muzahid S., Charlton J. C., Kacprzak G. G., Wakker B. P., Churchill C. W., 2021, *MNRAS*, **506**, 5640
- Penton S. V., Stocke J. T., Shull J. M., 2002, *ApJ*, **565**, 720
- Péroux C., Rahmani H., Arrigoni Battaia F., Augustin R., 2018, *MNRAS*, **479**, L50
- Peterson B. M., Wanders I., Bertram R., Hunley J. F., Pogge R. W., Wagner R. M., 1998, *ApJ*, **501**, 82
- Pilyugin L. S., Grebel E. K., Kniazev A. Y., 2014, *AJ*, **147**, 131
- Pointon S. K., Nielsen N. M., Kacprzak G. G., Muzahid S., Churchill C. W., Charlton J. C., 2017, *ApJ*, **844**, 23
- Pointon S. K., Kacprzak G. G., Nielsen N. M., Murphy M. T., Muzahid S., Churchill C. W., Charlton J. C., 2020, *AJ*, **159**, 216
- Pradeep J., Narayanan A., Muzahid S., Nagai D., Charlton J. C., Srianand R., 2019, *MNRAS*, **488**, 5327
- Rao S. M., Sardane G., Turnshek D. A., Thilker D., Walterbos R., Vanden Berk D., York D. G., 2013, *MNRAS*, **432**, 866
- Richter P., et al., 2018, *ApJ*, **868**, 112
- Rohatgi A., 2021, Webplotdigitizer: Version 4.5, <https://automeris.io/WebPlotDigitizer>
- Rosenberg J. L., Haislmaier K., Giroux M. L., Keeney B. A., Schneider S. E., 2014, *ApJ*, **790**, 64
- Sameer et al., 2021, *MNRAS*, **501**, 2112
- Schneider S., 1985, *ApJ*, **288**, L33
- Schneider S. E., et al., 1989, *AJ*, **97**, 666
- Sil’chenko O. K., Moiseev A. V., Afanasiev V. L., Chavushyan V. H., Valdes J. R., 2003, *The Astrophysical Journal*, **591**, 185
- Stocke J. T., Keeney B. A., Danforth C. W., Shull J. M., Froning C. S., Green J. C., Penton S. V., Savage B. D., 2013, *ApJ*, **763**, 148
- Tepper-García T., 2006, *MNRAS*, **369**, 2025
- Tremonti C. A., et al., 2004, *ApJ*, **613**, 898
- Tumlinson J., et al., 2011, *Science*, **334**, 948
- Tumlinson J., et al., 2013, *ApJ*, **777**, 59
- Tumlinson J., Peebles M. S., Werk J. K., 2017, *ARA&A*, **55**, 389
- Virtanen P., et al., 2020, *scipy/scipy: SciPy 1.5.3*, [doi:10.5281/zenodo.4100507](https://doi.org/10.5281/zenodo.4100507)
- Wakker B. P., Savage B. D., 2009, *ApJS*, **182**, 378
- Wakker B. P., Lockman F. J., Brown J. M., 2011, *ApJ*, **728**, 159
- Wakker B. P., Hernandez A. K., French D. M., Kim T.-S., Oppenheimer B. D., Savage B. D., 2015, *ApJ*, **814**, 40
- Walter F., Brinks E., de Blok W. J. G., Bigiel F., Kennicutt Robert C. J., Thornley M. D., Leroy A., 2008, *AJ*, **136**, 2563
- Wenger M., et al., 2000, *A&AS*, **143**, 9
- Werk J. K., Prochaska J. X., Thom C., Tumlinson J., Tripp T. M., O’Meara J. M., Peebles M. S., 2013, *ApJS*, **204**, 17
- Werk J. K., et al., 2014, *ApJ*, **792**, 8
- Wilde M. C., et al., 2021, *ApJ*, **912**, 9
- Winkel B., Kerp J., Flöer L., Kalberla P. M. W., Ben Bekhti N., Keller R., Lenz D., 2016, *A&A*, **585**, A41
- Wolfe S. A., Pisano D. J., Lockman F. J., McGaugh S. S., Shaya E. J., 2013, *Nature*, **497**, 224
- Xu X., Arav N., Miller T., Kriss G. A., Plesha R., 2020, *ApJS*, **247**, 42
- Zahedy F. S., Chen H.-W., Johnson S. D., Pierce R. M., Rauch M., Huang Y.-H., Weiner B. J., Gauthier J.-R., 2019, *MNRAS*, **484**, 2257
- Zahedy F. S., et al., 2021, *MNRAS*, **506**, 877

de Blok W. J. G., et al., 2018, [ApJ](#), 865, 26

This paper has been typeset from a $\text{\TeX}/\text{\LaTeX}$ file prepared by the author.

**APPENDIX A: COMPARISON OF $N(\text{H I}; 21 \text{ CM})$ WITH
 $N(\text{H I}; \text{Ly}\alpha)$**

In this section we present a comparison between measurement of $\log N(\text{H I})$ from EBHIS ([Winkel et al. 2016](#)) database and the $\log N(\text{H I})$ measured from a VP fit to the Galactic $\text{Ly}\alpha$.

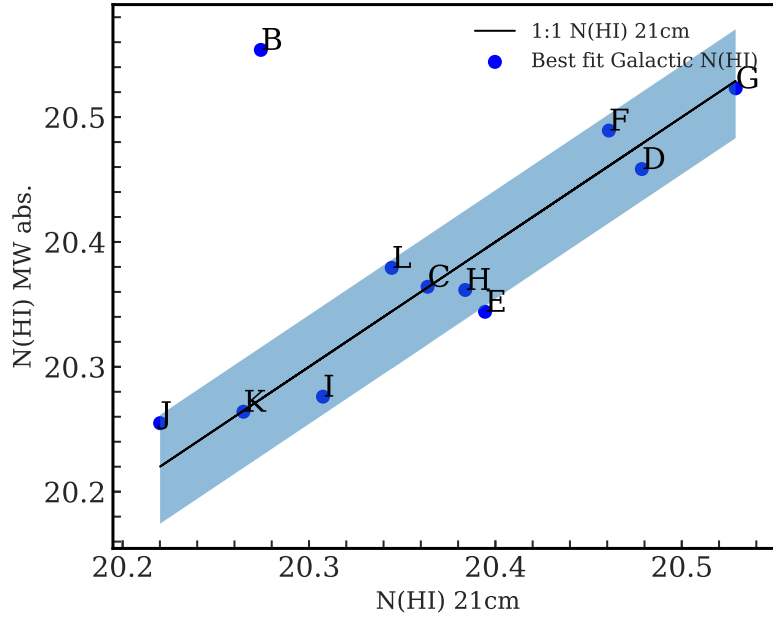


Figure A1. Comparison between $\log N(\text{H I}; \text{Ly } \alpha)$ and $\log N(\text{H I}; 21 \text{ cm})$ for the 11 sightlines in this study. The blue shaded region shows the 1σ uncertainty range for the ratio between $\log N(\text{H I}; \text{Ly } \alpha)$ and $\log N(\text{H I}; 21 \text{ cm})$ as determined in [Wakker et al. \(2011\)](#). All the values, except SB, are in good agreement. The Galactic $\text{Ly } \alpha$ in the case of SB is blended with very strong intrinsic absorption lines of $\text{Mg } \lambda 624$, $\text{Ca } \text{vII } \lambda 624$, $\text{O } \text{v}] \lambda 630$ which are associated with outflows from the background AGN ([Xu et al. 2020](#)), preventing an accurate modeling of the absorption. However, the uncertainty in the $\log N(\text{H I})$ of Galactic $\text{Ly } \alpha$ does not significantly affect the $\text{Ly } \alpha$ profile of the absorber of interest.

APPENDIX B: PLOTS FOR SB**B1 Airglow template fit towards SB**

In this section we present the airglow template fit to the geocoronal Ly α emission towards SB. The templates were obtained from the publically available community generated airglow templates⁵ (Bourrier et al. 2018) to fit the emission profile.

B2 Best VP fit to the Galactic Ly α towards SB

In this section we show the VP fit to the Galactic Ly α . We determine the unresolved component structure of Galactic Ly α using the component structure determined from a VP fit to the Galactic Si II lines. The best VP fit to Galactic Ly α is divided with the normalized spectrum towards a sightline to obtain the H I profile of interest.

B3 Posterior distributions for the absorber properties towards SB

In this section we present the posteriors summarizing the parameter distributions obtained from our Bayesian analysis. The prior distribution is defined in section 3 and the likelihood function is defined in S21.

⁵ <https://www.stsci.edu/hst/instrumentation/cos/calibration/airglow>

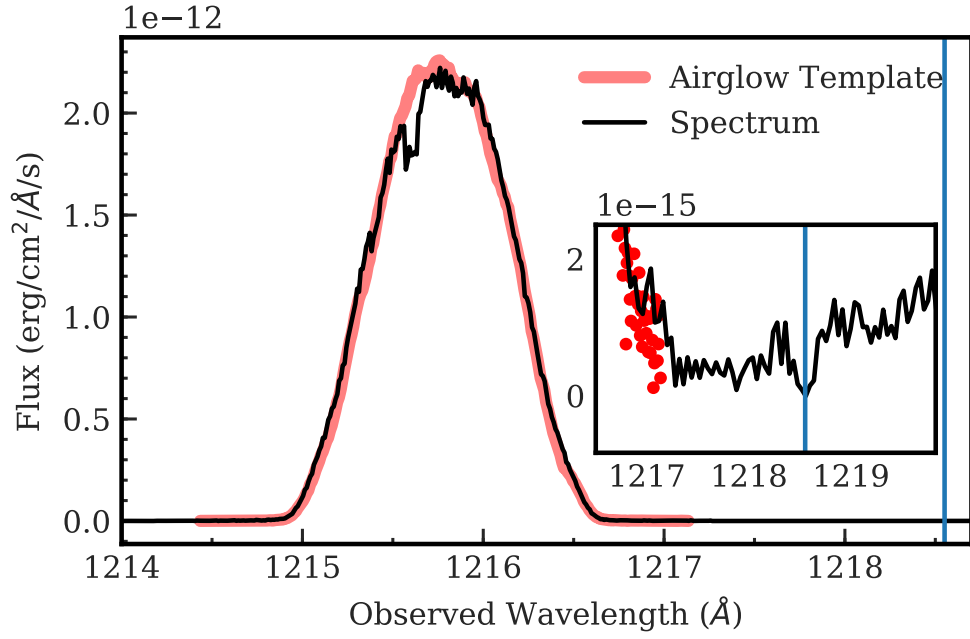


Figure B1. The airglow template fit to the spectrum. Inset shows the zoom of the region containing the absorption of interest; the vertical blue line is placed at the absorption centroid

. There is no contribution of the H I Ly α geocoronal emission to the H I Ly α absorption of interest.

Voigt profile fit to the Galactic Ly α absorption towards SB

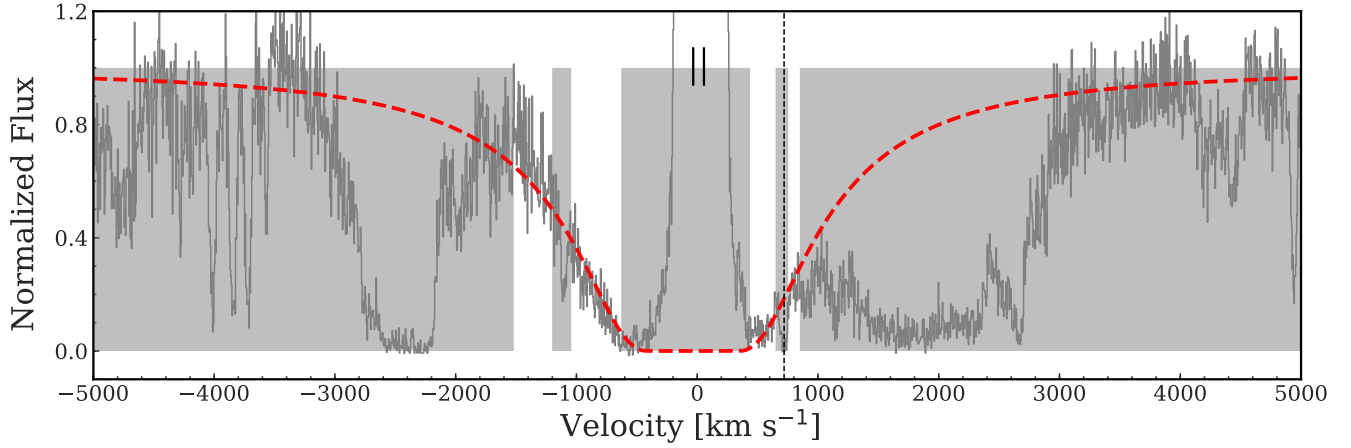


Figure B2. The VP fit to the MW Ly α absorption towards SB shown as a red curve. The two small thick vertical lines denote the absorption centroids determined from a VPfit to the Galactic Si II line. The absorption of interest is at $\approx 711 \text{ km s}^{-1}$, and identified with a vertical dashed line. The absorption between $\approx 1700 \text{ km s}^{-1} - 1800 \text{ km s}^{-1}$ is intrinsic O V] $\lambda 630$ absorption associated with an outflow from the background quasar at $z = 0.978$.

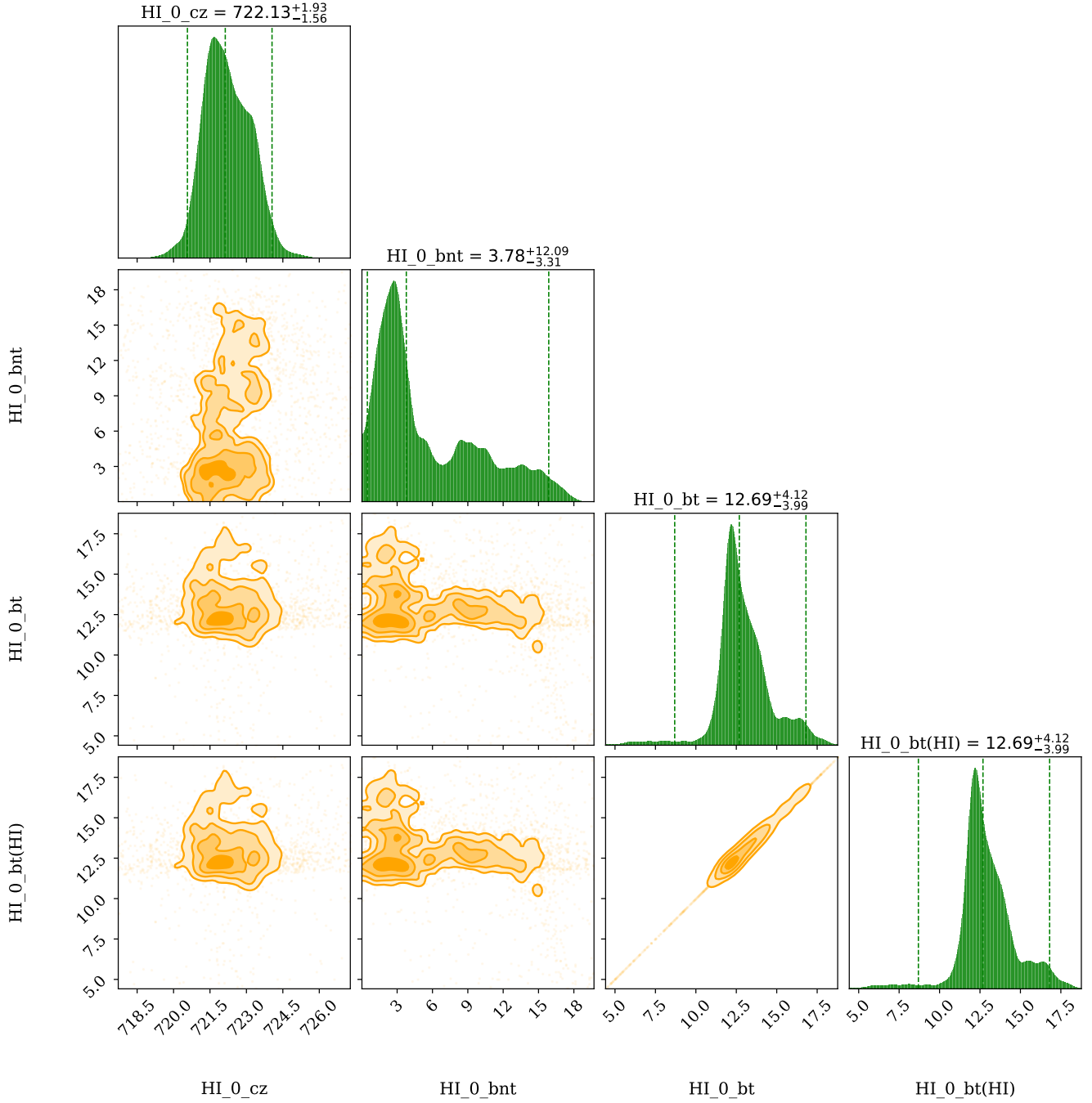


Figure B3. The corner plot showing the marginalized posterior distributions for the absorption centroid (z), non-thermal Doppler broadening (b_{nt}), thermal Doppler broadening (b_t), and total Doppler broadening (b), of the phase traced by the H I cloud of the $z = 0.0024$ absorber towards SB. The over-plotted vertical lines in the posterior distribution span the 95% credible interval. The contours indicate 0.5σ , 1σ , 1.5σ , and 2σ levels. The model results are summarised in Table 3, and the synthetic profiles based on these models are shown in Figure 4.

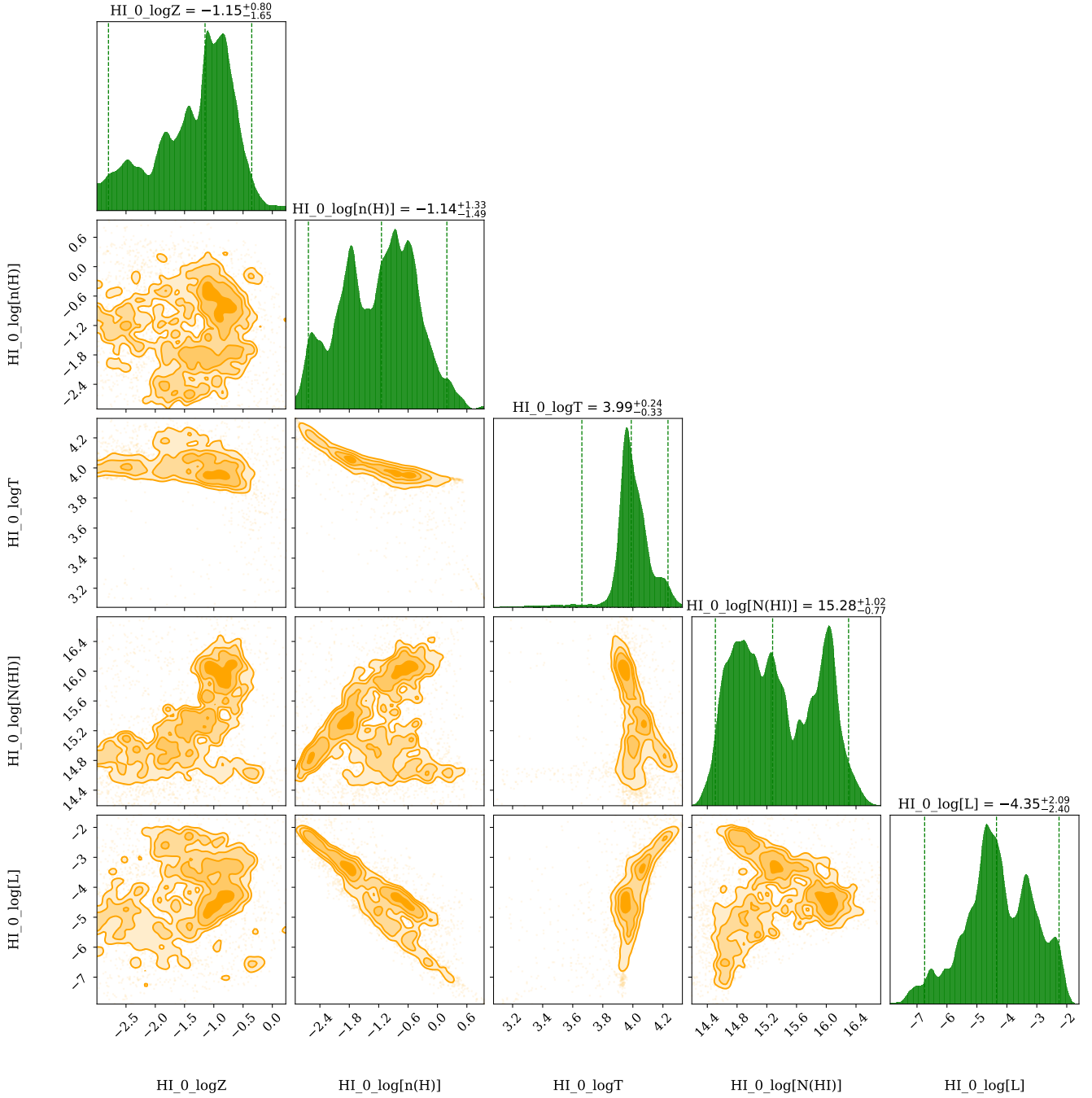


Figure B4. The corner plot showing the marginalized posterior distributions for the metallicity ($\log Z$), hydrogen number density ($\log n_{\text{H}}$), temperature ($\log T$), neutral hydrogen column density ($\log N(\text{H I})$), and the line of sight thickness ($\log L$), of the phase traced by the H I cloud of the $z = 0.0024$ absorber towards SB. The over-plotted vertical lines in the posterior distribution span the 95% credible interval. The contours indicate 0.5 σ , 1 σ , 1.5 σ , and 2 σ levels. The model results are summarised in Table 3, and the synthetic profiles based on these models are shown in Figure 4.

APPENDIX C: PLOTS FOR SC

- C1** Airglow template fit towards SC
- C2** Best VP fit to the Galactic Ly α towards SC
- C3** PC model for the high-ionization phase towards SC
- C4** MC exploration of the zero-point uncertainty for SC
- C5** Posterior distributions for the absorber properties towards SC

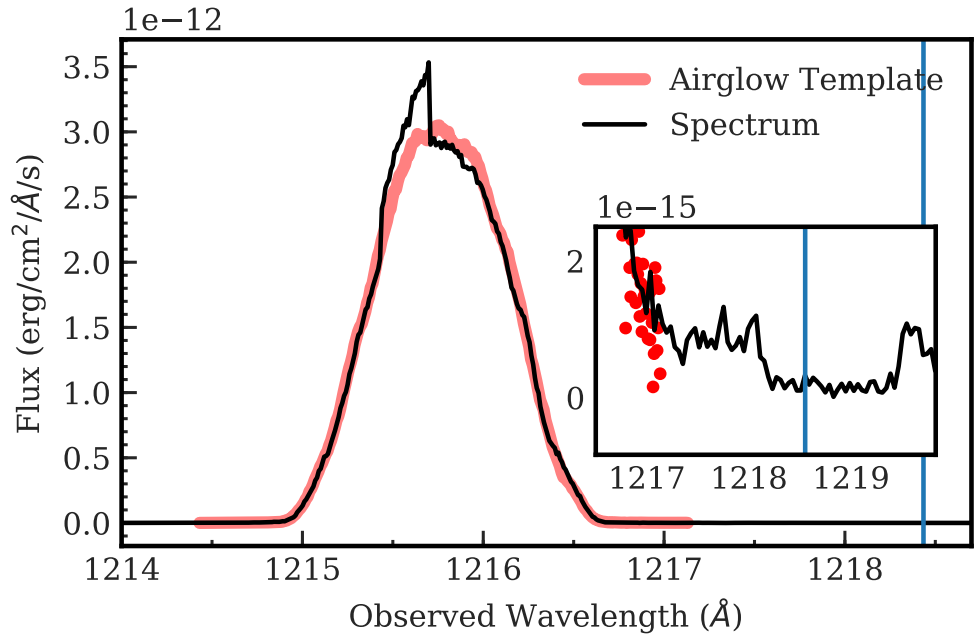


Figure C1. Same as in Figure B1, but for SC.

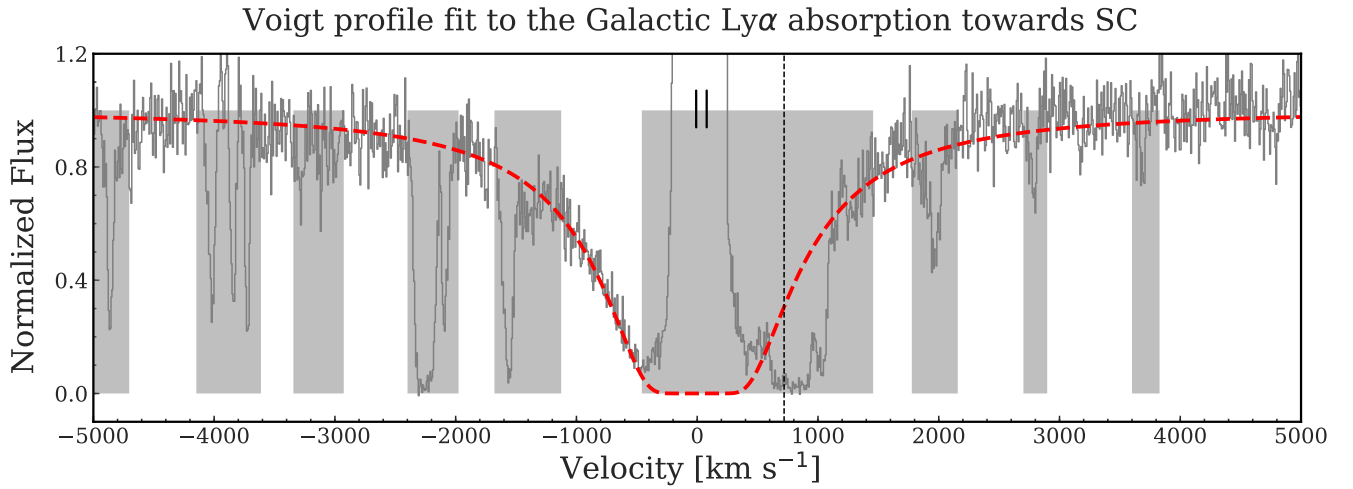


Figure C2. Same as in Figure B2, but for SC. Towards SC, we fit 3 components to the absorption profile of Galactic H I Ly α , as we identify 3 components in the Galactic Si II absorption profile.

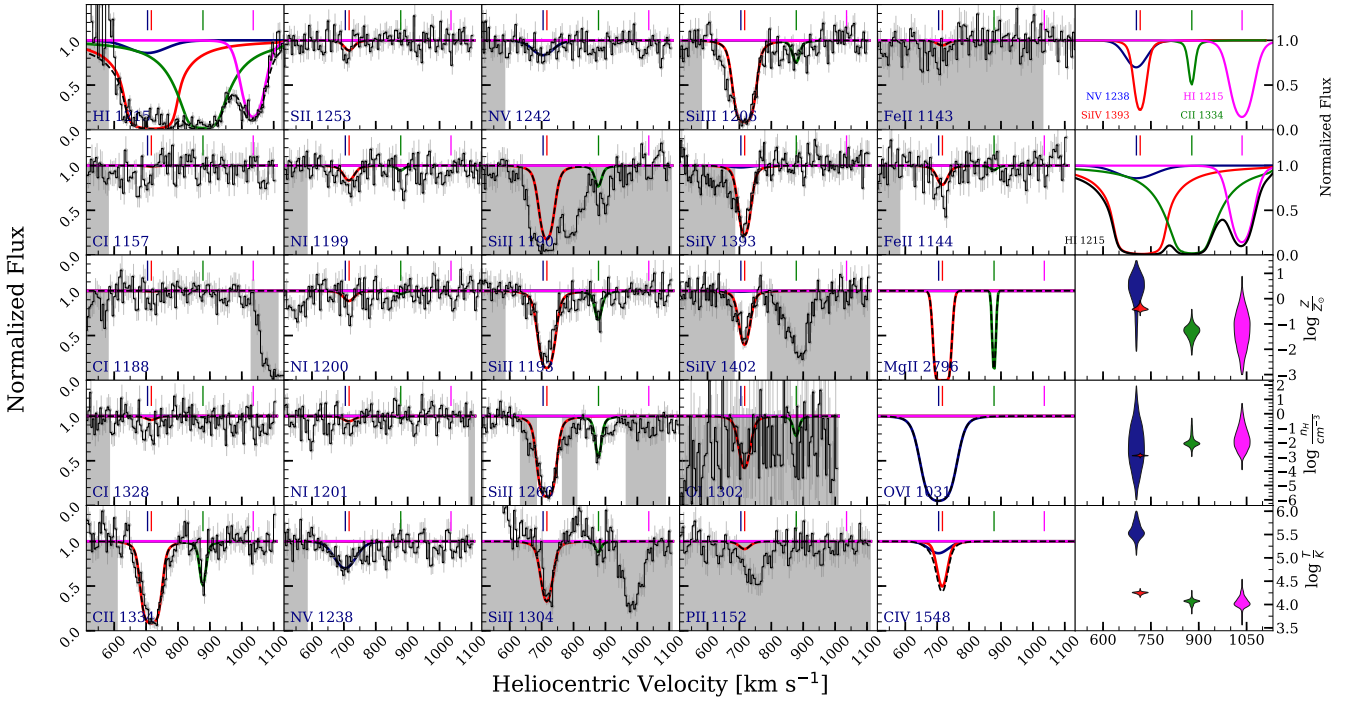


Figure C3. A PC model for the absorption towards SC. Only N v absorption (shown as a blue curve) is modeled as a collisionally ionized phase. The other phases are still modeled as photoionized only.

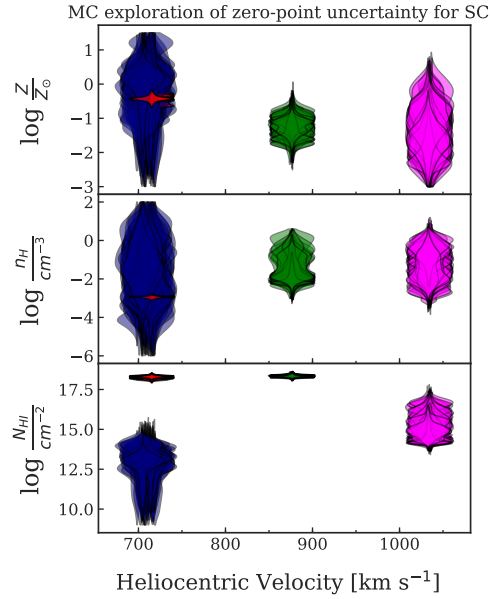


Figure C4. Violin plots showing the parameter distributions for 100 different realizations of the H I Ly α profile modified between 710–720 km s⁻¹ to account for the zero-point uncertainty. The blue violins show the parameters of N v, modeled as a collisionally ionized phase. The red violins correspond to the Si iv phase, the green violins correspond to the C II traced phase, and the magenta violins correspond to the H I only phase; all of which are PIE models.

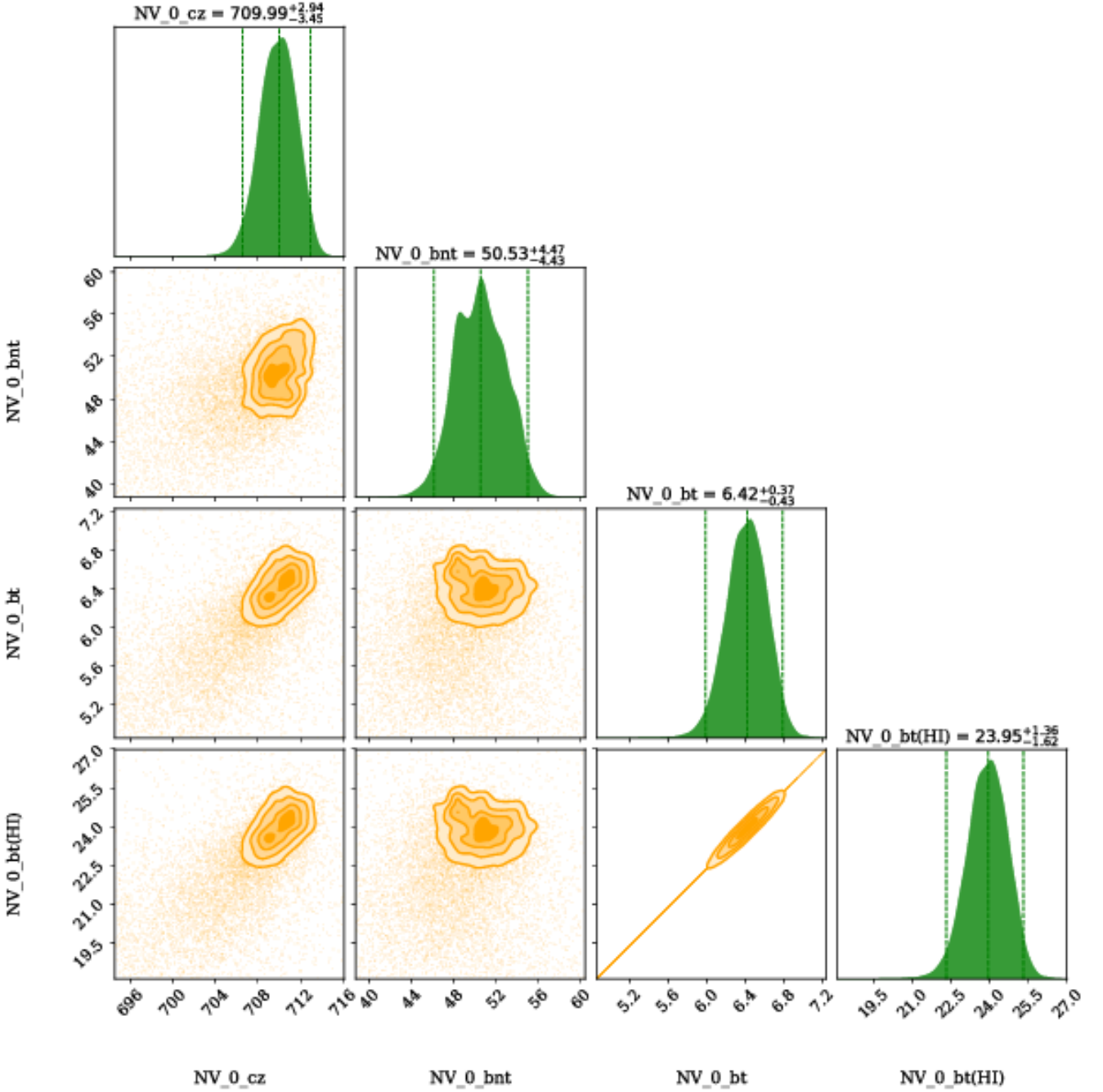


Figure C5. The corner plot showing the marginalized posterior distributions for the absorption centroid (z), non-thermal Doppler broadening (b_{nt}), thermal Doppler broadening (b_t), total Doppler broadening (b), of the phase traced by the broad N v cloud of the $z = 0.00238$ absorber towards SC. The over-plotted vertical lines in the posterior distribution span the 95% credible interval. The contours indicate 0.5 σ , 1 σ , 1.5 σ , and 2 σ levels. The model results are summarised in Table 3, and the synthetic profiles based on these models are shown in Figure 5.

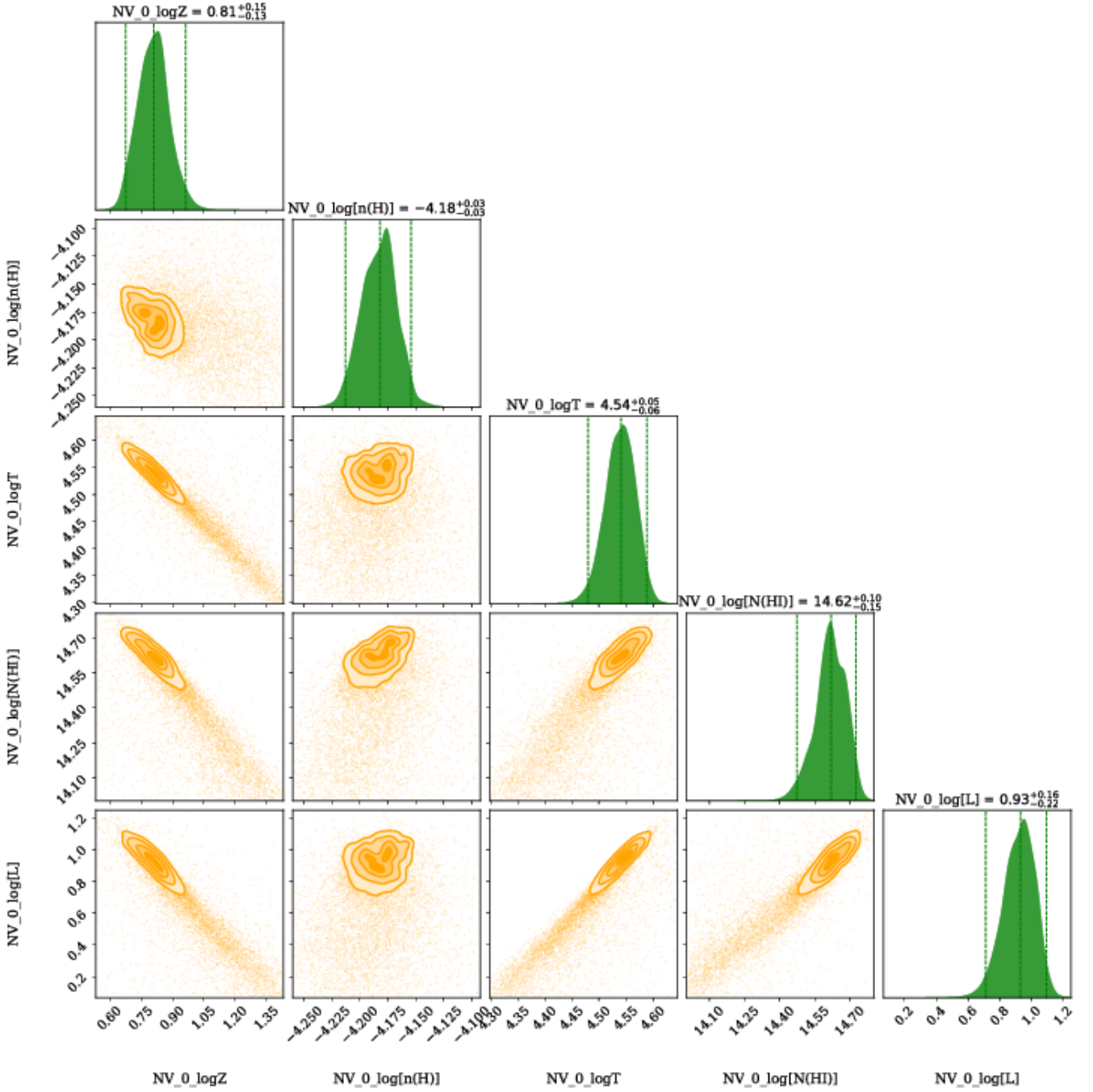


Figure C6. The corner plot showing the marginalized posterior distributions for the metallicity ($\log Z$), hydrogen number density ($\log n_H$), and other physical properties of the broad higher ionization phase gas traced by the N v cloud of the $z = 0.00238$ absorber towards SC. The over-plotted vertical lines in the posterior distribution span the 95% credible interval. The contours indicate 0.5σ , 1σ , 1.5σ , and 2σ levels. The model results are summarised in Table 3, and the synthetic profiles based on these models are shown in Figure 5.

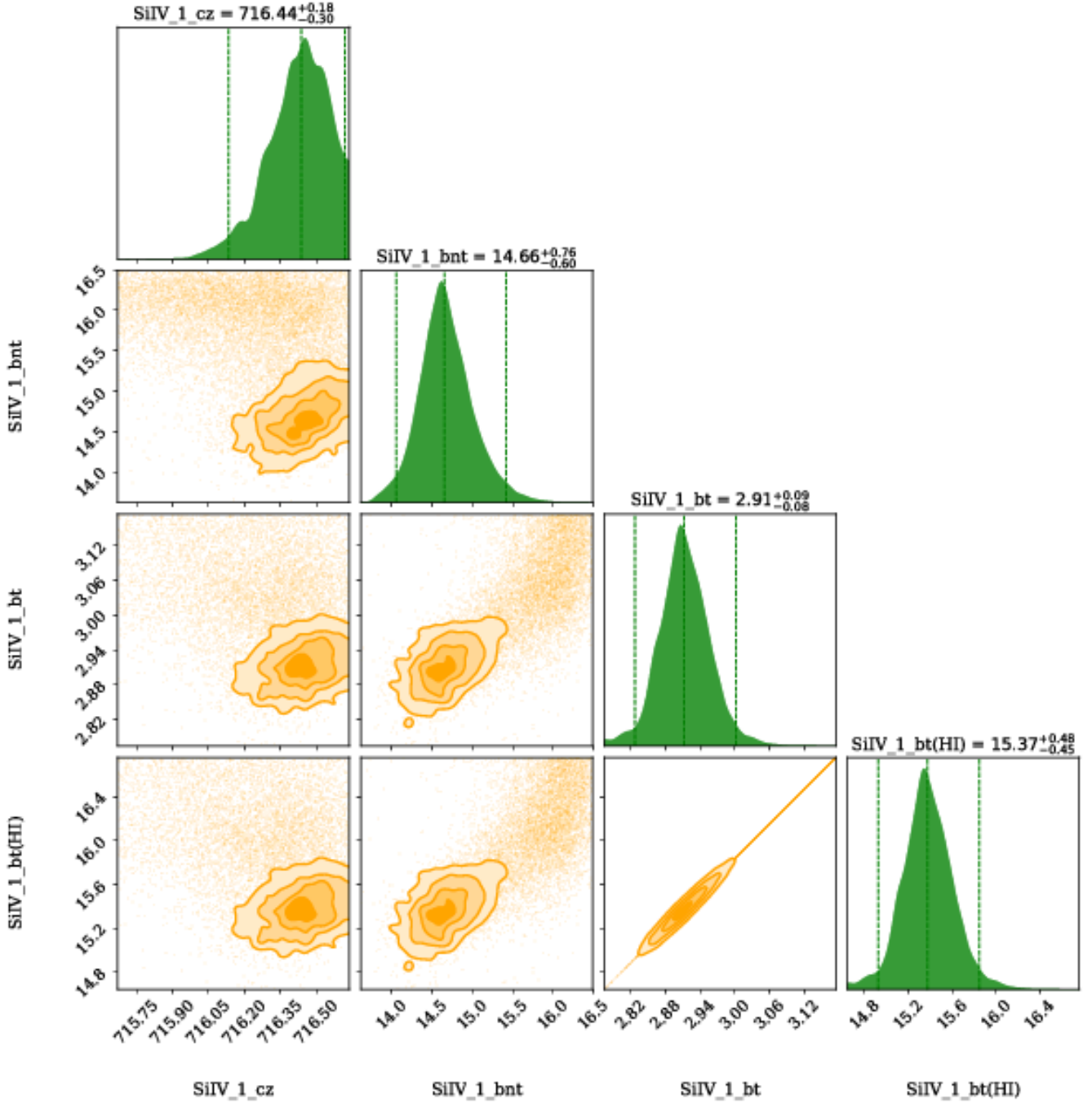


Figure C7. The corner plot showing the marginalized posterior distributions for the absorption centroid (z), non-thermal Doppler broadening (b_{nt}), thermal Doppler broadening (b_t), total Doppler broadening (b), of the lower ionization phase traced by the Si IV cloud of the $z = 0.00238$ absorber towards SC. The over-plotted vertical lines in the posterior distribution span the 95% credible interval. The contours indicate 0.5 σ , 1 σ , 1.5 σ , and 2 σ levels. The model results are summarised in Table 3, and the synthetic profiles based on these models are shown in Figure 5.

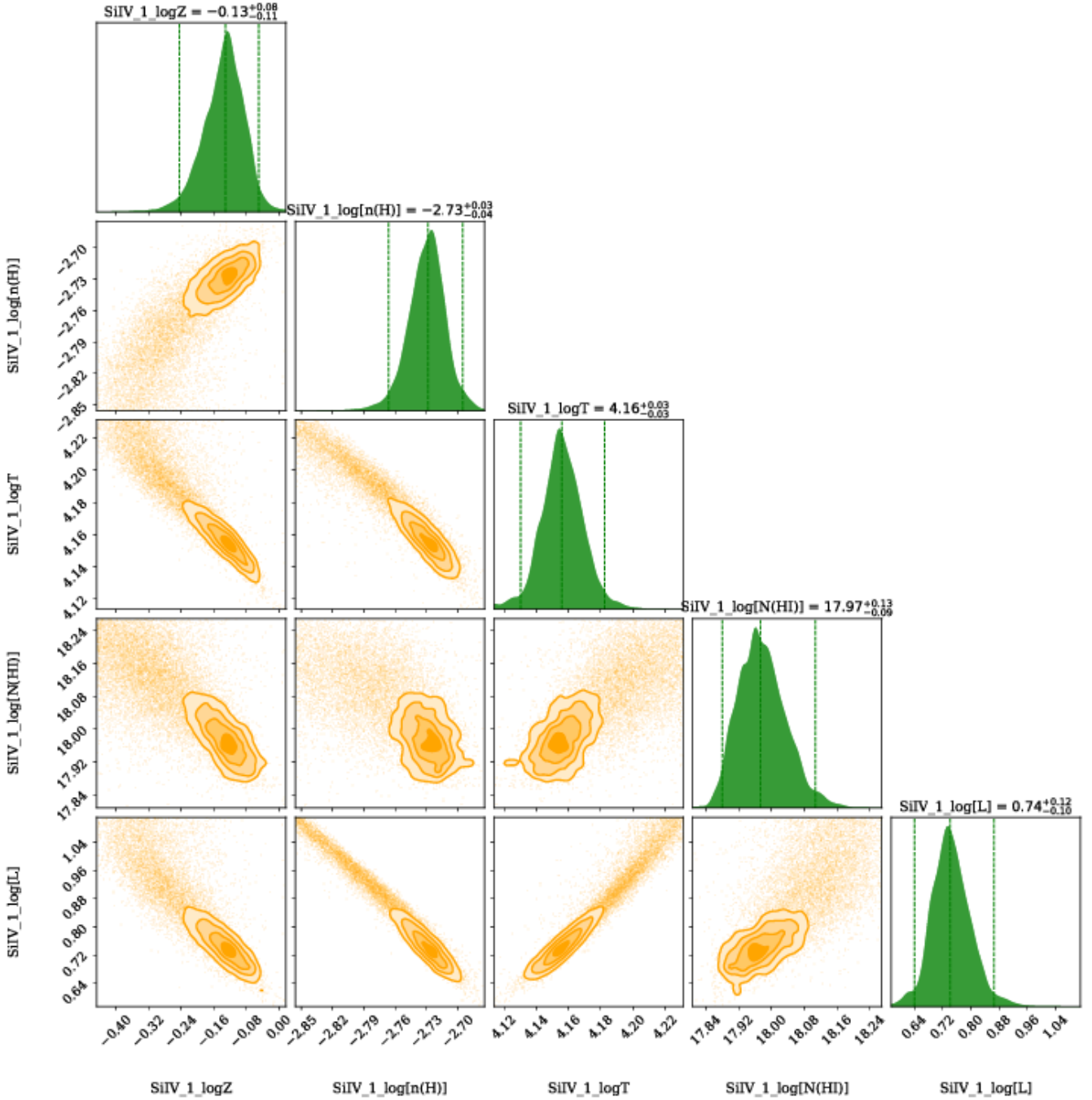


Figure C8. The corner plot showing the marginalized posterior distributions for the metallicity ($\log Z$), hydrogen number density ($\log n_H$), and other physical properties of the low ionization phase traced by the Si IV cloud of the $z = 0.00238$ absorber towards SC. The over-plotted vertical lines in the posterior distribution span the 95% credible interval. The contours indicate 0.5 σ , 1 σ , 1.5 σ , and 2 σ levels. The model results are summarised in Table 3, and the synthetic profiles based on these models are shown in Figure 5.

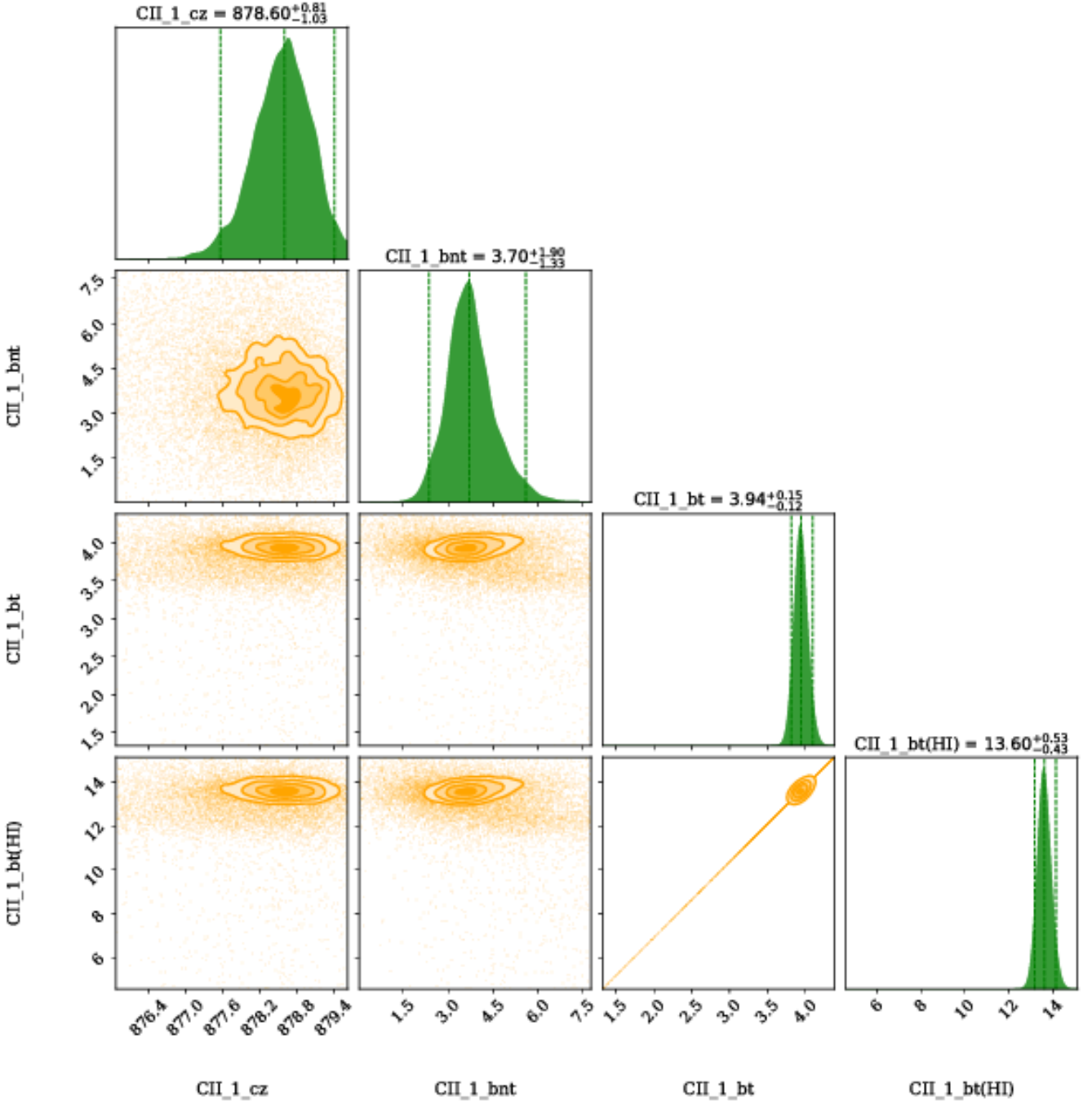


Figure C9. The corner plot showing the marginalized posterior distributions for the absorption centroid (z), non-thermal Doppler broadening (b_{nt}), thermal Doppler broadening (b_t), total Doppler broadening (b), of the phase traced by the C II cloud of the $z = 0.00238$ absorber towards SC. The over-plotted vertical lines in the posterior distribution span the 95% credible interval. The contours indicate 0.5σ , 1σ , 1.5σ , and 2σ levels. The model results are summarised in Table 3, and the synthetic profiles based on these models are shown in Figure 5.

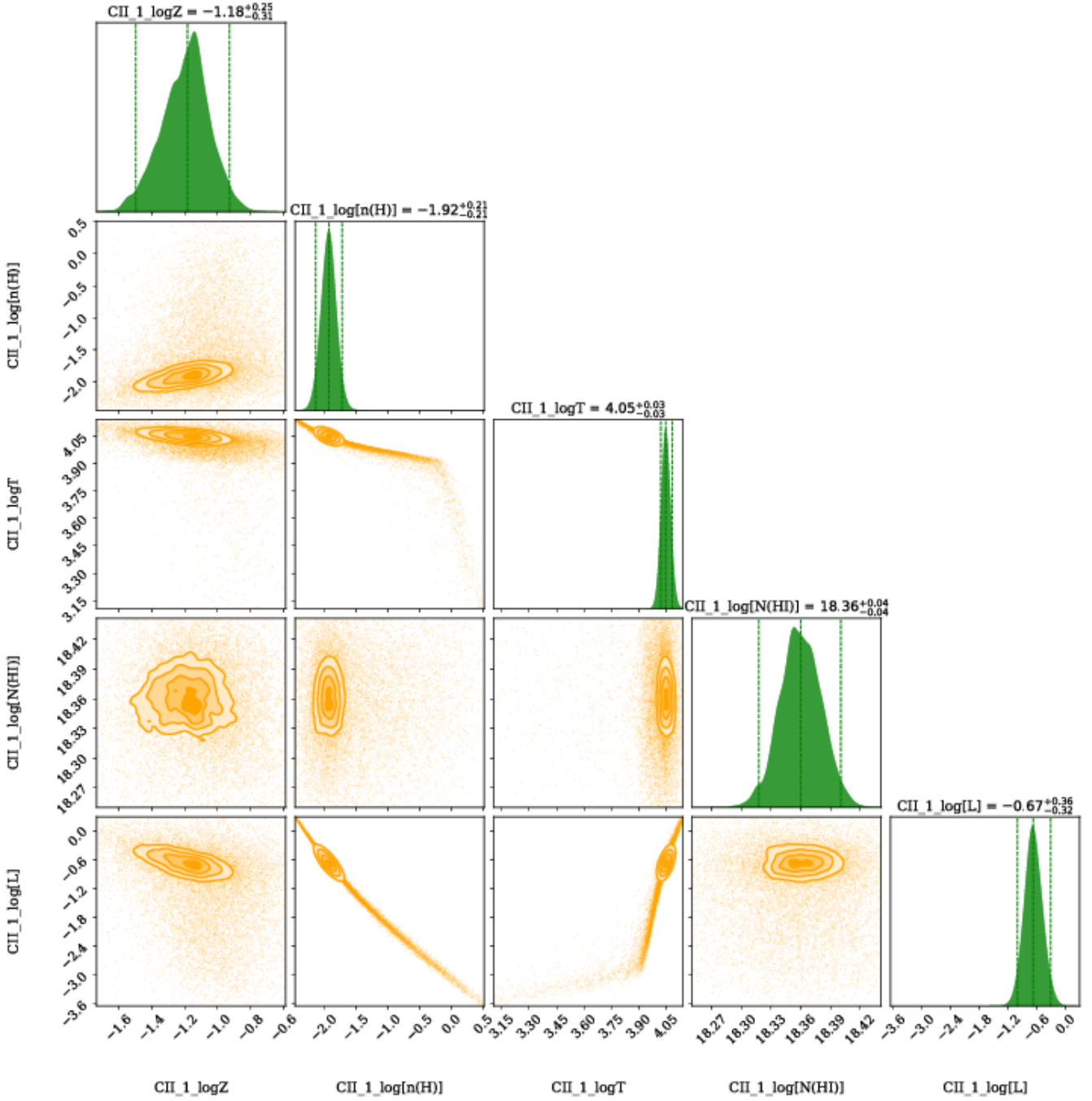


Figure C10. The corner plot showing the marginalized posterior distributions for the metallicity ($\log Z$), hydrogen number density ($\log n_H$), and other physical properties of the low ionization phase traced by the C II cloud of the $z = 0.00238$ absorber towards SC. The over-plotted vertical lines in the posterior distribution span the 95% credible interval. The contours indicate 0.5σ , 1σ , 1.5σ , and 2σ levels. The model results are summarised in Table 3, and the synthetic profiles based on these models are shown in Figure 5.

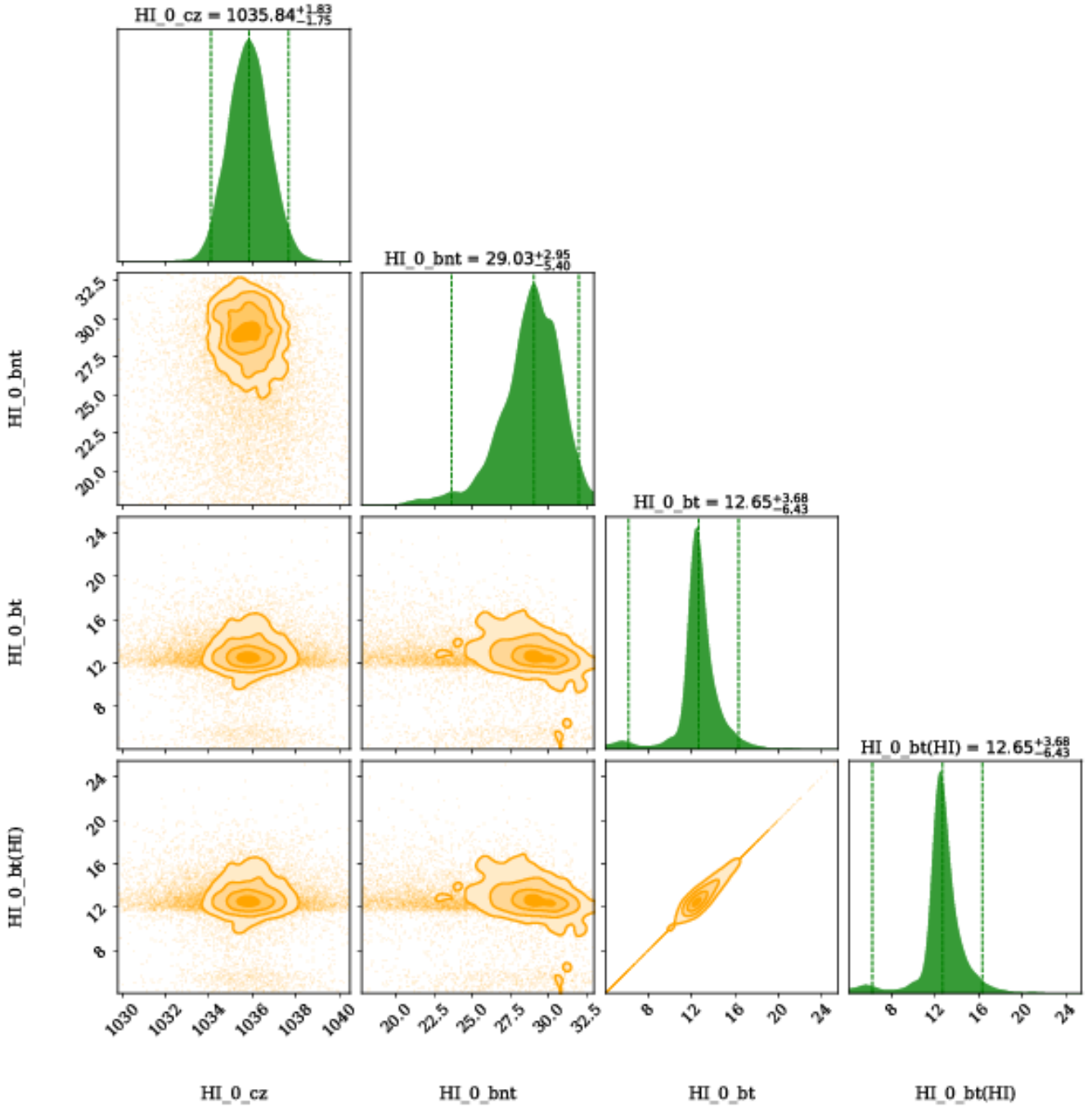


Figure C11. The corner plot showing the marginalized posterior distributions for the absorption centroid (z), non-thermal Doppler broadening (b_{nt}), thermal Doppler broadening (b_t), total Doppler broadening (b), of the phase traced by the H I cloud of the $z = 0.00238$ absorber towards SC. The over-plotted vertical lines in the posterior distribution span the 95% credible interval. The contours indicate 0.5σ , 1σ , 1.5σ , and 2σ levels. The model results are summarised in Table 3, and the synthetic profiles based on these models are shown in Figure 5.

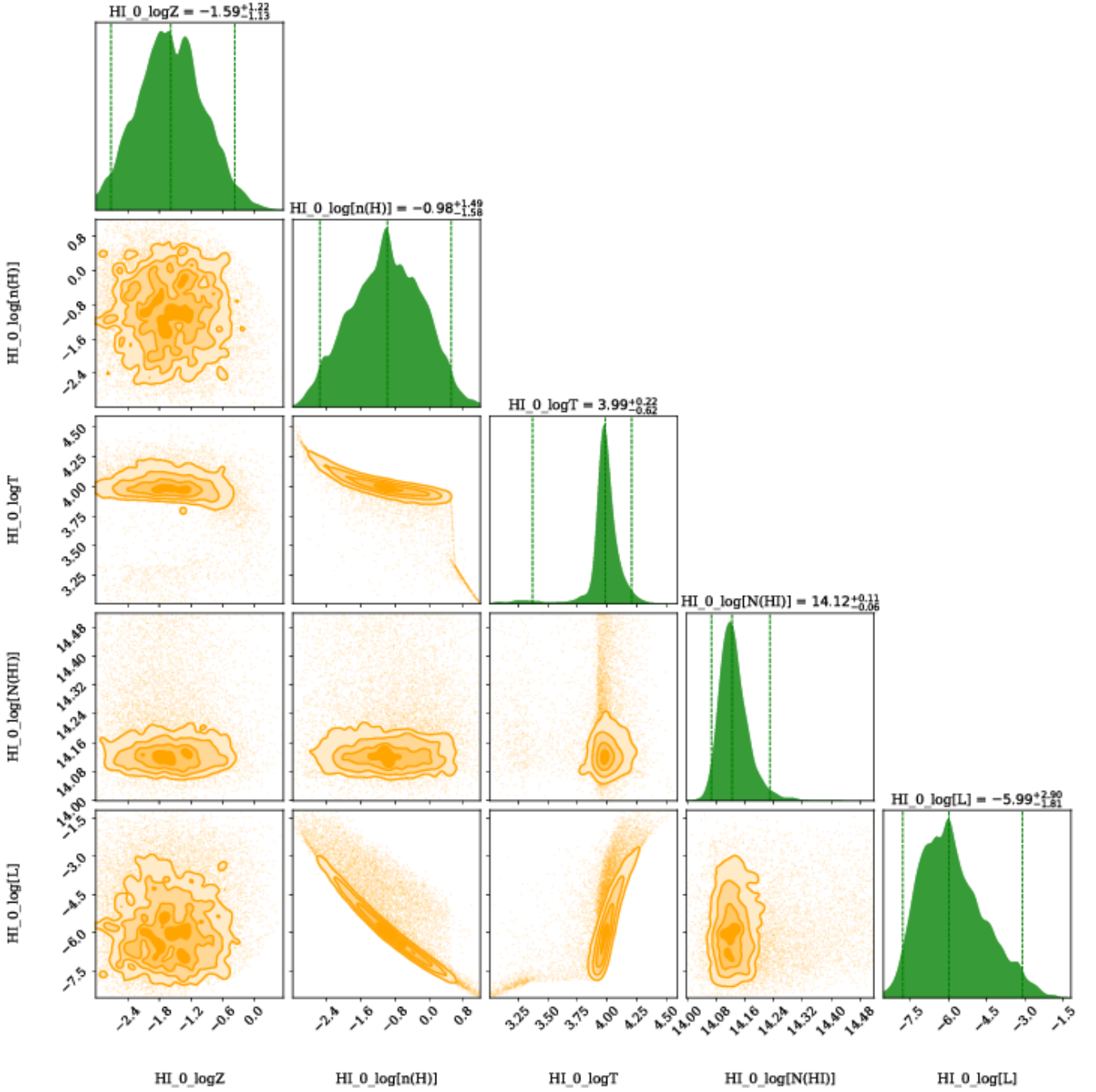


Figure C12. The corner plot showing the marginalized posterior distributions for the metallicity ($\log Z$), hydrogen number density ($\log n_{\text{H}}$), and other physical properties of the low ionization phase traced by the H I cloud of the $z = 0.00238$ absorber towards SC. The over-plotted vertical lines in the posterior distribution span the 95% credible interval. The contours indicate 0.5 σ , 1 σ , 1.5 σ , and 2 σ levels. The model results are summarised in Table 3, and the synthetic profiles based on these models are shown in Figure 5.

APPENDIX D: PLOTS FOR SD

- D1** Airglow template fit towards SD
- D2** Airglow template fit towards SD
- D3** Best VP fit to the Galactic Ly α towards SD
- D4** Posterior distributions for the absorber properties towards SD

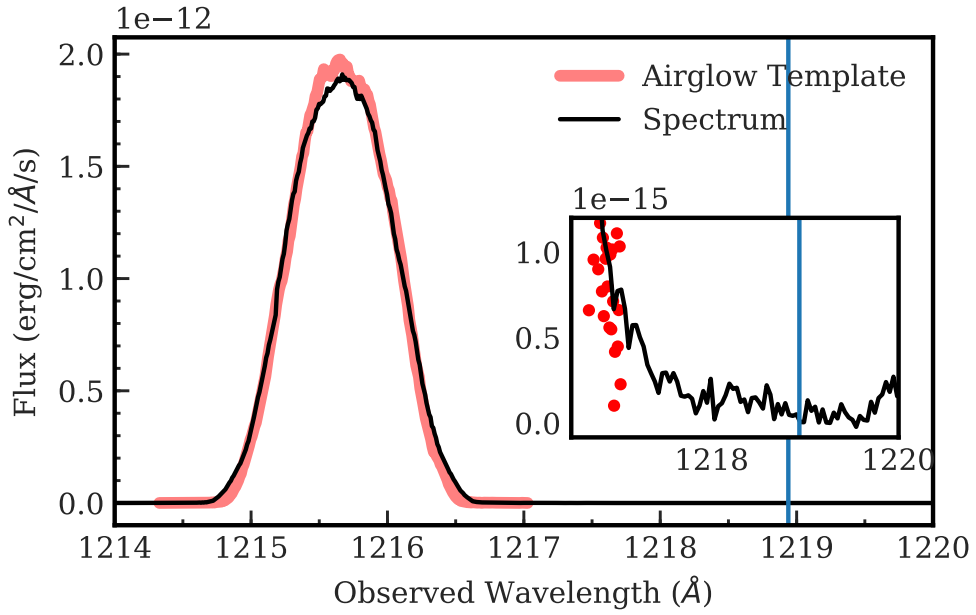


Figure D1. Same as in Figure B1, but for SD.

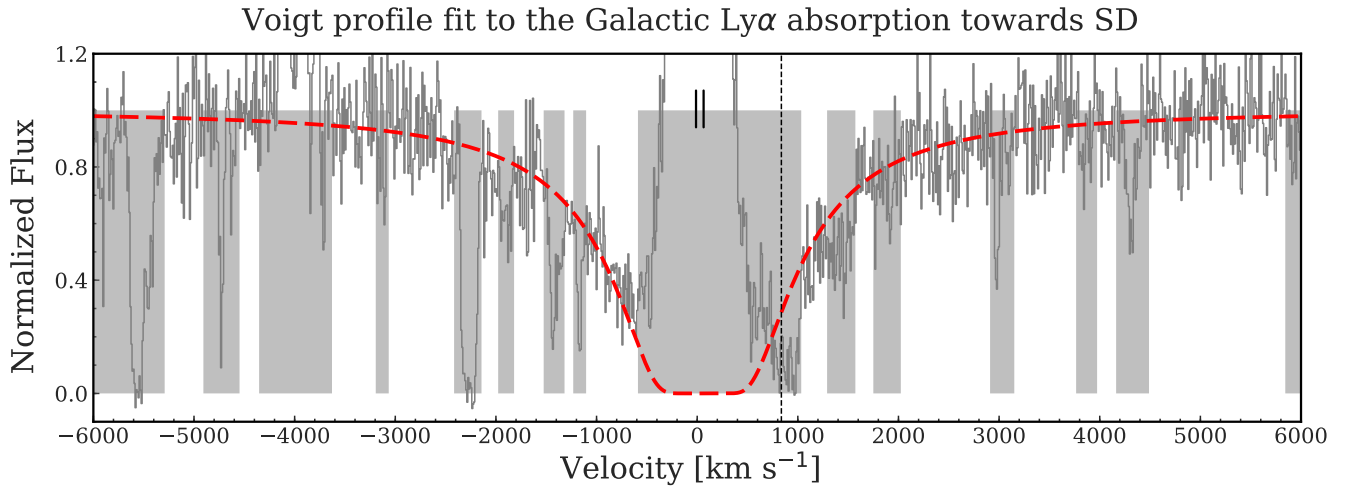


Figure D2. Same as in Figure B2, but for SD.

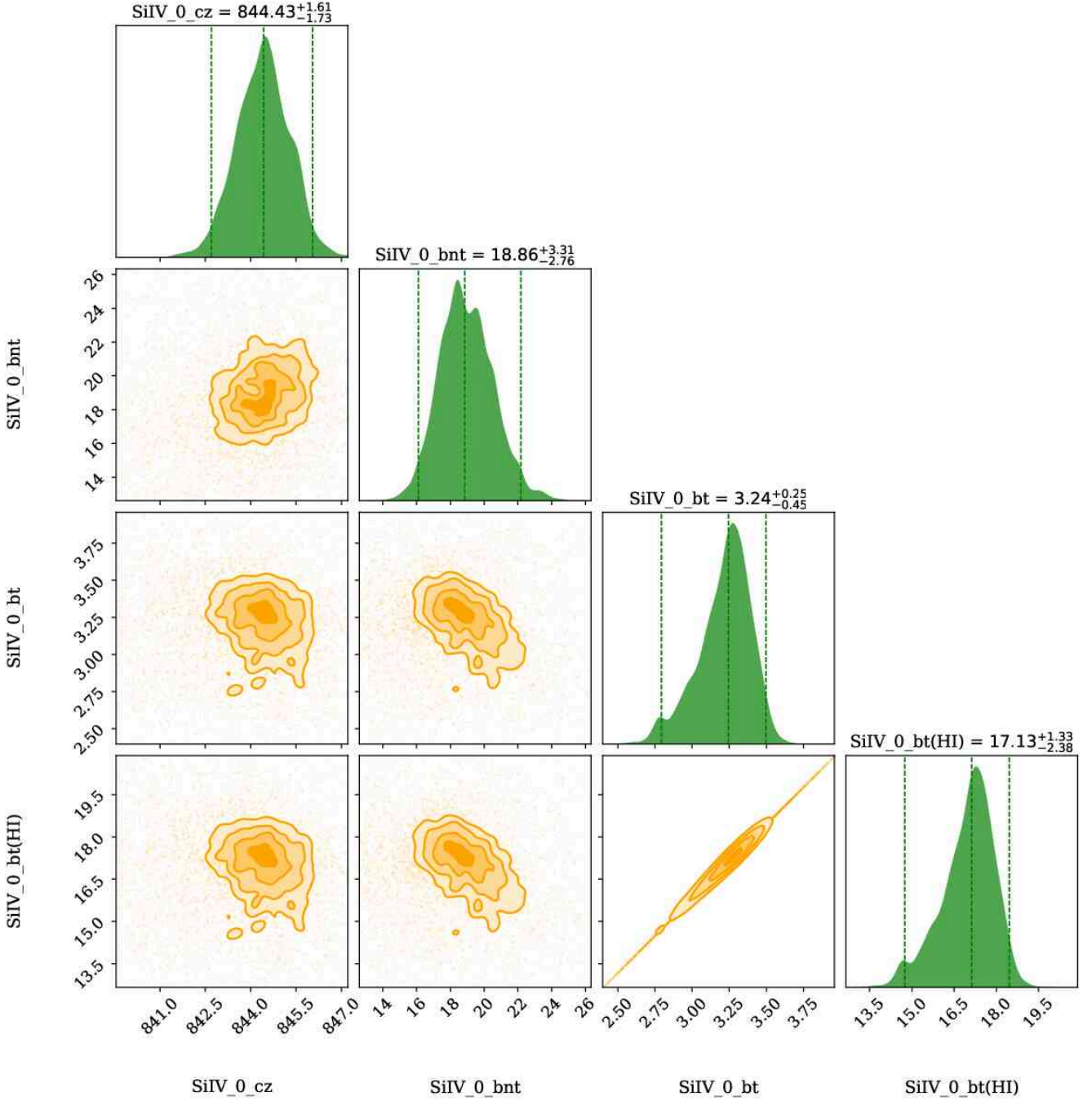


Figure D3. The corner plot showing the marginalized posterior distributions for the absorption centroid (z), non-thermal Doppler broadening (b_{nt}), thermal Doppler broadening (b_t), total Doppler broadening (b), of the phase traced by the blueward Si iv cloud of the $z = 0.00279$ absorber towards SD. The over-plotted vertical lines in the posterior distribution span the 95% credible interval. The contours indicate 0.5 σ , 1 σ , 1.5 σ , and 2 σ levels. The model results are summarised in Table 3, and the synthetic profiles based on these models are shown in Figure 6.

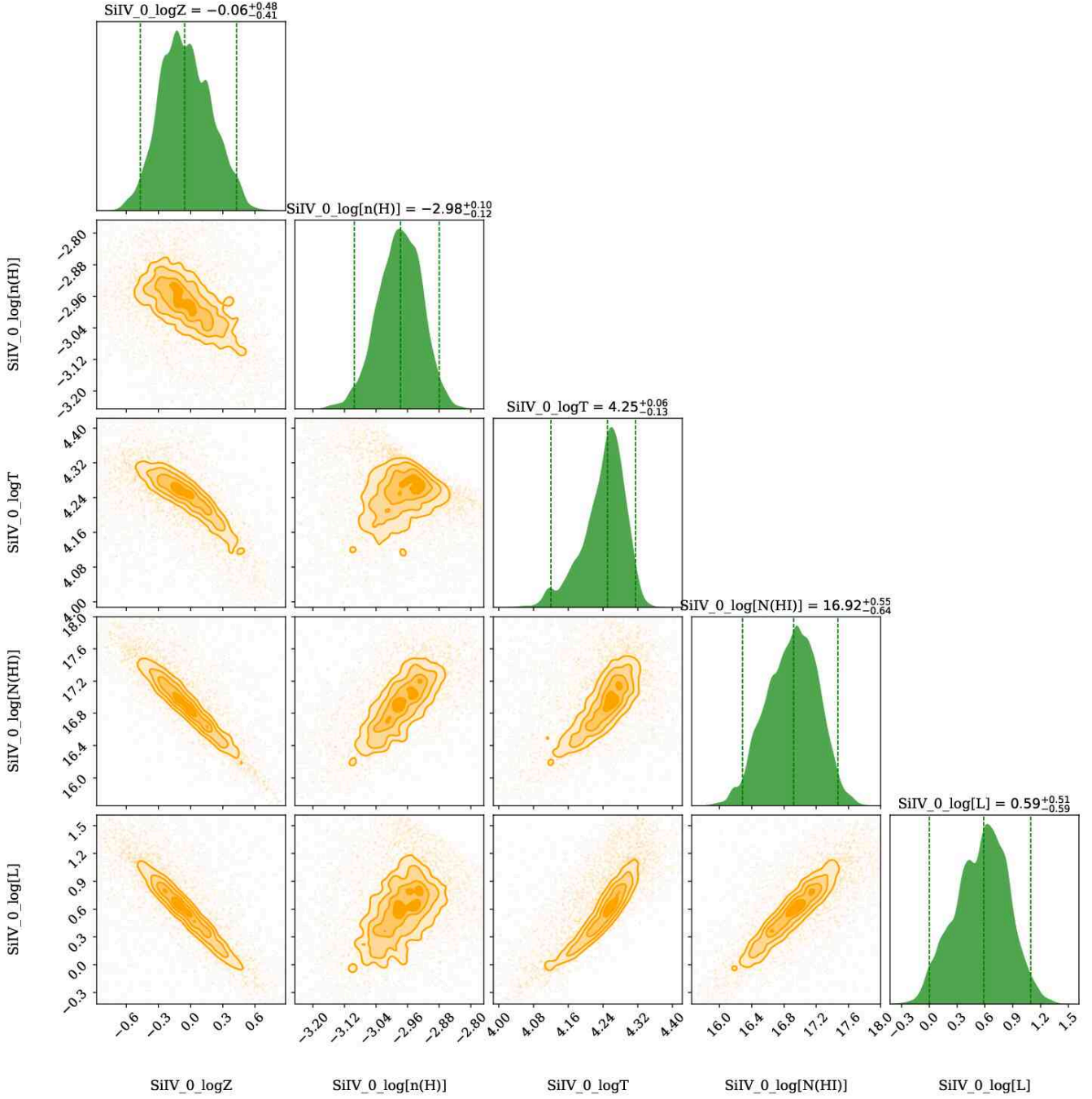


Figure D4. The corner plot showing the marginalized posterior distributions for the metallicity ($\log Z$), hydrogen number density ($\log n_H$), temperature ($\log T$), neutral hydrogen column density ($\log N(\text{H I})$), and the line of sight thickness ($\log L$), of the low ionization phase traced by the blueward Si IV cloud of the $z = 0.00279$ absorber towards SD. The over-plotted vertical lines in the posterior distribution span the 95% credible interval. The contours indicate 0.5σ , 1σ , 1.5σ , and 2σ levels. The model results are summarised in Table 3, and the synthetic profiles based on these models are shown in Figure 6.

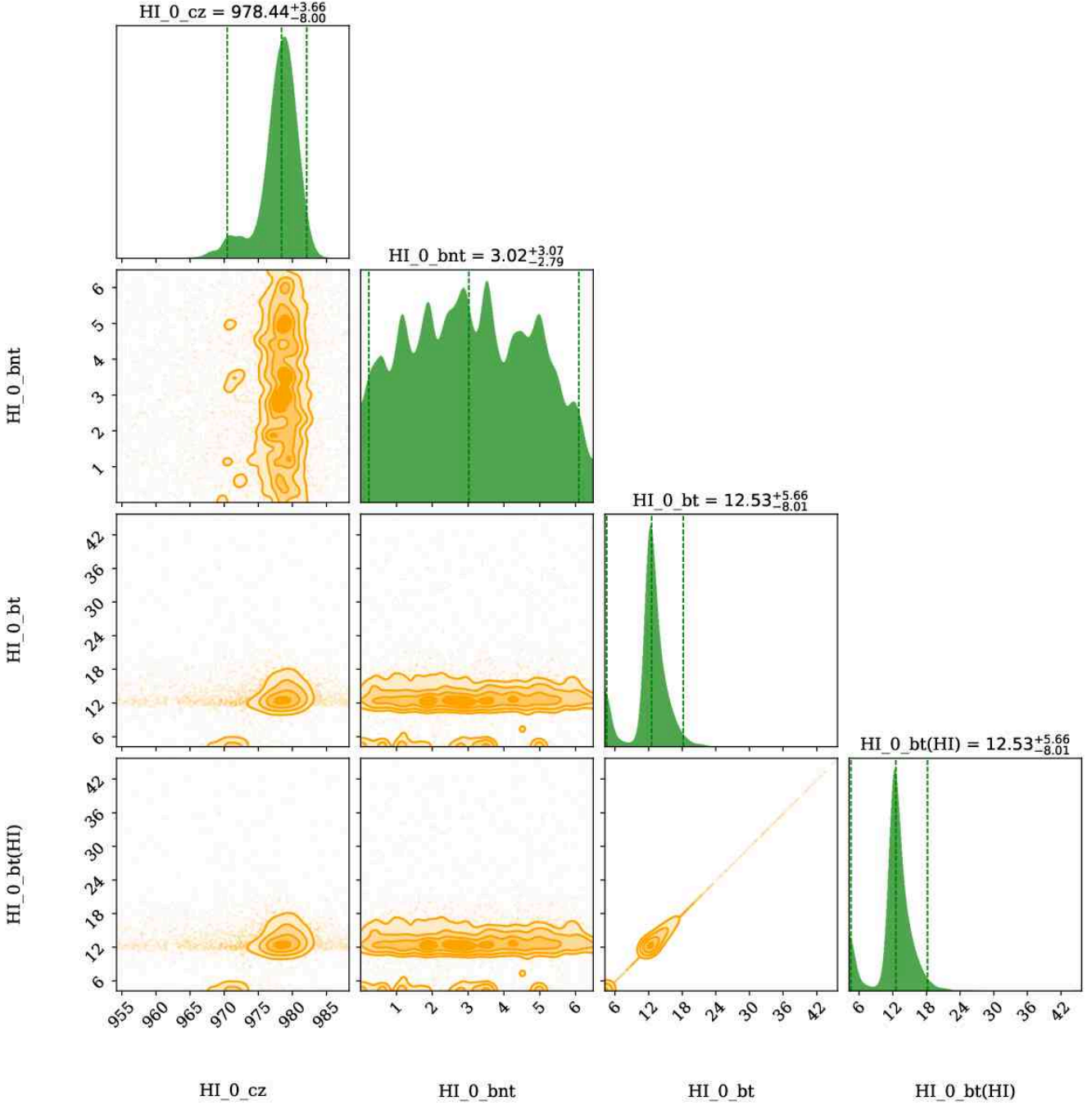


Figure D5. The corner plot showing the marginalized posterior distributions for the absorption centroid (z), non-thermal Doppler broadening (b_{nt}), thermal Doppler broadening (b_t), total Doppler broadening (b), of the phase traced by the redward H I cloud of the $z = 0.00279$ absorber towards SD. The over-plotted vertical lines in the posterior distribution span the 95% credible interval. The contours indicate 0.5σ , 1σ , 1.5σ , and 2σ levels. The model results are summarised in Table 3, and the synthetic profiles based on these models are shown in Figure 6.

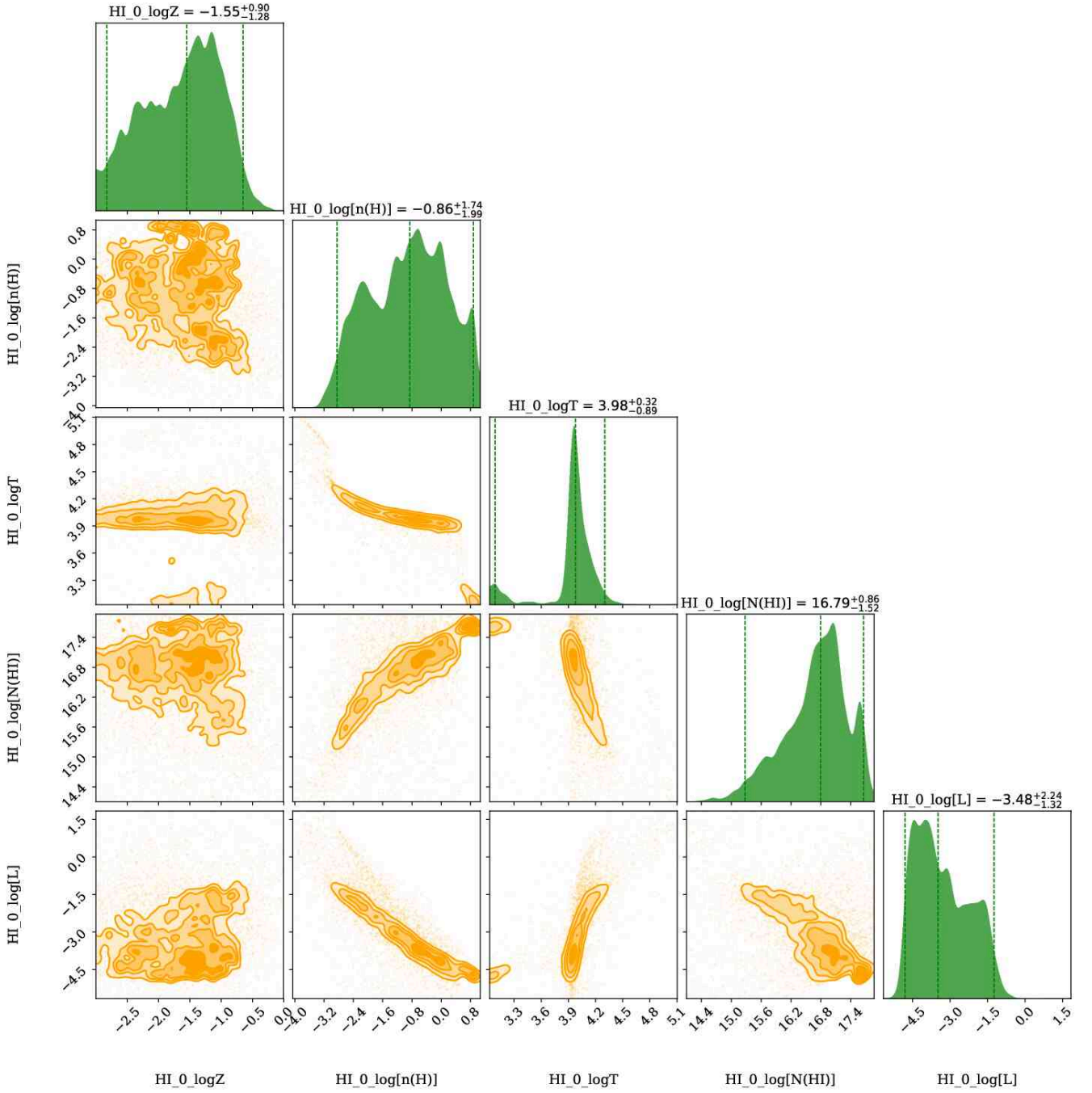


Figure D6. The corner plot showing the marginalized posterior distributions for the metallicity ($\log Z$), hydrogen number density ($\log n_{\text{H}}$), and other physical properties of the low ionization phase traced by the redward H I cloud of the $z = 0.00279$ absorber towards SD. The over-plotted vertical lines in the posterior distribution span the 95% credible interval. The contours indicate 0.5σ , 1σ , 1.5σ , and 2σ levels. The model results are summarised in Table 3, and the synthetic profiles based on these models are shown in Figure 6.

APPENDIX E: PLOTS FOR SE

- E1** Airglow template fit towards SE
- E2** Best VP fit to the Galactic Ly α towards SE
- E3** PC model for the high-ionization phase towards SE
- E4** Posterior distributions for the absorber properties towards SE

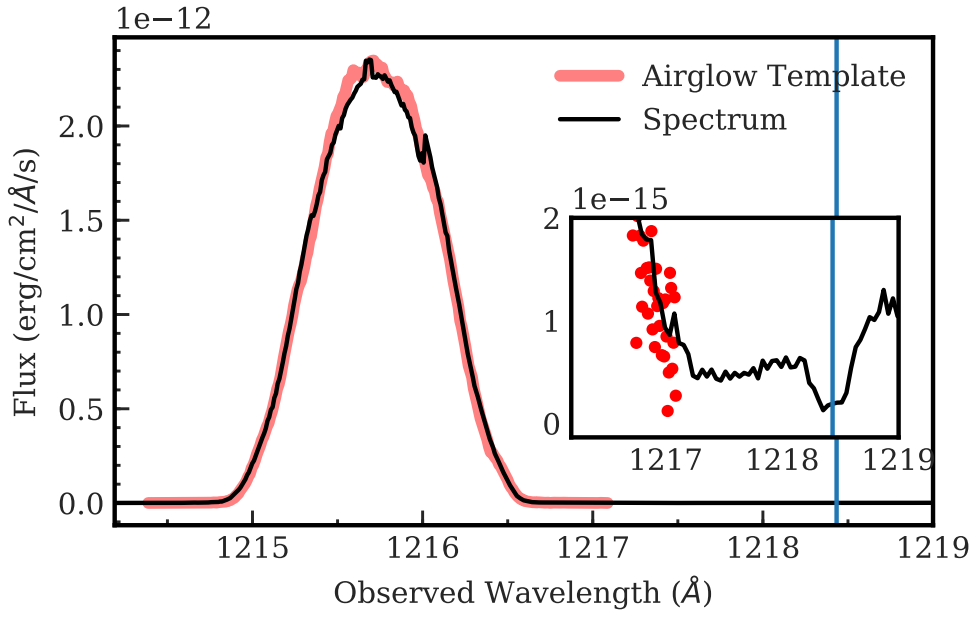


Figure E1. Same as in Figure B1, but for SE.

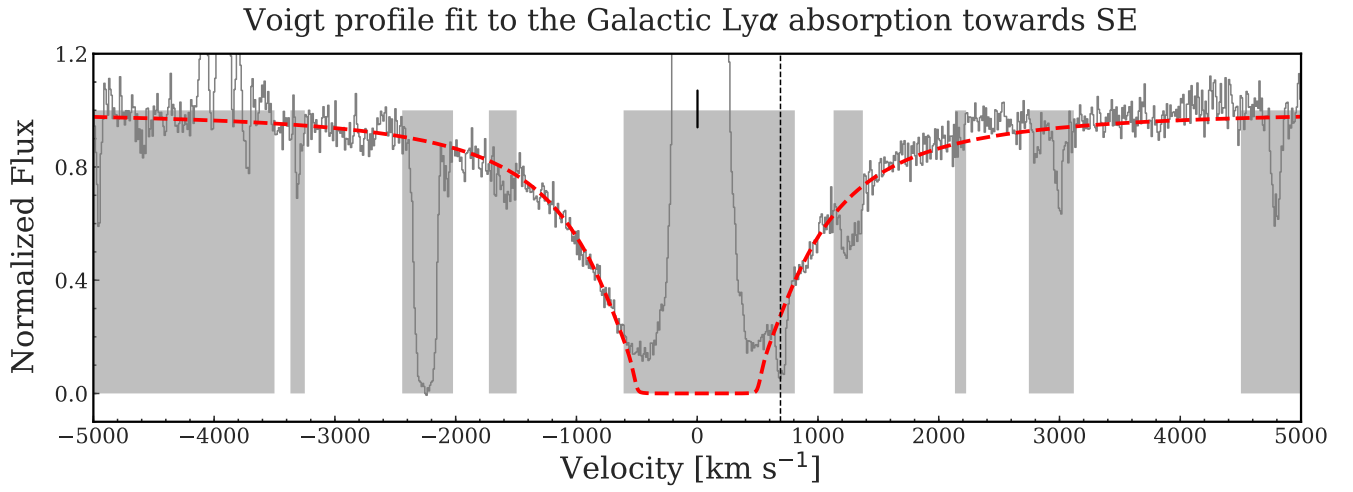


Figure E2. Same as in Figure B2, but for SE.

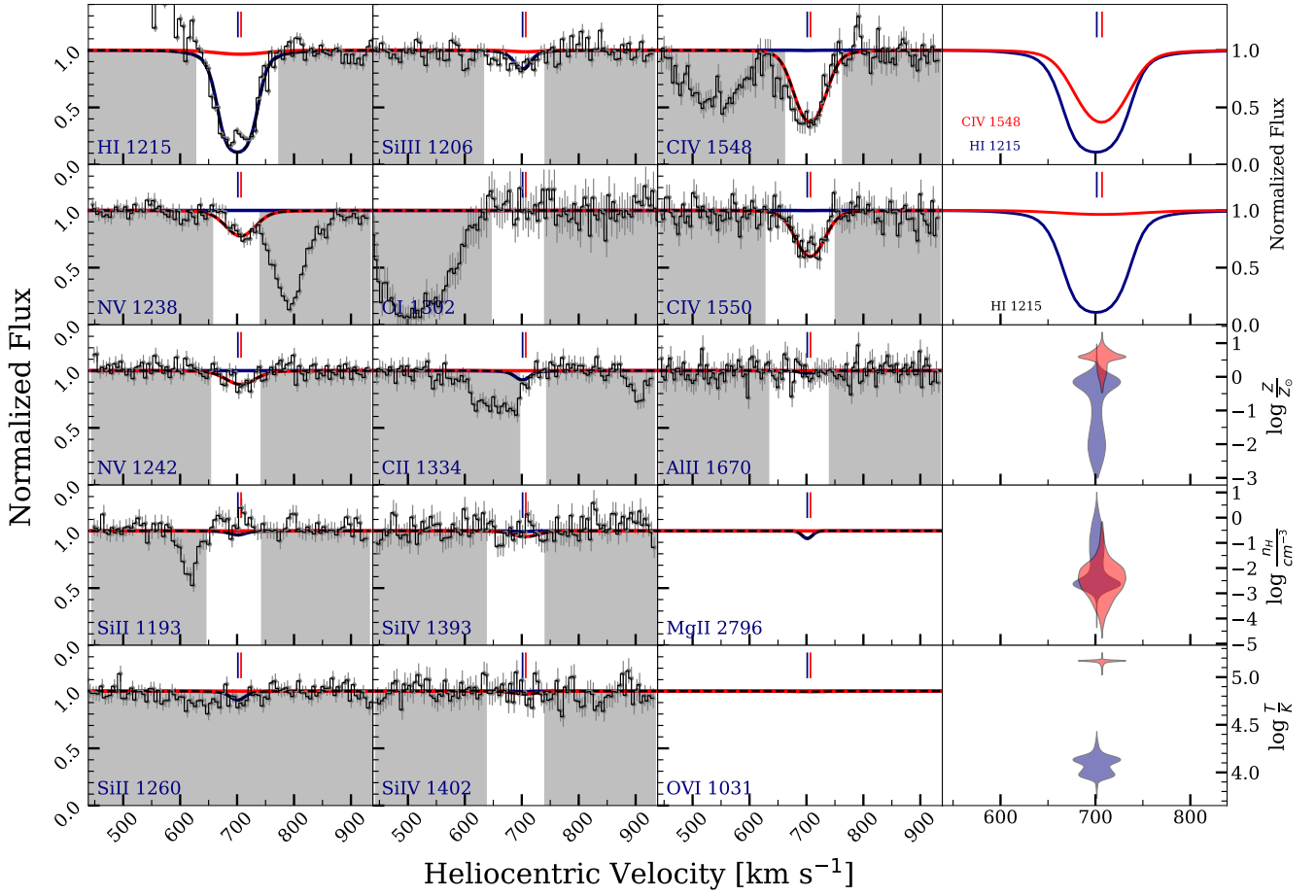


Figure E3. A PC model for the absorption towards SE. The C IV absorption is modelled as a collisionally ionized phase, and N v is also found to arise in the same phase with a temperature of $\log T \approx 5.2$. The dominant H I absorption, which also produces modest absorption in Si III is still modelled as a photoionized phase only.

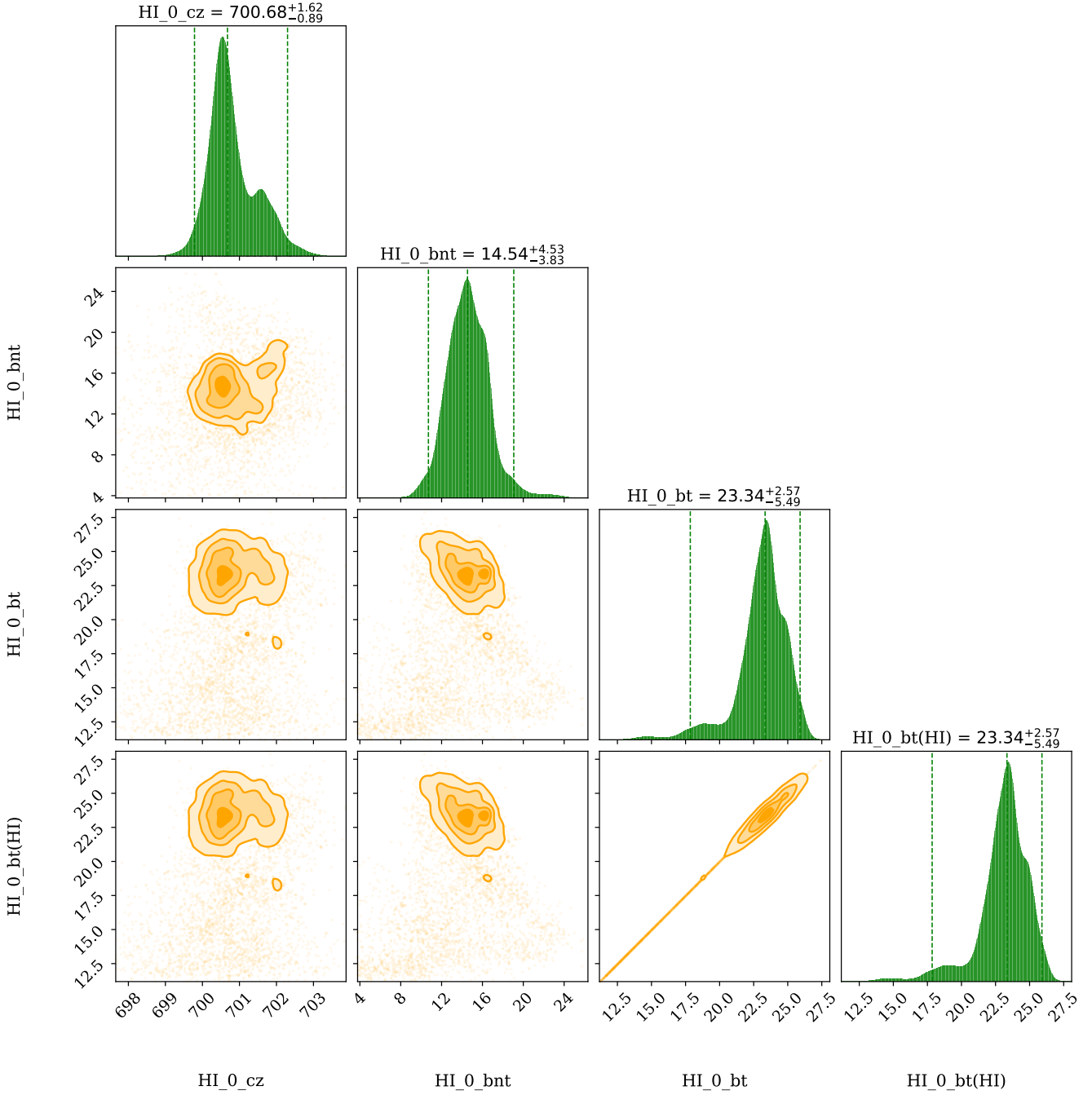


Figure E4. The corner plot showing the marginalized posterior distributions for the absorption centroid (z), non-thermal Doppler broadening (b_{nt}), thermal Doppler broadening (b_t), total Doppler broadening (b), of the phase traced by the dominant H I-producing absorption cloud of the $z = 0.0023$ absorber towards SE. The over-plotted vertical lines in the posterior distribution span the 95% credible interval. The contours indicate 0.5 σ , 1 σ , 1.5 σ , and 2 σ levels. The model results are summarised in Table 3, and the synthetic profiles based on these models are shown in Figure 7.

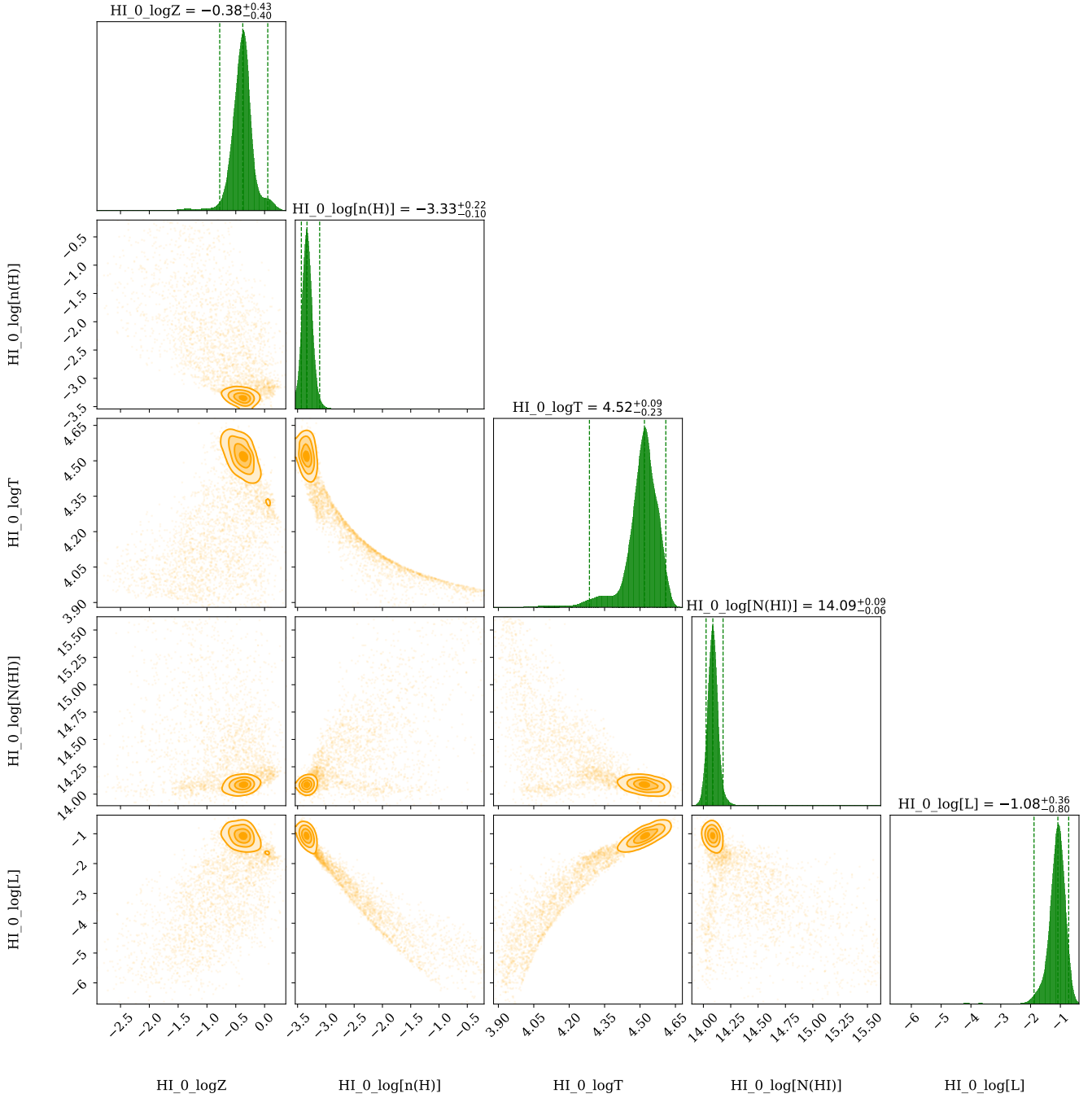


Figure E5. The corner plot showing the marginalized posterior distributions for the metallicity ($\log Z$), hydrogen number density ($\log n_H$), temperature ($\log T$), neutral hydrogen column density ($\log N(\text{H I})$), and the line of sight thickness ($\log L$), of the phase traced by the dominant H I-producing absorption cloud of the $z = 0.0023$ absorber towards SE. The over-plotted vertical lines in the posterior distribution span the 95% credible interval. The contours indicate 0.5σ , 1σ , 1.5σ , and 2σ levels. The model results are summarised in Table 3, and the synthetic profiles based on these models are shown in Figure 7.

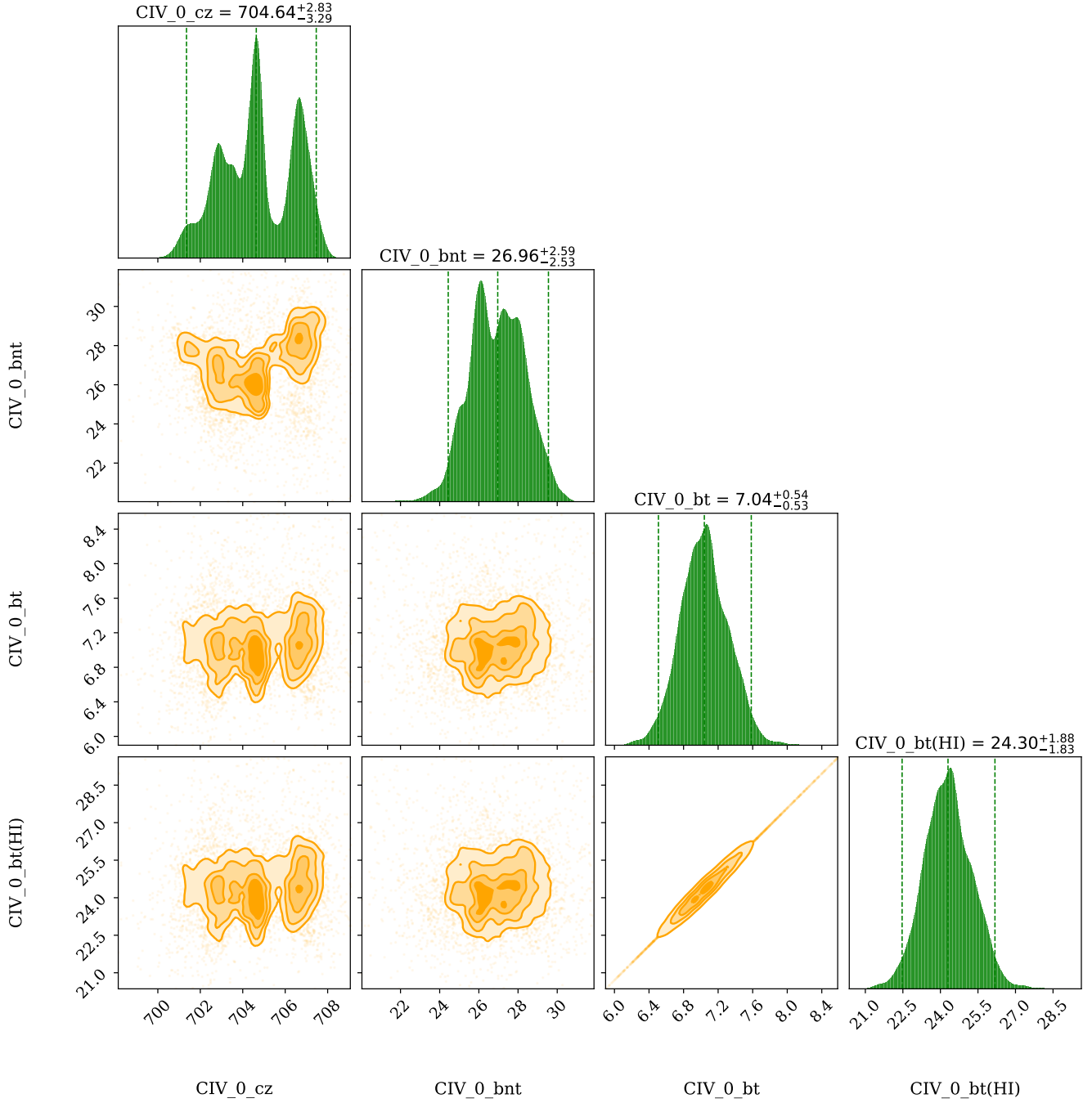


Figure E6. The corner plot showing the marginalized posterior distributions for the absorption centroid (z), non-thermal Doppler broadening (b_{nt}), thermal Doppler broadening (b_t), total Doppler broadening (b), of the phase traced by the C iv cloud of the $z = 0.0023$ absorber towards SE. The over-plotted vertical lines in the posterior distribution span the 95% credible interval. The contours indicate 0.5σ , 1σ , 1.5σ , and 2σ levels. The model results are summarised in Table 3, and the synthetic profiles based on these models are shown in Figure 7.

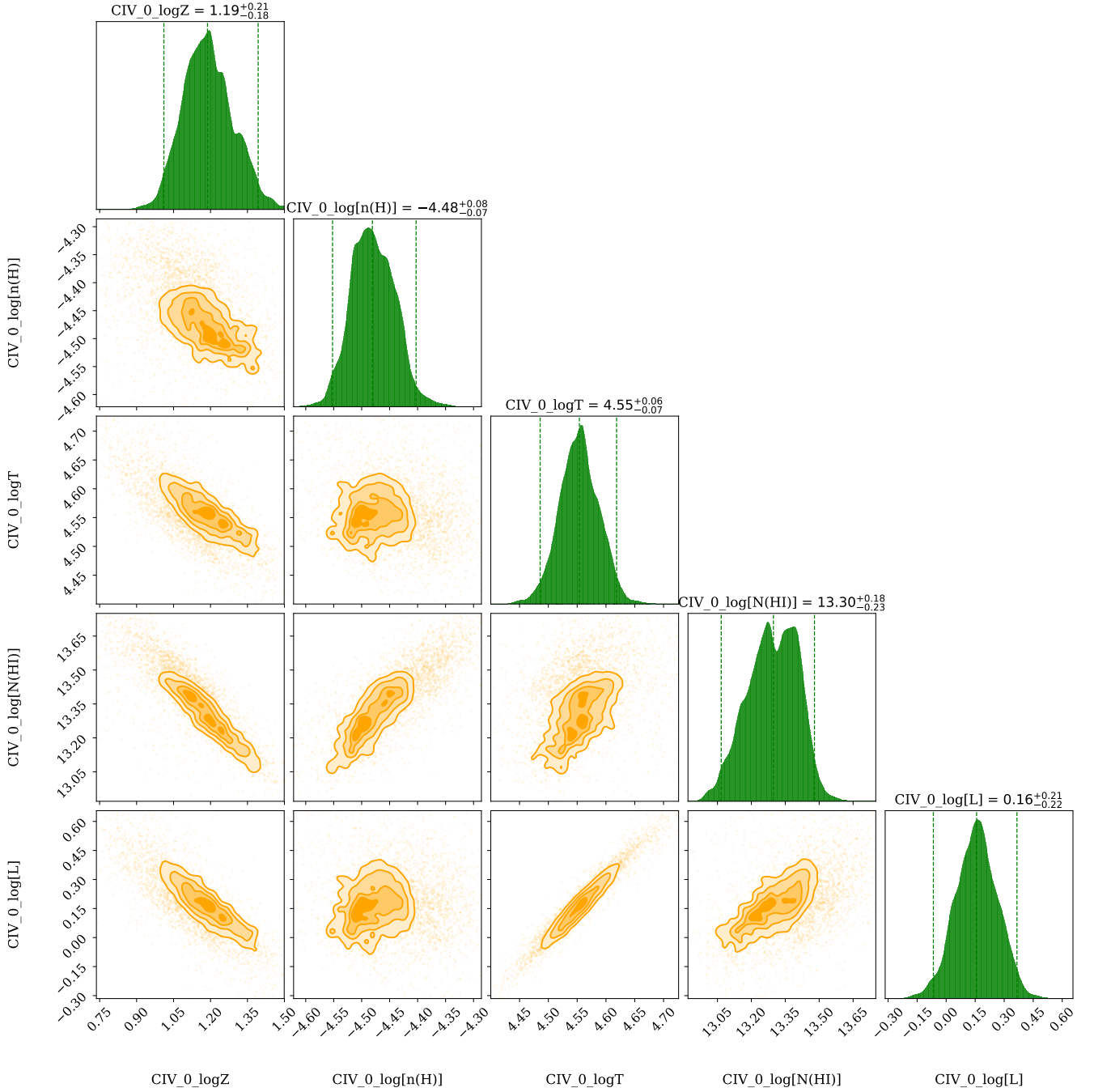


Figure E7. The corner plot showing the marginalized posterior distributions for the metallicity ($\log Z$), hydrogen number density ($\log n_H$), temperature ($\log T$), neutral hydrogen column density ($\log N(\text{H I})$), and the line of sight thickness ($\log L$), of the phase traced by the CIV cloud of the $z = 0.0023$ absorber towards SE. The over-plotted vertical lines in the posterior distribution span the 95% credible interval. The contours indicate 0.5σ , 1σ , 1.5σ , and 2σ levels. The model results are summarised in Table 3, and the synthetic profiles based on these models are shown in Figure 7.

APPENDIX F: PLOTS FOR SF

- F1** Airglow template fit towards SF
- F2** Best VP fit to the Galactic $\text{Ly}\alpha$ towards SF
- F3** System plot for sightline SF with H I data masked
- F4** System plot for sightline SF with a restricted prior on $\log N(\text{H I})$
- F5** Posterior distributions for the absorber properties towards SF

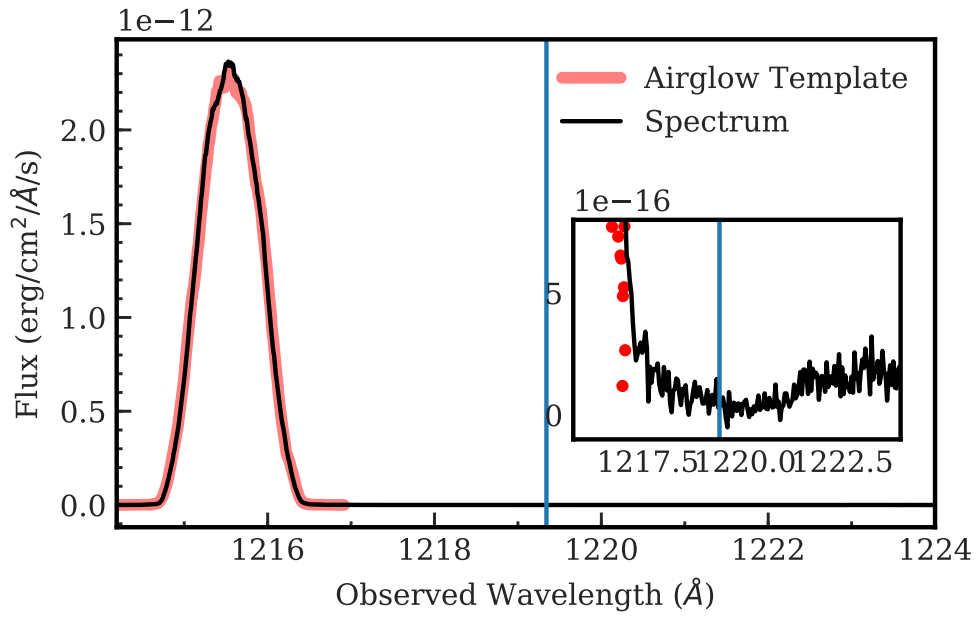


Figure F1. Same as in Figure B1, but for SF.

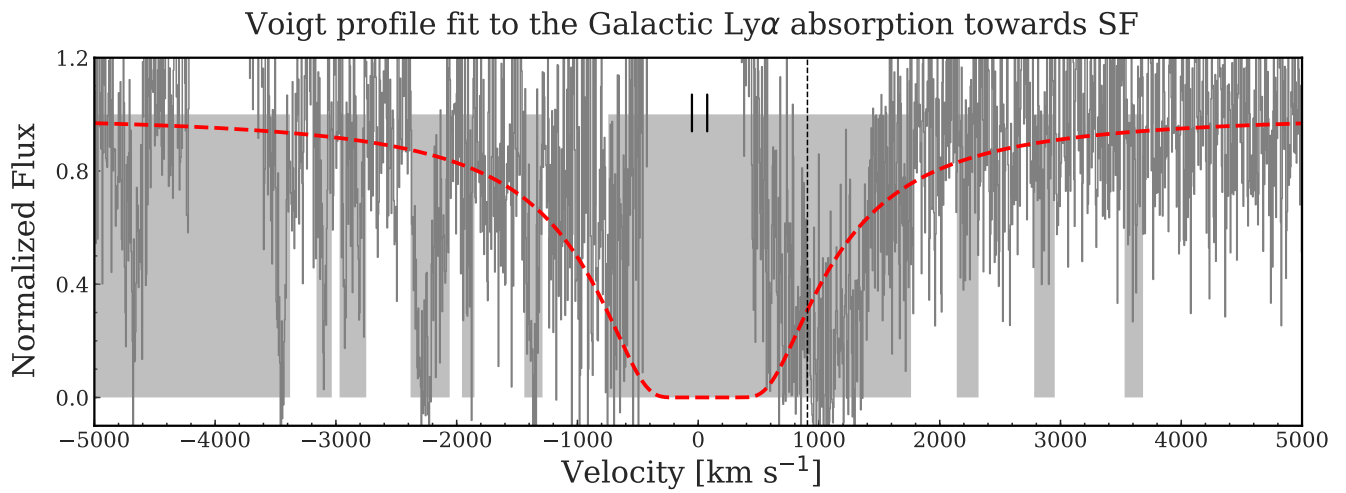


Figure F2. Same as in Figure B2, but for SF.

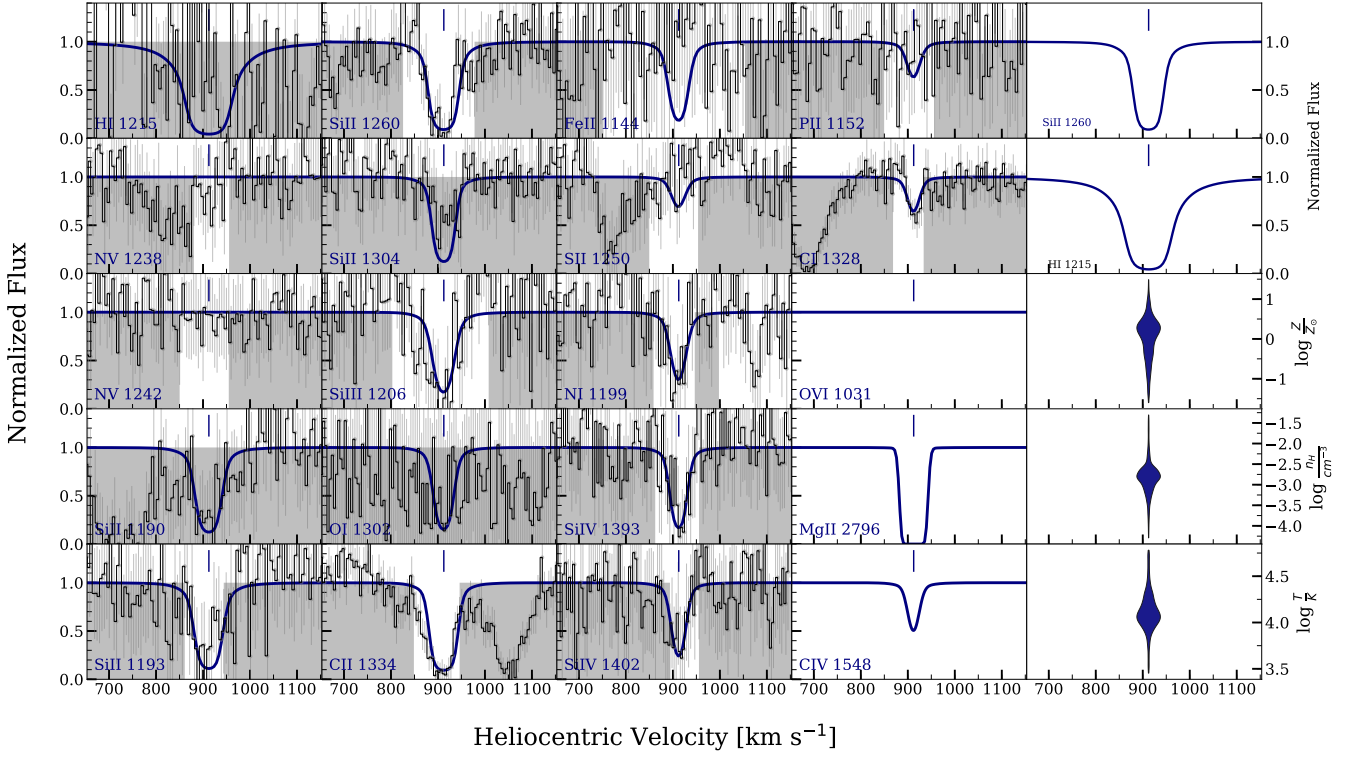


Figure F3. The system plots showing the model in which the H I data is masked. The detection of neutral species, C I and N I, provides a constraint on the metallicity and density of the phase.

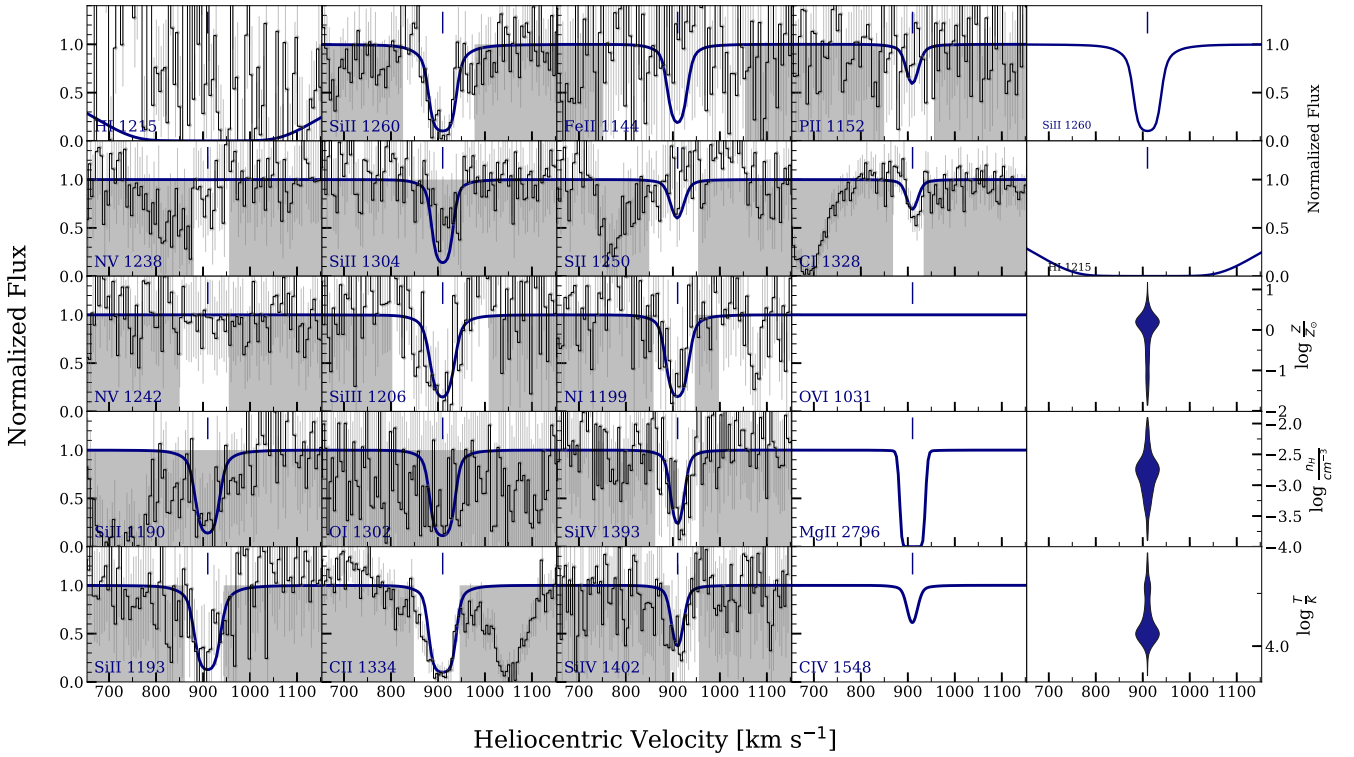


Figure F4. The system plots showing the model in which the prior on $\log N(\text{H I})$ is restricted to be greater than 19.5. Even for this larger value of $\log N(\text{H I})$, we find a high value of $\log Z/Z_{\odot} = 0.21 \pm 0.08$.

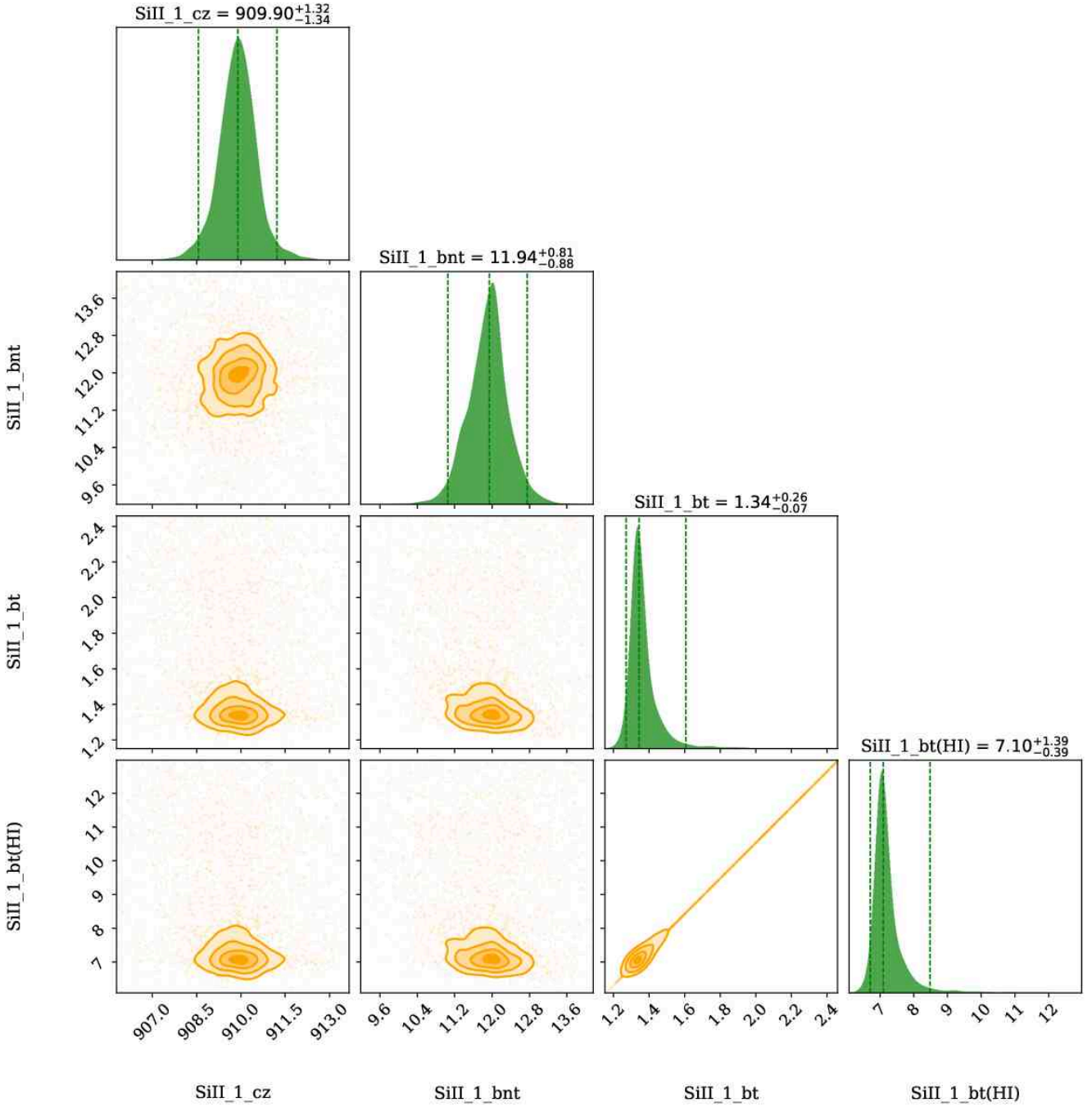


Figure F5. The corner plot showing the marginalized posterior distributions for the absorption centroid (z), non-thermal Doppler broadening (b_{nt}), thermal Doppler broadening (b_t), total Doppler broadening (b), of the phase traced by the Si II cloud of the $z = 0.0030$ absorber towards SF. The over-plotted vertical lines in the posterior distribution span the 95% credible interval. The contours indicate 0.5σ , 1σ , 1.5σ , and 2σ levels. The model results are summarised in Table 3, and the synthetic profiles based on these models are shown in Figure 8.

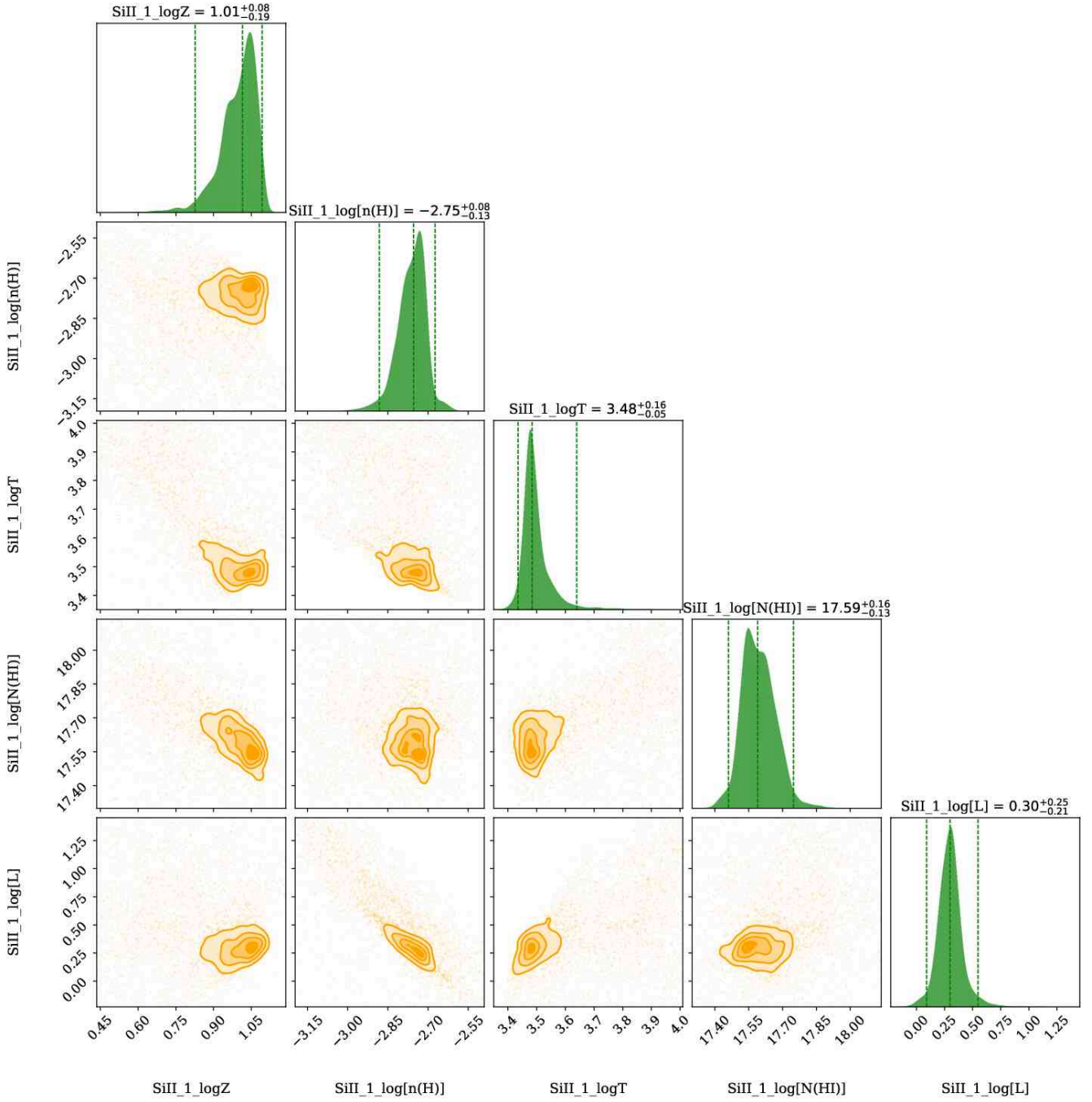


Figure F6. The corner plot showing the marginalized posterior distributions for the metallicity ($\log Z$), hydrogen number density ($\log n_H$), temperature ($\log T$), neutral hydrogen column density ($\log N(\text{H I})$), and the line of sight thickness ($\log L$), of the phase traced by the Si II cloud of the $z = 0.0030$ absorber towards SF. The over-plotted vertical lines in the posterior distribution span the 95% credible interval. The contours indicate 0.5σ , 1σ , 1.5σ , and 2σ levels. The model results are summarised in Table 3, and the synthetic profiles based on these models are shown in Figure 8.

APPENDIX G: PLOTS FOR SG

- G1** Airglow template fit towards SG
- G2** Best VP fit to the Galactic Ly α towards SG
- G3** MC exploration of the zero-point uncertainty for SG
- G4** Posterior distributions for the absorber properties towards SG

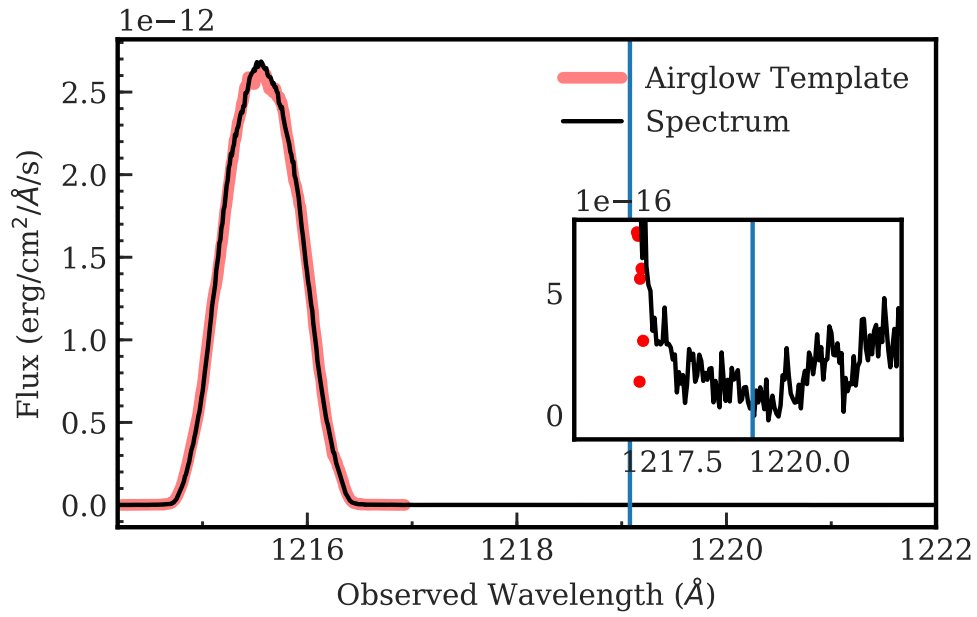


Figure G1. Same as in Figure B1, but for SG.

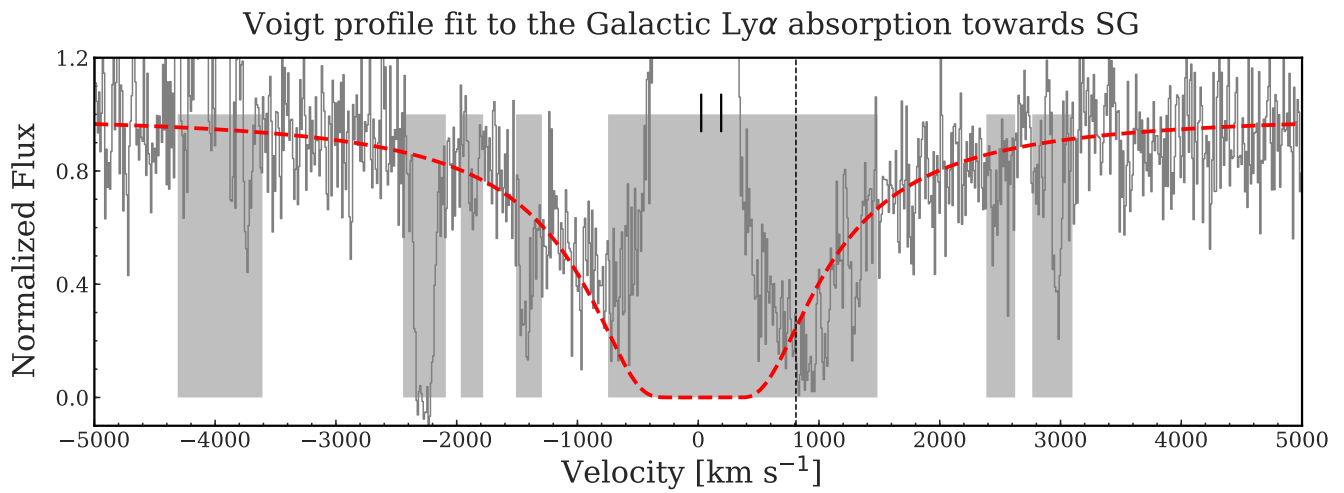


Figure G2. Same as in Figure B2, but for SG.

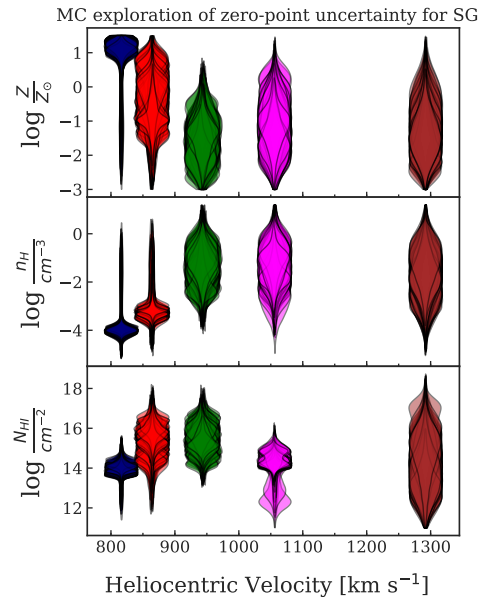


Figure G3. Violin plots showing the parameter distributions for 100 different realizations of the H I Ly α profile modified between 815–865 km s⁻¹ to account for the zero-point uncertainty. The blue violins show the parameters of C IV phase. The red violins correspond to the Si IV phase, the green, magenta, and brown violins correspond to the H I only phases.

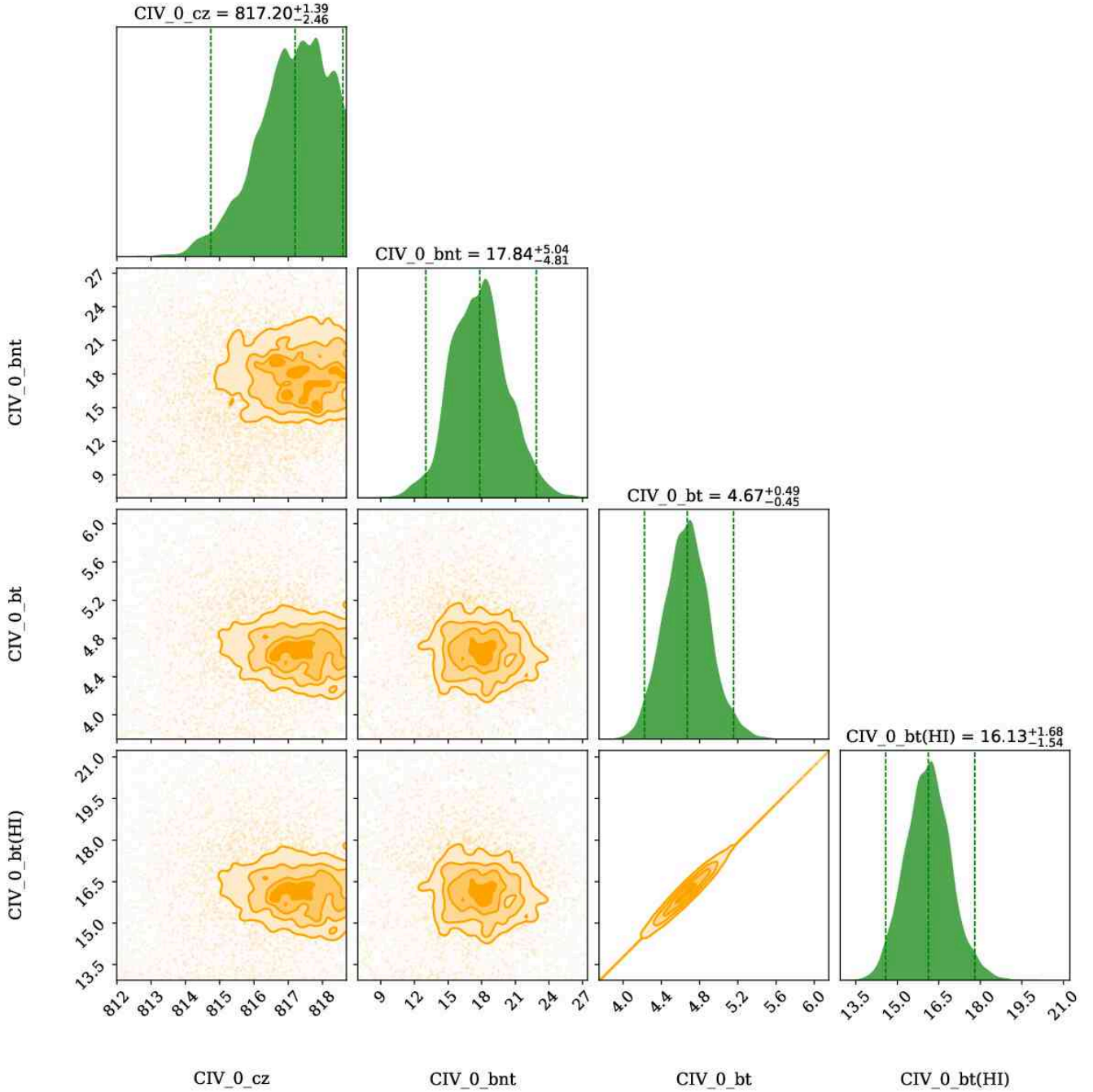


Figure G4. The corner plot showing the marginalized posterior distributions for the absorption centroid (z), non-thermal Doppler broadening (b_{nt}), thermal Doppler broadening (b_t), total Doppler broadening (b), of the phase traced by the C iv cloud of the $z = 0.0027$ absorber towards SG. The over-plotted vertical lines in the posterior distribution span the 95% credible interval. The contours indicate 0.5σ , 1σ , 1.5σ , and 2σ levels. The model results are summarised in Table 3, and the synthetic profiles based on these models are shown in Figure 9.

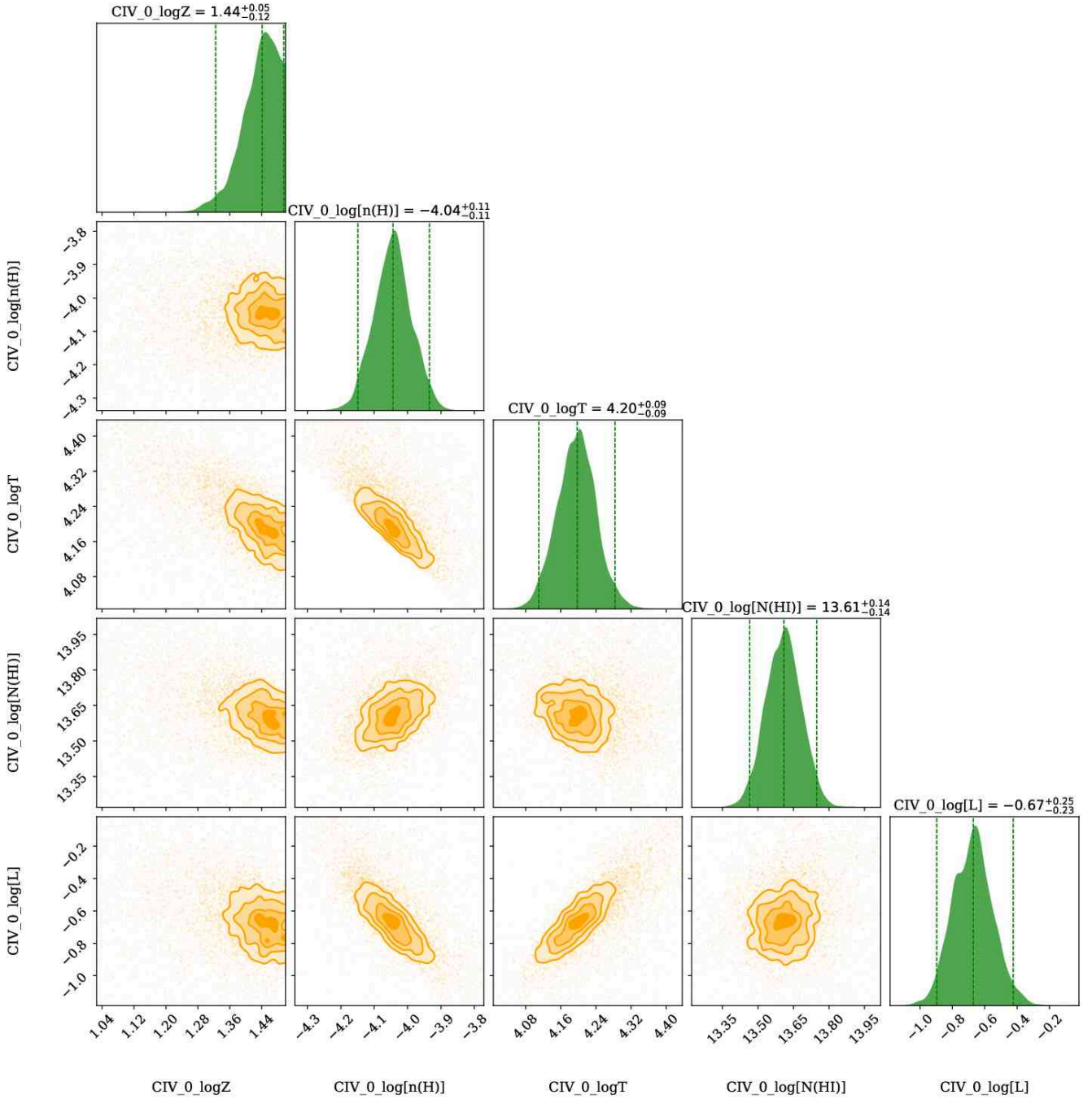


Figure G5. The corner plot showing the marginalized posterior distributions for the metallicity ($\log Z$), hydrogen number density ($\log n_H$), temperature ($\log T$), neutral hydrogen column density ($\log N(\text{H I})$), and the line of sight thickness ($\log L$), of the low ionization phase traced by the C IV cloud of the $z = 0.0027$ absorber towards SG. The over-plotted vertical lines in the posterior distribution span the 95% credible interval. The contours indicate 0.5σ , 1σ , 1.5σ , and 2σ levels. The model results are summarised in Table 3, and the synthetic profiles based on these models are shown in Figure 9.

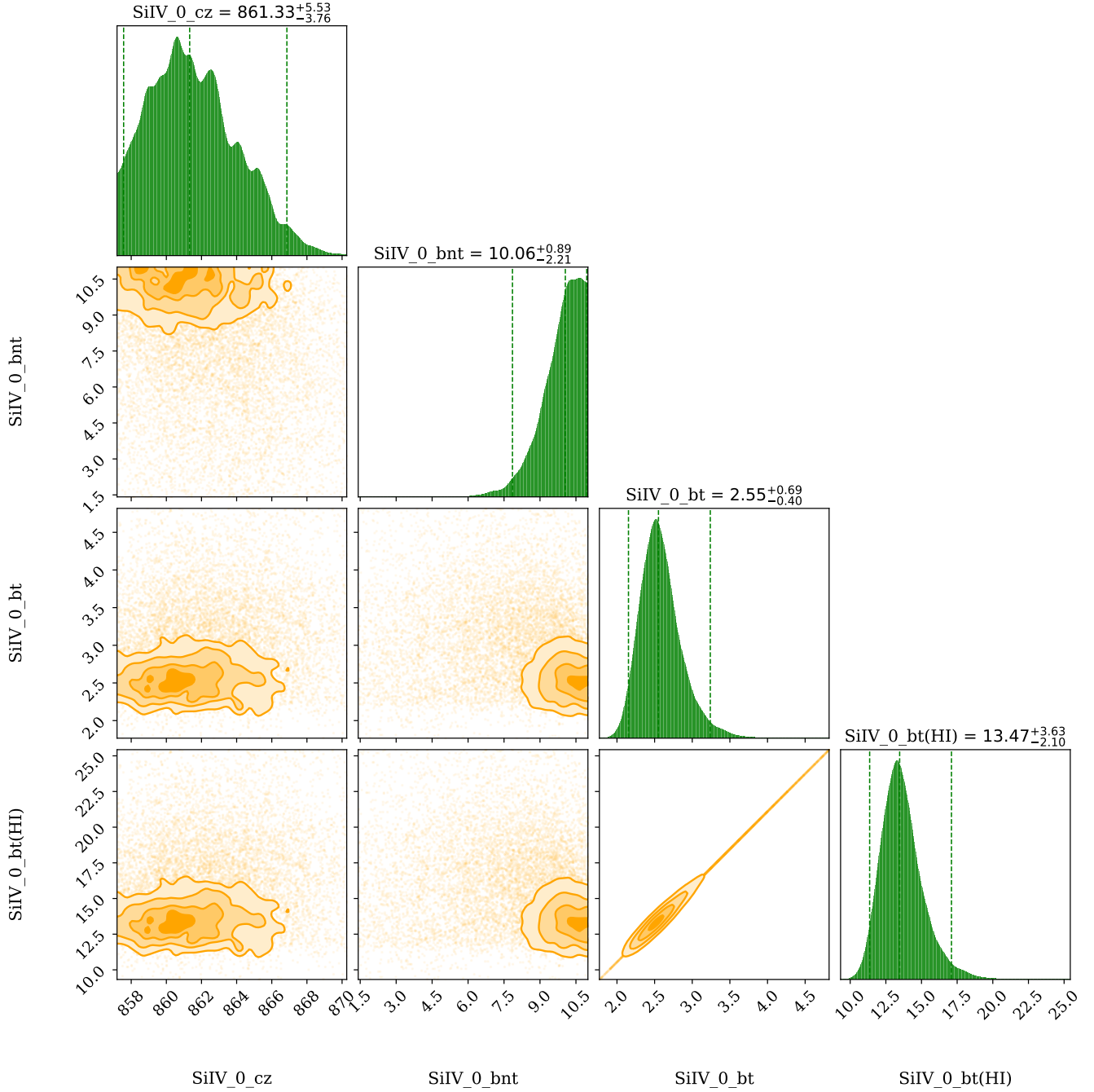


Figure G6. The corner plot showing the marginalized posterior distributions for the absorption centroid (z), non-thermal Doppler broadening (b_{nt}), thermal Doppler broadening (b_t), total Doppler broadening (b), of the phase traced by the Si iv cloud of the $z = 0.0027$ absorber towards SG. The over-plotted vertical lines in the posterior distribution span the 95% credible interval. The contours indicate 0.5 σ , 1 σ , 1.5 σ , and 2 σ levels. The model results are summarised in Table 3, and the synthetic profiles based on these models are shown in Figure 9.

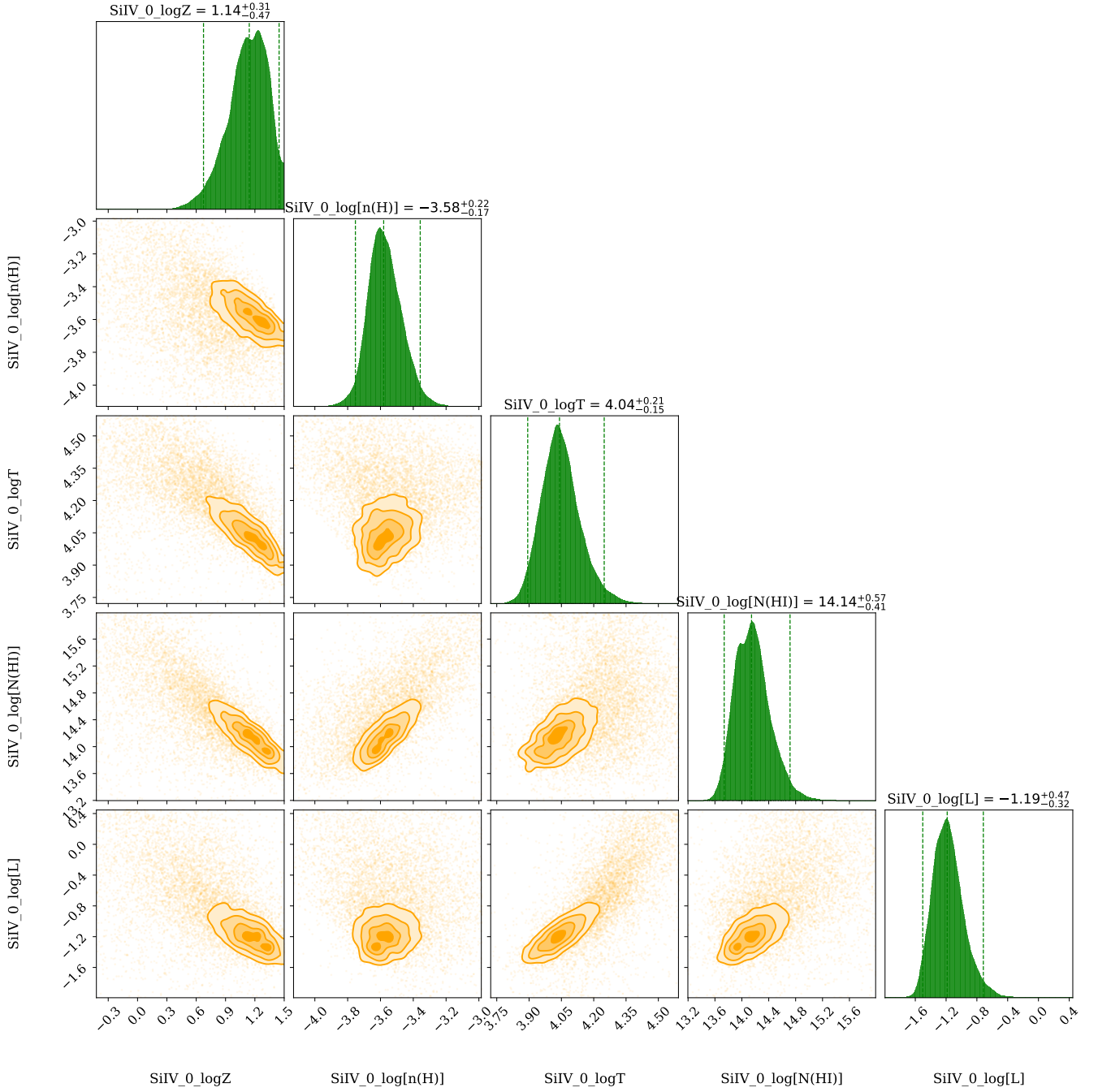


Figure G7. The corner plot showing the marginalized posterior distributions for the metallicity ($\log Z$), hydrogen number density ($\log n_H$), temperature ($\log T$), neutral hydrogen column density ($\log N(\text{H I})$), and the line of sight thickness ($\log L$), of the low ionization phase traced by the Si IV cloud of the $z = 0.0027$ absorber towards SG. The over-plotted vertical lines in the posterior distribution span the 95% credible interval. The contours indicate 0.5σ , 1σ , 1.5σ , and 2σ levels. The model results are summarised in Table 3, and the synthetic profiles based on these models are shown in Figure 9.

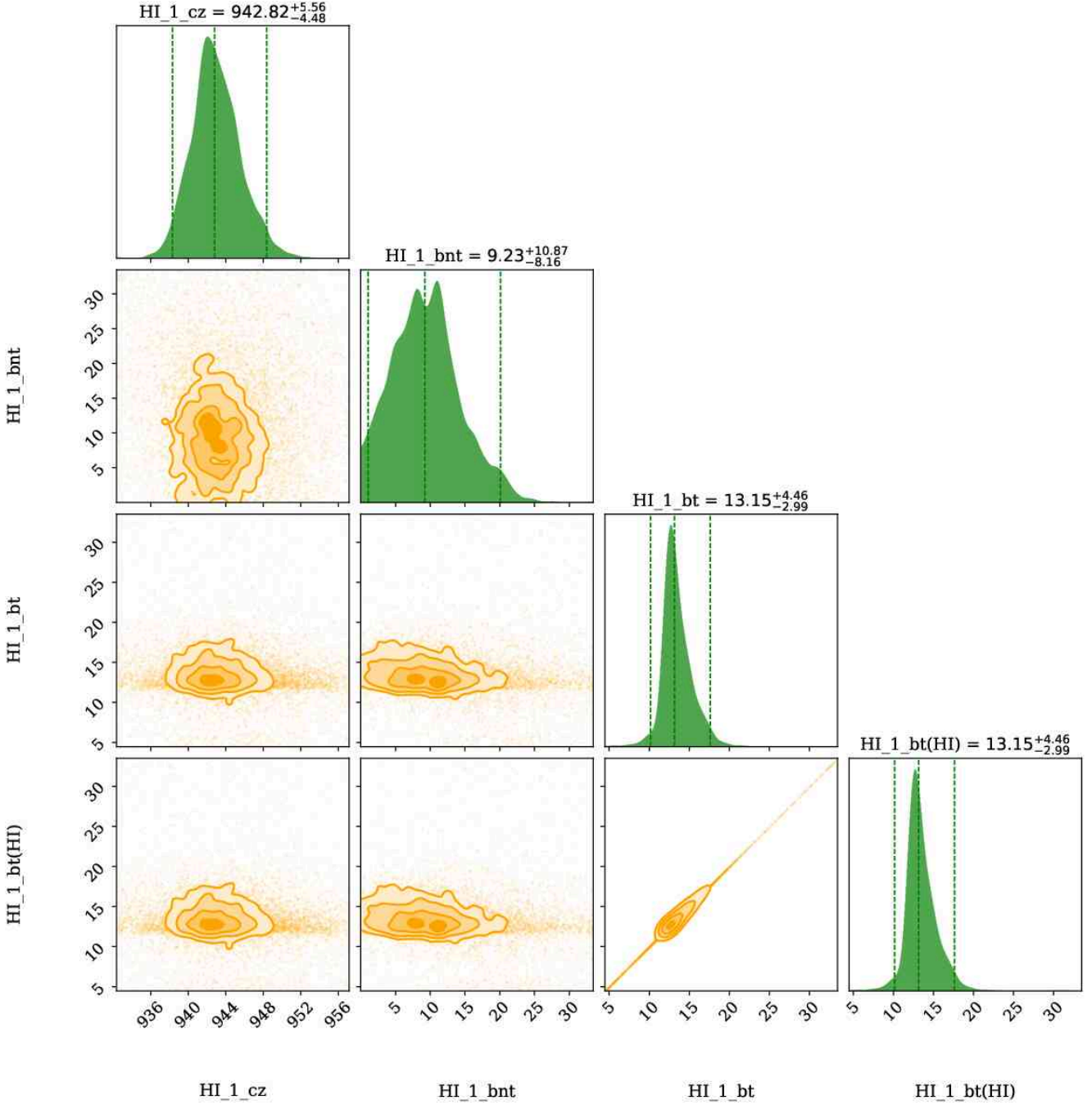


Figure G8. The corner plot showing the marginalized posterior distributions for the absorption centroid (z), non-thermal Doppler broadening (b_{nt}), thermal Doppler broadening (b_t), total Doppler broadening (b), of the phase traced by the blueward H I cloud of the $z = 0.0027$ absorber towards SG. The over-plotted vertical lines in the posterior distribution span the 95% credible interval. The contours indicate 0.5σ , 1σ , 1.5σ , and 2σ levels. The model results are summarised in Table 3, and the synthetic profiles based on these models are shown in Figure 9.

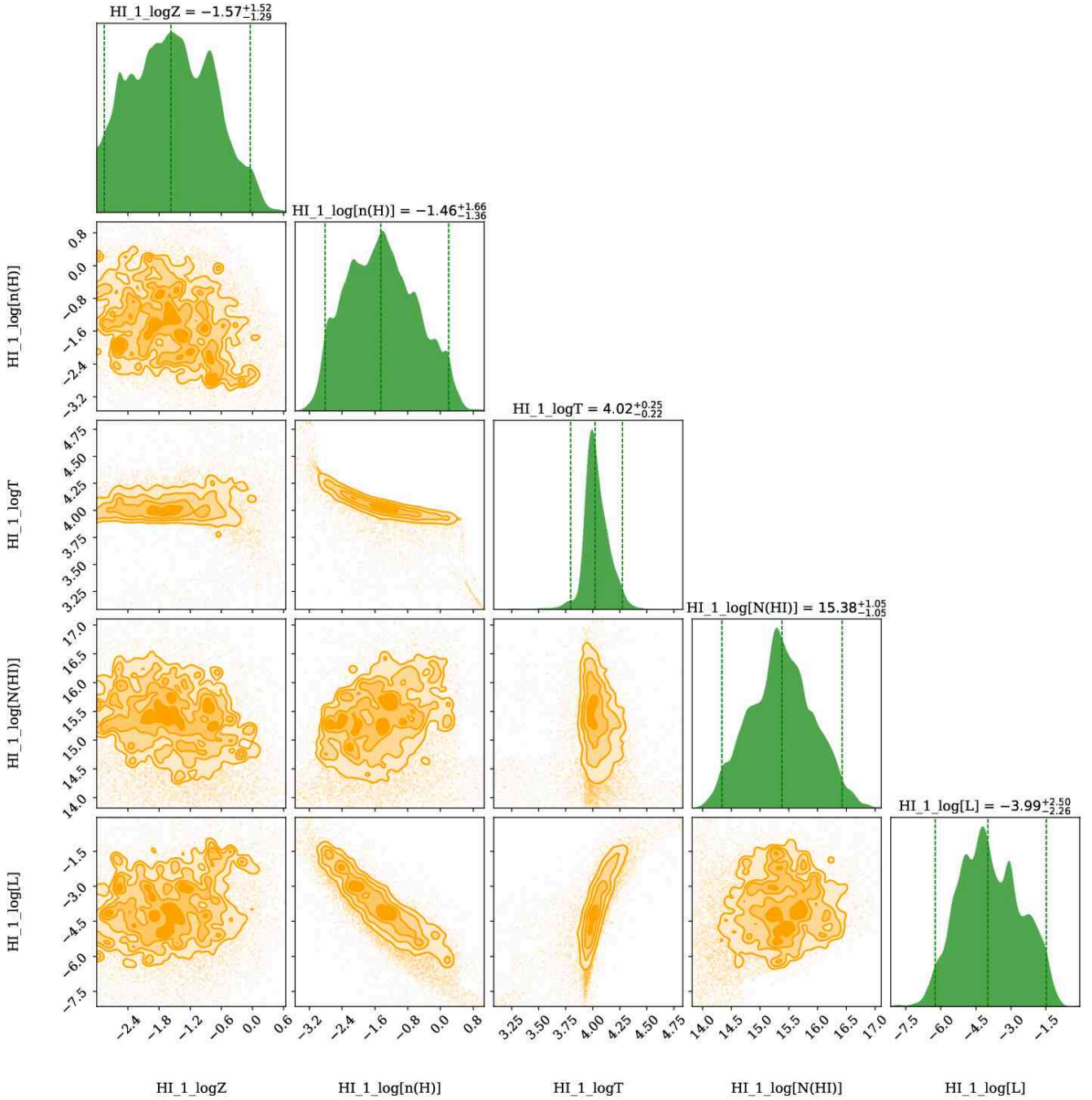


Figure G9. The corner plot showing the marginalized posterior distributions for the metallicity ($\log Z$), hydrogen number density ($\log n_H$), temperature ($\log T$), neutral hydrogen column density ($\log N(\text{H I})$), and the line of sight thickness ($\log L$), of the low ionization phase traced by the blueward H I cloud of the $z = 0.0027$ absorber towards SG. The over-plotted vertical lines in the posterior distribution span the 95% credible interval. The contours indicate 0.5σ , 1σ , 1.5σ , and 2σ levels. The model results are summarised in Table 3, and the synthetic profiles based on these models are shown in Figure 9.

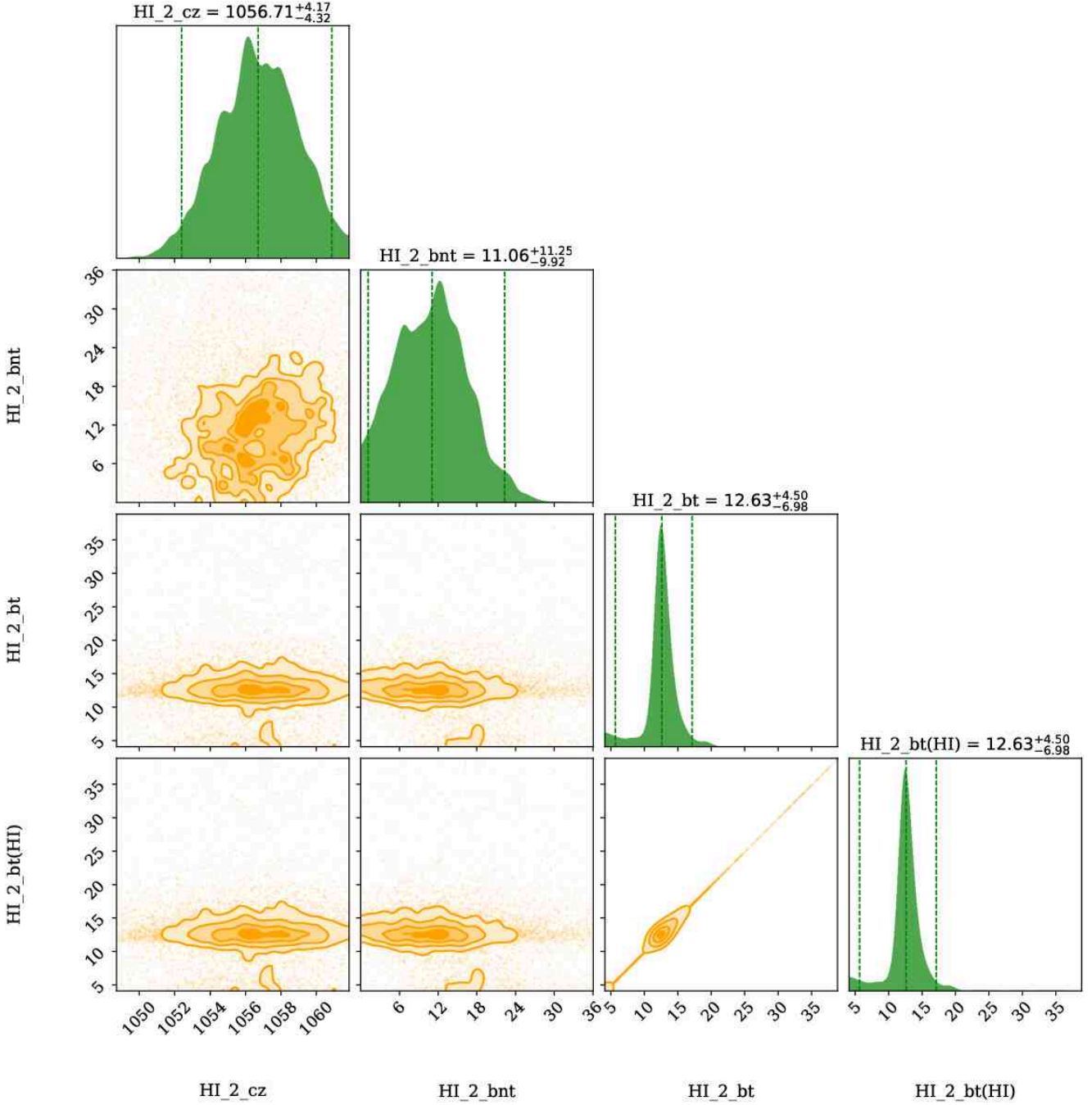


Figure G10. The corner plot showing the marginalized posterior distributions for the absorption centroid (z), non-thermal Doppler broadening (b_{nt}), thermal Doppler broadening (b_t), total Doppler broadening (b), of the phase traced by the central H I cloud of the $z = 0.0027$ absorber towards SG. The over-plotted vertical lines in the posterior distribution span the 95% credible interval. The contours indicate 0.5σ , 1σ , 1.5σ , and 2σ levels. The model results are summarised in Table 3, and the synthetic profiles based on these models are shown in Figure 9.

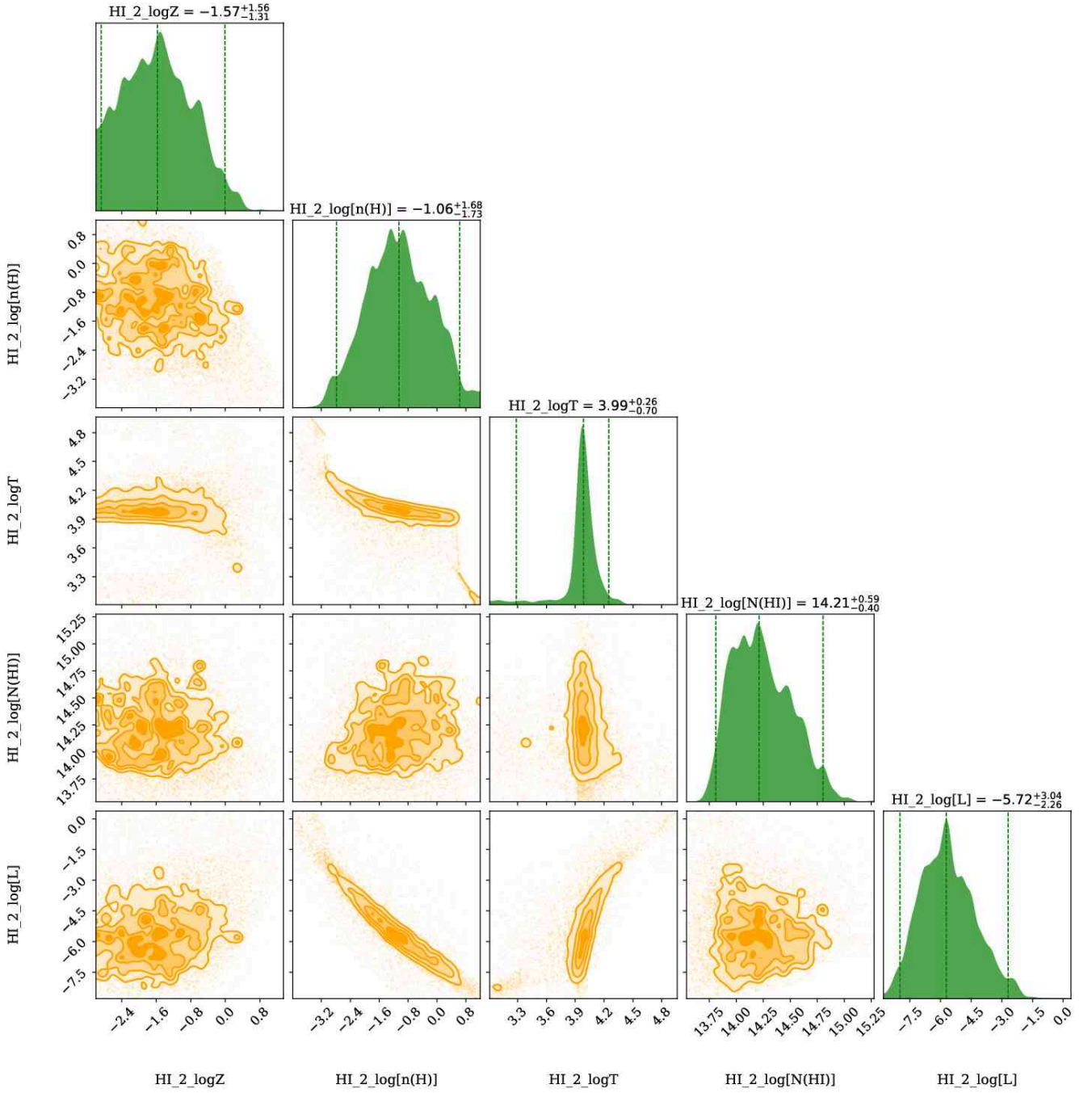


Figure G11. The corner plot showing the marginalized posterior distributions for the metallicity ($\log Z$), hydrogen number density ($\log n_H$), temperature ($\log T$), neutral hydrogen column density ($\log N(\text{H I})$), and the line of sight thickness ($\log L$), of the low ionization phase traced by the central H I cloud of the $z = 0.0027$ absorber towards SG. The over-plotted vertical lines in the posterior distribution span the 95% credible interval. The contours indicate 0.5σ , 1σ , 1.5σ , and 2σ levels. The model results are summarised in Table 3, and the synthetic profiles based on these models are shown in Figure 9.

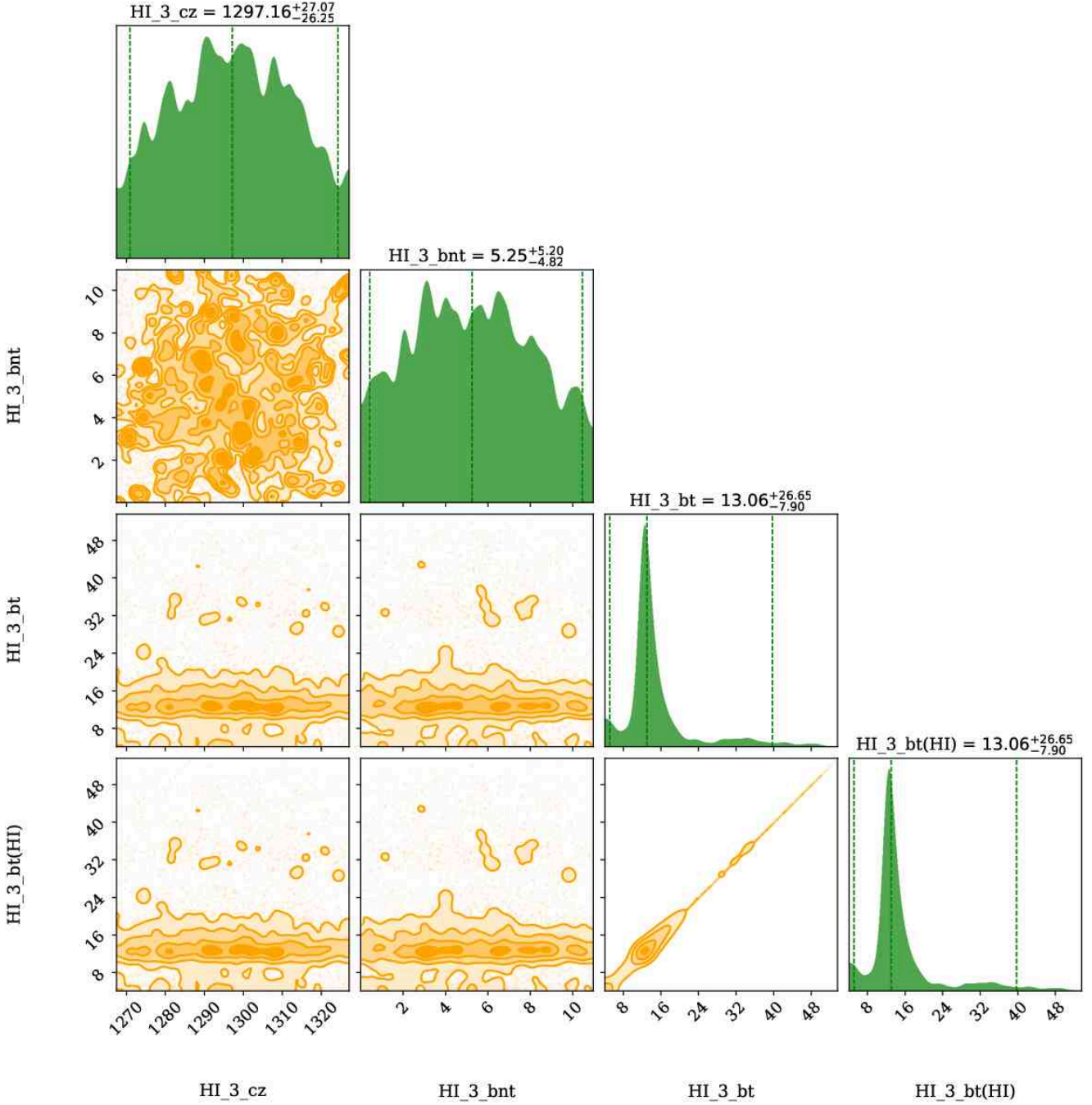


Figure G12. The corner plot showing the marginalized posterior distributions for the absorption centroid (z), non-thermal Doppler broadening (b_{nt}), thermal Doppler broadening (b_t), total Doppler broadening (b), of the phase traced by the redward H I cloud of the $z = 0.0027$ absorber towards SG. The over-plotted vertical lines in the posterior distribution span the 95% credible interval. The contours indicate 0.5σ , 1σ , 1.5σ , and 2σ levels. The model results are summarised in Table 3, and the synthetic profiles based on these models are shown in Figure 9.

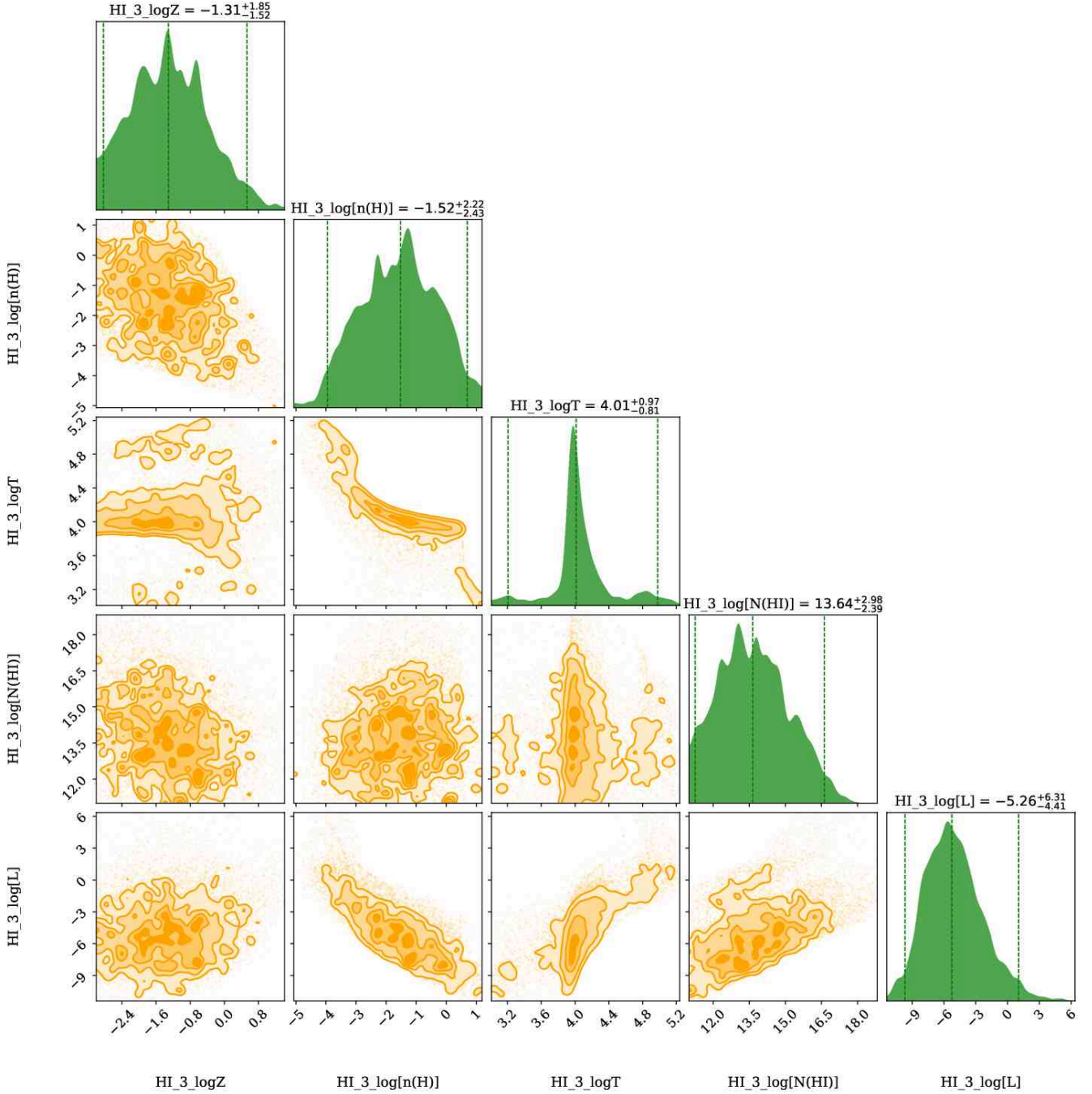


Figure G13. The corner plot showing the marginalized posterior distributions for the metallicity ($\log Z$), hydrogen number density ($\log n_{\text{H}}$), temperature ($\log T$), neutral hydrogen column density ($\log N(\text{H I})$), and the line of sight thickness ($\log L$), of the low ionization phase traced by the redward H I cloud of the $z = 0.0027$ absorber towards SG. The over-plotted vertical lines in the posterior distribution span the 95% credible interval. The contours indicate 0.5σ , 1σ , 1.5σ , and 2σ levels. The model results are summarised in Table 3, and the synthetic profiles based on these models are shown in Figure 9.

APPENDIX H: PLOTS FOR SH

- H1** Airglow template fit towards SH
- H2** Best VP fit to the Galactic $\text{Ly}\alpha$ towards SH
- H3** MC exploration of the zero-point uncertainty for SH
- H4** Posterior distributions for the absorber properties towards SH

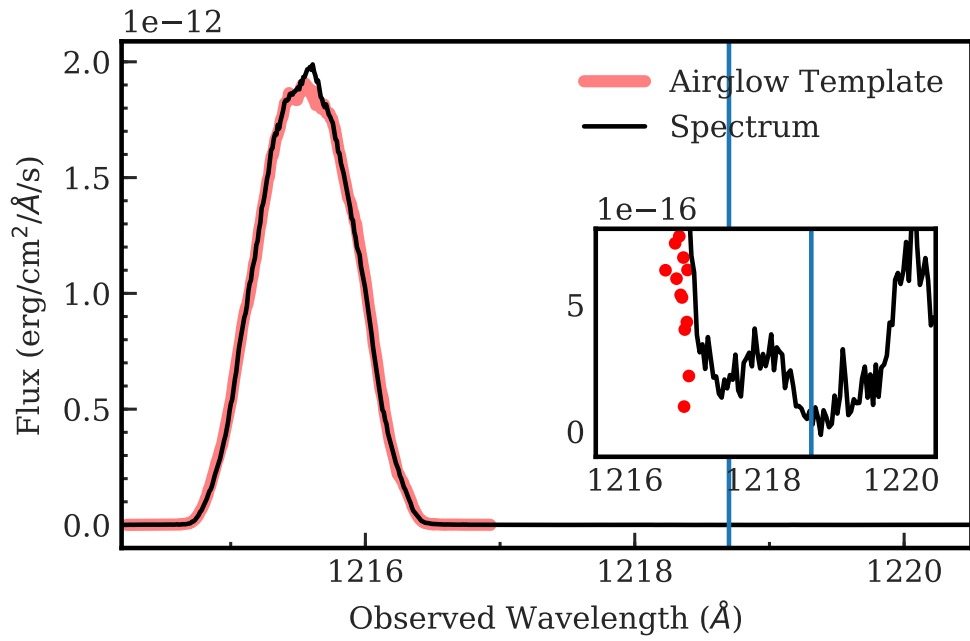


Figure H1. Same as in Figure B1, but for SH.

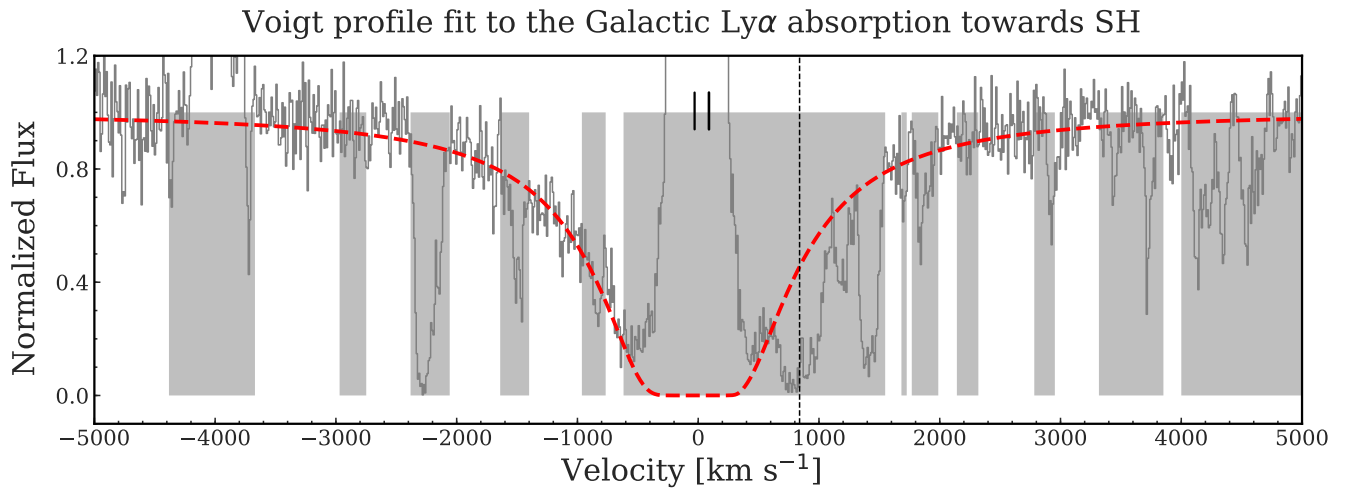


Figure H2. Same as in Figure B2, but for SH.

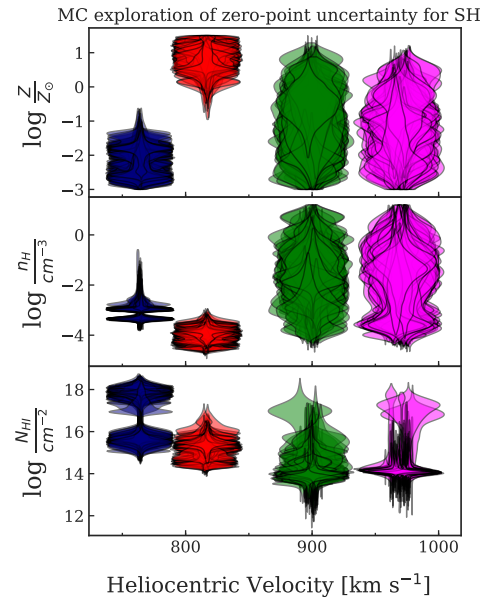


Figure H3. Violin plots showing the parameter distributions for 100 different realizations of the H I Ly α profile modified between 765–820 km s⁻¹ to account for the zero-point uncertainty. The blue violins show the parameters of blueward Si III phase. The red violins correspond to the redward Si III phase, the green and magenta violins correspond to the H I only phases.

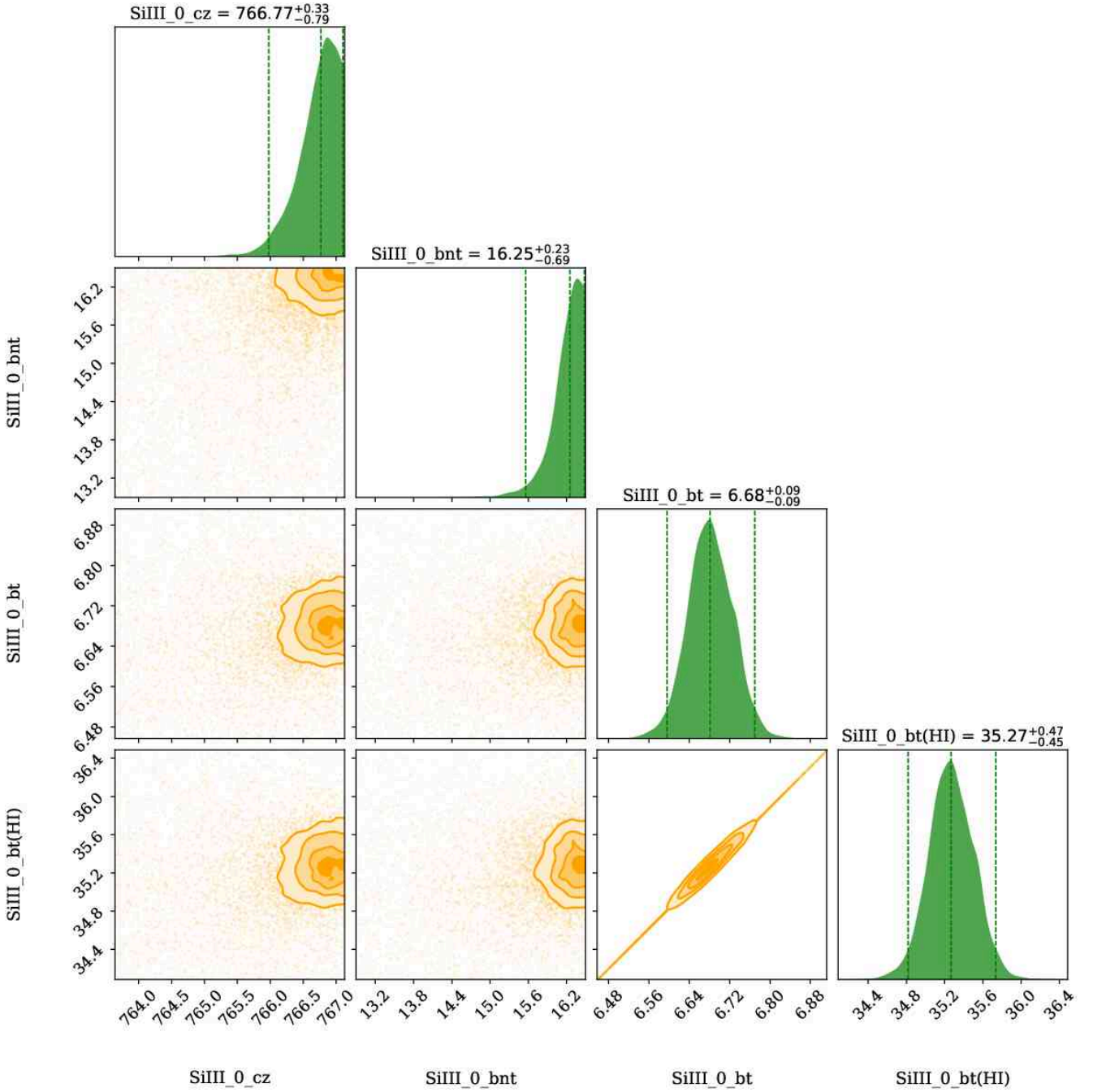


Figure H4. The corner plot showing the marginalized posterior distributions for the absorption centroid (z), non-thermal Doppler broadening (b_{nt}), thermal Doppler broadening (b_t), total Doppler broadening (b), of the phase traced by the blueward H I cloud of the $z = 0.0028$ absorber towards SH. The over-plotted vertical lines in the posterior distribution span the 95% credible interval. The contours indicate 0.5σ , 1σ , 1.5σ , and 2σ levels. The model results are summarised in Table 3, and the synthetic profiles based on these models are shown in Figure 10.

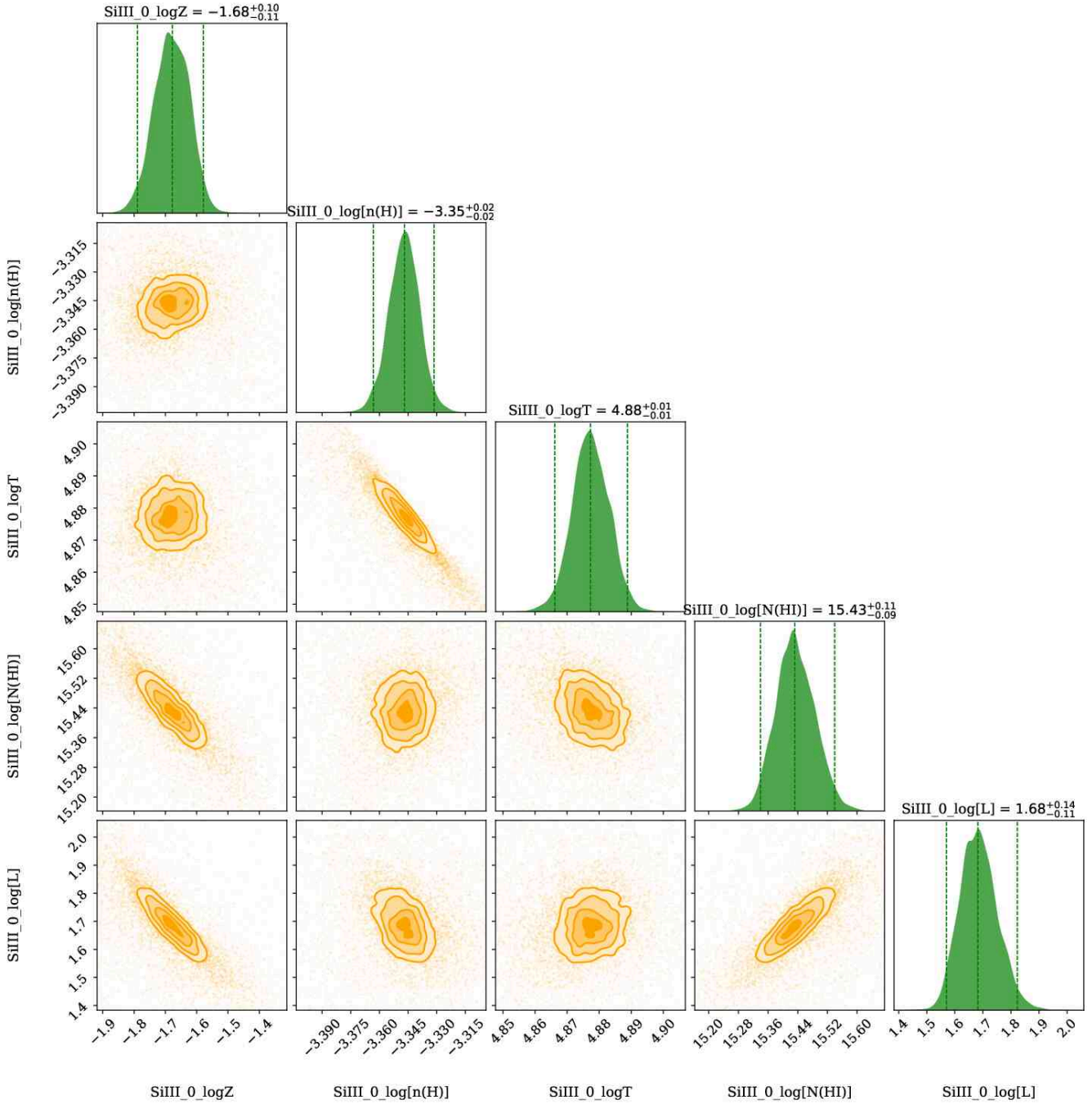


Figure H5. The corner plot showing the marginalized posterior distributions for the metallicity ($\log Z$), hydrogen number density ($\log n_H$), temperature ($\log T$), neutral hydrogen column density ($\log N(\text{H I})$), and the line of sight thickness ($\log L$), of the low ionization phase traced by the H I cloud of the $z = 0.0028$ absorber towards SH. The over-plotted vertical lines in the posterior distribution span the 95% credible interval. The contours indicate 0.5σ , 1σ , 1.5σ , and 2σ levels. The model results are summarised in Table 3, and the synthetic profiles based on these models are shown in Figure 10.

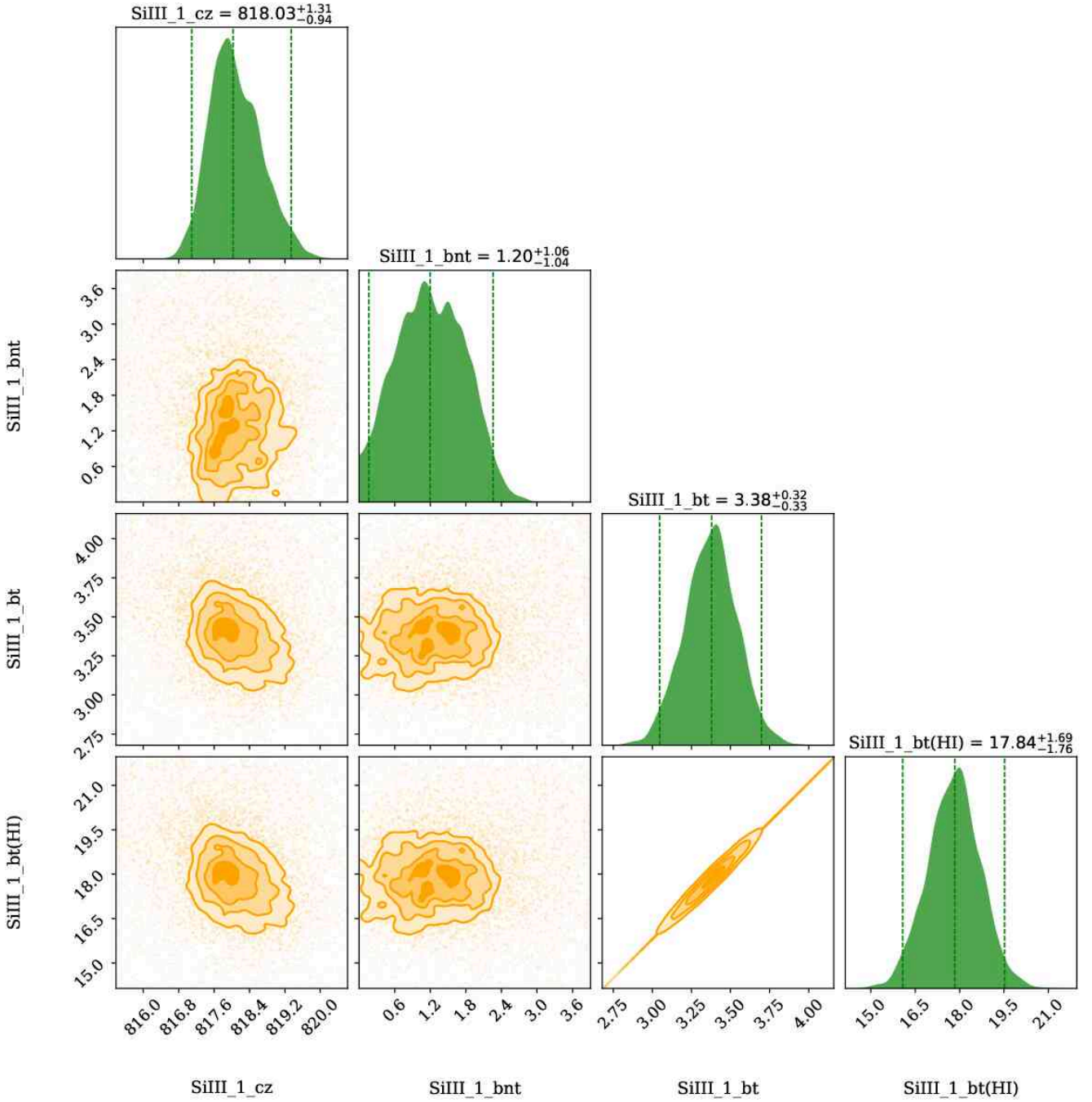


Figure H6. The corner plot showing the marginalized posterior distributions for the absorption centroid (z), non-thermal Doppler broadening (b_{nt}), thermal Doppler broadening (b_t), total Doppler broadening (b), of the phase traced by the blueward H I cloud of the $z = 0.0028$ absorber towards SH. The over-plotted vertical lines in the posterior distribution span the 95% credible interval. The contours indicate 0.5 σ , 1 σ , 1.5 σ , and 2 σ levels. The model results are summarised in Table 3, and the synthetic profiles based on these models are shown in Figure 10.

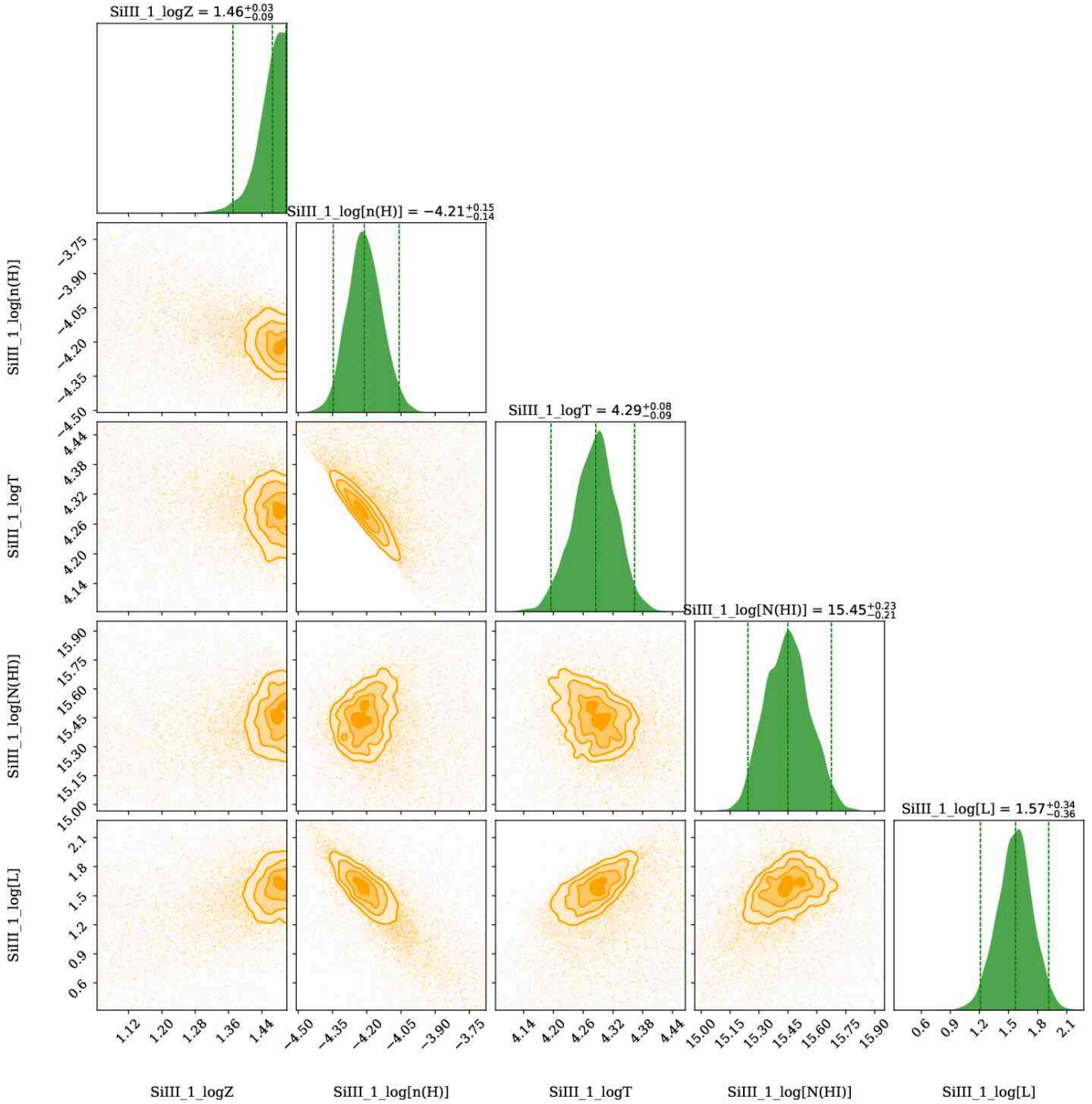


Figure H7. The corner plot showing the marginalized posterior distributions for the metallicity ($\log Z$), hydrogen number density ($\log n_H$), temperature ($\log T$), neutral hydrogen column density ($\log N(\text{H I})$), and the line of sight thickness ($\log L$), of the low ionization phase traced by the H I cloud of the $z = 0.0028$ absorber towards SH. The over-plotted vertical lines in the posterior distribution span the 95% credible interval. The contours indicate 0.5σ , 1σ , 1.5σ , and 2σ levels. The model results are summarised in Table 3, and the synthetic profiles based on these models are shown in Figure 10.

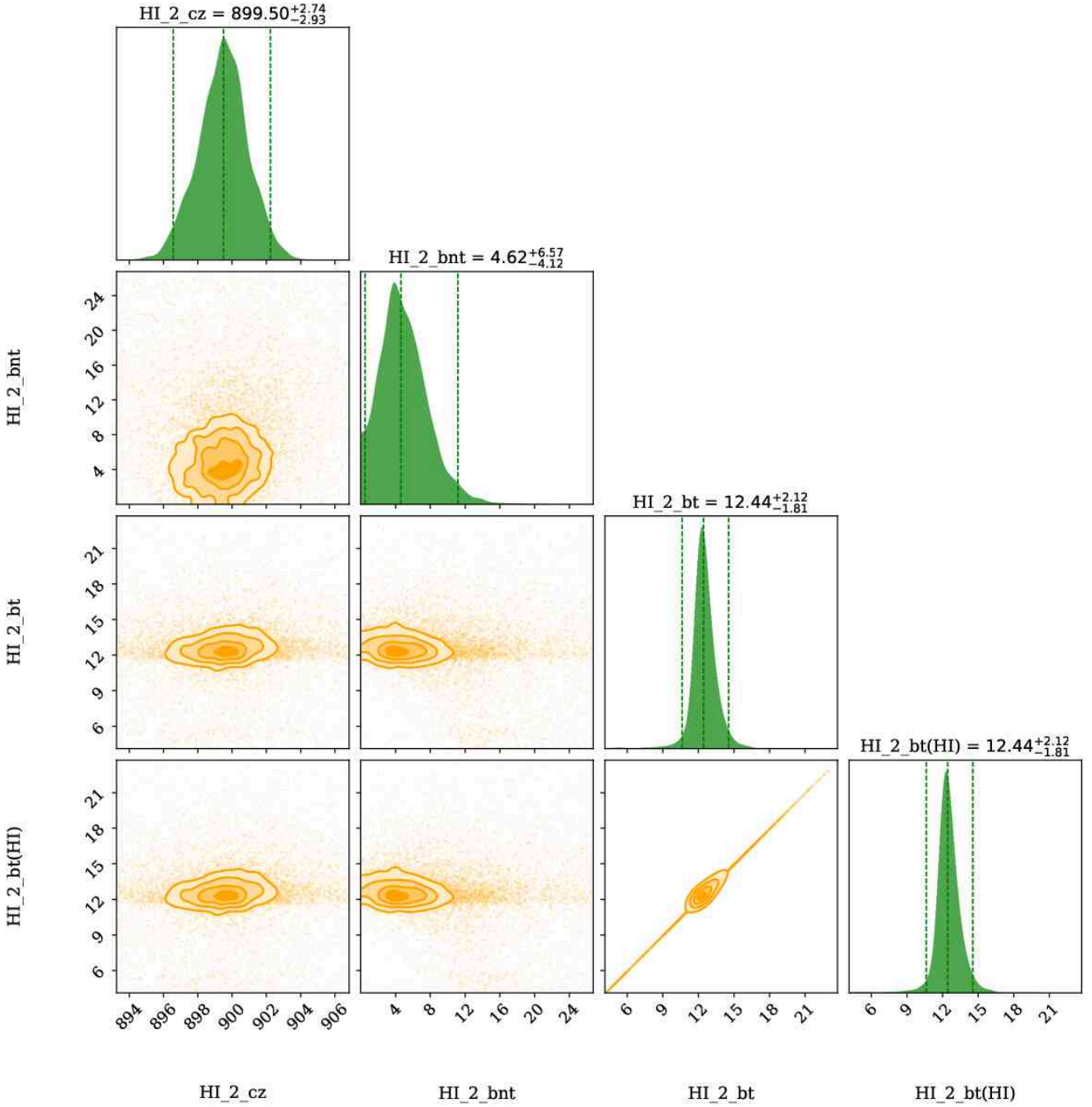


Figure H8. The corner plot showing the marginalized posterior distributions for the absorption centroid (z), non-thermal Doppler broadening (b_{nt}), thermal Doppler broadening (b_r), total Doppler broadening (b), of the phase traced by the middle redward H I cloud of the $z = 0.0028$ absorber towards SH. The over-plotted vertical lines in the posterior distribution span the 95% credible interval. The contours indicate 0.5σ , 1σ , 1.5σ , and 2σ levels. The model results are summarised in Table 3, and the synthetic profiles based on these models are shown in Figure 10.

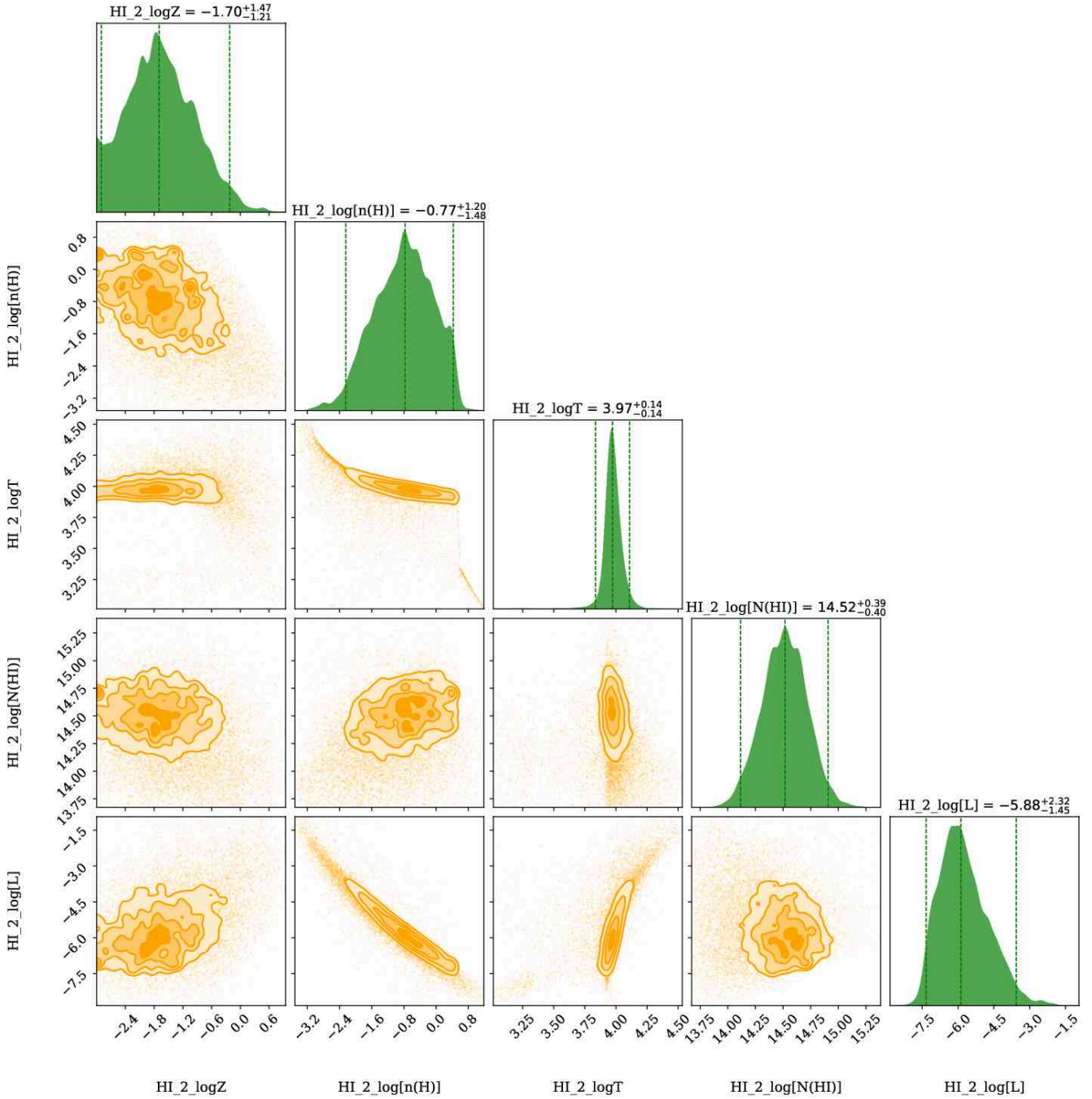


Figure H9. The corner plot showing the marginalized posterior distributions for the metallicity ($\log Z$), hydrogen number density ($\log n_{\text{H}}$), temperature ($\log T$), neutral hydrogen column density ($\log N(\text{H I})$), and the line of sight thickness ($\log L$), of the low ionization phase traced by the middle redward H I cloud of the $z = 0.0028$ absorber towards SH. The over-plotted vertical lines in the posterior distribution span the 95% credible interval. The contours indicate 0.5σ , 1σ , 1.5σ , and 2σ levels. The model results are summarised in Table 3, and the synthetic profiles based on these models are shown in Figure 10.

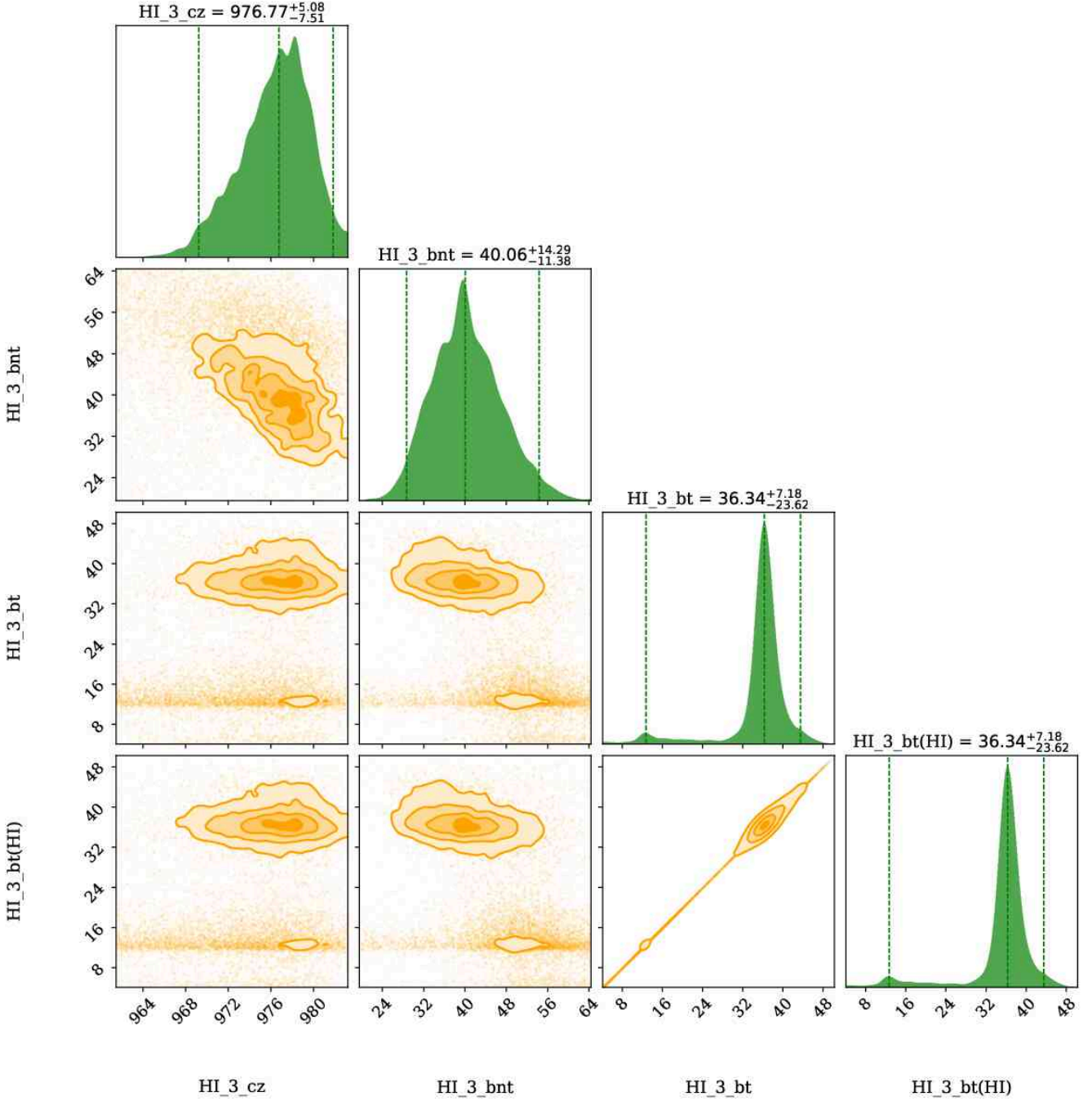


Figure H10. The corner plot showing the marginalized posterior distributions for the absorption centroid (z), non-thermal Doppler broadening (b_{nt}), thermal Doppler broadening (b_t), total Doppler broadening (b), of the phase traced by the redward H I cloud of the $z = 0.0028$ absorber towards SH. The over-plotted vertical lines in the posterior distribution span the 95% credible interval. The contours indicate 0.5σ , 1σ , 1.5σ , and 2σ levels. The model results are summarised in Table 3, and the synthetic profiles based on these models are shown in Figure 10.

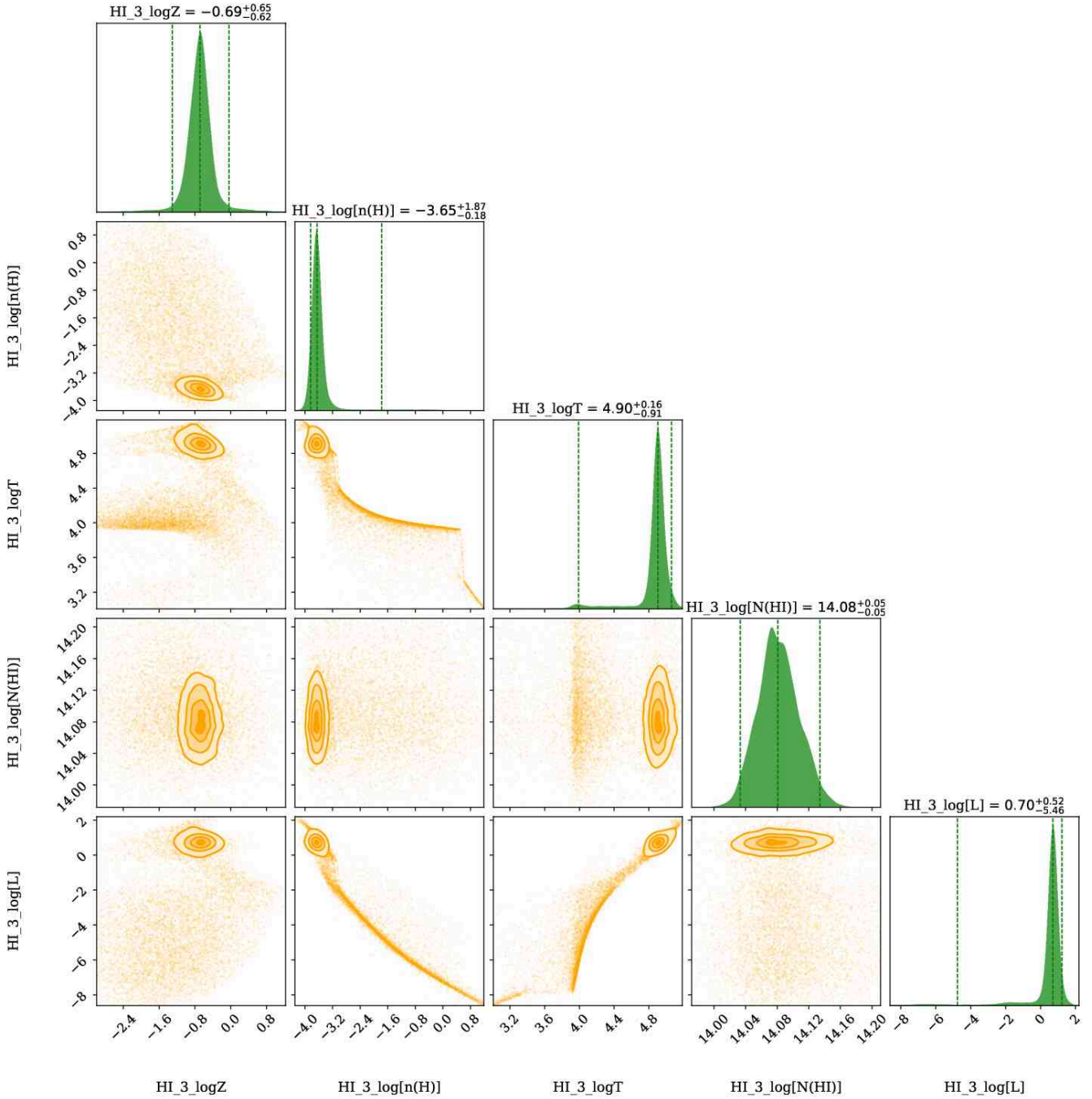


Figure H11. The corner plot showing the marginalized posterior distributions for the metallicity ($\log Z$), hydrogen number density ($\log n_H$), temperature ($\log T$), neutral hydrogen column density ($\log N(\text{H I})$), and the line of sight thickness ($\log L$), of the low ionization phase traced by the redward H I cloud of the $z = 0.0028$ absorber towards SH. The over-plotted vertical lines in the posterior distribution span the 95% credible interval. The contours indicate 0.5 σ , 1 σ , 1.5 σ , and 2 σ levels. The model results are summarised in Table 3, and the synthetic profiles based on these models are shown in Figure 10.

APPENDIX I: PLOTS FOR SI

I1 Airglow template fit towards SI

I2 Best VP fit to the Galactic Ly α towards SI

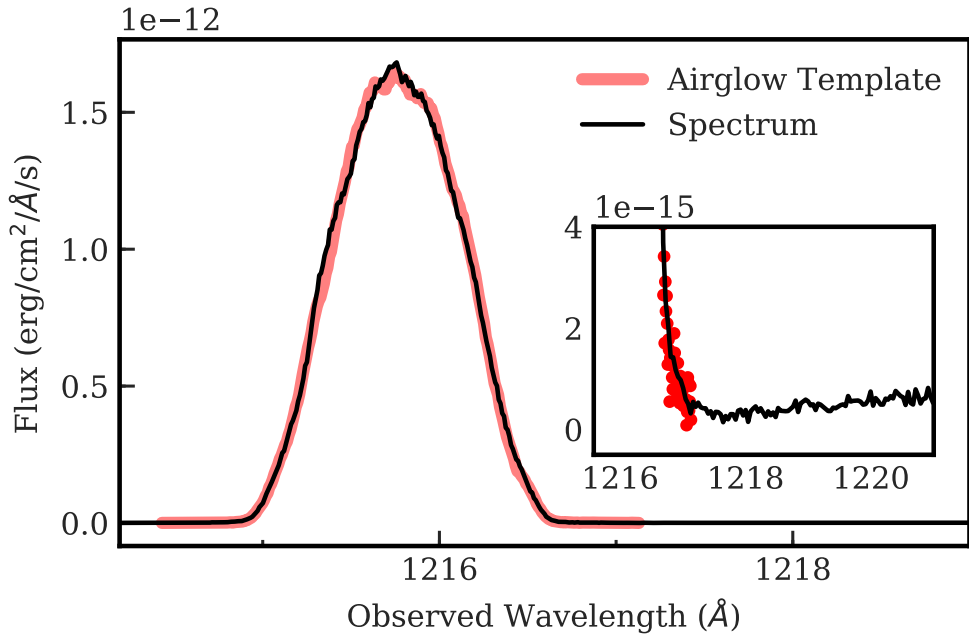


Figure 11. Same as in Figure B1, but for SI.

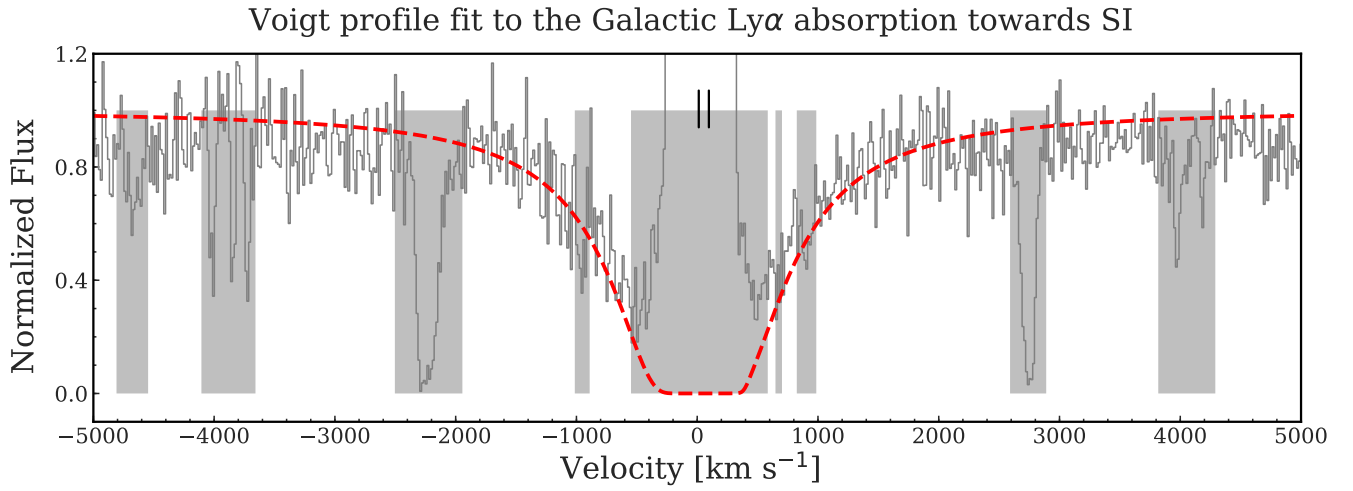


Figure 12. Same as in Figure B2, but for SI.

APPENDIX J: PLOTS FOR SJ

- J1** Airglow template fit towards SJ
- J2** Best VP fit to the Galactic Ly α towards SJ
- J3** Posterior distributions for the absorber properties towards SJ

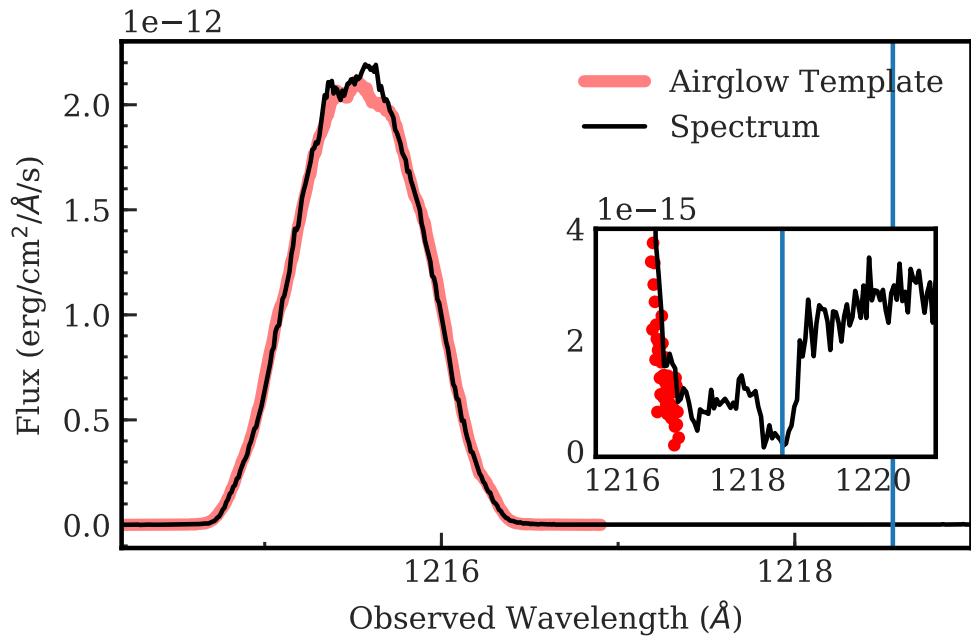


Figure J1. Same as in Figure B1, but for SJ.

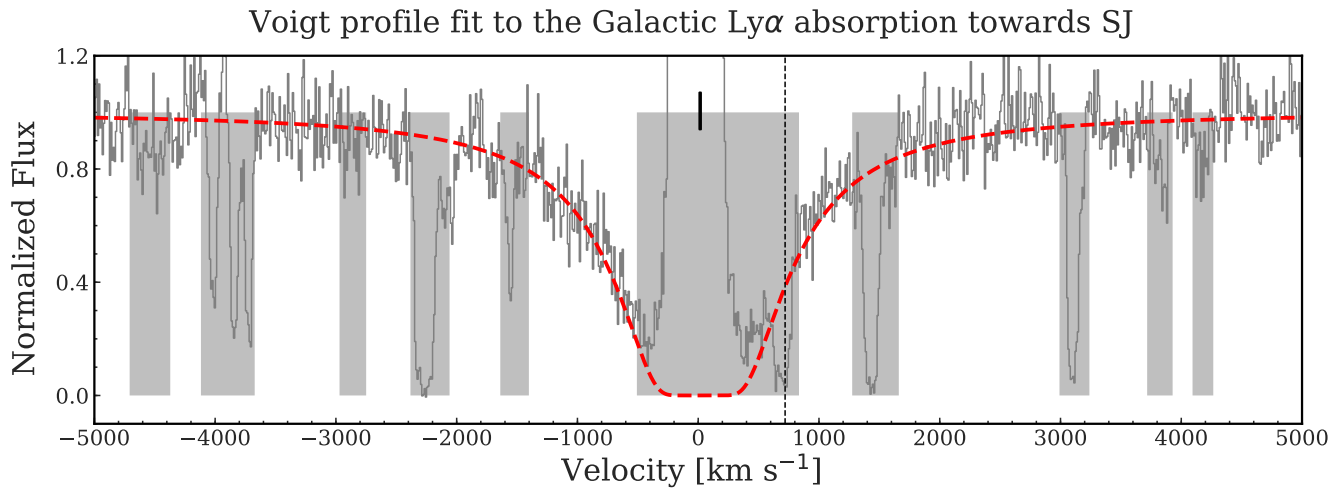


Figure J2. Same as in Figure B2, but for SJ.

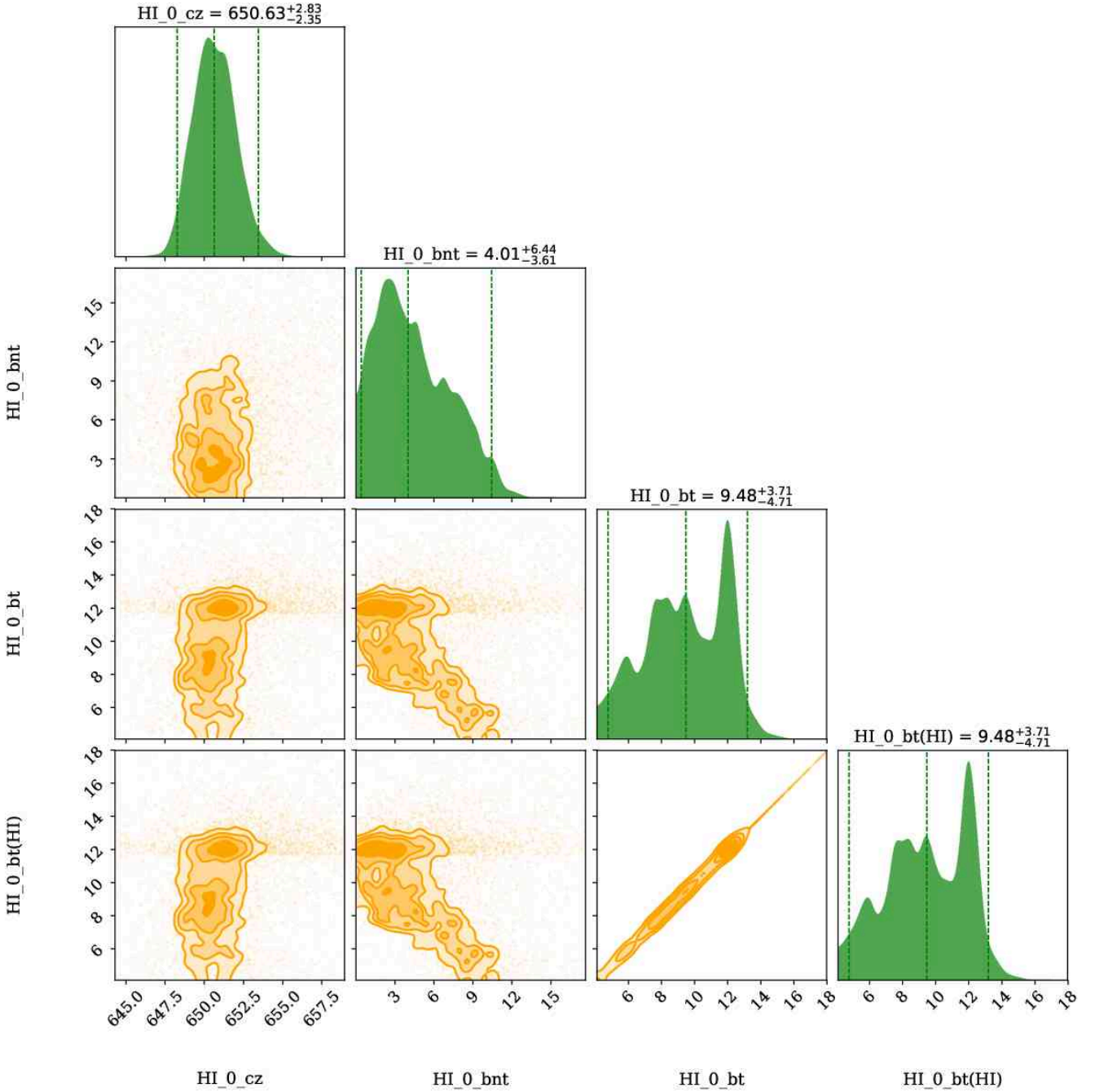


Figure J3. The corner plot showing the marginalized posterior distributions for the absorption centroid (z), non-thermal Doppler broadening (b_{nt}), thermal Doppler broadening (b_t), total Doppler broadening (b), of the phase traced by the blueward cloud of the $z = 0.0024$ absorber towards SJ. The over-plotted vertical lines in the posterior distribution span the 95% credible interval. The contours indicate 0.5σ , 1σ , 1.5σ , and 2σ levels. The model results are summarised in Table 3, and the synthetic profiles based on these models are shown in Figure 12

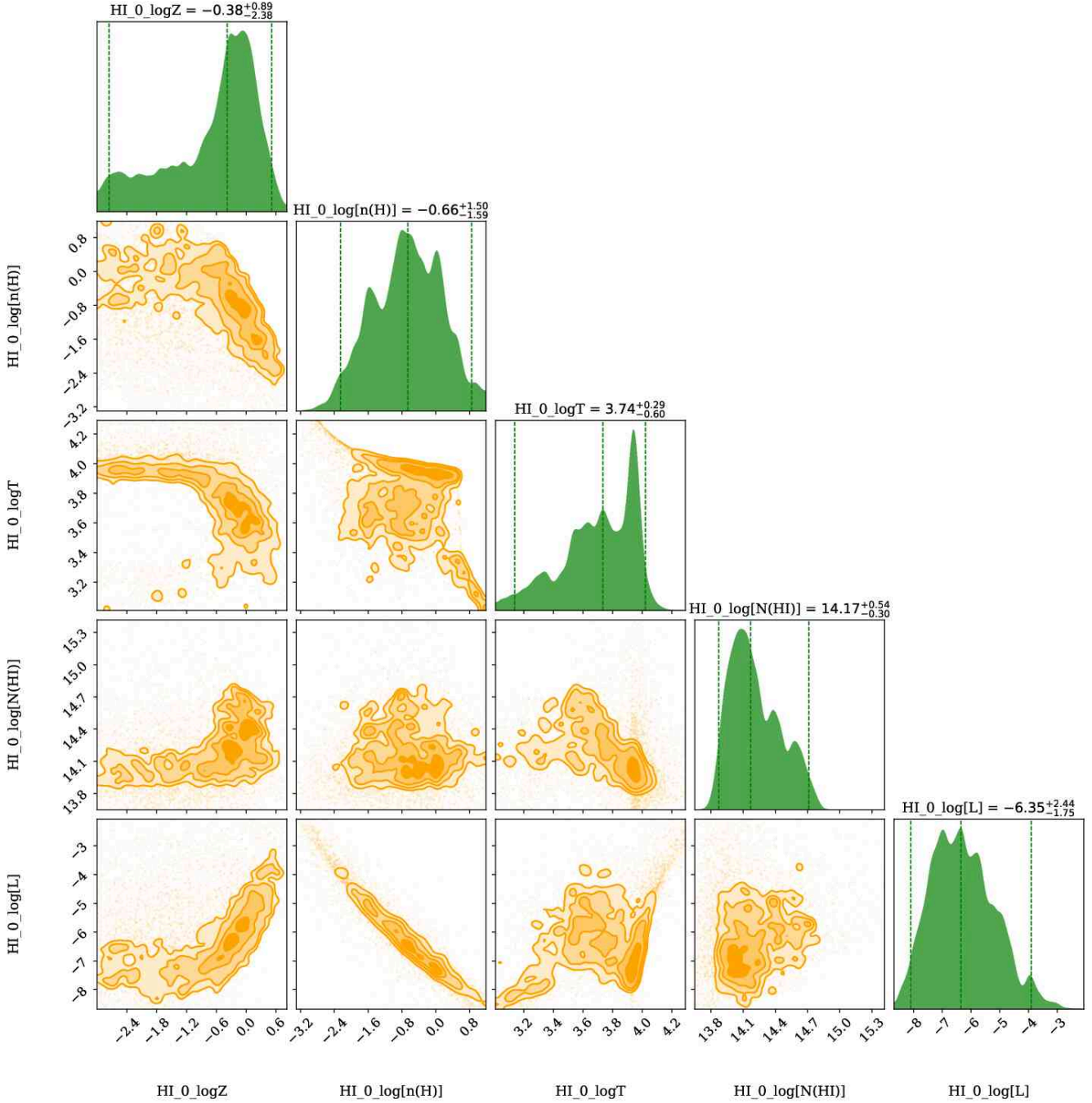


Figure J4. The corner plot showing the marginalized posterior distributions for the metallicity ($\log Z$), hydrogen number density ($\log n_H$), temperature ($\log T$), neutral hydrogen column density ($\log N(\text{H I})$), and the line of sight thickness ($\log L$), of the phase traced by the blueward cloud of the $z = 0.0024$ absorber towards SJ. The over-plotted vertical lines in the posterior distribution span the 95% credible interval. The contours indicate 0.5σ , 1σ , 1.5σ , and 2σ levels. The model results are summarised in Table 3, and the synthetic profiles based on these models are shown in Figure 12.

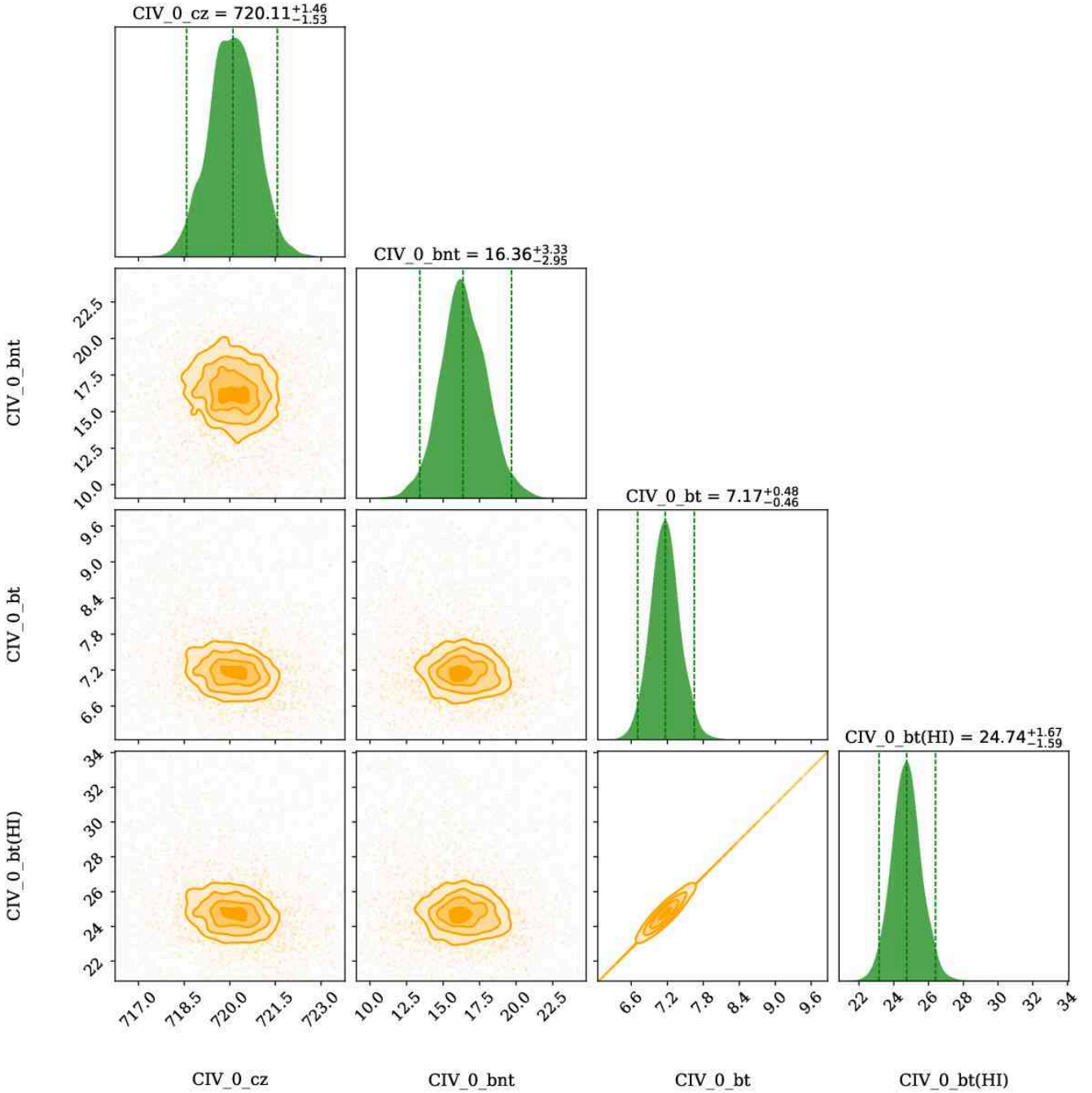


Figure J5. The corner plot showing the marginalized posterior distributions for the absorption centroid (z), non-thermal Doppler broadening (b_{nt}), thermal Doppler broadening (b_t), total Doppler broadening (b), of the phase traced by the redward C IV cloud of the $z = 0.0024$ absorber towards SJ. The over-plotted vertical lines in the posterior distribution span the 95% credible interval. The contours indicate 0.5 σ , 1 σ , 1.5 σ , and 2 σ levels. The model results are summarised in Table 3, and the synthetic profiles based on these models are shown in Figure 12.

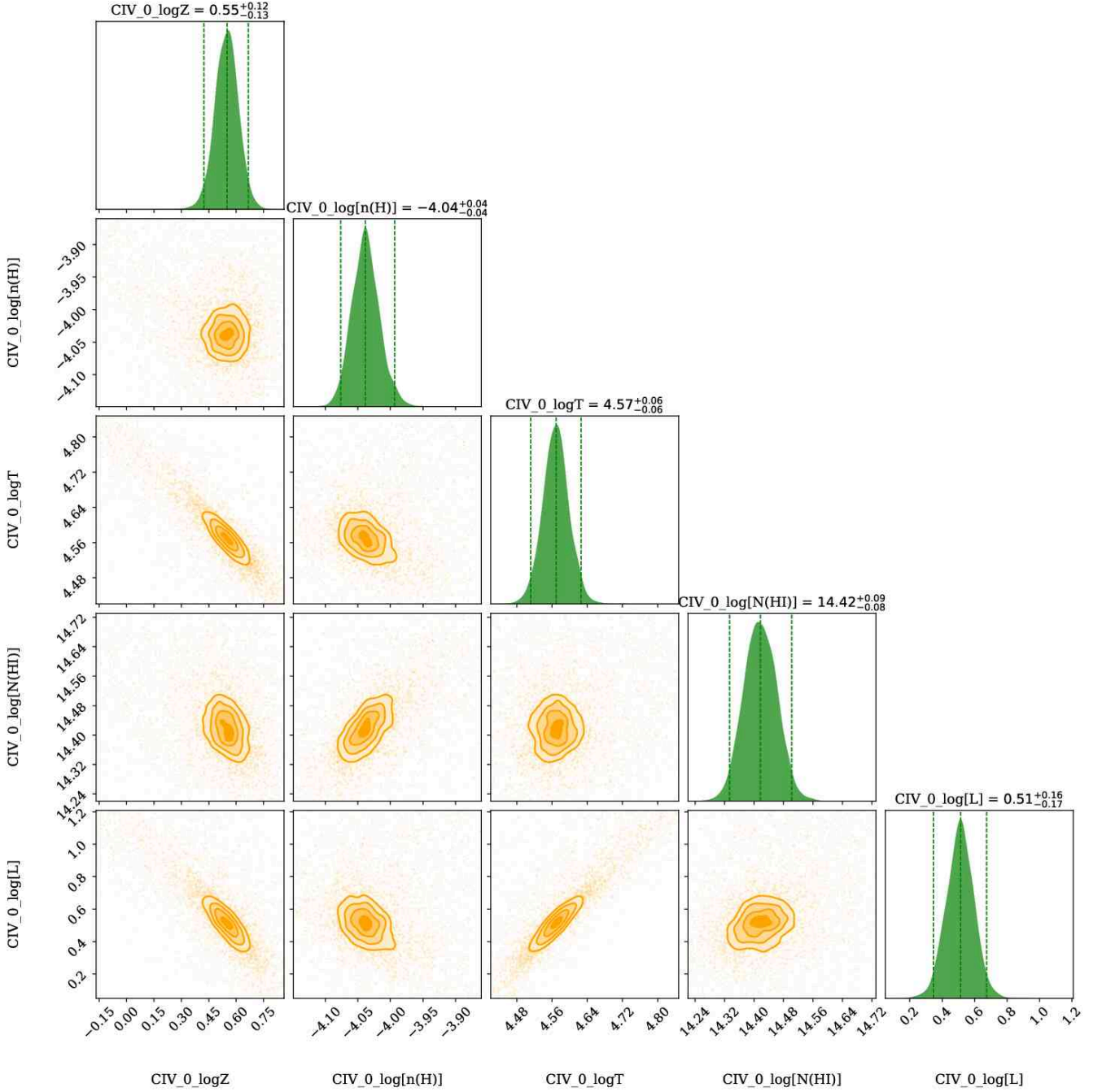


Figure J6. The corner plot showing the marginalized posterior distributions for the metallicity ($\log Z$), hydrogen number density ($\log n_H$), temperature ($\log T$), neutral hydrogen column density ($\log N(\text{HI})$), and the line of sight thickness ($\log L$), of the phase traced by the redward CIV cloud of the $z = 0.0024$ absorber towards SJ. The over-plotted vertical lines in the posterior distribution span the 95% credible interval. The contours indicate 0.5 σ , 1 σ , 1.5 σ , and 2 σ levels. The model results are summarised in Table 3, and the synthetic profiles based on these models are shown in Figure 12.

APPENDIX K: PLOTS FOR SK

K1 Airglow template fit towards SK

K2 Best VP fit to the Galactic $\text{Ly}\alpha$ towards SK

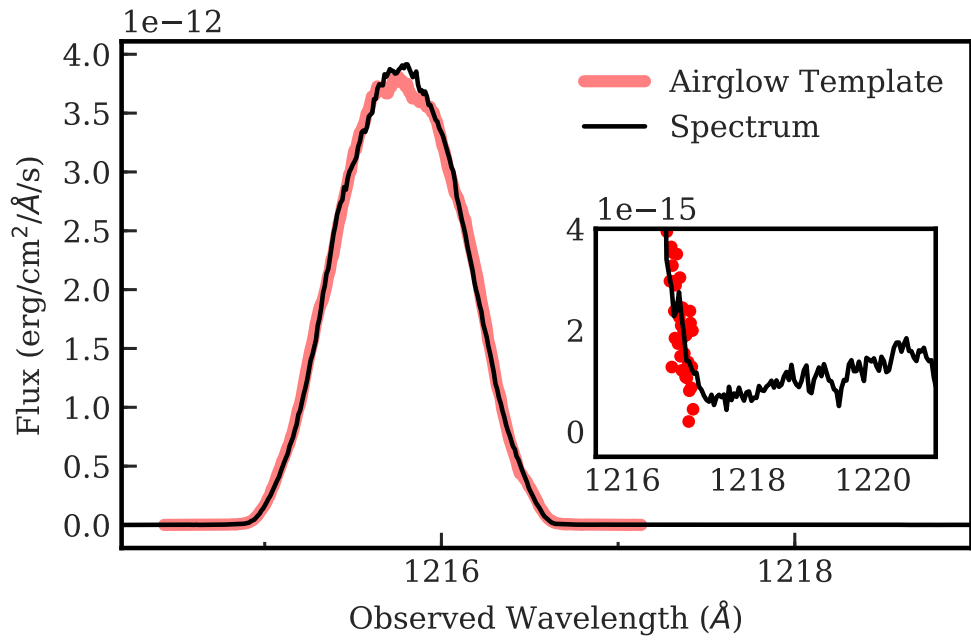


Figure K1. Same as in Figure B1, but for SK.

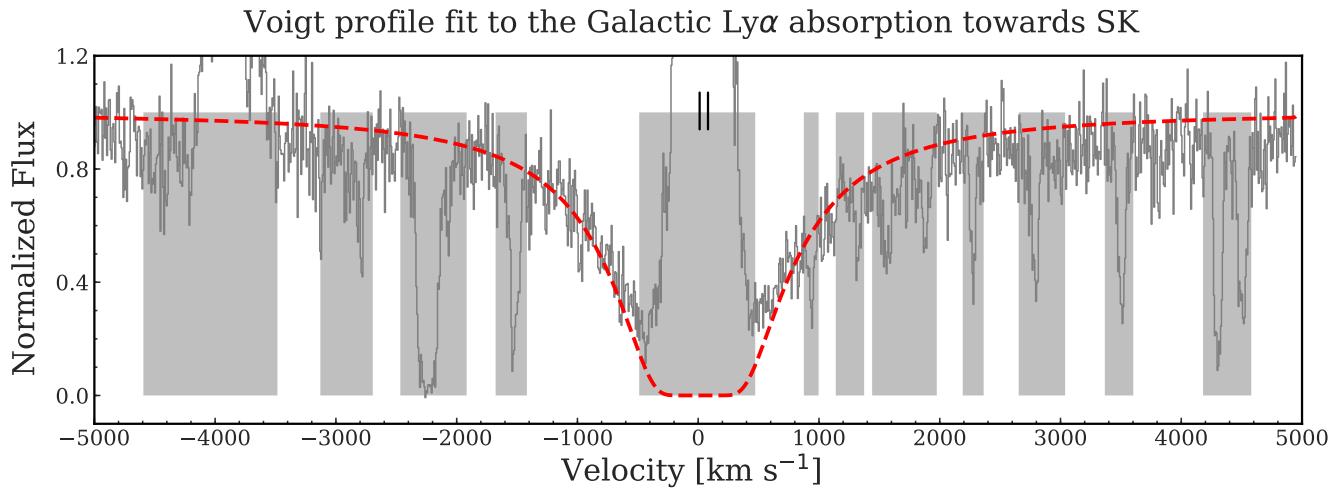


Figure K2. Same as in Figure B2, but for SK.

APPENDIX L: PLOTS FOR SL

L1 Airglow template fit towards SL

L2 Best VP fit to the Galactic Ly α towards SL

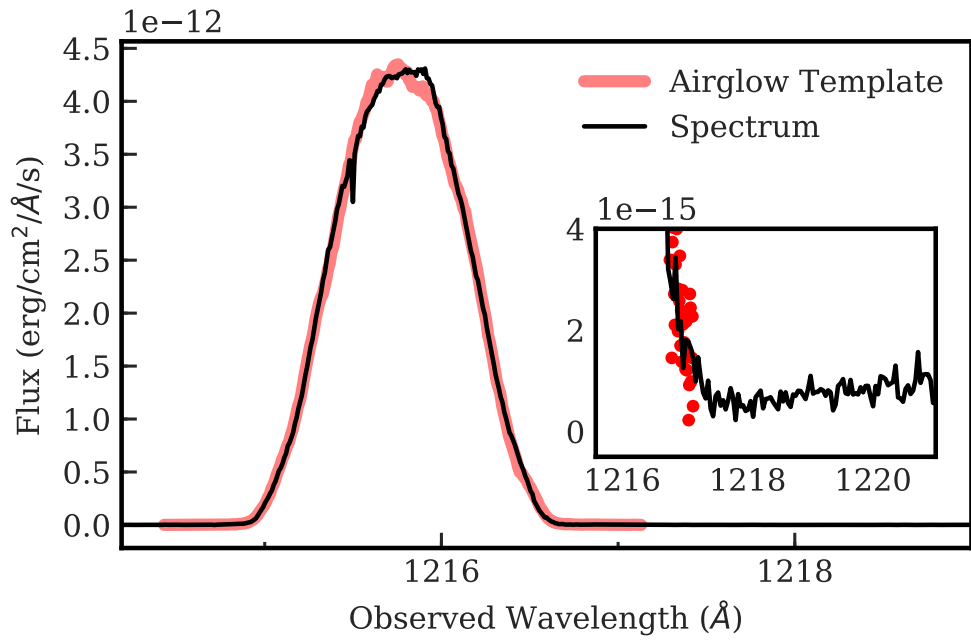


Figure L1. Same as in Figure B1, but for SL.

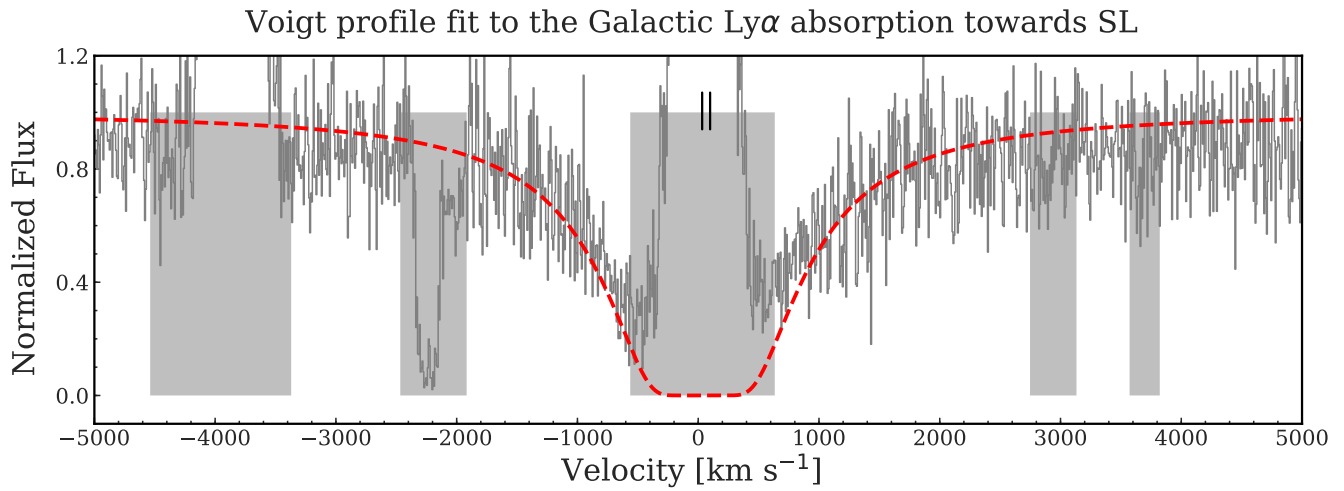


Figure L2. Same as in Figure B2, but for SL.

**APPENDIX M: COLUMN DENSITIES AND TOTAL
DOPPLER BROADENING PARAMETER
MEASUREMENTS**

In this section we present the column densities and total Doppler broadening parameter for various ions of interest across all model components, and along all the different sightlines.

Ion	b	$\log \frac{N}{\text{cm}^{-2}}$	Ion	b	$\log \frac{N}{\text{cm}^{-2}}$	Ion	b	$\log \frac{N}{\text{cm}^{-2}}$	Ion	b	$\log \frac{N}{\text{cm}^{-2}}$
(1)	(2)	(3)	(1)	(2)	(3)	(1)	(2)	(3)	(1)	(2)	(3)
SB	H_{I_0}	722.1 ^{+1.9} _{-1.6}	SC ^a	N_{v_0}	710.0 ^{+2.9} _{-3.5}	SC ^a	Si_{iv_1}	716.4 ^{+0.2} _{-0.3}	SC ^a	C_{ii_1}	878.6 ^{+0.8} _{-1.0}
Al II	4.6 ^{+11.5} _{-2.1}	9.3 ^{+1.2} _{-2.5}	Al II	50.7 ^{+4.5} _{-4.4}	10.5 ^{+0.1} _{-0.1}	Al II	15.0 ^{+0.8} _{-0.6}	13.6 ^{+0.0} _{-0.0}	Al II	4.5 ^{+1.7} _{-1.0}	12.1 ^{+0.2} _{-0.2}
C I	5.4 ^{+10.8} _{-1.9}	9.8 ^{+1.6} _{-2.1}	C I	51.0 ^{+4.4} _{-4.4}	10.8 ^{+0.2} _{-0.3}	C I	15.3 ^{+0.8} _{-0.6}	13.0 ^{+0.1} _{-0.1}	C I	5.4 ^{+1.5} _{-0.8}	12.3 ^{+0.3} _{-0.4}
C II	5.4 ^{+10.8} _{-1.9}	11.2 ^{+1.2} _{-2.5}	C II	51.0 ^{+4.4} _{-4.4}	14.0 ^{+0.1} _{-0.2}	C II	15.3 ^{+0.8} _{-0.6}	15.5 ^{+0.0} _{-0.0}	C II	5.4 ^{+1.5} _{-0.8}	14.0 ^{+0.2} _{-0.2}
C IV	5.4 ^{+10.8} _{-1.9}	6.4 ^{+2.8} _{-2.8}	C IV	51.0 ^{+4.4} _{-4.4}	14.7 ^{+0.1} _{-0.1}	C IV	15.3 ^{+0.8} _{-0.6}	13.2 ^{+0.1} _{-0.1}	C IV	5.4 ^{+1.5} _{-0.8}	9.5 ^{+0.2} _{-0.5}
Fe II	4.2 ^{+11.8} _{-2.4}	10.1 ^{+1.4} _{-2.2}	Fe II	50.6 ^{+4.5} _{-4.4}	9.2 ^{+0.1} _{-0.1}	Fe II	14.8 ^{+0.8} _{-0.6}	13.9 ^{+0.1} _{-0.1}	Fe II	4.1 ^{+1.8} _{-1.1}	13.0 ^{+0.2} _{-0.3}
H I	14.4 ^{+4.9} _{-2.8}	15.3 ^{+1.0} _{-0.8}	H I	55.9 ^{+4.0} _{-4.0}	14.6 ^{+0.1} _{-0.1}	H I	21.2 ^{+0.8} _{-0.6}	18.0 ^{+0.1} _{-0.1}	H I	14.1 ^{+1.0} _{-0.6}	18.4 ^{+0.0} _{-0.0}
Mg II	4.6 ^{+11.4} _{-2.1}	10.2 ^{+1.3} _{-2.3}	Mg II	50.8 ^{+4.5} _{-4.4}	10.2 ^{+0.2} _{-0.2}	Mg II	15.0 ^{+0.8} _{-0.6}	14.2 ^{+0.0} _{-0.1}	Mg II	4.6 ^{+1.6} _{-1.0}	13.0 ^{+0.2} _{-0.3}
N I	5.2 ^{+10.9} _{-1.9}	9.8 ^{+1.6} _{-2.1}	N I	51.0 ^{+4.4} _{-4.4}	10.0 ^{+0.2} _{-0.3}	N I	15.2 ^{+0.8} _{-0.6}	13.5 ^{+0.1} _{-0.1}	N I	5.2 ^{+1.5} _{-0.9}	12.9 ^{+0.3} _{-0.4}
N V	5.2 ^{+10.9} _{-1.9}	4.2 ^{+2.7} _{-2.6}	N V	51.0 ^{+4.4} _{-4.4}	13.8 ^{+0.1} _{-0.1}	N V	15.2 ^{+0.8} _{-0.6}	11.0 ^{+0.1} _{-0.1}	N V	5.2 ^{+1.5} _{-0.9}	5.2 ^{+1.1} _{-0.3}
O I	5.0 ^{+11.1} _{-1.9}	10.9 ^{+1.5} _{-2.1}	O I	50.9 ^{+4.4} _{-4.4}	9.9 ^{+0.2} _{-0.2}	O I	15.2 ^{+0.8} _{-0.6}	14.6 ^{+0.1} _{-0.1}	O I	5.0 ^{+1.6} _{-0.9}	13.9 ^{+0.3} _{-0.3}
O VI	5.0 ^{+11.1} _{-1.9}	2.5 ^{+2.4} _{-1.1}	O VI	50.9 ^{+4.4} _{-4.4}	14.0 ^{+0.1} _{-0.1}	O VI	15.2 ^{+0.8} _{-0.6}	8.3 ^{+0.6} _{-0.1}	O VI	5.0 ^{+1.6} _{-0.9}	3.8 ^{+0.6} _{-0.1}
P II	4.5 ^{+11.5} _{-2.2}	8.4 ^{+1.2} _{-2.5}	P II	50.7 ^{+4.5} _{-4.4}	11.1 ^{+0.1} _{-0.1}	P II	14.9 ^{+0.8} _{-0.6}	12.7 ^{+0.0} _{-0.0}	P II	4.4 ^{+1.7} _{-1.0}	11.2 ^{+0.2} _{-0.2}
S I	4.5 ^{+11.6} _{-2.2}	8.0 ^{+1.7} _{-2.1}	S I	50.7 ^{+4.5} _{-4.4}	7.7 ^{+0.1} _{-0.2}	S I	14.9 ^{+0.8} _{-0.6}	11.1 ^{+0.1} _{-0.1}	S I	4.4 ^{+1.7} _{-1.0}	10.5 ^{+0.3} _{-0.4}
S II	4.5 ^{+11.6} _{-2.2}	10.1 ^{+1.2} _{-2.4}	S II	50.7 ^{+4.5} _{-4.4}	12.4 ^{+0.2} _{-0.2}	S II	14.9 ^{+0.8} _{-0.6}	14.2 ^{+0.0} _{-0.1}	S II	4.4 ^{+1.7} _{-1.0}	12.9 ^{+0.2} _{-0.2}
Si I	4.6 ^{+11.5} _{-2.1}	7.8 ^{+1.5} _{-2.2}	Si I	50.7 ^{+4.5} _{-4.4}	8.1 ^{+0.1} _{-0.1}	Si I	14.9 ^{+0.8} _{-0.6}	11.1 ^{+0.1} _{-0.1}	Si I	4.5 ^{+1.7} _{-1.0}	10.3 ^{+0.3} _{-0.3}
Si II	4.6 ^{+11.5} _{-2.1}	10.4 ^{+1.2} _{-2.4}	Si II	50.7 ^{+4.5} _{-4.4}	12.0 ^{+0.1} _{-0.1}	Si II	14.9 ^{+0.8} _{-0.6}	14.5 ^{+0.1} _{-0.1}	Si II	4.5 ^{+1.7} _{-1.0}	13.2 ^{+0.2} _{-0.2}
Si III	4.6 ^{+11.5} _{-2.1}	8.9 ^{+1.9} _{-3.3}	Si III	50.7 ^{+4.5} _{-4.4}	13.4 ^{+0.1} _{-0.1}	Si III	14.9 ^{+0.8} _{-0.6}	14.7 ^{+0.0} _{-0.0}	Si III	4.5 ^{+1.7} _{-1.0}	12.2 ^{+0.3} _{-0.3}
Si IV	4.6 ^{+11.5} _{-2.1}	6.6 ^{+2.7} _{-3.4}	Si IV	50.7 ^{+4.5} _{-4.4}	13.1 ^{+0.1} _{-0.1}	Si IV	14.9 ^{+0.8} _{-0.6}	13.4 ^{+0.1} _{-0.1}	Si IV	4.5 ^{+1.7} _{-1.0}	10.3 ^{+0.4} _{-0.4}
Ion	b	$\log \frac{N}{\text{cm}^{-2}}$	Ion	b	$\log \frac{N}{\text{cm}^{-2}}$	Ion	b	$\log \frac{N}{\text{cm}^{-2}}$	Ion	b	$\log \frac{N}{\text{cm}^{-2}}$
(1)	(2)	(3)	(1)	(2)	(3)	(1)	(2)	(3)	(1)	(2)	(3)
SC ^a	H_{I_0}	1035.8 ^{+1.8} _{-1.8}	SC ^b	N_{v_0}	706.8 ^{+12.3} _{-9.1}	SC ^b	Si_{iv_1}	716.2 ^{+0.3} _{-0.4}	SC ^b	C_{ii_1}	878.6 ^{+0.8} _{-1.0}
Al II	29.1 ^{+2.9} _{-5.3}	7.5 ^{+1.6} _{-1.3}	Al II	44.3 ^{+15.6} _{-15.5}	6.2 ^{+0.5} _{-1.1}	Al II	16.7 ^{+0.1} _{-0.1}	13.6 ^{+0.0} _{-0.0}	Al II	4.3 ^{+1.3} _{-0.8}	12.1 ^{+0.2} _{-0.2}
C I	29.3 ^{+2.9} _{-5.3}	8.3 ^{+1.2} _{-1.1}	C I	46.9 ^{+15.0} _{-14.0}	1.5 ^{+2.2} _{-2.8}	C I	17.2 ^{+0.1} _{-0.1}	12.9 ^{+0.0} _{-0.0}	C I	5.3 ^{+1.1} _{-0.7}	12.2 ^{+0.2} _{-0.3}
C II	29.3 ^{+2.9} _{-5.3}	9.3 ^{+1.6} _{-1.4}	C II	46.9 ^{+15.0} _{-14.0}	8.1 ^{+0.7} _{-1.0}	C II	17.2 ^{+0.1} _{-0.1}	15.4 ^{+0.0} _{-0.0}	C II	5.3 ^{+1.1} _{-0.7}	14.1 ^{+0.2} _{-0.2}
C IV	29.3 ^{+2.9} _{-5.3}	4.8 ^{+3.6} _{-1.8}	C IV	46.9 ^{+15.0} _{-14.0}	13.2 ^{+0.2} _{-0.1}	C IV	17.2 ^{+0.1} _{-0.1}	13.6 ^{+0.1} _{-0.1}	C IV	5.3 ^{+1.1} _{-0.7}	10.0 ^{+0.5} _{-0.5}
Fe II	29.1 ^{+2.9} _{-5.4}	8.4 ^{+1.3} _{-1.2}	Fe II	43.1 ^{+15.9} _{-16.0}	4.7 ^{+1.2} _{-1.6}	Fe II	16.6 ^{+0.1} _{-0.1}	13.7 ^{+0.1} _{-0.1}	Fe II	3.9 ^{+1.4} _{-1.0}	13.0 ^{+0.2} _{-0.3}
H I	31.7 ^{+2.5} _{-4.3}	14.1 ^{+0.1} _{-0.1}	H I	85.3 ^{+12.8} _{-11.4}	13.1 ^{+0.5} _{-0.6}	H I	23.8 ^{+0.3} _{-0.3}	18.2 ^{+0.1} _{-0.1}	H I	14.4 ^{+0.6} _{-0.5}	18.3 ^{+0.0} _{-0.0}
Mg II	29.1 ^{+2.9} _{-5.3}	8.5 ^{+1.4} _{-1.3}	Mg II	44.5 ^{+15.5} _{-15.3}	7.6 ^{+0.7} _{-1.2}	Mg II	16.8 ^{+0.1} _{-0.1}	14.1 ^{+0.1} _{-0.0}	Mg II	4.4 ^{+1.3} _{-0.8}	13.0 ^{+0.2} _{-0.3}
N I	29.2 ^{+2.9} _{-5.3}	8.3 ^{+1.2} _{-1.1}	N I	46.3 ^{+15.1} _{-14.3}	3.3 ^{+1.7} _{-1.9}	N I	17.1 ^{+0.1} _{-0.1}	13.4 ^{+0.1} _{-0.1}	N I	5.0 ^{+1.1} _{-0.7}	12.8 ^{+0.2} _{-0.3}
N V	29.2 ^{+2.9} _{-5.3}	3.8 ^{+3.0} _{-2.5}	N V	46.3 ^{+15.1} _{-14.3}	13.8 ^{+0.1} _{-0.1}	N V	17.1 ^{+0.1} _{-0.1}	11.6 ^{+0.1} _{-0.1}	N V	5.0 ^{+1.1} _{-0.7}	5.7 ^{+1.7} _{-0.6}
O I	29.2 ^{+2.9} _{-5.3}	9.3 ^{+1.2} _{-1.1}	O I	45.8 ^{+15.2} _{-14.6}	4.9 ^{+1.7} _{-2.3}	O I	17.0 ^{+0.1} _{-0.1}	14.5 ^{+0.1} _{-0.1}	O I	4.8 ^{+1.2} _{-0.7}	13.8 ^{+0.2} _{-0.3}
O VI	29.2 ^{+2.9} _{-5.3}	2.1 ^{+3.7} _{-1.9}	O VI	45.8 ^{+15.2} _{-14.6}	15.5 ^{+0.3} _{-0.7}	O VI	17.0 ^{+0.1} _{-0.1}	10.3 ^{+0.1} _{-0.2}	O VI	4.8 ^{+1.2} _{-0.7}	4.1 ^{+0.4} _{-0.3}
P II	29.1 ^{+2.9} _{-5.3}	6.6 ^{+1.6} _{-1.3}	P II	44.0 ^{+15.6} _{-15.6}	3.9 ^{+0.7} _{-0.7}	P II	16.7 ^{+0.1} _{-0.1}	12.8 ^{+0.0} _{-0.0}	P II	4.2 ^{+1.3} _{-0.9}	11.2 ^{+0.2} _{-0.2}
S I	29.1 ^{+2.9} _{-5.4}	6.6 ^{+1.3} _{-1.2}	S I	43.9 ^{+15.6} _{-15.6}	-2.5 ^{+2.5} _{-3.1}	S I	16.7 ^{+0.1} _{-0.1}	10.8 ^{+0.1} _{-0.1}	S I	4.2 ^{+1.3} _{-0.9}	10.4 ^{+0.3} _{-0.3}
S II	29.1 ^{+2.9} _{-5.4}	8.3 ^{+1.5} _{-1.3}	S II	43.9 ^{+15.6} _{-15.6}	5.5 ^{+1.2} _{-1.3}	S II	16.7 ^{+0.1} _{-0.1}	14.2 ^{+0.0} _{-0.0}	S II	4.2 ^{+1.3} _{-0.9}	12.9 ^{+0.2} _{-0.2}
Si I	29.1 ^{+2.9} _{-5.3}	6.2 ^{+1.3} _{-1.2}	Si I	44.2 ^{+15.6} _{-15.5}	-0.2 ^{+2.2} _{-2.7}	Si I	16.7 ^{+0.1} _{-0.1}	10.9 ^{+0.1} _{-0.0}	Si I	4.3 ^{+1.3} _{-0.9}	10.2 ^{+0.2} _{-0.3}
Si II	29.1 ^{+2.9} _{-5.3}	8.6 ^{+1.5} _{-1.3}	Si II	44.2 ^{+15.6} _{-15.5}	6.7 ^{+0.4} _{-0.7}	Si II	16.7 ^{+0.1} _{-0.1}	14.4 ^{+0.1} _{-0.1}	Si II	4.3 ^{+1.3} _{-0.9}	13.2 ^{+0.2} _{-0.2}
Si III	29.1 ^{+2.9} _{-5.3}	6.8 ^{+3.1} _{-2.7}	Si III	44.2 ^{+15.6} _{-15.5}	10.0 ^{+0.2} _{-0.5}	Si III	16.7 ^{+0.1} _{-0.1}	14.8 ^{+0.0} _{-0.0}	Si III	4.3 ^{+1.3} _{-0.9}	12.5 ^{+0.3} _{-0.3}
Si IV	29.1 ^{+2.9} _{-5.3}	4.4 ^{+4.1} _{-2.5}	Si IV	44.2 ^{+15.6} _{-15.5}	12.0 ^{+0.2} _{-0.3}	Si IV	16.7 ^{+0.1} _{-0.1}	13.7 ^{+0.0} _{-0.0}	Si IV	4.3 ^{+1.3} _{-0.9}	10.7 ^{+0.4} _{-0.4}

Table M1. Basic properties of the different ions in different gas phases contributing to the absorption towards different sightlines summarized in Table 3. The first line in each table denotes the sightline, the constraining ion cloud, and the heliocentric velocity of the corresponding gas phase. The basic properties of the different ions arising in the gas phase follow. Notes: (1) Ion name; (2) Total Doppler broadening parameter of the ion; (3) log column density of the ion.

Ion	b (km s ⁻¹)	$\log \frac{N}{\text{cm}^{-2}}$	Ion	b (km s ⁻¹)	$\log \frac{N}{\text{cm}^{-2}}$	Ion	b (km s ⁻¹)	$\log \frac{N}{\text{cm}^{-2}}$	Ion	b (km s ⁻¹)	$\log \frac{N}{\text{cm}^{-2}}$
(1)	(2)	(3)	(1)	(2)	(3)	(1)	(2)	(3)	(1)	(2)	(3)
SC ^b	H _I _0	1035.8 ^{+1.6} _{-1.8}	SD	Si _{IV} _0	844.4 ^{+1.6} _{-1.7}	SD	H _I _0	978.4 ^{+3.7} _{-8.0}	SE ^a	H _I _0	700.7 ^{+1.6} _{-1.0}
Al II	28.1 ^{+3.1} _{-3.9}	8.8 ^{+1.1} _{-1.3}	Al II	19.1 ^{+3.2} _{-2.7}	13.1 ^{+0.2} _{-0.3}	Al II	3.9 ^{+2.8} _{-2.2}	10.2 ^{+1.0} _{-1.5}	Al II	15.2 ^{+4.3} _{-3.4}	10.0 ^{+0.4} _{-0.4}
C I	28.3 ^{+3.1} _{-3.9}	8.9 ^{+0.9} _{-1.0}	C I	19.5 ^{+3.2} _{-2.6}	12.3 ^{+0.3} _{-0.4}	C I	4.9 ^{+2.5} _{-3.0}	10.8 ^{+1.8} _{-1.7}	C I	16.0 ^{+4.0} _{-3.1}	10.0 ^{+0.2} _{-0.4}
C II	28.3 ^{+3.1} _{-3.9}	10.7 ^{+1.2} _{-1.4}	C II	19.5 ^{+3.2} _{-2.6}	14.9 ^{+0.2} _{-0.2}	C II	4.9 ^{+2.5} _{-3.0}	12.0 ^{+1.0} _{-1.5}	C II	16.0 ^{+4.0} _{-3.1}	12.5 ^{+0.3} _{-0.4}
C IV	28.3 ^{+3.1} _{-3.9}	7.1 ^{+3.0} _{-3.0}	C IV	19.5 ^{+3.2} _{-2.6}	13.6 ^{+0.2} _{-0.2}	C IV	4.9 ^{+2.5} _{-3.0}	7.4 ^{+3.3} _{-2.1}	C IV	16.0 ^{+4.0} _{-3.1}	11.6 ^{+0.4} _{-0.7}
Fe II	28.0 ^{+3.1} _{-4.0}	9.3 ^{+1.2} _{-1.1}	Fe II	19.0 ^{+3.3} _{-2.7}	12.7 ^{+0.3} _{-0.2}	Fe II	3.5 ^{+2.9} _{-2.2}	10.9 ^{+1.2} _{-1.5}	Fe II	14.9 ^{+4.4} _{-3.6}	9.0 ^{+0.7} _{-0.2}
H I	31.4 ^{+2.8} _{-3.4}	14.1 ^{+0.1} _{-0.1}	H I	25.5 ^{+2.0} _{-2.2}	16.9 ^{+0.5} _{-0.6}	H I	13.1 ^{+5.3} _{-8.0}	16.8 ^{+0.9} _{-1.5}	H I	27.5 ^{+1.9} _{-2.6}	14.1 ^{+0.1} _{-0.1}
Mg II	28.1 ^{+3.1} _{-3.9}	9.5 ^{+1.0} _{-1.2}	Mg II	19.2 ^{+3.2} _{-2.7}	13.4 ^{+0.2} _{-0.2}	Mg II	4.0 ^{+2.8} _{-2.3}	11.0 ^{+1.1} _{-1.5}	Mg II	15.3 ^{+4.3} _{-3.4}	9.6 ^{+1.0} _{-0.5}
N I	28.2 ^{+3.1} _{-3.9}	8.9 ^{+1.0} _{-1.0}	N I	19.4 ^{+3.2} _{-2.6}	12.2 ^{+0.4} _{-0.4}	N I	4.7 ^{+2.5} _{-2.8}	10.8 ^{+1.7} _{-1.7}	N I	15.8 ^{+4.1} _{-3.2}	9.4 ^{+0.2} _{-0.3}
N V	28.2 ^{+3.1} _{-3.9}	5.2 ^{+3.0} _{-3.3}	N V	19.4 ^{+3.2} _{-2.6}	11.6 ^{+0.2} _{-0.3}	N V	4.7 ^{+2.5} _{-2.8}	6.1 ^{+2.9} _{-2.4}	N V	15.8 ^{+4.1} _{-3.2}	10.1 ^{+0.5} _{-0.8}
O I	28.2 ^{+3.1} _{-3.9}	10.0 ^{+1.0} _{-1.0}	O I	19.3 ^{+3.2} _{-2.6}	13.2 ^{+0.3} _{-0.3}	O I	4.5 ^{+2.6} _{-2.6}	11.8 ^{+1.5} _{-1.7}	O I	15.6 ^{+4.1} _{-3.2}	9.6 ^{+0.8} _{-0.2}
O VI	28.2 ^{+3.1} _{-3.9}	2.8 ^{+4.4} _{-2.2}	O VI	19.3 ^{+3.2} _{-2.6}	10.5 ^{+0.4} _{-0.6}	O VI	4.5 ^{+2.6} _{-2.6}	4.4 ^{+3.9} _{-2.0}	O VI	15.6 ^{+4.1} _{-3.2}	9.8 ^{+0.5} _{-1.2}
P II	28.1 ^{+3.1} _{-4.0}	7.9 ^{+1.2} _{-1.4}	P II	19.1 ^{+3.3} _{-2.7}	12.3 ^{+0.2} _{-0.3}	P II	3.8 ^{+2.8} _{-2.2}	9.2 ^{+1.0} _{-1.6}	P II	15.1 ^{+4.3} _{-3.5}	9.6 ^{+0.2} _{-0.4}
S I	28.1 ^{+3.1} _{-4.0}	7.1 ^{+1.0} _{-1.1}	S I	19.1 ^{+3.3} _{-2.7}	10.2 ^{+0.3} _{-0.3}	S I	3.8 ^{+2.8} _{-2.2}	9.1 ^{+2.0} _{-1.9}	S I	15.1 ^{+4.3} _{-3.5}	7.0 ^{+0.4} _{-0.3}
S II	28.1 ^{+3.1} _{-4.0}	9.5 ^{+1.1} _{-1.3}	S II	19.1 ^{+3.3} _{-2.7}	13.6 ^{+0.2} _{-0.2}	S II	3.8 ^{+2.8} _{-2.2}	10.9 ^{+1.0} _{-1.5}	S II	15.1 ^{+4.3} _{-3.5}	11.0 ^{+0.2} _{-0.4}
Si I	28.1 ^{+3.1} _{-3.9}	6.9 ^{+1.0} _{-1.0}	Si I	19.1 ^{+3.2} _{-2.7}	10.2 ^{+0.3} _{-0.3}	Si I	3.8 ^{+2.8} _{-2.2}	8.7 ^{+1.9} _{-1.6}	Si I	15.2 ^{+4.3} _{-3.5}	7.6 ^{+0.1} _{-0.3}
Si II	28.1 ^{+3.1} _{-3.9}	9.8 ^{+1.1} _{-1.3}	Si II	19.1 ^{+3.2} _{-2.7}	13.7 ^{+0.2} _{-0.1}	Si II	3.8 ^{+2.8} _{-2.2}	11.2 ^{+1.0} _{-1.5}	Si II	15.2 ^{+4.3} _{-3.5}	10.8 ^{+0.2} _{-0.4}
Si III	28.1 ^{+3.1} _{-3.9}	9.3 ^{+1.9} _{-2.5}	Si III	19.1 ^{+3.2} _{-2.7}	14.5 ^{+0.2} _{-0.2}	Si III	3.8 ^{+2.8} _{-2.2}	9.3 ^{+2.7} _{-3.5}	Si III	15.2 ^{+4.3} _{-3.5}	12.1 ^{+0.2} _{-0.4}
Si IV	28.1 ^{+3.1} _{-3.9}	7.5 ^{+2.5} _{-3.3}	Si IV	19.1 ^{+3.2} _{-2.7}	13.5 ^{+0.1} _{-0.1}	Si IV	3.8 ^{+2.8} _{-2.2}	6.8 ^{+3.9} _{-2.2}	Si IV	15.2 ^{+4.3} _{-3.5}	11.2 ^{+0.3} _{-0.5}
Ion	b (km s ⁻¹)	$\log \frac{N}{\text{cm}^{-2}}$	Ion	b (km s ⁻¹)	$\log \frac{N}{\text{cm}^{-2}}$	Ion	b (km s ⁻¹)	$\log \frac{N}{\text{cm}^{-2}}$	Ion	b (km s ⁻¹)	$\log \frac{N}{\text{cm}^{-2}}$
(1)	(2)	(3)	(1)	(2)	(3)	(1)	(2)	(3)	(1)	(2)	(3)
SE ^a	C _{IV} _0	704.6 ^{+2.8} _{-3.3}	SE ^b	H _I _0	701.7 ^{+0.6} _{-0.6}	SE ^b	C _{IV} _0	706.6 ^{+2.2} _{-2.8}	SF	Si _{III} _1	909.9 ^{+1.3} _{-1.3}
Al II	27.4 ^{+2.5} _{-2.5}	8.9 ^{+0.3} _{-0.3}	Al II	8.4 ^{+3.4} _{-3.4}	11.0 ^{+0.2} _{-0.2}	Al II	27.2 ^{+3.5} _{-2.4}	7.6 ^{+0.0} _{-0.1}	Al II	12.0 ^{+0.8} _{-0.9}	14.2 ^{+0.2} _{-0.2}
C I	27.8 ^{+2.5} _{-2.4}	9.3 ^{+0.3} _{-0.3}	C I	9.1 ^{+3.0} _{-3.0}	10.4 ^{+0.3} _{-0.3}	C I	29.2 ^{+3.3} _{-2.3}	7.3 ^{+0.2} _{-0.2}	C I	12.1 ^{+0.8} _{-0.8}	13.8 ^{+0.1} _{-0.1}
C II	27.8 ^{+2.5} _{-2.4}	12.7 ^{+0.2} _{-0.2}	C II	9.1 ^{+3.3} _{-3.0}	12.9 ^{+0.2} _{-0.2}	C II	29.2 ^{+3.3} _{-2.3}	11.1 ^{+0.1} _{-0.1}	C II	12.1 ^{+0.8} _{-0.8}	16.1 ^{+0.1} _{-0.1}
C IV	27.8 ^{+2.5} _{-2.4}	14.0 ^{+0.0} _{-0.0}	C IV	9.1 ^{+3.3} _{-3.0}	10.9 ^{+0.4} _{-0.5}	C IV	29.2 ^{+3.3} _{-2.3}	13.9 ^{+0.0} _{-0.0}	C IV	12.1 ^{+0.8} _{-0.8}	13.4 ^{+0.4} _{-0.4}
Fe II	27.2 ^{+2.6} _{-2.5}	7.4 ^{+0.3} _{-0.3}	Fe II	8.2 ^{+3.5} _{-3.5}	11.2 ^{+0.3} _{-0.5}	Fe II	26.3 ^{+3.6} _{-2.5}	7.9 ^{+0.1} _{-0.1}	Fe II	12.0 ^{+0.8} _{-0.9}	14.9 ^{+0.2} _{-0.2}
H I	36.2 ^{+2.5} _{-2.2}	13.3 ^{+0.2} _{-0.2}	H I	17.1 ^{+2.3} _{-1.7}	15.1 ^{+0.4} _{-0.4}	H I	55.7 ^{+1.8} _{-1.3}	12.6 ^{+0.2} _{-0.3}	H I	13.9 ^{+0.9} _{-0.7}	17.6 ^{+0.2} _{-0.1}
Mg II	27.4 ^{+2.5} _{-2.5}	8.5 ^{+0.4} _{-0.4}	Mg II	8.5 ^{+3.4} _{-3.3}	11.5 ^{+0.2} _{-0.3}	Mg II	27.3 ^{+3.5} _{-2.4}	9.3 ^{+0.0} _{-0.2}	Mg II	12.0 ^{+0.8} _{-0.9}	15.1 ^{+0.1} _{-0.2}
N I	27.7 ^{+2.5} _{-2.5}	8.5 ^{+0.3} _{-0.4}	N I	8.9 ^{+3.3} _{-3.1}	10.6 ^{+0.3} _{-0.4}	N I	28.7 ^{+3.3} _{-2.3}	7.7 ^{+0.2} _{-0.2}	N I	12.1 ^{+0.8} _{-0.9}	14.2 ^{+0.1} _{-0.1}
N V	27.7 ^{+2.5} _{-2.5}	13.4 ^{+0.1} _{-0.1}	N V	8.9 ^{+3.3} _{-3.1}	8.6 ^{+0.7} _{-0.7}	N V	28.7 ^{+3.3} _{-2.3}	13.5 ^{+0.1} _{-0.1}	N V	12.1 ^{+0.8} _{-0.9}	11.7 ^{+0.0} _{-0.1}
O I	27.6 ^{+2.5} _{-2.5}	8.4 ^{+0.3} _{-0.4}	O I	8.8 ^{+3.4} _{-3.1}	11.7 ^{+0.3} _{-0.4}	O I	28.3 ^{+3.4} _{-2.3}	8.5 ^{+0.2} _{-0.2}	O I	12.1 ^{+0.8} _{-0.9}	15.2 ^{+0.2} _{-0.1}
O VI	27.6 ^{+2.5} _{-2.5}	13.8 ^{+0.1} _{-0.1}	O VI	8.8 ^{+3.4} _{-3.1}	5.8 ^{+2.2} _{-1.2}	O VI	28.3 ^{+3.4} _{-2.3}	12.0 ^{+0.5} _{-0.2}	O VI	12.1 ^{+0.8} _{-0.9}	8.4 ^{+0.0} _{-0.2}
P II	27.3 ^{+2.5} _{-2.5}	9.6 ^{+0.2} _{-0.3}	P II	8.4 ^{+3.5} _{-3.4}	10.2 ^{+0.1} _{-0.1}	P II	27.0 ^{+3.5} _{-2.5}	7.2 ^{+0.1} _{-0.1}	P II	12.0 ^{+0.8} _{-0.9}	13.4 ^{+0.1} _{-0.2}
S I	27.3 ^{+2.5} _{-2.5}	6.1 ^{+0.3} _{-0.4}	S I	8.4 ^{+3.5} _{-3.4}	8.6 ^{+0.3} _{-0.4}	S I	26.9 ^{+3.5} _{-2.5}	4.2 ^{+0.2} _{-0.2}	S I	12.0 ^{+0.8} _{-0.9}	11.9 ^{+0.1} _{-0.1}
S II	27.3 ^{+2.5} _{-2.5}	11.0 ^{+0.3} _{-0.3}	S II	8.4 ^{+3.5} _{-3.4}	11.7 ^{+0.2} _{-0.2}	S II	26.9 ^{+3.5} _{-2.5}	9.7 ^{+0.1} _{-0.1}	S II	12.0 ^{+0.8} _{-0.9}	14.9 ^{+0.1} _{-0.1}
Si I	27.4 ^{+2.5} _{-2.5}	6.3 ^{+0.3} _{-0.3}	Si I	8.4 ^{+3.4} _{-3.4}	8.5 ^{+0.3} _{-0.4}	Si I	27.1 ^{+3.5} _{-2.4}	1.2 ^{+0.6} _{-1.5}	Si I	12.0 ^{+0.8} _{-0.9}	12.2 ^{+0.1} _{-0.1}
Si II	27.4 ^{+2.5} _{-2.5}	10.5 ^{+0.2} _{-0.2}	Si II	8.4 ^{+3.4} _{-3.4}	11.9 ^{+0.2} _{-0.3}	Si II	27.1 ^{+3.5} _{-2.4}	8.7 ^{+0.1} _{-0.1}	Si II	12.0 ^{+0.8} _{-0.9}	15.4 ^{+0.1} _{-0.1}
Si III	27.4 ^{+2.5} _{-2.5}	11.9 ^{+0.2} _{-0.2}	Si III	8.4 ^{+3.4} _{-3.4}	12.2 ^{+0.1} _{-0.2}	Si III	27.1 ^{+3.5} _{-2.4}	11.3 ^{+0.1} _{-0.1}	Si III	12.0 ^{+0.8} _{-0.9}	13.9 ^{+0.4} _{-0.3}
Si IV	27.4 ^{+2.5} _{-2.5}	11.8 ^{+0.2} _{-0.2}	Si IV	8.4 ^{+3.4} _{-3.4}	11.0 ^{+0.3} _{-0.4}	Si IV	27.1 ^{+3.5} _{-2.4}	12.2 ^{+0.0} _{-0.1}	Si IV	12.0 ^{+0.8} _{-0.9}	13.7 ^{+0.4} _{-0.2}

Ion	b	$\log \frac{N}{\text{cm}^{-2}}$	Ion	b	$\log \frac{N}{\text{cm}^{-2}}$	Ion	b	$\log \frac{N}{\text{cm}^{-2}}$	Ion	b	$\log \frac{N}{\text{cm}^{-2}}$
	(km s ⁻¹)			(km s ⁻¹)			(km s ⁻¹)			(km s ⁻¹)	
(1)	(2)	(3)	(1)	(2)	(3)	(1)	(2)	(3)	(1)	(2)	(3)
SG	C iv_0	817.2 ^{+1.4} _{-2.5}	SG	Si iv_0	861.3 ^{+5.5} _{-3.8}	SG	H i_1	942.8 ^{+5.6} _{-4.5}	SG	H i_2	1056.7 ^{+4.2} _{-4.3}
Al II	18.1 ^{+4.9} _{-4.7}	10.4 ^{+0.2} _{-0.2}	Al II	10.4 ^{+0.9} _{-2.1}	11.0 ^{+0.4} _{-0.3}	Al II	9.6 ^{+10.7} _{-6.7}	9.0 ^{+1.8} _{-1.7}	Al II	11.3 ^{+11.1} _{-8.4}	7.6 ^{+1.9} _{-1.5}
C I	18.4 ^{+4.9} _{-4.6}	9.3 ^{+0.9} _{-0.2}	C I	10.8 ^{+0.9} _{-2.0}	10.0 ^{+0.4} _{-0.4}	C I	10.1 ^{+10.5} _{-5.9}	9.6 ^{+1.5} _{-1.6}	C I	11.7 ^{+10.9} _{-7.6}	8.5 ^{+1.5} _{-1.5}
C II	18.4 ^{+4.9} _{-4.6}	13.0 ^{+0.1} _{-0.1}	C II	10.8 ^{+0.9} _{-2.0}	13.3 ^{+0.2} _{-0.3}	C II	10.1 ^{+10.5} _{-5.9}	10.8 ^{+1.9} _{-1.8}	C II	11.7 ^{+10.9} _{-7.6}	9.5 ^{+2.0} _{-1.7}
C IV	18.4 ^{+4.9} _{-4.6}	14.0 ^{+0.2} _{-0.2}	C IV	10.8 ^{+0.9} _{-2.0}	13.2 ^{+0.4} _{-0.3}	C IV	10.1 ^{+10.5} _{-5.9}	6.8 ^{+4.1} _{-2.8}	C IV	11.7 ^{+10.9} _{-7.6}	5.5 ^{+4.1} _{-2.5}
Fe II	18.0 ^{+5.0} _{-4.8}	9.3 ^{+0.4} _{-0.4}	Fe II	10.2 ^{+0.9} _{-2.1}	10.7 ^{+0.5} _{-0.7}	Fe II	9.4 ^{+10.8} _{-7.3}	9.7 ^{+1.5} _{-1.5}	Fe II	11.2 ^{+11.2} _{-9.1}	8.5 ^{+1.8} _{-1.4}
H I	24.0 ^{+4.2} _{-3.3}	13.6 ^{+0.1} _{-0.1}	H I	16.8 ^{+2.9} _{-2.1}	14.1 ^{+0.6} _{-0.4}	H I	16.5 ^{+7.8} _{-3.8}	15.4 ^{+1.0} _{-1.0}	H I	16.9 ^{+9.1} _{-4.4}	14.2 ^{+0.6} _{-0.4}
Mg II	18.1 ^{+4.9} _{-4.7}	10.7 ^{+0.4} _{-0.4}	Mg II	10.4 ^{+0.9} _{-2.1}	11.7 ^{+0.3} _{-0.5}	Mg II	9.7 ^{+10.7} _{-6.6}	9.9 ^{+1.5} _{-1.6}	Mg II	11.4 ^{+11.1} _{-8.4}	8.6 ^{+1.8} _{-1.5}
N I	18.4 ^{+4.9} _{-4.6}	8.8 ^{+0.3} _{-0.3}	N I	10.7 ^{+0.9} _{-2.0}	9.9 ^{+0.5} _{-0.5}	N I	10.0 ^{+10.5} _{-6.0}	9.6 ^{+1.5} _{-1.6}	N I	11.6 ^{+11.0} _{-7.8}	8.5 ^{+1.6} _{-1.5}
N V	18.4 ^{+4.9} _{-4.6}	12.9 ^{+0.3} _{-0.3}	N V	10.7 ^{+0.9} _{-2.0}	11.7 ^{+0.5} _{-0.5}	N V	10.0 ^{+10.5} _{-6.0}	5.7 ^{+3.2} _{-3.4}	N V	11.6 ^{+11.0} _{-7.8}	4.4 ^{+3.6} _{-3.1}
O I	18.3 ^{+4.9} _{-4.6}	9.6 ^{+0.4} _{-0.4}	O I	10.6 ^{+0.9} _{-2.0}	10.9 ^{+0.5} _{-0.6}	O I	9.9 ^{+10.6} _{-6.2}	10.6 ^{+1.5} _{-1.6}	O I	11.5 ^{+11.0} _{-7.9}	9.4 ^{+1.6} _{-1.4}
O VI	18.3 ^{+4.9} _{-4.6}	12.9 ^{+0.4} _{-0.4}	O VI	10.6 ^{+0.9} _{-2.0}	11.3 ^{+0.6} _{-0.7}	O VI	9.9 ^{+10.6} _{-6.2}	4.2 ^{+4.0} _{-2.9}	O VI	11.5 ^{+11.0} _{-7.9}	2.8 ^{+4.5} _{-2.6}
P II	18.1 ^{+5.0} _{-4.7}	10.3 ^{+0.2} _{-0.2}	P II	10.4 ^{+0.9} _{-2.1}	10.7 ^{+0.3} _{-0.3}	P II	9.6 ^{+10.7} _{-6.8}	8.1 ^{+1.9} _{-1.8}	P II	11.3 ^{+11.1} _{-8.6}	6.7 ^{+2.0} _{-1.5}
S I	18.1 ^{+5.0} _{-4.7}	7.1 ^{+0.3} _{-0.3}	S I	10.4 ^{+0.9} _{-2.1}	8.1 ^{+0.4} _{-0.5}	S I	9.6 ^{+10.7} _{-6.8}	7.8 ^{+1.5} _{-1.7}	S I	11.3 ^{+11.1} _{-8.6}	6.8 ^{+1.5} _{-1.6}
S II	18.1 ^{+5.0} _{-4.7}	11.5 ^{+0.2} _{-0.2}	S II	10.4 ^{+0.9} _{-2.1}	12.0 ^{+0.3} _{-0.3}	S II	9.6 ^{+10.7} _{-6.8}	9.7 ^{+1.7} _{-1.7}	S II	11.3 ^{+11.1} _{-8.6}	8.4 ^{+1.8} _{-1.5}
Si I	18.1 ^{+4.9} _{-4.7}	7.0 ^{+0.2} _{-0.2}	Si I	10.4 ^{+0.9} _{-2.1}	8.0 ^{+0.4} _{-0.5}	Si I	9.6 ^{+10.7} _{-6.7}	7.5 ^{+1.5} _{-1.6}	Si I	11.3 ^{+11.1} _{-8.5}	6.3 ^{+1.6} _{-1.5}
Si II	18.1 ^{+4.9} _{-4.7}	11.6 ^{+0.2} _{-0.2}	Si II	10.4 ^{+0.9} _{-2.1}	12.3 ^{+0.3} _{-0.4}	Si II	9.6 ^{+10.7} _{-6.7}	10.0 ^{+1.7} _{-1.7}	Si II	11.3 ^{+11.1} _{-8.5}	8.6 ^{+1.8} _{-1.5}
Si III	18.1 ^{+4.9} _{-4.7}	12.8 ^{+0.1} _{-0.2}	Si III	10.4 ^{+0.9} _{-2.1}	13.1 ^{+0.2} _{-0.2}	Si III	9.6 ^{+10.7} _{-6.7}	8.8 ^{+3.1} _{-2.6}	Si III	11.3 ^{+11.1} _{-8.5}	7.0 ^{+3.5} _{-2.7}
Si IV	18.1 ^{+4.9} _{-4.7}	13.0 ^{+0.1} _{-0.2}	Si IV	10.4 ^{+0.9} _{-2.1}	12.9 ^{+0.2} _{-0.3}	Si IV	9.6 ^{+10.7} _{-6.7}	6.6 ^{+4.3} _{-3.2}	Si IV	11.3 ^{+11.1} _{-8.5}	4.8 ^{+4.4} _{-3.0}

Ion	b	$\log \frac{N}{\text{cm}^{-2}}$	Ion	b	$\log \frac{N}{\text{cm}^{-2}}$	Ion	b	$\log \frac{N}{\text{cm}^{-2}}$	Ion	b	$\log \frac{N}{\text{cm}^{-2}}$
	(km s ⁻¹)			(km s ⁻¹)			(km s ⁻¹)			(km s ⁻¹)	
(1)	(2)	(3)	(1)	(2)	(3)	(1)	(2)	(3)	(1)	(2)	(3)
SG	H i_3	1297.2 ^{+27.1} _{-26.3}	SH	Si III_0	766.8 ^{+0.3} _{-0.8}	SH	Si III_1	818.0 ^{+1.3} _{-0.9}	SH	H i_2	899.5 ^{+2.7} _{-2.9}
Al II	6.2 ^{+4.8} _{-4.0}	7.5 ^{+2.9} _{-3.0}	Al II	17.6 ^{+0.2} _{-0.6}	8.8 ^{+0.1} _{-0.1}	Al II	3.7 ^{+0.5} _{-0.5}	12.2 ^{+0.4} _{-0.3}	Al II	5.3 ^{+6.1} _{-2.7}	7.7 ^{+2.0} _{-1.4}
C I	7.0 ^{+6.2} _{-4.0}	8.2 ^{+2.7} _{-2.9}	C I	19.2 ^{+0.2} _{-0.6}	10.1 ^{+0.1} _{-0.2}	C I	5.3 ^{+0.5} _{-0.6}	11.1 ^{+0.2} _{-0.2}	C I	5.9 ^{+5.7} _{-2.2}	8.7 ^{+1.3} _{-1.2}
C II	7.0 ^{+6.2} _{-4.0}	9.7 ^{+3.1} _{-3.4}	C II	19.2 ^{+0.2} _{-0.6}	13.2 ^{+0.1} _{-0.1}	C II	5.3 ^{+0.5} _{-0.6}	14.8 ^{+0.2} _{-0.2}	C II	5.9 ^{+5.7} _{-2.2}	9.5 ^{+2.1} _{-1.5}
C IV	7.0 ^{+6.2} _{-4.0}	6.9 ^{+6.3} _{-4.3}	C IV	19.2 ^{+0.2} _{-0.6}	13.5 ^{+0.1} _{-0.1}	C IV	5.3 ^{+0.5} _{-0.6}	16.1 ^{+0.2} _{-0.3}	C IV	5.9 ^{+5.7} _{-2.2}	5.1 ^{+3.8} _{-1.7}
Fe II	5.8 ^{+4.9} _{-4.1}	8.1 ^{+2.9} _{-2.8}	Fe II	16.9 ^{+0.2} _{-0.7}	9.1 ^{+0.1} _{-0.1}	Fe II	2.7 ^{+0.6} _{-0.4}	10.7 ^{+0.6} _{-0.5}	Fe II	4.9 ^{+6.3} _{-3.1}	8.6 ^{+1.7} _{-1.3}
H I	14.8 ^{+25.5} _{-7.8}	13.6 ^{+3.0} _{-2.4}	H I	38.8 ^{+0.4} _{-0.5}	15.4 ^{+0.1} _{-0.1}	H I	17.9 ^{+1.7} _{-1.8}	15.4 ^{+0.2} _{-0.2}	H I	13.5 ^{+3.4} _{-1.6}	14.5 ^{+0.4} _{-0.4}
Mg II	6.3 ^{+4.8} _{-4.0}	8.3 ^{+3.0} _{-2.9}	Mg II	17.8 ^{+0.2} _{-0.6}	9.0 ^{+0.1} _{-0.1}	Mg II	3.9 ^{+0.5} _{-0.5}	12.2 ^{+0.6} _{-0.5}	Mg II	5.3 ^{+6.1} _{-2.6}	8.7 ^{+1.8} _{-1.3}
N I	6.8 ^{+5.8} _{-4.0}	8.1 ^{+2.8} _{-2.7}	N I	18.8 ^{+0.2} _{-0.6}	9.7 ^{+0.1} _{-0.1}	N I	5.0 ^{+0.5} _{-0.6}	10.4 ^{+0.4} _{-0.2}	N I	5.8 ^{+5.8} _{-2.3}	8.6 ^{+1.4} _{-1.2}
N V	6.8 ^{+5.8} _{-4.0}	6.4 ^{+6.3} _{-5.4}	N V	18.8 ^{+0.2} _{-0.6}	11.6 ^{+0.1} _{-0.1}	N V	5.0 ^{+0.5} _{-0.6}	15.3 ^{+0.3} _{-0.4}	N V	5.8 ^{+5.8} _{-2.3}	4.0 ^{+5.1} _{-2.6}
O I	6.7 ^{+5.5} _{-3.9}	9.0 ^{+3.0} _{-2.7}	O I	18.5 ^{+0.2} _{-0.6}	9.8 ^{+0.1} _{-0.1}	O I	4.7 ^{+0.5} _{-0.5}	11.0 ^{+0.6} _{-0.4}	O I	5.6 ^{+5.9} _{-2.4}	9.6 ^{+1.5} _{-1.2}
O VI	6.7 ^{+5.5} _{-3.9}	5.9 ^{+6.7} _{-6.6}	O VI	18.5 ^{+0.2} _{-0.6}	11.0 ^{+0.1} _{-0.1}	O VI	4.7 ^{+0.5} _{-0.5}	15.3 ^{+0.4} _{-0.5}	O VI	5.6 ^{+5.9} _{-2.4}	3.0 ^{+4.9} _{-2.1}
P II	6.1 ^{+4.8} _{-4.0}	6.7 ^{+3.0} _{-3.1}	P II	17.5 ^{+0.2} _{-0.6}	9.4 ^{+0.1} _{-0.1}	P II	3.5 ^{+0.5} _{-0.5}	12.0 ^{+0.3} _{-0.2}	P II	5.2 ^{+6.2} _{-2.8}	6.7 ^{+2.0} _{-1.4}
S I	6.1 ^{+4.8} _{-4.0}	6.2 ^{+3.0} _{-3.1}	S I	17.4 ^{+0.2} _{-0.6}	6.5 ^{+0.1} _{-0.2}	S I	3.4 ^{+0.5} _{-0.5}	8.6 ^{+0.5} _{-0.4}	S I	5.2 ^{+6.2} _{-2.8}	7.0 ^{+1.3} _{-1.2}
S II	6.1 ^{+4.8} _{-4.0}	8.4 ^{+3.0} _{-3.1}	S II	17.4 ^{+0.2} _{-0.6}	11.3 ^{+0.1} _{-0.1}	S II	3.4 ^{+0.5} _{-0.5}	13.2 ^{+0.3} _{-0.2}	S II	5.2 ^{+6.2} _{-2.8}	8.4 ^{+2.0} _{-1.4}
Si I	6.2 ^{+4.8} _{-4.0}	6.0 ^{+2.8} _{-3.1}	Si I	17.6 ^{+0.2} _{-0.6}	7.6 ^{+0.1} _{-0.2}	Si I	3.6 ^{+0.5} _{-0.5}	8.8 ^{+0.3} _{-0.2}	Si I	5.2 ^{+6.1} _{-2.7}	6.4 ^{+1.5} _{-1.2}
Si II	6.2 ^{+4.8} _{-4.0}	8.6 ^{+2.8} _{-3.0}	Si II	17.6 ^{+0.2} _{-0.6}	11.0 ^{+0.1} _{-0.1}	Si II	3.6 ^{+0.5} _{-0.5}	13.3 ^{+0.3} _{-0.3}	Si II	5.2 ^{+6.1} _{-2.7}	8.7 ^{+2.0} _{-1.4}
Si III	6.2 ^{+4.8} _{-4.0}	7.7 ^{+4.6} _{-5.0}	Si III	17.6 ^{+0.2} _{-0.6}	12.9 ^{+0.1} _{-0.1}	Si III	3.6 ^{+0.5} _{-0.5}	14.7 ^{+0.3} _{-0.3}	Si III	5.2 ^{+6.1} _{-2.7}	6.8 ^{+3.2} _{-2.0}
Si IV	6.2 ^{+4.8} _{-4.0}	5.8 ^{+6.1} _{-5.2}	Si IV	17.6 ^{+0.2} _{-0.6}	12.8 ^{+0.0} _{-0.0}	Si IV	3.6 ^{+0.5} _{-0.5}	14.8 ^{+0.3} _{-0.3}	Si IV	5.2 ^{+6.1} _{-2.7}	4.3 ^{+4.1} _{-2.3}

Ion	b (km s ⁻¹)	$\log \frac{N}{\text{cm}^{-2}}$	Ion	b (km s ⁻¹)	$\log \frac{N}{\text{cm}^{-2}}$	Ion	b (km s ⁻¹)	$\log \frac{N}{\text{cm}^{-2}}$
(1)	(2)	(3)	(1)	(2)	(3)	(1)	(2)	(3)
SH	H _I _3	976.8 ^{+5.1} _{-7.5}	SJ	H _I _0	650.6 ^{+2.8} _{-2.4}	SJ	C _{IV} _0	720.1 ^{+1.5} _{-1.5}
Al II	40.7 ^{+14.0} _{-11.1}	8.1 ^{+2.1} _{-0.9}	Al II	4.5 ^{+6.1} _{-2.4}	8.5 ^{+1.6} _{-2.6}	Al II	17.1 ^{+3.2} _{-2.8}	10.3 ^{+0.3} _{-0.3}
C I	41.4 ^{+13.6} _{-10.7}	9.7 ^{+0.5} _{-1.7}	C I	5.0 ^{+5.6} _{-2.1}	9.7 ^{+0.8} _{-2.5}	C I	17.9 ^{+3.0} _{-2.7}	10.7 ^{+0.1} _{-0.2}
C II	41.4 ^{+13.6} _{-10.7}	12.7 ^{+0.4} _{-2.3}	C II	5.0 ^{+5.6} _{-2.1}	10.4 ^{+1.7} _{-2.7}	C II	17.9 ^{+3.0} _{-2.7}	13.7 ^{+0.1} _{-0.1}
C IV	41.4 ^{+13.6} _{-10.7}	13.3 ^{+0.3} _{-3.5}	C IV	5.0 ^{+5.6} _{-2.1}	6.0 ^{+2.7} _{-2.4}	C IV	17.9 ^{+3.0} _{-2.7}	14.1 ^{+0.1} _{-0.1}
Fe II	40.3 ^{+14.1} _{-11.2}	8.9 ^{+0.7} _{-0.9}	Fe II	4.2 ^{+6.3} _{-2.7}	9.5 ^{+1.6} _{-2.6}	Fe II	16.7 ^{+3.3} _{-2.9}	9.1 ^{+0.1} _{-0.1}
H I	53.9 ^{+9.7} _{-7.5}	14.1 ^{+0.1} _{-0.0}	H I	10.9 ^{+3.4} _{-2.9}	14.2 ^{+0.5} _{-0.3}	H I	29.7 ^{+2.2} _{-2.1}	14.4 ^{+0.1} _{-0.1}
Mg II	40.7 ^{+14.0} _{-11.0}	8.3 ^{+1.9} _{-0.3}	Mg II	4.5 ^{+6.0} _{-2.4}	9.6 ^{+1.5} _{-2.6}	Mg II	17.1 ^{+3.2} _{-2.8}	9.9 ^{+0.4} _{-0.4}
N I	41.2 ^{+13.7} _{-10.8}	9.5 ^{+0.4} _{-1.3}	N I	4.9 ^{+5.7} _{-2.2}	9.7 ^{+0.9} _{-2.6}	N I	17.7 ^{+3.0} _{-2.7}	9.9 ^{+0.2} _{-0.2}
N V	41.2 ^{+13.7} _{-10.8}	11.8 ^{+0.7} _{-2.6}	N V	4.9 ^{+5.7} _{-2.2}	6.7 ^{+1.2} _{-4.3}	N V	17.7 ^{+3.0} _{-2.7}	13.1 ^{+0.1} _{-0.1}
O I	41.1 ^{+13.8} _{-10.9}	9.8 ^{+0.4} _{-0.9}	O I	4.8 ^{+5.8} _{-2.2}	10.6 ^{+1.0} _{-2.6}	O I	17.5 ^{+3.1} _{-2.8}	9.8 ^{+0.1} _{-0.1}
O VI	41.1 ^{+13.8} _{-10.9}	11.5 ^{+0.8} _{-2.9}	O VI	4.8 ^{+5.8} _{-2.2}	3.5 ^{+1.9} _{-2.2}	O VI	17.5 ^{+3.1} _{-2.8}	13.2 ^{+0.1} _{-0.1}
P II	40.6 ^{+14.0} _{-11.1}	8.8 ^{+1.0} _{-1.8}	P II	4.4 ^{+6.2} _{-2.4}	7.6 ^{+1.6} _{-2.6}	P II	17.0 ^{+3.2} _{-2.8}	10.8 ^{+0.1} _{-0.1}
S I	40.6 ^{+14.0} _{-11.1}	6.1 ^{+1.3} _{-1.4}	S I	4.4 ^{+6.2} _{-2.5}	8.0 ^{+0.8} _{-2.5}	S I	17.0 ^{+3.2} _{-2.8}	7.6 ^{+0.1} _{-0.1}
S II	40.6 ^{+14.0} _{-11.1}	10.9 ^{+0.5} _{-1.8}	S II	4.4 ^{+6.2} _{-2.5}	9.3 ^{+1.6} _{-2.6}	S II	17.0 ^{+3.2} _{-2.8}	12.1 ^{+0.1} _{-0.1}
Si I	40.6 ^{+14.0} _{-11.1}	6.8 ^{+0.8} _{-2.4}	Si I	4.4 ^{+6.1} _{-2.4}	7.6 ^{+1.1} _{-2.7}	Si I	17.0 ^{+3.2} _{-2.8}	8.0 ^{+0.1} _{-0.1}
Si II	40.6 ^{+14.0} _{-11.1}	10.2 ^{+0.8} _{-1.5}	Si II	4.4 ^{+6.1} _{-2.4}	9.6 ^{+1.7} _{-2.6}	Si II	17.0 ^{+3.2} _{-2.8}	11.8 ^{+0.2} _{-0.2}
Si III	40.6 ^{+14.0} _{-11.1}	12.2 ^{+0.3} _{-3.6}	Si III	4.4 ^{+6.1} _{-2.4}	6.3 ^{+3.1} _{-3.7}	Si III	17.0 ^{+3.2} _{-2.8}	13.1 ^{+0.1} _{-0.1}
Si IV	40.6 ^{+14.0} _{-11.1}	12.1 ^{+0.1} _{-5.1}	Si IV	4.4 ^{+6.1} _{-2.4}	5.0 ^{+4.0} _{-3.4}	Si IV	17.0 ^{+3.2} _{-2.8}	12.7 ^{+0.1} _{-0.1}